Trinity College Dublin
Coláiste na Tríonóide, Baile Átha Cliath
The University of Dublin

School of Physics

Modelling and Monitoring Geomagnetic and Geoelectric Fields in Ireland

John Malone-Leigh

June 11, 2024

A Thesis submitted in fulfilment
of the requirements for the degree of
Doctor of Philosophy

Declaration

I declare that this thesis has not been submitted as an exercise for a degree at this or any other university and it is entirely my own work.

I agree to deposit this thesis in the University's open access institutional repository or allow the Library to do so on my behalf, subject to Irish Copyright Legislation and Trinity College Library conditions of use and acknowledgement.

I consent to the examiner retaining a copy of the thesis beyond the examining period, should they so wish (EU GDPR May 2018).

Signed: _____ Date: _____

"Nothing is too wonderful to be true, if it is consistent with the laws of nature"
- M. Faraday, 1849

Acknowledgements

Firstly, I would like to wholeheartedly thank my supervisors Joan Campanyà and Peter Gallagher for all there help and support over these past four years. To Peter, I'd be lost without your enthusiasm and keen eye for precision. Joan, thank you for all the know-how and guidance on all aspects of the project, for the late Monday morning meetings and for your ability to remain ice-cold in the face of crisis.

I must thank both technical teams in DIAS and TCD for the support given to the project, with special mention for Colin, Joe and Sophie. Colin, the "road-trips" were always a welcome distraction from writing. Joe, there was never a dull moment in Birr. Thanks for all the help with proposal writing and the website Sophie. I also sincerely thank Jim Hodgson and Geological Survey Ireland for the contribution and support they gave to the project.

I was fortunate enough to meet so many lovely people I can call friends from the Astrophysics department at Fitzwilliam and Dunsink. Thanks to Eileen, Ruben, Maria K, Tadhg, Aoife, Pearse, Ciara, Brendan, Eoin, Eoin2, Mario, Shane, Maria M, Camille, Anton, David, Alberto (particularly for the hole incident), Caitríona, Jeremy, Seán, Shilpi, Beth, Corentin, Dale, Alexandra, Davit, Chris, Jonathan, Robert, Sadhbh, Stephenie, Shauna-Rose, Jeroen, Jack, Tom, Gerhard, Dev, Oisin, Pauline, Philippe, Stephen, Jef, Tony, Mika, Charlie, Matt, Paul, Gary, Hans and the Dunsink cows, just to name a few! And of course, I have to thank my family and existing friends for putting up with me for another four years.

This work was funded by the Irish Research Council's Enterprise Partnership Scheme with Geological Survey Ireland.

Abstract

Geomagnetic storms form in response to the arrival of solar storms at the Earth, which interact with the Earth's magnetic field and can lead to geomagnetic storms. Magnetic field variations generated during geomagnetic storms can interact with the subsurface geology of the Earth and in turn generate electric fields at the Earth's surface (geoelectric fields). These electric fields then drive geomagnetically induced currents in long ground-based conductors, most notably power grids, causing damage in extreme events. In this thesis, I report the research activities carried out in the last four years on the topic of modelling and monitoring geomagnetic and geoelectric fields. The main goal of this research was to monitor and expand the understanding of the potential ground-based effects across Ireland caused by space weather events.

The magnetometer network of Ireland (MagIE) is a network of geomagnetic observatories first established for research by Blake (2017). Here, this network was maintained, with an additional magnetometer observatory at Dunsink added to the network. A website (`www.magie.ie`) was created to display real-time plots of magnetic activity and to provide access to the archived data from the network. Using magnetometer data as inputs, a spherical elementary current system (SECS) interpolation model is used to estimate the magnetic field variations across Ireland with its accuracy mapped and quantified.

Measured geoelectric field time series from the space weather electromagnetic database in Ireland (SWEMDI) were used to construct a mapped three-dimensional model of geoelectric fields across the island. Transfer functions (TF) were used to relate the modelled SECS derived magnetic field to the geoelectric fields using the method from Campanyà et al. (2019), with an altered version of this model optimised and validated against measurements to model geoelectric fields in near-real time (1-minute delay). Two models were considered, one with and without a galvanic distortion correction. Galvanic distortions are caused by localised near-surface inhomogeneities recorded during geoelectric field measurements, which alter the appearance of large regional structures in the geoelectic field. Whether one model with or without a correction works better is not known, hence both are analysed here in parallel. Patterns in the geo-

electric field were then derived by modelling geoelectric field time series between 1991 – 2019, with hazard maps used to display these regions prone to significant geoelectric fields (defined as 500 mV/km here). The geoelectric field in Ireland is found to be highly directionally polarised, with peak regions identified in the South-West and Northern coast. The main effect of a galvanic distortion correction was an alteration of the dominant direction the geoelectric field is oriented in.

Finally, the effect of using three-dimensional (3D) geoelectric field inputs on modelled GIC was explored. A GIC model created by Blake (2017) simulated GIC in the Irish power grid using one-dimensional (1D) geoelectric field inputs. These inputs were updated to 3D geoelectric fields (both galvanic corrected and non-corrected), and compared to the 1D model to examine the effect of including directionally, compared against measured GIC. The 3D model improves on the 1D model at the validation site, with little difference between the galvanic corrected and non-corrected in terms of the performance metrics. The 3D models were simulated between 1989 – 2023, with the largest GIC expected in the South-West and Eastern coast. In particular, the Moneypoint site in the South-West of the island was prone to large GIC, with a maximum of 105/120A (corrected/non-corrected) modelled for the November, 1991 geomagnetic storm, with the largest duration in excess of 10A (defined as the beginning of hazardous conditions) for 153/181 (corrected/non-corrected) minutes during the Halloween, 2003 geomagnetic storm.

List Of Publications

- **Malone-Leigh, J.**,Campanyà, J., Gallagher, P.T., Neukirch, M., Hogg, C., Hodgson, J.A. Nowcasting Geoelectric Fields in Ireland using Magnetotelluric Transfer Functions, *Journal of Space Weather and Space Climate*, 2023, doi: `https://doi.org/10.1051/swsc/2023004`
- **Malone-Leigh, J.**, Campanyà, J., Gallagher, P.T., Hodgson, J.A., Hogg, C., Mapping Geoelectric Field Hazards in Ireland, *Space Weather*, 2024, doi: `https://doi.org/10.1029/2023SW003638`.
- **Malone-Leigh, J.**, Campanyà, J., Gallagher, P.T., Blake, S.P., Hodgson, J.A, Hogg, C., Updated 3D Modelling of GIC across Ireland, *Space Weather*, 2024, in prep.
- Fogg, A. R., Jackman, C. M., **Malone-Leigh, J.**, Gallagher, P.T., Smith, A. W., Lester, M., Waters, J. E., Extreme value analysis of ground magnetometer observations at Valentia observatory, Ireland, *Space Weather*, 2023, doi: `https://doi.org/10.22541/essoar.168500313.34097280/v1`
- Hudson, H., **Malone-Leigh, J.**, Woan, G., Osborne, C. "A Glasgow geomagnetic observation of a solar flare", *RHESSI Science Nuggets*, 2023.
- Fogg, A. R., Lester, M., Yeoman, T. K., Carter, J. A., Milan, S. E., Sangha, H. K., Elsden, T., Wharton, S. J., James, M. K., **Malone-Leigh, J.**, Paxton, L. J., Anderson, B. J., Vines, S. K., " Multi-Instrument Observations of the Effects of a Solar Wind Pressure Pulse on the High Latitude Ionosphere: A Detailed Case Study of a Geomagnetic Sudden Impulse", *Journal of Geophysical Research: Space Physics*, 2023, doi: `https://doi.org/10.1029/2022JA031136`

Contents

List of Figures

List of Tables

List of abbreviations

AC	Alternating Current
ADC	Analogue to Digital Converter
AE	Auroral Electrojet Index
AL	Westward Electrojet Index
AU	Eastward Electrojet Index
BGS	British Geological Survey
CIR	Corotating Interaction Region
CME	Coronal Mass Ejection
DC	Direct Current
DIAS	Dublin Institute for Advanced Studies
DST	Disturbance Storm Time Index
EM	Electromagnetic
ESA	European Space Agency
EUV	Extreme Ultraviolet
FAC	Field Aligned Currents
FFT	Fast Fourier Transform
GFZ	German Research Centre for Geosciences
GIC	Geomagnetically Induced Current
GSI	Geological Survey Ireland
GSNI	Geological Survey Northern Ireland
IGRF	International Geomagnetic Field Reference
IMF	Interplanetary Magnetic Field
INTERMAGNET	International Real-time Magnetic Observatory Network
IRETHERM	Irish Geothermal Energy Project
IRECCSEM	Irish Clare Carboniferous Seismic and Electromagnetic Survey
ISLE-MT	Irish Magnetotelluric Lithosphere Experiment
ITF	Inter-station Transfer Function
K-Index	Kennziffer Indicator
Kp-Index	Planetary Kennziffer Indicator
MagIE	Magnetometer Network of Ireland
MT	Magnetotelluric
PoE	Power Over Ethernet
Rpi	Raspberry Pi

SECS	Spherical Elementary Current Systems
SFe	Solar Flare Effect
SONI	System Operator for Northern Ireland
SSC	Sudden Storm Commencement
SWEMDI	Space Weather Electromagnetic Database in Ireland
TCD	Trinity College Dublin
TF	Transfer Function
VLF	Very Low Frequency
YY	Two Winding Transformer
1D	1-Dimensional
2D	2-Dimensional
3D	3-Dimensional

List of constants

All constants are in standard units as defined by the International System unless stated otherwise:

ϵ_0 =8.8541878128 $\times 10^{-12}$ F·m^{-1}
k_b=1.380649 $\times 10^{-23}$ J·K^{-1}
μ_0 = 1.25663706212$\times$ 10^{-6} N·A^2

1 Introduction

Space weather is concerned with understanding and evaluating the impact of solar activity, related to features/mechanisms on the Sun such as sunspots and solar flares, on the Earth and near-Earth space. Space weather impacts the Earth's atmosphere and particularly the Earth's magnetic field. Charged particles, expelled from the Sun that travel in the solar wind pose a hazard to many modern technologies, as they can impact the Earth's magnetic field, initiating a geomagnetic storm. The induction of geomagnetically-induced-currents (GICs) in power-grids, currents which can form on ground based conductors during geomagnetic storms, is a significant threat during geomagnetic storms. Large GIC, capable of damaging infrastructure, is not generated directly by magnetic variations related to geomagnetic storms, but indirectly from the resistive Earth. Magnetic variations charge the Earth's lithosphere (crust and upper mantle), which drives an electric field at the surface, which in turn drives GICs. In this chapter, some context behind space weather, geomagnetism and geoelectric field induction is explained, including a history of their discovery, and a summary of the physics behind how they work and how they can impact ground-based technologies such as power-grids. This is then followed by a brief overview of this thesis as a whole.

1.1 A History of Space Weather and Geomagnetism

1.1.1 Discovery of Sunspots

Alongside many other branches within the scientific domain, space weather and geomagnetism were not known to exist until relatively recently in history. Some of the phenomena related to space weather, primarily the aurora, were well known for centuries/millennia prior, but the physical reasoning for their formation was unknown. The first major discovery in the field of space weather was the discovery of sunspots (dark spots on the Sun, that are cooler than surrounding areas, caused by magnetic activity at the surface of the Sun). While some reported observations of sunspots existed prior to 1600 in ancient Chinese records (Xu et al., 2000), the first to document, record and publish a detailed report of a sunspot, comes from Johannes Fabricius in 1611 (Fabricius, 1611; Casanovas, 1997). Fabricius tracked sunspots using a camera obscura (a dark room with a tiny slit to allow sunlight in) alongside a telescope and

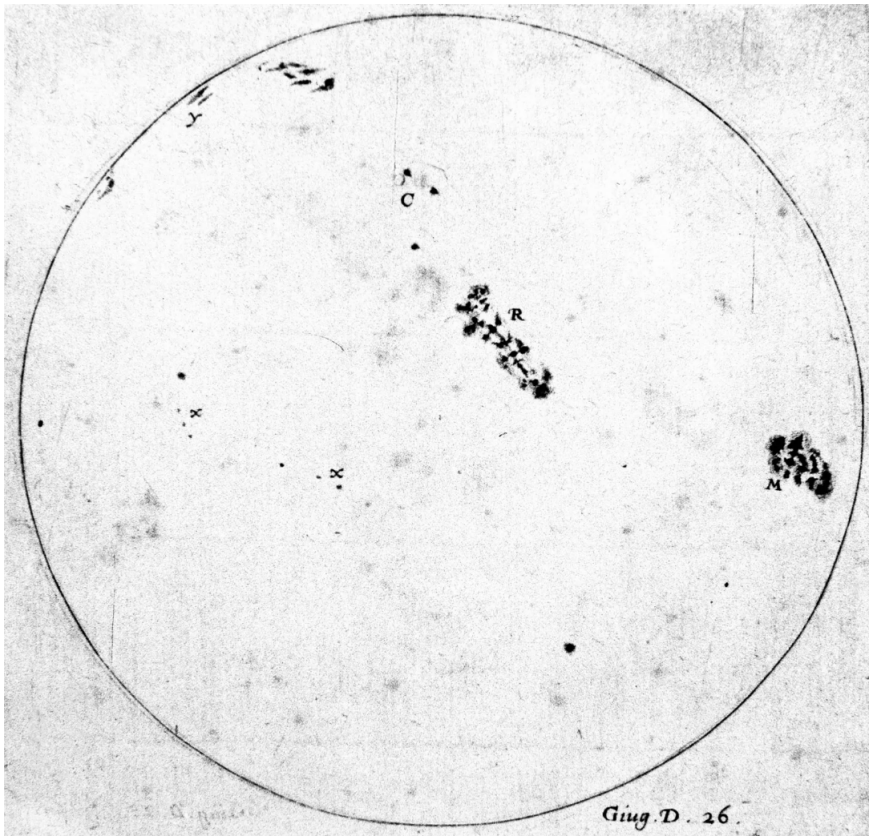

Figure 1.1: One of the earliest illustrations of sunspots, with sunspots denoted by letters C, R, M and X (Galilei, 1613).

found that they appeared to rotate, and hypothesised that the Sun itself must also be rotating. Shortly thereafter, Galileo Galilei (Figure 1.1) and Scheiner, also published work in support of the existence of sunspots and fiercely contested as to who discovered them first (Casanovas, 1997). It wasn't until later in the mid 1800's however that astronomers began to hypothesise that activity related to sunspots could be responsible for changes in the Earth's magnetic field.

1.1.2 Geomagnetism, the Aurorae and Induced Currents

Following the discovery of sunspots there was exploration into understanding the connection between the Sun, the Earth and geomagnetism. A first connection was drawn between geomagnetic activity and the aurorae separately by Graham, and Hjorter and Celsius in 1741 (Stempels, 2011; Svalgaard, 2017), as they noticed fluctuations in compass readings when aurorae were overhead. Later more thorough observations proved the existence of a connection between the aurorae and magnetic fluctuations beyond reasonable doubt, where Von Humboldt observed magnetic fluctuations, alongside auroral observations every half hour for six and a half hours in December, 1806 (Von Humboldt, 1808; Lakhina and Tsurutani, 2016). This connection between the two phenomena later led to some, such as Faraday, to hypothesise that the aurorae were some form of electricity (Hackmann, 1995). We now understand that the auro-

rae are in fact due to the emission of light caused by ionised particles in the upper atmosphere (the ionosphere), which themselves can form electrical currents. These currents are mostly responsible for the large magnetic variations measured at the surface of the Earth by magnetometers and hence can interact indirectly with ground based conductors. Telegraph wires were the first of these conductors impacted by the effects of space weather. Telegraph lines were often hundreds of kilometres long, which made them ideal for inducing large currents. The first report of telegraph lines being affected comes from Barlow (1849), who reported that during his observation of an aurora on the 19th May 1847, "strong alternating deflections occurred on all the telegraph devices". This observation was validated by many other reports of similar geomagnetic/auroral events in the following decades, such that by 1875, the relation between telegraph failures and geomagnetism was widely accepted and published in many books regarding telegraph operation (Prescott, 1875; Lanzerotti, 2017). While the connection between aurorae, electricity, magnetic activity and induced currents on the ground was distinguished early on, the connection between magnetic field variations and its origin on the Sun took some more time to discover and was more controversial.

1.1.3 The Carrington Event and the Sun-Earth Connection

The establishment of magnetometer observatories contributed greatly to the discovery of the Sun-Earth connection, the earliest of which including Greenwich (1817) and Observatoire de Paris (1823), with 53 magnetometer observatories worldwide by 1841, including the likes of Trinity College Dublin (1835), Toronto (1840) and Mumbai (1841). Researchers began trying to identify the source of these magnetic fluctuations and auroral currents, with some incorrectly hypothesising that meteors/comets must be somehow generating "atmospheric electricity", at first (Morton Briggs, 1967). The discovery of the solar cycle (variations in the number of sunspots over 11 years) by Schwabe (1843) was the first step to unraveling the mystery. In 1850, Edward Sabine discovered a similar 11 year cycle in the minima and maxima of geomagnetic field variations, that he noticed matched up remarkably well with the aforementioned solar cycle (Sabine, 1850). This led to Sabine hypothesising that the solar cycle and geomagnetic cycle are the same and that the Sun must somehow be magnetic and is causing these geomagnetic variations. Between 30th August to 4th September 1859, the biggest piece of evidence to support the Sun-Earth connection was obtained after arguably the largest geomagnetic storm in recorded history occurred, the Carrington event (Carrington, 1859; Hodgson, 1859). Carrington observed the evolution of a growing sunspot (Figure 1.2), when he saw a bright rapid flash come from this region of the Sun (the first recorded solar flare). This flash occurred near-simultaneously to a large dip or "crochet" in magnetic field in magnetometers across the world, what we know today to be the "Solar Flare effect" (SFe), where X-rays and UV light from the flare ionise particles in the Earth's upper atmosphere. Approximately nineteen hours following

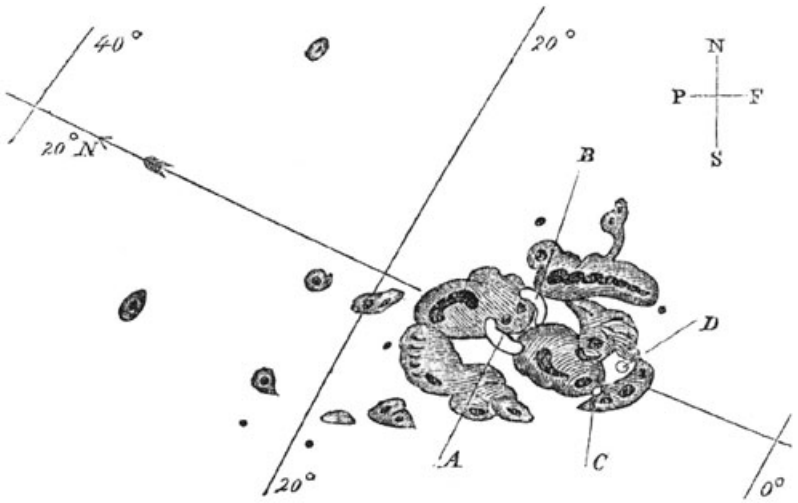

Figure 1.2: A sketch of the sunspot region which led to the large geomagnetic storms by Carrington (1859). A and B denote the areas in which "white light broke out" which we now know to be a solar flare, with its last recorded position at C and D.

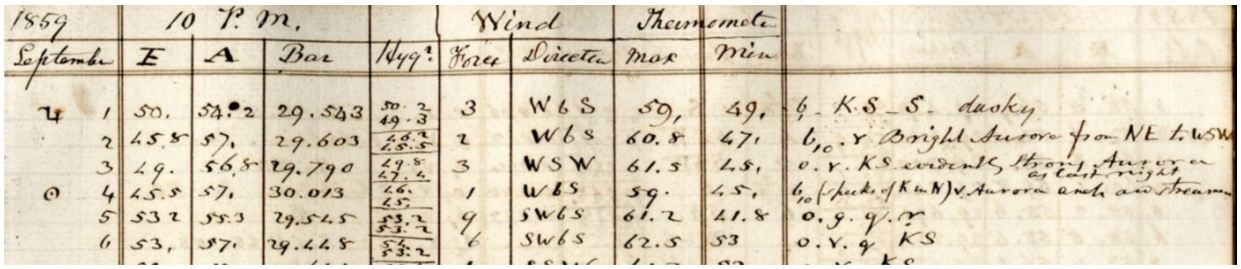

Figure 1.3: Meteorological records noting the strong auroral display between the 2nd – 4th of September 1859, from Armagh Observatory (Infield, 2009).

this, the largest magnetic field variations ever observed were recorded, accompanied by the largest known auroral display, with aurorae seen as far south as Cuba and Morocco and lasting the span of three nights from 1st to 3rd of September (de la Rive, 1859; Green et al., 2006; Cliver and Dietrich, 2013). In Ireland, records of the auroral display from Armagh Observatory (Figure 1.3), indicate that strong aurorae were visible for a relatively long period of the nights, with an aurora on the night of the 2nd, spanning across the sky from the North-East to the South-West-West (Butler and Hoskin, 1987; Hayakawa et al., 2019). The Carrington event was also the first recorded instance of damage caused by space weather, in the aforementioned telegraph line network. There are many instances from historical records of fires breaking out on telegraph poles at this time. In some instances, telegraph operators reported being able to still communicate, despite turning off the power source to the telegraph, due to induced electrical currents caused by the event (Clement, 1860; Boteler, 2006). During this period of the past, technology was not nearly as sophisticated. Without the presence of larger-scale infrastructure susceptible to space weather that now exists in modern society, such as power lines or electrified rail-lines, damage was ultimately limited.

After the Carrington event, many scientists were still sceptical about the Sun-Earth

connection. Most famously, president of the Royal Society and renowned physicist Lord Kelvin proposed that the Sun-Earth connection did not exist, stating in 1892 that "It seems as if we may also be forced to conclude that the supposed connection between magnetic storms and sunspots is unreal, and that the seeming agreement between the periods has been mere coincidence", as he supposed the heat and light output of the Sun was insufficient to cause these magnetic variations (Thomson, 1893). The observational evidence for the Sun-Earth connection became more and more clear over time with arguments against it dwindling, however the mechanism behind the connection had not yet been deduced. This missing piece of the puzzle was the solar wind. Fitzgerald (1892) suggested that sunspots could emanate material "like a comets' tail" and could be the source of geomagnetic storms, with Lodge (1900) expanding on this point, suggesting that geomagnetic storms were caused by "a torrent or flying cloud of charged atoms or ions" originating from sunspots. It was much later however that the solar wind was confirmed to exist. Biermann (1951) demonstrated that comet tails always point away from the Sun, and hypothesised that a gas blowing out of the Sun must be the cause. Parker (1958), suggested a mechanism for this loss, that electrically charged particles were ejected from open magnetic field lines on the Sun. Magnetic observations by the Pioneer V and particle observations from the Mariner II satellites in 1960 and 1962, respectively, later confirmed the existence of the solar wind (Neugebauer, 1997). These open magnetic field lines are one source of the solar wind, but there is another. In 1971, the coronagraph onboard the OSO-7 spacecraft observed the first coronal mass ejection (CME), a massive explosive ejection of charged particles originating from a sunspot and accompanied by a solar flare (Tousey, 1973). Following this observation it was deduced that the aforementioned Carrington event in 1859, must have been caused by a CME related to the solar flare that Carrington observed.

Now that the solar sources had been deduced, the connection to the Earth's magnetic field was the last piece in the puzzle to be explained. Dungey (1961) and Axford and Hines (1961) proposed the mechanism as plasma transport between the Earth and the solar wind. When the solar wind's magnetic field (interplanetary magnetic field, IMF) is anti-parallel to the magnetic field of the Earth, the magnetic fields join, and particles propagate down the magnetic field lines towards the poles of the Earth. Finally we have our mechanism(s) for the Sun-Earth connection. The basis for the Sun-Earth connection and space weather has been provided. Later in this thesis, more of the how and why these structures form and interact will be explored.

1.2 Modern Impacts of Space Weather

The threat posed by potential extreme space weather events, such as by a geomagnetic storm on a similar scale to the Carrington event, have been heavily studied regarding

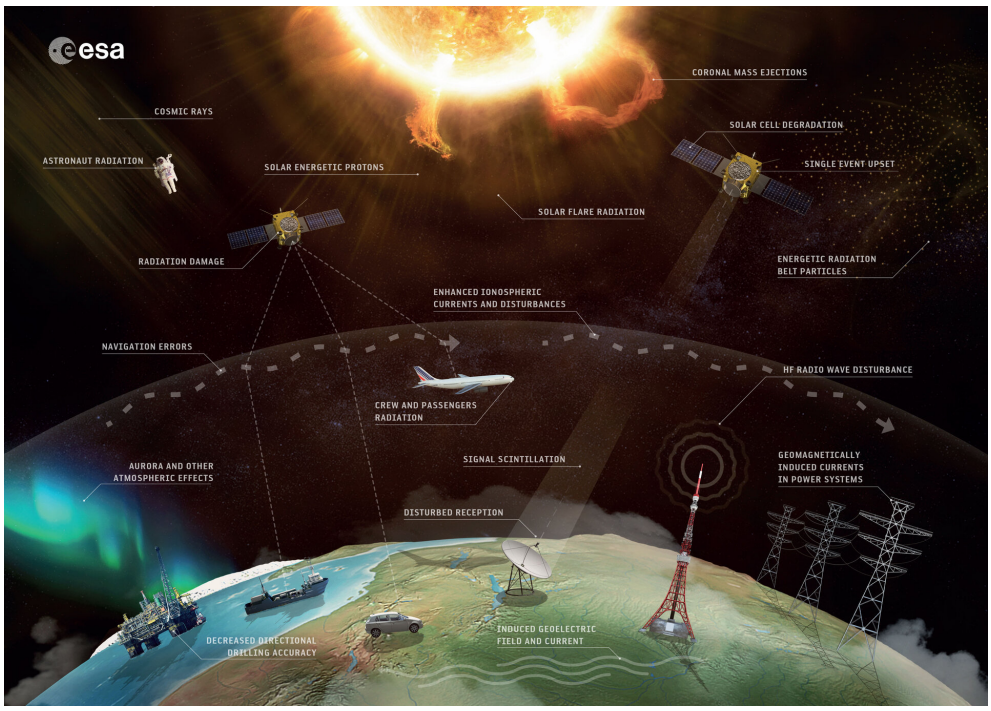

Figure 1.4: A general summary of the types of objects impacted by and phenomena related to space weather within near-Earth space. (Image from the ESA website `https://www.esa.int/`).

impacts on Earth, as well as the impact on satellites. In 1859, infrastructure affected by geomagnetic storms was limited to the telegraph. However, in today's technologically advanced society a much wider variety of infrastructure is now at risk to the hazardous effects of space weather. The effects of a large event of that scale nowadays (Figure 1.4) could include: a) large scale power blackouts due to GIC; b) increased corrosion in pipelines (Campbell, 1986; Pulkkinen et al., 2001); c) false signaling in railway systems (Patterson et al., 2023); d) a complete loss of radio communication and transmission for the duration of the storm (Redmon et al., 2018); e) significant disruption and possible damage to satellites (MacAlester and Murtagh, 2014) and e) grounding aviation (Kauristie et al., 2021), among other effects. Of all of these impacts, the concern due to power outages is the greatest in terms of the costs of damage (Eastwood et al., 2017b).

The most recent significant example of geomagnetic storms causing large scale damage is the geomagnetic storm of March, 1989. During this storm, power grids suffered from large GIC which led to instability within the power network in some parts of the US and Canada, but particularly in Québec, Canada, where damage to the network led to a nine hour blackout, with power equipment damage totalling US$ 13.2 million. However, US$ 2.9 billion was estimated in losses for the US and Canada due to the knock-on damage following the event due to loss of operation, including all industries and facilities reliant on power grids (Centra-Technology-Inc., 2011). A Carrington like event's impact would be significantly more damaging than the 1989 storm. For example, it could lead to a

sustained global power outage event, which would further lead to a significant financial cost related to both damage and disruption. There are two cases to consider when determining the potential cost of damage from a large geomagnetic storm: a) direct damage, mostly related to damage to transformers in power grids; b) indirect damage, related to the knock-on impact of a sustained damage. Regarding direct impact, if a geomagnetic storm was large enough to down enough transformers, it could potentially take months to fully repair the power grid (production of transformers is limited, delaying the time taken for the replacement of a transformer in the grid), with the power grid not just down for the duration of the geomagnetic storm (Oughton et al., 2017). Transformers are expensive and would be costly to replace and it can be difficult to integrate a new transformer properly into a power grid. Indirectly, most modern institutes and facilities rely almost entirely on electricity, including the likes of food and water distribution/preservation, the operation of hospitals and banks, stock markets, computerisation and all that comes with it, family homes, among many many others. Some estimates for the worst case scenario, assuming a large Carrington event occurs approximate that the total economic cost, in the US alone, of up to US$40 billion a day (Schrijver et al., 2014; Oughton et al., 2017). Similar costs would likely be incurred for many countries across the world.

Countries at higher latitudes near the auroral oval ($> 60^{o}$ N, $< 75^{o}$), are at particular risk from GICs, where geomagnetic activity is larger and more frequent (Pirjola, 2000). While most areas closer to the poles/auroral ovals have greater magnetic activity, this does not always equate to the induction of GIC. Induction of GIC is not caused directly by magnetic variations, which are greatest near the auroral ovals, but rather by magnetic variations inducing a bulk charge in the top layer of the Earth, the lithosphere made up of the crust and upper part of the mantle (Anderson, 1995), with this charge exerting an electric field on the surface which drives GIC (Figure 1.5). Significant GIC can still occur at lower latitudes, provided the conductivity structure of the lithosphere is resistive enough. A more recent example of GIC occurring at a middle latitude country occurred during the "Halloween storm" in October 2003, in South Africa, where the geomagnetic field variation was less intense compared to March 1989 (Katamzi and Habarulema, 2014), but the impact was significant, with one downed transformer, and significant damage to multiple others, leading to their replacement a year later (Koen and Gaunt, 2003, see example in Figure 1.6). This example originated in a region with a strongly resistive and complex lithosphere (Jones et al., 2007; Moorkamp et al., 2022), which led to the enhanced induction of strong geoelectric fields (resistivity increases with geoelectric field as the charge cannot be dissipated easily by the subsurface) demonstrating the link also between lithospheric resistivity and GIC. Ireland, while at a mid latitude, is a region with a complex resistive lithosphere (Rao et al., 2014) which can drive large geoelectric fields at the surface (Campanyà et al., 2019) and is thus

vulnerable to GIC. Due to the smaller scale of Ireland's power grid compared to other countries, this risk is more limited. However, previous work in Ireland, by Blake et al. (2016), Blake (2017), and Blake et al. (2018) estimated that GIC in excess of a hundred Amperes (A) could have been induced for both the March, 1989 and Halloween, 2003 storms, an amount sufficient to cause some damage to transformers (Rosenqvist et al., 2022). Historical evidence of GICs causing damage and disruption in Ireland does exist for telegraph lines. The Irish Times reports on significant interference by a "mysterious atmospheric influence" coinciding with the May, 1921 geomagnetic storm, arguably the second largest geomagnetic storm after the Carrington event, as well as some more minor events in the early 1900's (Hapgood, 2019). National electrification across Ireland did not occur until after these events, beginning only in 1929, thus no damage could be done to a power grid (McCarthy, 1957). While no damage has occurred to the Irish power network historically, hypothetically the network could be damaged should another Carrington scale geomagnetic storm or similar occur. Therefore, research into the possible induction of GICs in Ireland is necessary to help predict large events and safeguard infrastructures and in particular power grids in Ireland and hence performed later in this manuscript.

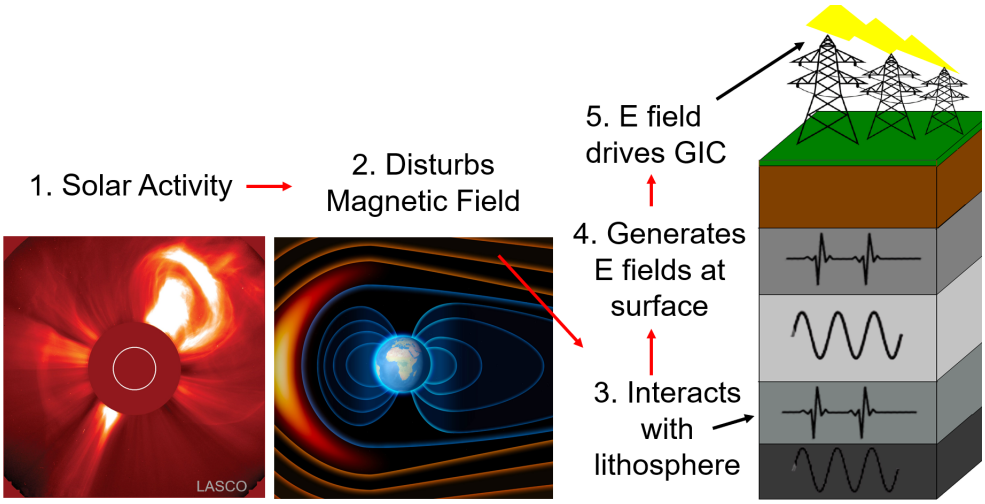

Figure 1.5: A summary of the steps involved between solar activity inevitably leading to induced currents in power lines. Outbursts from active regions on the Sun can impact and disturb the Earth's magnetic field, causing a geomagnetic storm. Magnetic field variations during the storm interact with the resistive lithosphere of the Earth, effectively charging the Earth. This charge generates an electric field at the surface of the Earth, which can drive induced currents in any ground-conductors, such as power-lines

1.3 Objectives and Outline

The aim of this project is to study geomagnetic storms in Ireland using the Magnetometer Network of Ireland (MagIE), particularly by focusing on the underlying geomagnetic and geoelectric fields variations across Ireland, which can drive GICs, to determine if

Figure 1.6: Failure in a transformer three weeks following the Halloween storm, 2003, in South Africa (Thomson et al., 2010). Damage sustained from the storm led to overheating in the transformer, later leading to an arcing fault (an electrical fire).

specific areas or times are more vulnerable to geomagnetic storms. Ultimately, this research was performed to help understand and perhaps mitigate potential damage, for when a large-scale impact like the Carrington event inevitably impacts the Earth. This required both: a) a physical aspect, regarding the installation and maintenance of equipment such as magnetometers used to observe storms and; b) a modelling aspect, modelling the geomagnetic field, geoelectric fields and GICs in Ireland. Each chapter in this thesis is outlined below.

Chapter 2: Theory and Background - A comprehensive background is provided on the main physical concepts of geomagnetism, space weather and ground-based effects, so that the reader can form an understanding of the topic as a whole, before delving deeper in content.

Chapter 3: Monitoring Geomagnetic Storms - A description of MagIE, is presented, including a description of the network, the MagIE website and quantifying magnetic disturbances. A description of instrumentation used in the project is provided, including types of magnetometer, how magnetometer sites are installed, as well as new installations, maintenance and automation of data to the MagIE website.

Chapter 4: Modelling Geomagnetic Fields - The methods of modelling geomagnetic fields used are explained. An investigation into a) the interpolation methods used here to model geomagnetic fields across Ireland b) seasonality in the geomagnetic field.

Chapter 5: Surveying, Modelling and Nowcasting Geoelectric Fields - The techniques used to model and map geoelectric fields are described. Following this description, a new approach of modelling geoelectric fields in near real time, or nowcasting, developed during this project is presented, including details related to how it works, why it is needed and how it expands on the state of the art in the field.

Chapter 6: Hazard Mapping Geoelectric Fields - The workflow, generation and result of applying a hazard mapping approach to geoelectric fields to identify areas more susceptible to large potentially damaging events.

Chapter 7: Modelling GIC - A previous state-of-the-art 1D geoelectric field input GIC modelling in Ireland's power grid is updated and compared to a model using 3D geoelectric field inputs. A newer, more accurate model provides information on where the largest predicted GIC is predicted to occur in the Irish network.

Chapter 8: Conclusions - A quick general discussion of the work in the thesis as a whole is provided with the main conclusions grouped together.

Chapter 9: Future Work - Detail on plans for the future of the network and modelling ground-based effects are discussed.

2 Theory and Background

This chapter provides a literature review for the reader, with an overview of the state-of-the-art in research alongside an explanation of the underlying theory. Firstly, a background on the Sun, solar storms and how solar storms generate geomagnetic storms is provided. This is followed by a background on the environment within the Earth's magnetic field, detailing how and why geomagnetic storms form. Then geoelectric field induction is explored, including details on the mechanism behind induction, with a background in magnetotellurics and how geoelectric fields can be modelled. Finally, a description of how GICs are induced in power grids is presented, followed by a description on how GICs can be computationally modelled.

2.1 Solar Activity

The Sun is the primary source of space weather, with solar activity ultimately driving space weather at the Earth. High energy electromagnetic (EM) radiation and particularly particle and mass plasma ejection originating from the atmosphere of the Sun can impact the Earth's magnetosphere and atmosphere. Charged particles are continually escaping the Sun along open magnetic field lines and form the solar wind, which can impact the Earth's environment to a minor extent during quiet periods. However, the greatest impact comes when the quantity of high energy EM radiation and particles is enhanced, due to phenomena related to active regions on the Sun.

2.1.1 Sunspots

Sunspots are relatively dark regions on the surface of the Sun, caused by complex magnetic structures at the surface, that can form temporarily on the sun on the order of months (van Driel-Gesztelyi and Green, 2015), remaining roughly in the same area of the Sun during its lifetime. Magnetic flux in these regions inhibits convection leading to a lower temperature and thus appearing darker than the rest of the surface. A basic sunspot is generally composed of two poles, one positive and one negative. However, sunspots can become much more complex as they develop and become capable of releasing trapped magnetic energy explosively, which could ultimately impact the Earth. For this reason, sunspots are categorised based on their polarity and complexity, most

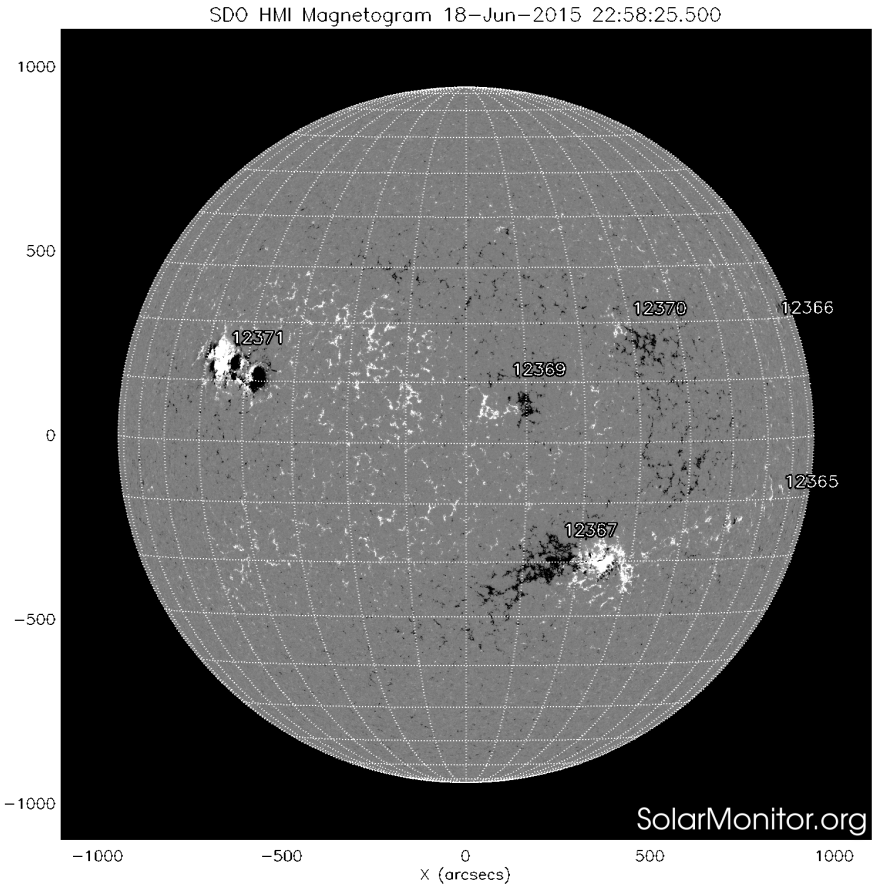

Figure 2.1: A magnetogram of the Sun on the 18th June 2015. Black and white represent the polarity within sunspots, with each sunspot number denoted. Each example of sunspot mentioned in the text is present on this day. Region 12365 is a small α sunspot, 12369 is a β sunspot, 12367 is a large $\beta\gamma$ sunspot and 12371 is a $\beta\gamma\delta$ sunspot. A coronal mass ejection from region 12371 led to the largest geomagnetic storm in the last solar cycle on the 22nd – 23rd of June 2015.

commonly by the Mount Wilson Classification system (Künzel, 1965). An α sunspot is composed only of spots of a single polarity, a β sunspot is composed of the basic bipolar example mentioned previously. A suffix γ can be added to a β sunspot to denote that the sunspot has added complexity, in which the two major spots are accompanied by multiple minor spots as well. Another suffix δ can also be added if two opposite poles within the spot are very close ($< 2^o$). $\beta\gamma\delta$ sunspots are the most complex sunspots and thus most unstable, which can lead to the explosive release of magnetic energy trapped within these sunspots, particularly if they interact with other nearby sunspots (examples of each are shown in Figure 2.1). Hence, these are generally considered the most geo-effective type of sunspots.

2.1.2 Solar Flares

Solar flares are an intense burst of high energy EM radiation (particularly bright in X-ray and Extreme Ultraviolet or EUV spectra) that generally originate above or nearby sunspots within the corona of the Sun. Magnetic loops known as filaments or promi-

nences can form. When oppositely aligned magnetic fields within these prominences join or reconnect (see Figure 2.2, also explained more in Section 2.2.2) an enormous amount of built up magnetic energy is released, which can generate solar flares. Solar flares have the smallest, but most immediate effect on the geomagnetic field. The region of the Earth's upper atmosphere known as the ionosphere absorbs X-ray and EUV radiation from the Sun instantaneously with the arrival of sunlight, which ionise particles in this region, and these particles then form current systems due to the magnetic force exerted by the Earth's magnetic field on them. Solar flares are particularly bright at this wavelength range and thus lead to significantly enhanced ionisation. Solar flares are also indirectly related to other phenomena related to the release of magnetic energy on the Sun, such as coronal mass ejections and thus can be used as possible precursors for geomagnetic storms.

2.1.3 Coronal Mass Ejections and Coronal Holes

Two features on the Sun lead to the enhanced release of charged particles into the solar wind. Coronal mass ejections (CMEs) are ejections of charged particles from active regions on the sun (such as sunspots), which occur during the explosive release of magnetic energy from these regions (hence CMEs often, but not always, accompany large solar flares). Magnetic field lines at the surface of the Sun can become twisted and distorted causing them to rise above the solar surface and forming solar prominences (Figure 2.2). Large quantities of plasma from the surface/atmosphere of the Sun can become trapped within these twisted magnetic field lines (flux ropes). When anti-parallel magnetic field lines in prominences join or "reconnect" the solar prominences can erupt explosively releasing these flux ropes and the charged particles into the solar wind.

The other main source of plasma enhancement in the solar wind are coronal holes. Coronal holes are less dense regions in the Sun's atmosphere where the Sun's magnetic field lines are open and extend into space. These regions are usually located at the solar poles, but can form at lower solar altitudes. Coronal holes allow plasma to escape the Sun's surface at a much faster rate than in areas with closed field lines, particularly amplifying the speed, but also the density of the solar wind. This faster solar wind catches up with slower solar wind, forming a co-rotating interaction region (CIR), with a significantly increased density in plasma, which can then impact the Earth. However, CIRs are normally less geoeffective than CMEs. Plasma speeds and densities in CIRs are normally lower than those from large CMEs, with CIRs leading to relatively smaller storms and never solely generating historically large storms such as the Carrington or March 1989 events mentioned in Chapter 1.

While many CIRs and CMEs form over the course of the solar cycle (Section 2.1.5),

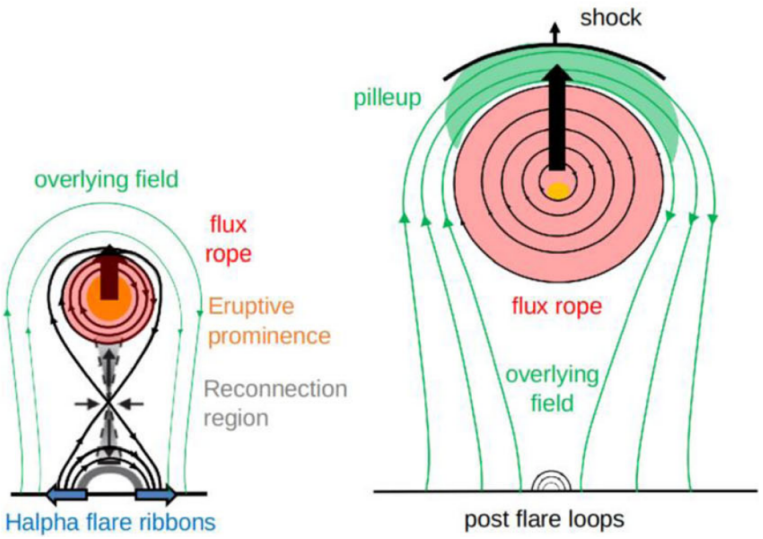

Figure 2.2: A diagram describing reconnection in a prominence. Oppositely aligned magnetic field lines join, which releases built up magnetic energy. This can then release a flux rope, containing large amounts of plasma (red region) from the Sun into the solar wind (Zhang et al., 2021).

most are not geoeffective (i.e. affect the Earth) as most are directed away from the Earth. The origin of the sunspot or coronal hole most often needs to be near the centre, or between the centre and western limb of the Sun (the right-hand side of the Sun from the perspective of the Earth) to affect the Earth. The Sun rotates at a rate of approximately 27 days every month at its equator, with a roughly 7 – 10 day window in which these active regions could possibly impact the Earth (Hathaway, 2010).

2.1.4 Solar Wind

The solar wind is the stream of charged particles continuously ejected from the Sun's outer atmosphere, the corona. The corona is superheated to approximately 1.5×10^6 K, forming a plasma that is almost entirely ionised (Morgan and Taroyan, 2017). At these temperatures, free electrons within the plasma can attain thermal velocities of thousands of km/s, exceeding the thermal velocity of the Sun $\approx$ 400 km/s, and pull protons and positively charged ions such as alpha particles along with them through electrostatic attraction. The velocity of the solar wind can vary depending on the region the plasma originates from. In regions with closed magnetic field lines (more generally near the equator of the Sun), the slow solar wind flows at $<$ 500 km/s, while in areas with open magnetic field lines (such as coronal holes), the plasma can become accelerated and flows at $>$ 800km/s. This plasma takes roughly 2 – 5 days to reach the Earth dependent on this velocity. When plasma gets far enough away from the influence of the solar magnetic field, it escapes radially from the Sun. As it does however, the Sun is rotating and thus this leads to the formation of an Archimedean spiral (see Figure 2.3), known as the "Parker" spiral (Parker, 1969). As the plasma

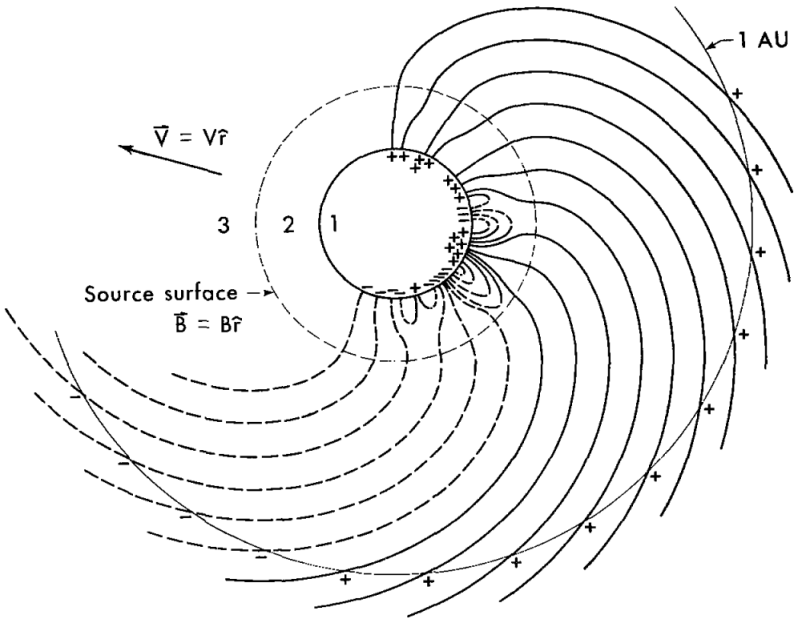

Figure 2.3: A representation of a Parker spiral from Schatten et al. (1969) looking down on the ecliptic plane with regions 1 (the Sun), 2 (the corona) and 3 (interplanetary space). Region 1 is the surface of the Sun, with the "+" and "-" signs denoting the magnetic field at each site on the Sun. Plasma escapes from the region of the corona and flows radially outwards from the entire Sun (denoted by the vector $\vec{V}$) and draws out a Parker spiral, with the imprint of frozen magnetic fields.

travels in the solar wind, it extends out a magnetic field out into space (frozen or imprinted into the plasma from when it leaves the corona) known as the interplanetary magnetic field (IMF).

2.1.5 Solar cycle

The solar cycle is the change in the number of sunspots observed on the surface of the Sun matching with the Hale cycle, whereby the Sun's magnetic field orientation flips with an average duration of 11 years (Hathaway, 2010). At the start of the cycle, the magnetic field of the Sun is in a stable orientation, with relatively few sunspots or regions of magnetic complexity. Sunspots begin to appear at a latitude of 40°. As the magnetic field reverses, the field becomes less stable with more and more sunspot regions forming on the Sun, with sunspots moving equator-ward. As flaring and CMEs occur mostly within sunspots, they both correlate strongly with the solar cycle sunspot number. However, the most intense flaring (and hence largest CMEs) usually occur two to three years after sunspot number maximum. This is hypothesised to be due to increased interaction between sunspots from opposite hemispheres as they move closer together (McIntosh and Leamon, 2014, see Figure 2.4). Hence, peak geomagnetic activity is generally also observed two to three years after maximum (Chapman et al., 2020). Solar cycles often vary significantly in strength from cycle to cycle, for which the underlying physics is not well understood. The last solar cycle (24) for example

was the weakest on record since the 1910's and hence little geomagnetic activity was observed (Nandy, 2021). The current solar cycle (25) has exceeded the strength of the prior cycle, and is expected to peak in late 2024. However, relative to the other cycles in the last 100 years, it is expected to be relatively weak (Upton and Hathaway, 2023). Hence, the largest geomagnetic storms are most likely to occur between 2026 – 2027 for this solar cycle, though a storm with the magnitude of the Carrington event is unlikely.

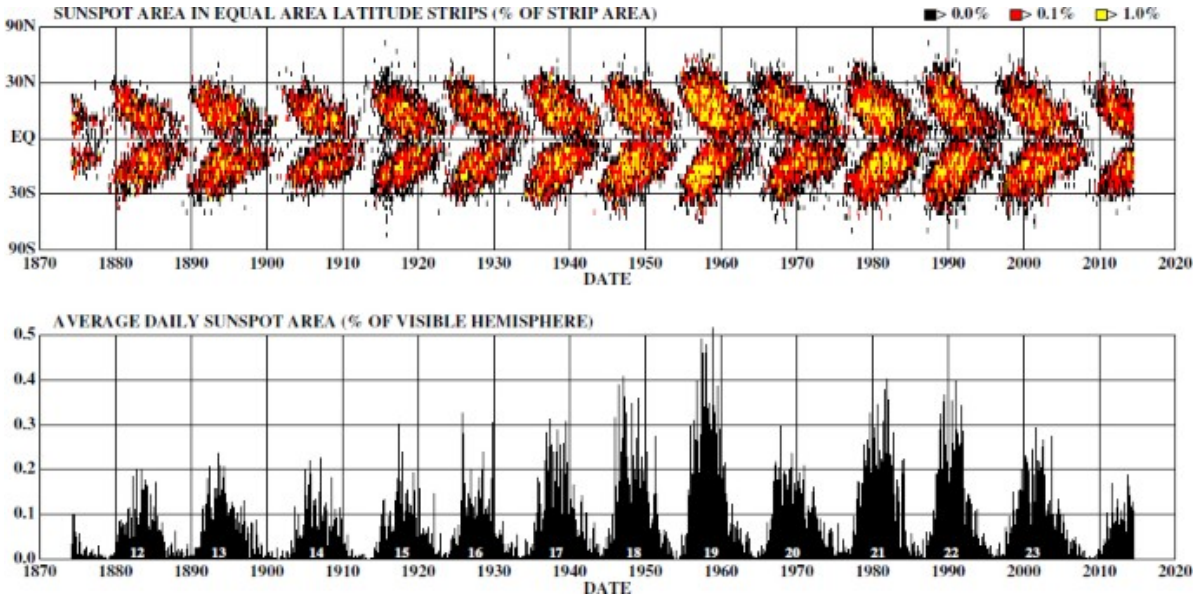

Figure 2.4: The solar cycles between 1870 – 2020 displayed in terms of: top) relative latitude of spots on the Sun as the cycle progresses and bottom) total area occupied by sunspots. Sunspots within a cycle first appear at approximately 40° latitude before moving equatorward, peaking in number (and hence area) when sunspots are around 15°, before numbers decline with the last stops forming nearer 5°. All this occurs over the course of approximately 11 years before repeating again. Image from Hathaway (2015).

2.2 The Environment of Earth's Magnetic Field

2.2.1 The Geomagnetic Field

The geomagnetic field, the magnetic field belonging to the Earth, extends from the Earth's interior out into space and forms the bulk of the magnetic field measured at the surface. The Earth generates this intrinsic magnetic field, which helps protect us on the surface of the Earth, from plasma originating from the solar wind. The main hypothesis which is suspected to generate the intrinsic magnetic field is known as dynamo theory, which suggests that a rotating body of electrically superconducting fluid will generate and maintain a stable magnetic field (Roberts and Glatzmaier, 2000). This electrically conducting fluid is thought to be molten nickel and iron in the outer core of the Earth, with the convection of heat between the solid inner and molten outer core of the Earth generating motion of this fluid. The coriolis force acting on this fluid

causes it to circulate and hence generates a magnetic field. The magnetic field strength varies across the surface, with strengths of 3×10^5T close to the equator, and 6×10^5T towards the poles at solar quiet times (Thébault et al., 2015). The magnetic field of the Earth is relatively stable on timescales of years, but over a longer duration it is dynamic, due to slow changes in the currents in the Earth's core (Figure 2.5). The magnetic field effectively "wobbles", with slight increases/decreases in magnetic field strength and orientation of the poles. For example the geomagnetic pole has wandered 4^o away from its original position in the last 120 years and weakened to 91% its original strength (Thébault et al., 2015). Occasionally the geomagnetic field can flip during a magnetic reversal, leading to a weakened magnetic field, however this is rare, with occurrence rates of hundreds of thousands to millions of years (Kent and Gradstein, 1985). Due to the slow nature of the change in the magnetic field, there is virtually no effect in terms of induced currents. However marginal changes in the orientation of the magnetic field could indirectly impact which areas are more affected by GIC (discussed more later in Section 2.2.9).

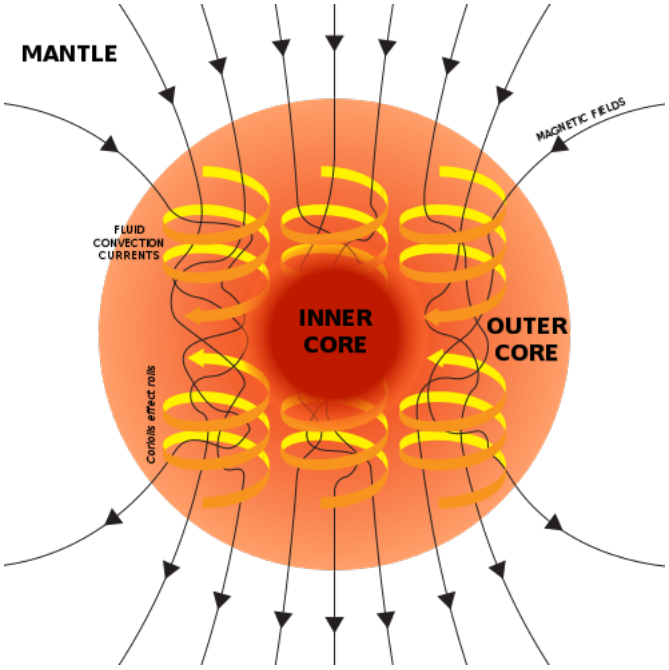

Figure 2.5: The circulating liquid currents (yellow) in the outer core surrounding the inner core, hypothesised by dynamo theory. The Earth's magnetic field (black) is generated by circulation of these currents (Image from the US Geological Survey Website).

2.2.2 Formation of the Magnetosphere

The magnetosphere of the Earth is the invisible bubble of magnetic field lines surrounding the Earth. The magnetosphere is shaped by the interaction between the solar wind and Earth's magnetic field and is not symmetric about the Earth. Instead, the solar wind exerts pressure on the Earth's magnetic field lines which causes the Earth's magnetic field lines to compress on the day-side of the Earth and elongate

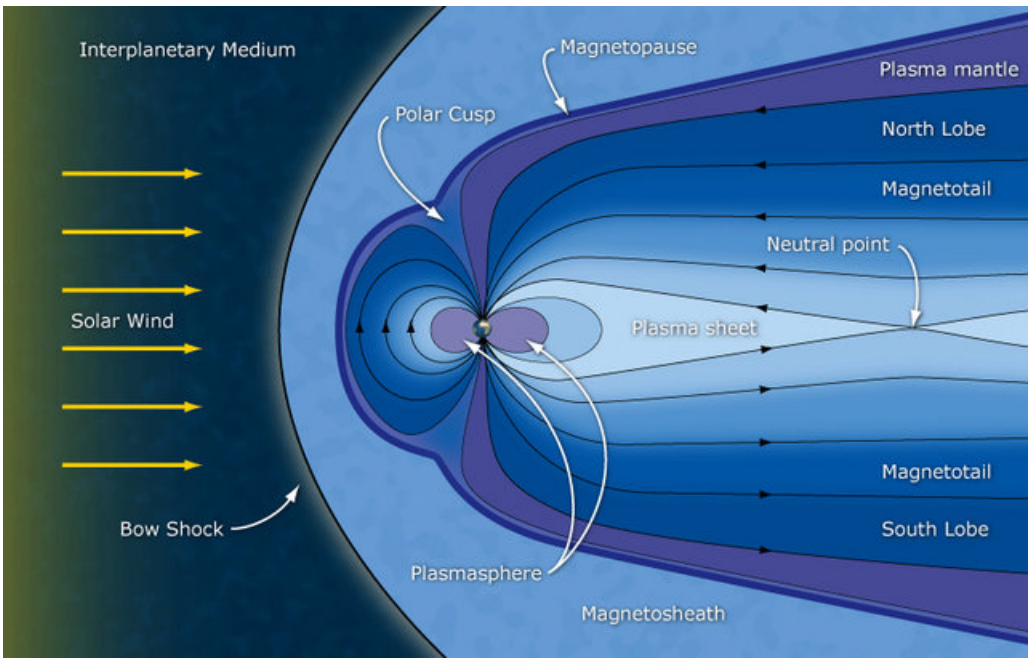

Figure 2.6: The Earth's magnetosphere and it's interaction with the solar wind, with names provided of regions within the magnetosphere (Image from the ESA website `https://www.esa.int/`).

on the night-side. The boundary of the magnetosphere (magnetopause) is defined as the point where the dynamic pressure exerted by the solar wind is equal to magnetic pressure of the geomagnetic field, which is given by:

$$P_{mag} = \frac{B_{mag}^2}{2\mu_0} = \frac{1}{2}\rho_{sw} v_{sw}^2 = P_{sw} \tag{2.1}$$

where the subscripts mag refers to the Earth's Magnetic field and sw to the solar wind. P represents pressure, B represents the magnetic field strength, ρ is density, v is velocity.

When the geomagnetic field is impacted by CMEs and/or CIRs, the density/velocity of the solar wind increases and hence P_{SW} strengthens. The geomagnetic field strength B_{mag} remains stable however, so the magnetosphere becomes compressed to equalise the pressure. As the magnetosphere compresses and expands due to these density/velocity changes, electrical current systems can be driven and/or disturbed. How these current systems are driven and impact the surface of the Earth magnetic field via magnetic field variations is explained in the next few Sections (Sections 2.2.3 – 2.2.9).

2.2.3 Motion of Charged Particles within Magnetic Fields

Charged particles or plasma from the solar wind can enter the magnetic field of the Earth and during geomagnetic storms. The motions of these particles induce large magnetic variations felt at the surface. Understanding how this plasma moves about

the magnetic field and within regions of the magnetosphere is necessary to explain the existence of current systems within the magnetosphere. Plasma can move both within and between magnetic fields of differing bodies like the Earth or the solar wind. The properties of plasma can vary greatly depending on many factors including magnetic field strength, density of plasma and velocity. For partially ionised gas to be considered a plasma, the plasma criteria must be fulfilled:

1. Plasma oscillations can only develop if the mean-free-time between collisions of particles (τ_c) is significantly longer than the oscillation period (τ_p), $\tau_p >> \tau_c$. If this first criteria is not fulfilled, the partially ionised gas instead behaves like a neutral gas.

2. The length scale of the system is significantly greater than the Debye length $\lambda_d << L$, where λ_d is given by.

$$\lambda_d = \sqrt{\frac{\epsilon_0 k_B T_e}{e^2 n}} \tag{2.2}$$

   where, T_e is the temperature of an individual electron, k_b is the Boltzmann constant, ϵ_0 is the permittivity of free space. The Debye length describes the maximum distance an electron can travel due to thermal effects. Effectively, if $L >> \lambda$, the system is dominated by magnetic effects, instead of thermal.

The force acting on the particle in a plasma can expressed by:

$$F = m\frac{d\mathbf{v}}{dt} = q(\mathbf{E} + \mathbf{v} \times \mathbf{B}) \tag{2.3}$$

where m is the mass of the particle, v is the velocity and q it's charge, t describes time, F is the force on the particle and $\mathbf{E}$ and $\mathbf{B}$ are external magnetic and electric fields, assuming the particle is non relativistic. This is derived from the Coulomb Force, $q\mathbf{E}$ exerted by external electric fields, and the Lorentz Force, $q\ (\mathbf{v} \times \mathbf{B})$, exerted by external magnetic fields. The motion of the charged particle within a magnetic field can be determined using this equation, which will be explored in terms of forces.

Gyration and Helical Motion

To understand the motion of a particle in a plasma, first only the Lorentz force will be considered followed by the introduction of the Coulomb force after. If one assumes the electric field experienced by a single charge in a plasma to be zero, the motion of a single particle in a homogeneous magnetic field is given simply by the Lorentz force:

$$m\frac{d\mathbf{v}}{dt} = q(\mathbf{v} \times \mathbf{B}) \tag{2.4}$$

The velocity of the particle can be broken down into a parallel and perpendicular component:

$$\mathbf{v} = \mathbf{v}_{||} + \mathbf{v}_{\perp} \tag{2.5}$$

As no external electric field is present, $\mathbf{E}_{||}$ can be assumed to be 0. Thus equating Equations 2.4 and 2.5 gives:

$$m\frac{d\mathbf{v}_{\perp}}{dt} = q(\mathbf{v}_{\perp} \times \mathbf{B}) \tag{2.6}$$

Thus, the perpendicular motion of the particle can be represented as a particle circling or gyrating about the magnetic field line, in the absence of an electric field (Figure 2.7).

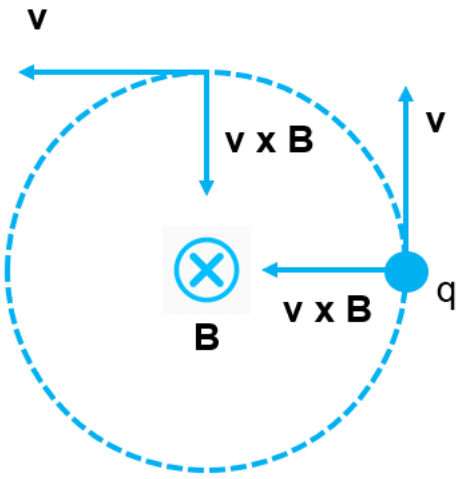

Figure 2.7: The gyromotion of a particle in a magnetic field, assuming no electric field. The "x" represents the magnetic field line, denoting that the view of the system is as if looking in the direction of the magnetic field line. The particle circles the central magnetic field due to the Lorentz Force ($\mathbf{v} \times \mathbf{B}$) acting on the particle.

Imagine now that the particle has a velocity parallel to the magnetic field line, due either to a driving electric field or a varying magnetic field strength, alongside this perpendicular velocity component. The particle will move in what's known as a helical path, whereby the particle continues to circle the magnetic field line, but also drifts along the field line (Figure 2.8).

Magnetic Mirroring and Trapped Plasma

The phenomena known as magnetic mirroring can occur if a particle following a helical trajectory travels from a weak magnetic field region to a sufficiently strong region. Magnetic mirroring describes the effect whereby as particles gyrate and drift along converging magnetic fields, the drift velocity of the particle decreases until its velocity

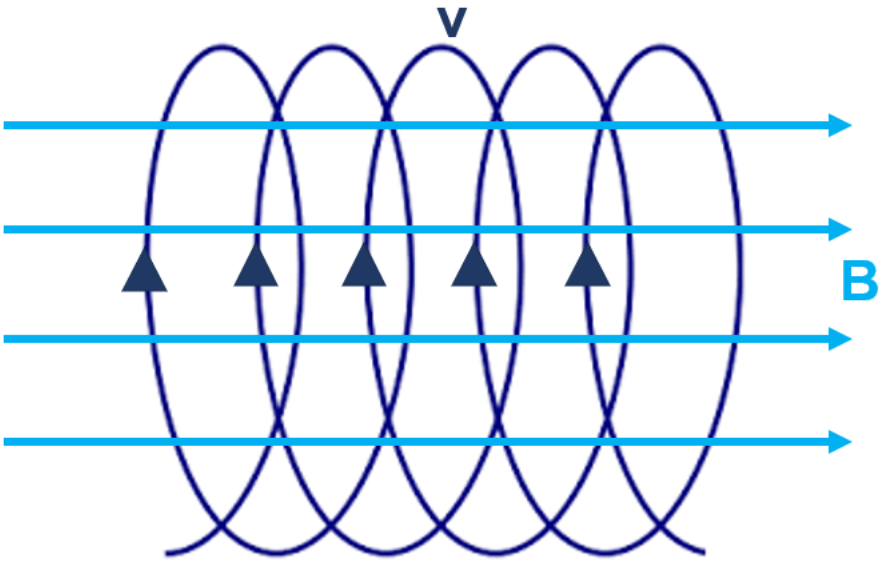

Figure 2.8: The motion of a particle (dark blue) in a magnetic field (light blue) with parallel velocity to the magnetic field. The particle continues to gyrate about the magnetic field, however the particle will now also drift along the magnetic field.

reaches zero. Then the velocity switches direction and travels back along diverging field lines, due to the increase in magnetic field strength (and hence magnetic force exerted on the particle). Mathematically this can be demonstrated as follows:

A gyrating particle in a magnetic field constitutes an electric dipole with a dipole moment, μ:

$$\mu = \frac{mv_{\perp}^2}{2B} \tag{2.7}$$

The point at which the parallel velocity of the particle becomes zero, is the point at which the velocity of the particle shifts direction at a pitch angle θ. By conservation of energy:

$$v_1^2 = v_{1,\perp}^2 = v_0^2 \tag{2.8}$$

Imagine this particle is moving along a converging field line. Think of this particle at two points in space, one in a weak field and the other in a strong field.

$$\mu = \frac{mv_{0,\perp}^2}{2B} = \frac{mv_{1,\perp}^2}{2B} \tag{2.9}$$

Equating both sides gives:

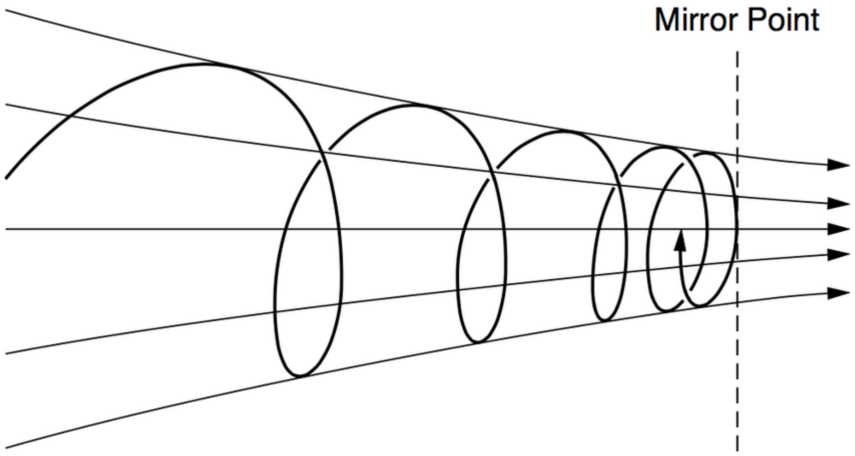

Figure 2.9: A schematic of magnetic mirroring of an ion gyrating about a converging/strengthening magnetic field from Baumjohann and Treumann (1996). As the ion moves to an area of high larger magnetic field, the parallel velocity reduces until it becomes zero.

$$\frac{B_0}{B_1} = \frac{{v_{0,\perp}}^2}{{v_{1,\perp}}^2} = \frac{v_{0,\perp}^2}{{v_0}^2} \tag{2.10}$$

The pitch angle is be represented by the velocities:

$$\sin\theta = \frac{v_{0,\perp}}{v_0} \tag{2.11}$$

Thus,

$$\frac{B_0}{B_1} = \sin\theta^2 \tag{2.12}$$

As the particle moves from a region of low magnetic field strength to high, the pitch angle and hence the perpendicular velocity increases. However the total energy of the system needs to be conserved. Therefore, the parallel velocity of the particle must fall. Assuming the magnetic field becomes strong enough, the velocity eventually becomes entirely perpendicular, with no parallel velocity (Figure 2.9). Here, if the particle gains a parallel velocity from a high to low region, from an external force (i.e. an electric field from nearby plasma), the particle's velocity will continue increasing, effectively mirroring back the way it came.

Plasma can be trapped if two magnetic mirrors are present, as particles "bounce" between the two mirrors. Examples of bounce motion exist in the Earth's magnetic field, most notably the radiation belts, as well as the plasma sheet on the night side of the Earth (Figure 2.6).

2.2.4 Reconnection in the Magnetosphere

Magnetic reconnection is the main process that transfers energy between the Earth's magnetic field and the solar wind. When anti-parallel or oppositely aligned magnetic field lines collide, the magnetic field lines join. Reconnection occurs throughout the magnetosphere, but is particularly important in two regions. Firstly, directly between the solar wind and the edge of the magnetosphere, which can lead to charged particles in the solar wind entering the magnetic field of the Earth. Secondly, on the night-side of the Earth. When the solar wind collides with the magnetic field of the Earth, the magnetosphere can compress. This can lead to oppositely aligned magnetic field lines reconnecting on the night-side of the Earth. The region where they reconnect is an area of previously trapped plasma, known as the plasma sheet. The reconnection creates an electric field which then drives plasma up the magnetic field lines towards the Earth. The largest effect of geomagnetic storms is seen from currents related to this night-side reconnection as opposed to the dayside (which itself is still significant).

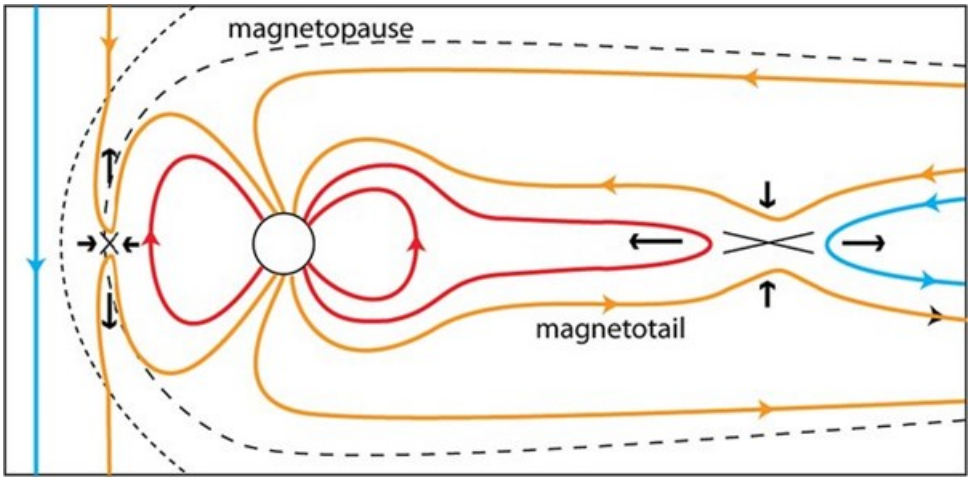

Figure 2.10: Magnetic reconnection occurs in the regions where the opposite facing magnetic field lines join, marked by the 'X's. Two main regions exist on the dayside and the nightside of the Earth. The direction of the electric field, driving currents in the magnetosphere, is marked by black arrows (Eastwood et al., 2017a).

2.2.5 Geomagnetic Activity

The quiet time interaction between the magnetosphere and solar wind has been explained, however storm time needs to be addressed. Geomagnetic storms often disturb and energise many of the existing current systems in the magnetosphere through various processes. The storms themselves are described in this section, followed by their relative effect on current systems in the sections following. During the course of a geomagnetic storm there are generally three main phases of activity.

1. The Initial Phase
2. The Main Phase

3. The Substorm Phase

1. Initial Phase

The initial phase marks the start of a geomagnetic storm. Interplanetary shocks form when fast solar wind plasma overtakes slower solar wind material, increasing the overall density of the solar wind. This forms a shock front due to the sudden increase in density. When the shock front reaches the Earth's magnetic field it perturbs the magnetosphere and disturbs the current systems already trapped in the magnetosphere. Shocks can be marked by their sudden spike in magnetometer data upon arrival (Ontiveros and Gonzalez-Esparza, 2010), known as sudden storm commencements (SSC). An example of SSC on magnetometers is provided for the arrival of the 22nd – 23rd June 2015 storm in Figure 2.11. The effect is usually global (most pronounced on the dayside) and can be seen on magnetometers all over the world.

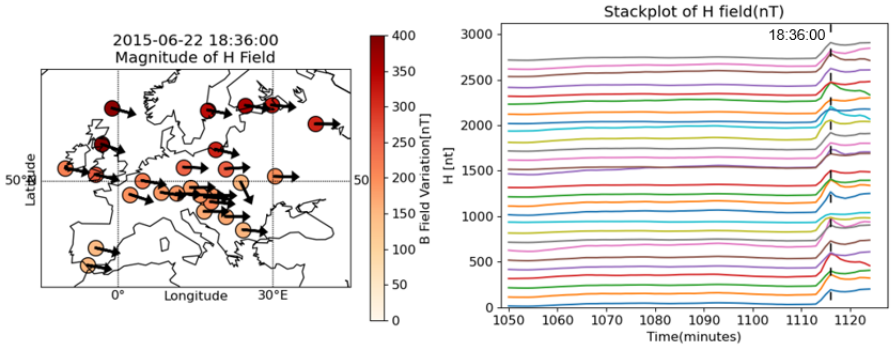

Figure 2.11: The arrival of an interplanetary shock is shown for magnetometer observatories across Europe for the 22nd/23rd June 2015 storm. Measured magnetic field amplitudes and orientations are mapped on the left at the arrival, with each individual magnetic time series in a stack-plot on the right. The arrival can clearly be seen on the right at approximately 1,115 minutes, by the sharp step change in field strength.

The global effect of initial impact leads to the most damage to satellites due to this sharp global effect (Lakhina and Tsurutani, 2016) in the magnetosphere, however due to the short impulsive nature of shocks, ground-based infrastructure is significantly less impacted when compared to later phases of geomagnetic storms (Oyedukun et al., 2020; Heyns et al., 2021).

2. The Main Phase

During the main phase, plasma transfer between the Earth's magnetosphere and the solar wind is near-direct. Plasma transfer can occur when the Earth's magnetic field "reconnects" or is anti-parallel to the magnetic field of the solar wind. This occurs when the solar wind orientation is anti-aligned with the magnetic field direction (e.g. IMFs Bz component < 0, see Section 2.2.7 for a more in depth explanation). This results in the magnetic field lines joining, allowing charges to enter the geomagnetic

field line, where the electric fields drives plasma along magnetic field lines (described in Section 2.2.3). At latitudes like Ireland's, the main phase is when the largest magnetic variation is usually observed (Fogg et al., 2023). In terms of ground-based effects of geomagnetic storms (example in Figure 2.12), this is the phase when the largest variation in geoelectric fields and GIC is present (Oyedukun et al., 2020; Heyns et al., 2021).

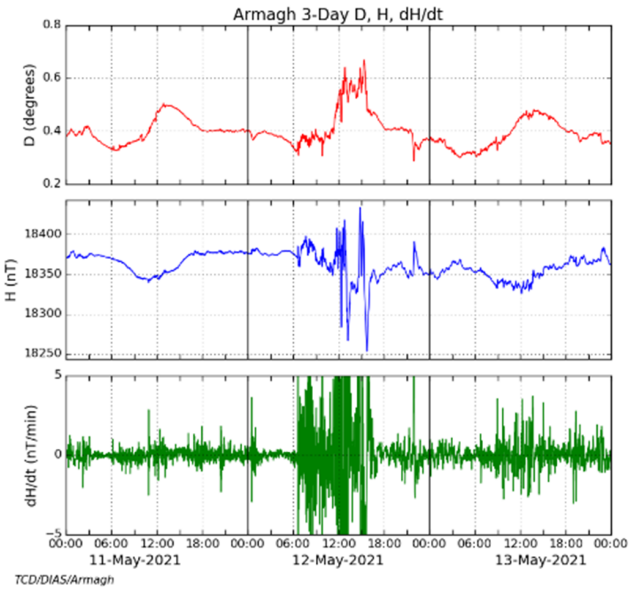

Figure 2.12: An example of a geomagnetic storm from 12 May 2021 is shown on the Armagh magnetometer with the main phase evident in the magnetic field. On the left the magnetic variability is shown; D , declination or the angle between magnetic and geographic north, H, strength of the magnetic field in the direction of magnetic north, and the rate of change of H is shown on the bottom (see Section 3.2). The arrival of the storm from the CME can clearly be seen in the dH/dt at 07:00 UTC and persists for 10 hours (the main phase). During this time reconnections, plasma transfer and small shocks occur throughout the magnetosphere depending on solar wind conditions, enhancing geomagnetic activity.

3. Substorm Phase

Magnetic reconnection can occur on the nightside of the Earth as well as the dayside. When reconnection occurs on the dayside, plasma from the solar wind can precipitate into the geomagnetic field. The substorm phase as opposed to the main phase is located approximately between areas of the Earth between 20 – 03 Local time (LT) centred around the 23h line, sometimes referred to as the Harang discontinuity (Erickson et al., 1991). While substorms are temporally briefer than the main phase of the storm, they occur more frequently as they can occur even during weak solar wind/IMF conditions. However during geomagnetic storms, substorms become enhanced and strengthen the auroral electrojet, via Birkeland current systems connecting the magnetosphere to the ionosphere (see Section 2.2.7).

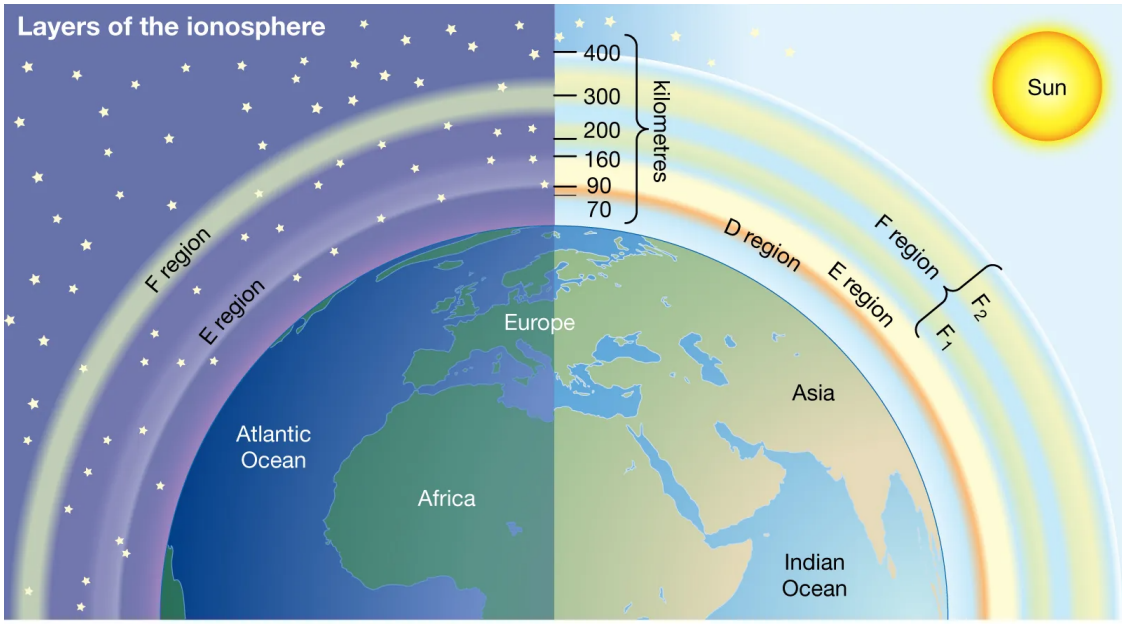

Figure 2.13: A general depiction of the ionosphere during quiet conditions, with its associated layers (D, E, F), with their existence depicted between the day (left) and night (right).

2.2.6 The Ionosphere

The ionosphere is a region of partially ionised particles in the upper atmosphere of the Earth (Figure 2.13), between approximately 60 – 1,500 km (Bilitza et al., 2011). Unlike the magnetosphere which is purely a hot plasma, depending on conditions, the ionosphere varies between a hot (usually at higher altitudes) and a cold plasma (usually at lower altitudes). In terms of space weather phenomena, the ionosphere was discovered very early compared to most magnetospheric phenomena, approximately 1902 (Griffiths, 2018). The plasma in the ionosphere allows for the transmission of radio communication, due to total internal reflection bouncing radio waves off specific regions, which was quickly exploited. There are two main processes which generate/feed ions in the ionosphere: a) directly due to solar photoionisation b) indirectly due to energetic particle precipitation. At these altitudes, the atmosphere is thin enough so that the timescale of collisions between particles to recombine becomes relatively long (which occurs at lower altitudes). Thus a plasma temporarily forms, subject to the magnetic force of the geomagnetic field, which in turn leads to the formation of electrical currents. Typically densities of ions and electrons can vary between 10^8 – 10^{12} m^{-1}, but these densities vary significantly depending on the: a) the layer (i.e. height) of the ionosphere, b) the time of day and c) the presence of a geomagnetic storm or solar flare.

Particles in the atmosphere can become ionised when EUV and X-ray radiation from the Sun impacts neutral particles, which can liberate electrons from the particle pro-

vided the energy of the radiation is great enough. This is the main process which generates plasma in the ionosphere as it can be independent of large magnetic disturbances such as geomagnetic storms, as the Sun always outputs at least a small amount of X-ray and EUV radiation. This dependence on the Sun leads to the ionosphere having a diurnal nature (varying based on time of day). The peak ionisation generally occurs at midday when the Sun is most intense, while when the Sun sets, the number of free ions and electrons become depleted due to recombination. The lowest layer of the ionosphere, the D layer usually only exists during the day as the recombination rates are too great, the E layer becomes depleted more slowly than the D layer, while the F layer remains relatively intact. This is the typical photoionisation effect, although enhancements in photoionisation occur during solar flares. Solar flares emit strongly, albeit briefly, in the X-ray and EUV spectra, with a flux orders of magnitude greater than quiet times on the Sun (see Figure 2.14). As a result, solar flares generate significantly enhanced ionisation in the ionosphere. In turn, a magnetic field variation or magnetic "crochet" occurs due to currents that form in the atmosphere from enhanced ionisation during larger solar flare events (Whitten et al., 1965; Hayes et al., 2021, provide a more detailed explanation). These currents, along with any other currents higher up in the magnetosphere, generate magnetic fields according to Ampère's law:

$$\nabla \times \mathbf{B} = \mu_0 \mathbf{J} \tag{2.13}$$

where J is the current density. A clear depiction of this is provided in Figure 2.14, where the magnetic field crochet from an X-class solar flare is compared to X-ray fluxes.

However it must be noted, that while photoionisation can generate magnetic variations, they are generally at most, an order of magnitude smaller than the variations related to geomagnetic storms (10 nT's compared to 100 nT's), which can cause damage to ground-based infrastructure.

Ions can also enter the ionosphere from the magnetosphere, though to a lesser extent, during quiet solar conditions. During geomagnetic storms however, disrupted current systems in the magnetosphere transfer significantly more energetic particles into the ionosphere. These particles originate from regions of trapped plasma within the magnetosphere (trapped via magnetic mirroring), such as the radiation belts, or the plasma sheet (Gasdia and Marshall, 2021). Particles lose energy during collisions and thus the more energetic the particle, the lower in altitude it can penetrate to. In terms of ground-based magnetic effects, the E layer is generally dominant, with Hall currents (see Section 2.2.8) strongest in this region (Wilkinson et al., 1986), with a relatively small effect from the D and F regions.

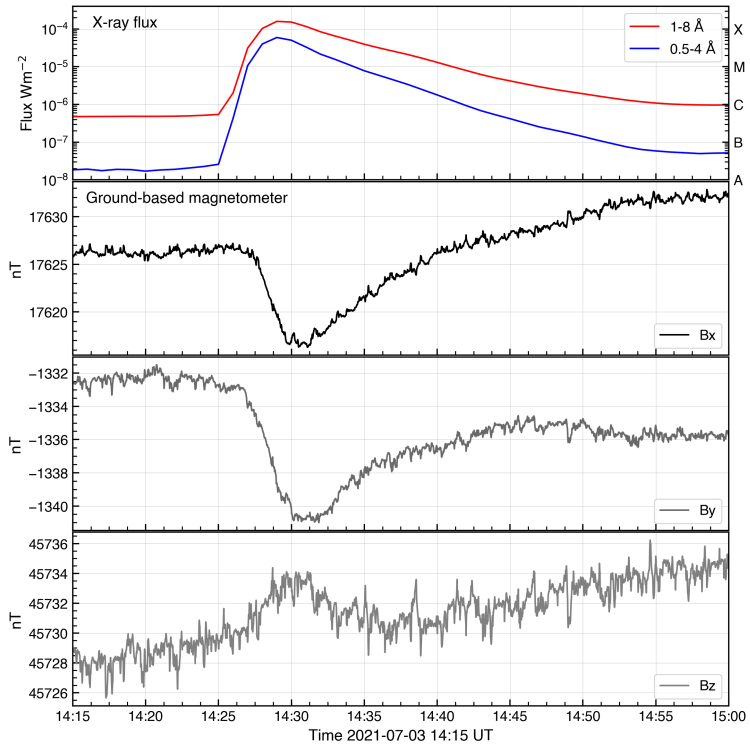

Figure 2.14: A significant X-class flare from 03/07/2021. The X-ray flux from the GOES satellite (top panel) is compared to the three components of magnetic field variation at Dunsink Observatory (Bx, By and Bz). A sizeable reduction in the magnetic field strength occurs in response to the X-class flare at around 14:30 UT. After 14:30 UT, the magnetic field dips due to ions and electrons recombining.

2.2.7 Ionosphere-Magnetosphere Coupling

The ionosphere and magnetosphere current systems are complicated, in many cases are interconnected. The primary driver of magnetosphere ionosphere coupling is known as the Dungey cycle, where ultimately the solar wind and magnetic field interaction drives the transport of magnetic flux within the magnetosphere, via magnetic reconnections (Dungey, 1961) in a repeating loop. The magnetic field lines of the Earth point from South to North at the reconnection point between the Earth and IMF, so hence when the IMF's Bz component is negative (North to South), reconnection can occur most readily. Magnetic flux is transported from the dayside of the Earth to the nightside of the Earth (by these newly opened magnetic field lines), where the magnetic field lines undergo reconnection again, this time between lines northern and southern hemisphere before returning to the dayside (see Figure 2.10). At each point these magnetic field lines are connected to the ionosphere at the pole by these open magnetic field lines, along which current systems can transport energy from the magnetosphere to the ionosphere and vice-versa, known as field aligned currents (FAC) or Birkeland currents (Birkeland, 1908). A schematic of this interaction is shown in Figure 2.15.

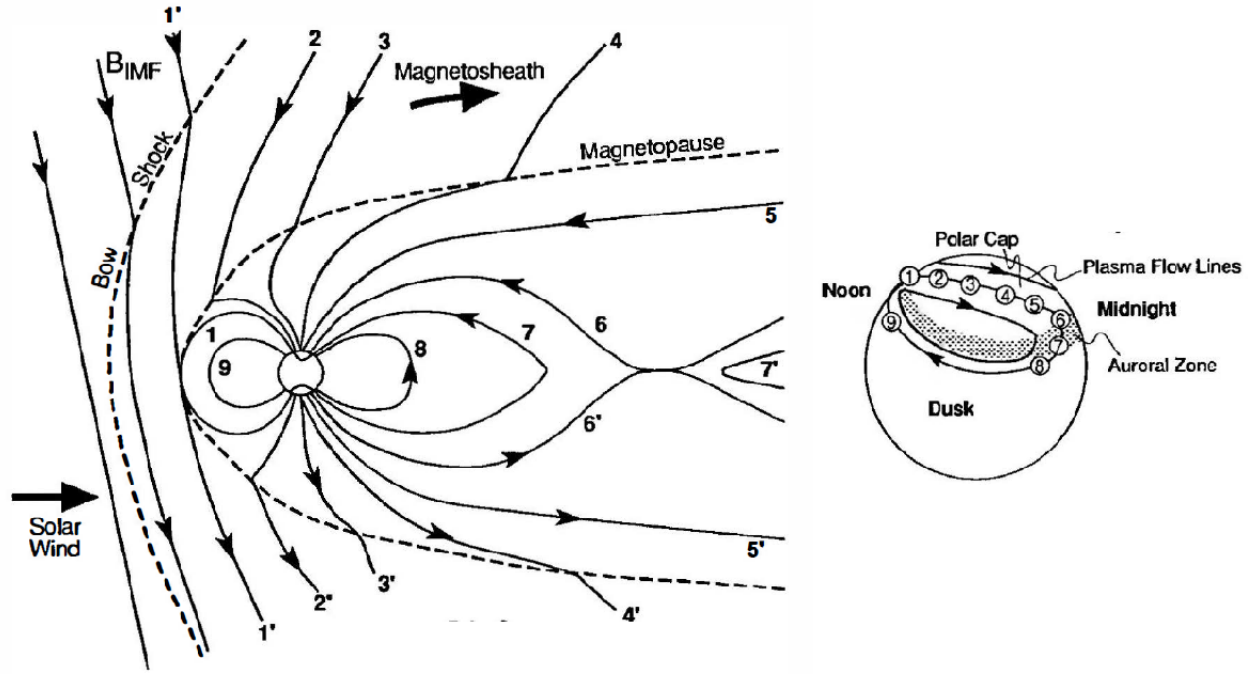

Figure 2.15: The motion of magnetic field lines through the process of the Dungey cycle (Hughes, 1995). The corresponding magnetosphere and ionospheric FAC are shown via the numbering in order of progression. After reconnection open magnetic field lines flow from day-side to night-side, also leading to ionospheric convection, before reconnecting on the night-side.

2.2.8 The Auroral Electrojet

The principal ionospheric current system of main concern is the auroral electrojet, which coincides in time with the appearance of visible aurorae and during geomagnetic storms can generate currents in excess of 1 million amps (Kamide and Baumjohann, 1993). The auroral electrojet is a Hall current (flows primarily horizontally not vertically) and is generally confined close to the northern and southern geographic poles. It peaks around an area known as the auroral oval, which during quiet times is generally located 65 – 75^o geomagnetic latitude in the northern hemisphere (Johnsen, 2013). However, this can expand significantly further North and South during geomagnetic storms. Due to its amplitude and proximity to the surface of the Earth, it generates the largest magnetic variation and hence the largest induction in conductors such as power grids.

An example of the magnetic amplitude generated by the auroral electrojet can be estimated at the surface of the Earth, to help demonstrate how the electrojet can generate large magnetic variations. The Biot-Savart law, can be used estimate the magnetic field due to an electrical current:

$$\mathbf{B} = \int \frac{\mu_0 I}{4\pi} \frac{d\mathbf{l} \times \hat{r}}{\mathbf{r}^2} = \int \frac{\mu_0 I}{4\pi} \frac{d\mathbf{l} \sin(\theta)}{\mathbf{r}^2} \tag{2.14}$$

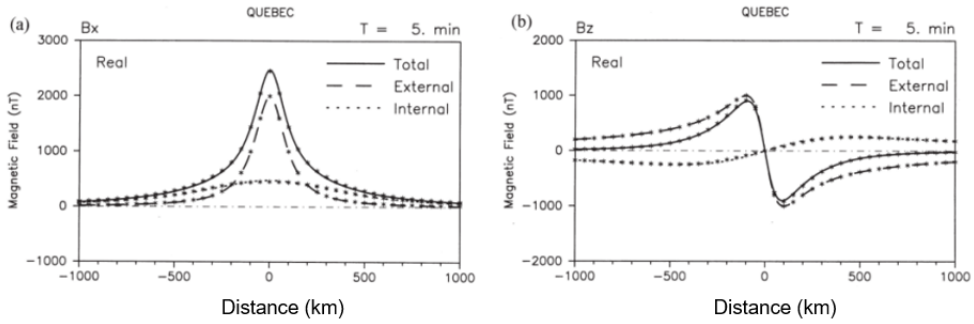

Figure 2.16: The simulated horizontal (H) and vertical (Z) components of the magnetic field generated due to a line current of 1 million amps, 100 km above the surface of the Earth (Boteler and Pirjola, 1998). The magnetic field consists of "external" and "internal" parts, with the total being the sum of these two components. "Internal" represents magnetic variation driven directly by the electrojet, "external" for the induced Earth currents.

where $\boldsymbol{I}$ is current, $\mathbf{r}$ is the distance between the electrojet and the surface, d$\mathbf{l}$ is the length of each infinitesimal-segment of the electrojet and θ is the angle between the surface and electrojet, relaltive to the direction in which the jet is travelling.

Using a few simplifications, an estimate for the magnetic field strength can be derived: a) If one assumes the electrojet is directly overhead, then $\sin\theta = \sin 90 = 1$; b) Assume that the length, l, is straight and can be approximated by $\int_0^L d\mathbf{l} = L$. Here, the strength of the electrojet to be is estimated to be 1,000,000 A, the distance, r, to be 100 km from the surface and the length of the electrojet to be 600 km (Campbell, 2003, a good estimate):

$$B = \frac{\mu_0 IL}{4\pi r^2} = \frac{4\pi \times 10^{-7}(10^6)(6 \times 10^5)}{4\pi(10^5)^2} = 6,000nT \tag{2.15}$$

This estimate is slightly worse than the better derived and tested estimate of $\approx$ 2,500 nT for 1,000,000 A from Boteler and Pirjola (1998), but within the same order of magnitude (see Figure 2.16). To put this into perspective, 2,500nT is about 3 – 5% the strength of the Earth's internal magnetic field felt at the surface.

To explain why the auroral electrojet generates the greatest magnetic field at surface level, some terms of the Biot-Savart law can be used (Equation 2.15). The auroral electrojet is the current system in the ionosphere where the r^2 is low. Larger amplitude current systems exist higher in the magnetosphere, however the distance to these systems is at least an order of magnitude greater, so the inverse r^2 relation leads to a comparatively low magnetic effect on the surface. An example the magnetic signature of the auroral electrojet is plotted in Figure 2.17

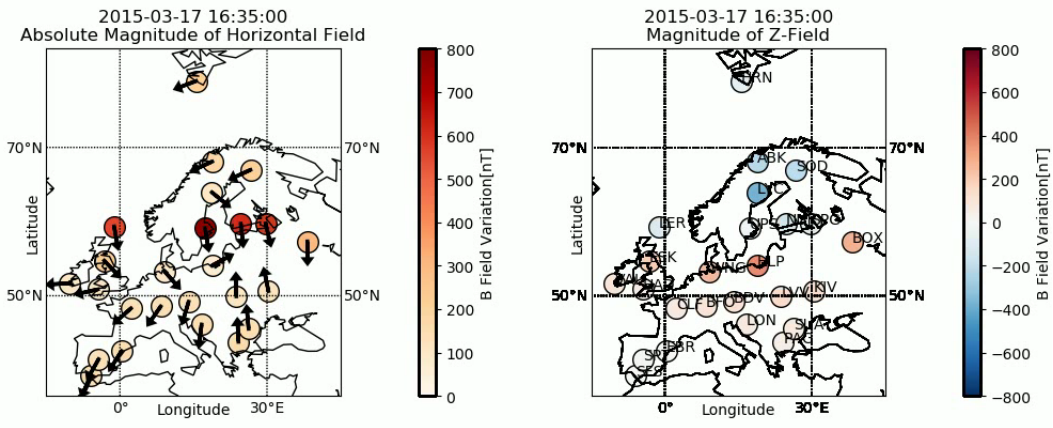

Figure 2.17: An example of the magnetic variation due to the auroral electrojet is shown for the St. Patrick's day storm, 2015. The electrojet can be seen at approximately 60°. The same shape of the H and Z components in Figure 2.16 are present across the map of magnetometer sites (a large peak in H is associated with the Hall currents directly overhead, with peaks in Z north and south of the peak H, denoted the position of the FAC).

2.2.9 Seasonality in Geomagnetic Fields

Seasonal patterns are present in geomagnetic activity which should be considered when analysing the geomagnetic field. Patterns in geomagnetic activity are present during: a) the course of a solar cycle (see Section 2.1.5); b) monthly; c) diurnal, d) longer term (i.e. decades and beyond). An explanation of each of these maxima unrelated to the solar cycle is provided in this subsection.

Monthly Patterns

Monthly seasonality exists in geomagnetic activity and peaks during equinoxes, seen both in frequency and intensity of geomagnetic storms (Patowary et al., 2013), as well as historically by frequency of auroral observations (Chapman and Bartels, 1940). The main hypothesis to explain this seasonal effect is the Russell-McPherson effect, whereby the angle of the magnetosphere relative to the solar wind velocity direction is to blame (Russell and McPherson, 1973). During the Spring and Autumn the relative angle between the Earth and the orbital plane (and hence the magnetosphere) is approximately 90° to the velocity of solar wind (Figure 2.18). This angle changes to $90 \pm 23.5°$ during the Summer and Winter and leads to poorer coupling between the geomagnetic field and the solar wind and thus poorer reconnection between the two, leading to relatively less geomagnetic activity.

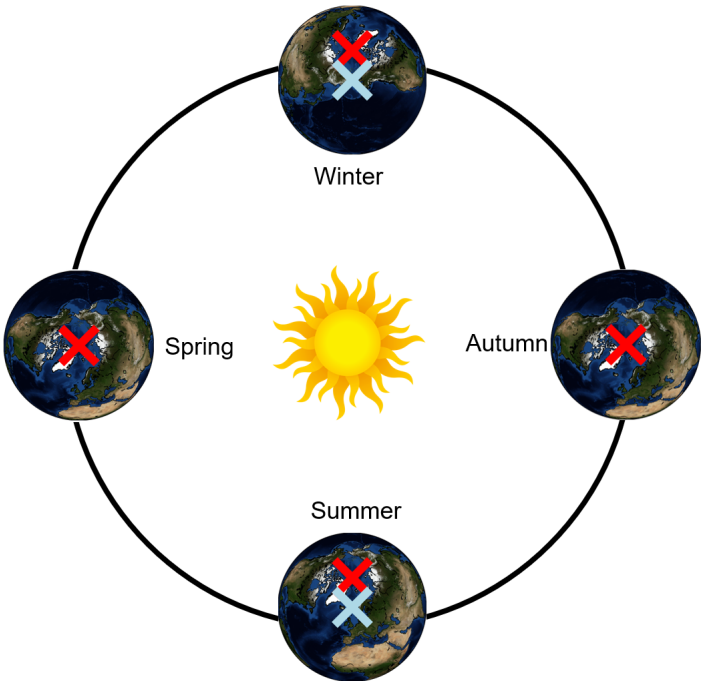

Figure 2.18: The axis of the Earth as it orbits the Sun, looking down on the Earth from above (northern hemisphere). Red denotes position of the geographic poles (approximately the position of the current geomagnetic pole), while light blue denotes right angle point to the solar wind (in the ecliptic plane). During Spring and Autumn, the pole is at a right angle to the relative direction to the solar wind, while during Summer the pole points towards the Sun and away during the winter

Diurnal Patterns

Diurnal patterns relate mainly to the phases within geomagnetic storms, described in Section 2.2.5. The largest amount of activity is observed at the night sector of the Earth and relates to the substorm phase of geomagnetic storms, while the weakest activity is seen at the day-side of the Earth, with ionospheric current systems weakest in this region during storms (Figure 2.19). The initial phase generally peaks approximately on the day-side of the Earth (09 – 15 hours local time), the substorm is only observed on the night side (approximately 21 – 03 hours), while the main phase is usually most prominent in the dawn and dusk sectors (approximately 03 – 09 hours, 15 – 21 hours) (Lakhina and Tsurutani, 2016).

Longer Term Trends

Over significantly longer timescales, the geomagnetic field is dynamic, varying in terms of both amplitude and orientation. This is probably related to changes in the dynamo at the core of the Earth, which are poorly understood. For the most part these changes can be observed as a slow "wobble", whereby the magnetic field strength weakens/strengthens slightly and magnetic poles shift marginally before returning closer to their geographic pole and original amplitude (Nilsson et al., 2022). Locally, proximity to the poles is strongly related to the strength of magnetic variations felt during geo-

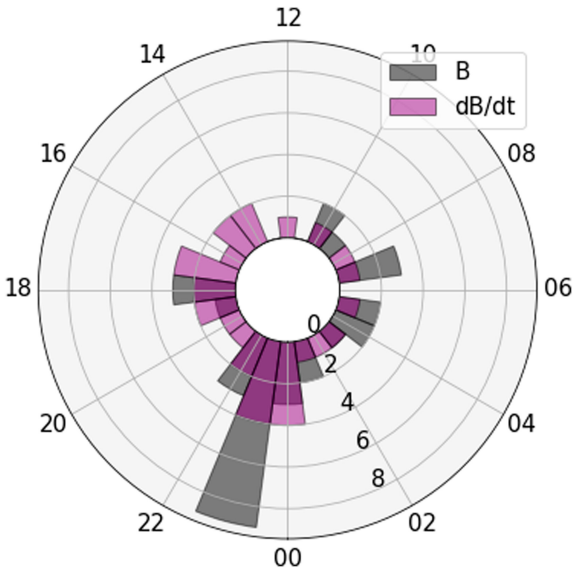

Figure 2.19: A daily plot highlighting extreme values in magnetic field strength and variation between 1991 – 2023 for the Valentia magnetometer (Fogg et al., 2023). The majority of peak values occur around 21:00 – 01:00, related to the substorm phase of the geomagnetic storms.

magnetic storms, but particularly near the 50° mark, and thus studies extrapolating to longer-term predictions need to account for this factor (Pulkkinen et al., 2012; Rogers et al., 2020).

2.3 Transition from Geomagnetic to Geoelectric Fields

Up until this point, the "space" side of space weather has been the focal point. Now, a more geophysical standpoint is taken, focusing on the response of the Earth and Earth-based systems driven by these magnetic variations During geomagnetic storms, the magnetic field variation interacts with the resistive subsurface of the Earth's uppermost layer, called the lithosphere. This layer consists of the crust and uppermost rigid part of the mantle, Figure 2.20). The lithosphere most often extends to depths of ≈ 100 km, but can extend to depths up to 500 – 600 km in specific regions (Anderson, 1995), related to the subduction of tectonic plates beneath each other. In Ireland, electrical resistivity profile mapping suggests that this boundary between the lithosphere and underlying astenosphere (the more fluid like mantle) lies at ≈ 150 – 200 km depth (Kiyan et al., 2018).

The magnetotelluric (MT) method is a technique used to image the electrical properties of the lithosphere by exploiting the natural variation of the geomagnetic field (most notably due to space weather effects) and measuring the geoelectric fields induced in response to magnetic variations at the surface. "telluric" refers to the electric currents induced in geological structures, while the "magneto-" refers to the varying magnetic fields driving these currents. The method was devised first by Tikhonov (1950) and

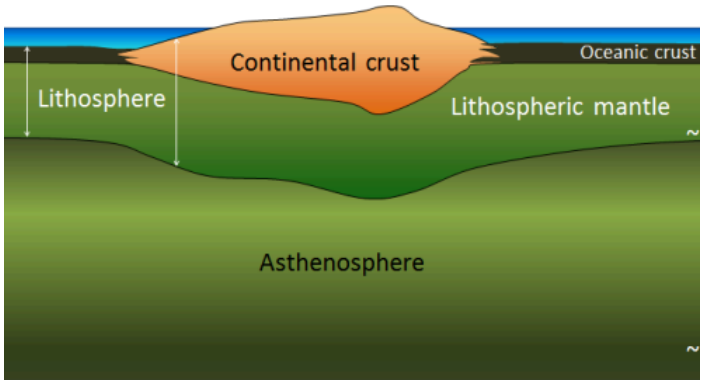

Figure 2.20: An example case of the structure of the crust and upper mantle of the Earth (Earle et al., 2019). The lithosphere is made up of the crust and the uppermost rigid part of the mantle. Below the lithosphere is the asthenosphere, which is relatively conductive compared to the lithosphere and hence generates comparatively weak geoelectric fields at the surface.

Cagniard (1953). By measuring both the magnetic and electric field at the surface of the Earth, the electrical properties of the Earth (i.e. how resistive the underlying rock is) can be derived. In terms of space weather, the geoelectric field is the driver of GIC in power-lines, hence why it is considered here. The MT method is used to calculate the geoelectric field at the surface of the Earth. This can be done either directly, using transfer functions, or indirectly using resistivity models derived from MT measurements instead to model the geoelectric field. Aside from space weather, magnetotellurics has many other useful purposes. Information about the resistivity of subsurfaces can be used for mineral exploration, carbon sequestration, thermal energy and hazard prevention/prediction.

2.3.1 An explanation of MT sources

Theoretically speaking, for any source that has a time-varying magnetic field, the response of the subsurface can be measured using the MT method. Usually to have any noticeable effect, the amplitudes of the varying fields must be relatively large. While space weather is the most significant source, other sources also exist. While some of these sources are useful for understanding the subsurface, more often than not these sources can be a nuisance (particularly artificial man-made sources), effectively leading to noise in MT data that needs to be carefully considered. Signals can be separated by frequencies, with frequency being a good proxy to determine the depth at which the response originates from in the subsurface. Shallow structures generally respond to short periods, with deep structures responding with long periods. Examples of natural sources include:

1. For period ranges $\approx 10 - 10{,}000$ s, space weather is the main source of variations. Changes in the magnetospheric and ionospheric sources are slow and thus the induced response is as well.

2. A daily variations exists related to the ionisation of the ionosphere from Solar variation, between $\approx$ 1,000 s – 24 hr.

3. Lightning affects almost all frequencies when it strikes nearby, from 0.001 Hz to 1,000 Hz. However this is rare. A more notable peak caused by lightning, however, is called the Schumann resonance, a peak at $\approx$ 7Hz, related to the wave generated in the ionosphere after a lightning strike.

4. The long-term variation of the Earth's magnetic field, due to changes in the currents generating the magnetic field in the core. These changes however, exist at much much higher periods, within a period ranging from years to thousands of years.

5. Motion of the tides at the coast affects long periods, >1,000 s (Beggan et al., 2021). For this reason, many surveys often avoid coastal areas.

An MT "dead-band" exists between the $\approx 1 - 7$ Hz range, where natural sources rarely generate any signals. Many wave-cycles are needed to accurately reproduce a signal and at least a month of data should be measured to return enough data for the purpose of space weather. Before getting into the intricate mathematics behind MT a description of the basics of electromagnetism is provided below to help grasp some basic principles, which eventually scale up to the method behind MT. So I will attempt to use basic electromagnetism to help explain why currents are induced in the Earth's subsurface. Firstly, the basic Faraday's law and Ohm's law (in terms of electric fields) will be used:

$$\nabla \times \mathbf{E} = -\frac{d\mathbf{B}}{dt} \tag{2.16}$$

$$\mathbf{E} = \rho \mathbf{J} \tag{2.17}$$

where $\mathbf{E}$ is the electric field, $\mathbf{B}$ is the magnetic field, $\mathbf{J}$ is current density and ρ is the resistivity of a material.

In the case of the Earth, a magnetic field variation occurs (due to space weather, or some other phenomena). This magnetic field then induces an electric field, $\mathbf{E}$. This electric field in turn, induces a current into nearby conducting materials. The conducting material in this case is the Earth. From Ohm's law, we see that the current induced is inversely proportional to the conductivity, so hence the more resistive the material is, the larger the induced current will be. When we compare the conductivity of different matter within the Earth, rock is generally the most resistive and hence where the largest charge is induced (rock $\approx 10^{-6} - 10^{-1}$ S/m, Sea water $\approx$ 10 S/m, atmosphere $\approx 10^{18}$ S/m). This is due to the combined effect of this high resistivity, and the simple fact that rock is the most abundant material on the Earth.

Now imagine an example of a grounded conductor that is affected by the electric force of

this subsurface current. For simplicity, imagine this subsurface current is a point source a distance r from the conductor. We can describe this electric force by Coulomb's law for a point charge (the Earth) and a horizontal line:

$$F_{cond} = kqQ_{Earth}\frac{2L}{r^2\sqrt{r^2L^2}} \propto qQ_{Earth} \tag{2.18}$$

where k is a constant, Q is the total charge of the Earth, q is the charge of the conductor, the $cond$ subscript is used to denote the conductor and L is the length of the conductor. Converting to electric field, to express the electric field exerted by the Earth on the conductor, $\mathbf{E}_{cond}$, we get:

$$\mathbf{E_{cond}} = \frac{\mathbf{F}_{cond}}{q} \propto Q_{Earth} \tag{2.19}$$

Focusing on the proportionality between terms, we can show that the driver of a GIC is the charge of the Earth itself.

$$I_{cond} \propto V_{cond} \propto E_{cond} \propto Q_{Earth} \tag{2.20}$$

where V is the voltage on the conductor. In this simplified case, the charge of the Earth generates an electric field which drives a current in our conductor. In the same general manner, GIC are induced in power grids although with significantly less simplifications. On the topic of rock types, type strongly affects how resistive the subsurface is, though factors like temperature, pressure and water content of a rock can augment or weaken the resisivity by orders of magnitude. Resistivity generally decreases with an increase in temperature, an increase in water content and an increase in temperature. Metamorphic rocks are generally the most resistive rock type, with sedimentary rock types being the least resistive, with igneous rocks in between (Loke, 2001).

2.3.2 Assumptions of the MT method

The MT method has a particular set of assumptions and simplifications which are used when estimating the electromagnetic (EM) response of the Earth. This method is detailed and explained in more depth in Simpson and Bahr (2005). Here, a list of simplified assumptions which are used are stated below:

- Maxwell's equations are always obeyed.
- The Earth only absorbs and dissipates EM energy. It generates no EM energy of its own.
- All EM fields are conservative and differentiable away from their sources.

- EM source fields, generated by relatively far away ionospheric currents sheets are treated as uniform plane-polarised EM waves generated at a distance, which propagate into the Earth at a near-vertical angle of incidence. This is called the plane wave assumption or approximation.
- The Earth is a conductor that strictly follows Ohm's laws (Equation 2.17).
- The bulk resistive properties of underlying rocks are more important than the resistive properties of individual minerals within rocks.
- No charges are accumulated in a 1D Earth. In a 2/3D Earth, charges can accumulate along conductivity discontinuities.
- The 'quasi-static' approximation holds true for the total current density ($\frac{d\mathbf{J}}{dt} = 0$). A quasi-static system is a system in which a quantity vary slowly. In this case, this means that time-varying displacement currents are negligible compared to conduction currents, essentially indicating that induction is a diffusive process.

Of each of these simplifications the plane wave assumption is perhaps the most limiting, as it neglects to account for the curvature of the Earth. This means that for cases where the curvature of the Earth is more significant, the MT model performs more poorly. One such case is for very long period magnetic variations, which induce charge deeper into the Earth , > 10,000 s (Madden and Nelson, 1964). For space weather, the majority of the signal is concentrated below this range. The other main case is when lower-lying ionospheric currents are present, most notably the auroral and equatorial electrojets (Section 2.2.8), the method will no longer perform as accurately as the assumption that the currents are far away is no longer valid (Simpson and Bahr, 2005). This indicates the method should not perform as well for polar and equatorial countries.

2.3.3 Diffusion Equations

The following vector identity can be applied to Faraday's law (Equation 2.16), when the curl of Faraday's law is taken, to determine the diffusion equation of the electric field ($\nabla^2\mathbf{E}$):

$$\nabla \times \nabla \times \mathbf{E} = (\nabla \cdot \nabla\mathbf{E}) - \nabla^2\mathbf{E} = -\nabla^2\mathbf{E} \tag{2.21}$$

Following the assumption that the Earth generates no EM energy of it's own, $\nabla \cdot \mathbf{E} = 0$ and subbing Faraday's law into the identity:

$$\nabla \times \nabla \times \mathbf{E} = -\nabla^2\mathbf{E} => \nabla^2\mathbf{E} = \frac{d}{dt}(\nabla \times \mathbf{B}) \tag{2.22}$$

The curl of the magnetic field can be represented by maxwell-ampere law:

$$\nabla \times \mathbf{B} = \mu_0(\mathbf{J} + \epsilon_0 \frac{d\mathbf{E}}{dt}) = \mu_0(\frac{\mathbf{E}}{\rho} + \epsilon_0 \frac{d\mathbf{E}}{dt}) \tag{2.23}$$

Provided the plane wave assumption holds true, the electric and similarly magnetic fields can be expressed as waves, in the form

$$\mathbf{E} = \mathbf{E_0} e^{-(\mathbf{k}z - iwt)} \tag{2.24}$$

$$\mathbf{B} = \mathbf{B_0} e^{-(\mathbf{k}z - iwt)} \tag{2.25}$$

where E_0 and B_0 are the amplitudes of $\mathbf{E}$ and $\mathbf{B}$ at origin, ω is the angular frequency and $\mathbf{k}$ is the wavenumber. By differentiating each side of these equations with respect to time, the rate of change of $\mathbf{B}$ and $\mathbf{E}$ can be related to the electric and magnetic wave functions, by:

$$\frac{d\mathbf{B}}{dt} = i\omega\mathbf{B} \tag{2.26}$$

$$\frac{d\mathbf{E}}{dt} = i\omega\mathbf{E} \tag{2.27}$$

Hence, the diffusion equation of the electric field, and the magnetic field can be represented by:

$$\nabla^2\mathbf{E} = \frac{i\omega\mu_0\mathbf{E}}{\rho} \tag{2.28}$$

$$\nabla^2\mathbf{B} = \frac{i\omega\mu_0\mathbf{B}}{\rho} \tag{2.29}$$

The diffusion equations describe how the EM signals are dissipated as they travel through a medium. What is important to note is the proportionality between the frequency of the signal and the diffusion. What this signifies in terms of the induction of the Earth, is that high period signals (e.g., 10,000s) can propagate to greater depths than low period signals (e.g., 1s).

2.3.4 Electromagnetic Skin Depth and Resistive Structure

The depth to which a signal strength can propagate to can be quantified by the skin depth. The solution for the partial differential Equation 2.28, assuming a vertical source field is:

$$\mathbf{E} = \mathbf{E}_1 e^{iwt - qz} + \mathbf{E}_2 e^{iwt + qz} \tag{2.30}$$

where z is the depth, q is the complex skin depth term. To satisfy the assumption that the Earth does not generate energy, E_2 is set to zero. If we assume the resistivity distribution is homogeneous, and thus ρ is constant with depth, the second derivative with respect to depth of Equation 2.30, the complex skin depth can be solved for relative to **E**:

$$\frac{d^2\mathbf{E}}{dz^2} = q^2\mathbf{E}_1 e^{iwt-qz} = q^2\mathbf{E} \tag{2.31}$$

As the medium is uniform, $\frac{d\mathbf{E}}{dt} = 0$, and hence

$$\nabla^2\mathbf{E} = \frac{d^2E}{dz^2} \tag{2.32}$$

By equating Equation 2.28 with Equations 2.31 and 2.32.

$$q^2\mathbf{E} = \frac{i\omega\mu_0\mathbf{E}}{\rho} \tag{2.33}$$

$$q = \sqrt{\frac{i\omega\mu_0}{\rho}} \tag{2.34}$$

The electromagnetic skin depth, $\delta(\omega)$, the real part of the inverse of the complex skin depth $(1/q)$, is the depth to which an EM wave with angular frequency, ω, travelling through a medium with electrical resistivity, ρ, dissipates to $1/e$ its original amplitude in metres. The skin depth is:

$$\delta(\omega) = \sqrt{\frac{2\rho}{\omega\mu_0}} \approx 503\sqrt{\rho T} \tag{2.35}$$

where T is the period of the signal. The relation between the depth the signal propagates to and the frequency/period of the signal can be estimated using skin depth. Skin depth is generally used as a proxy to mark the depth to which a signal's amplitude is great enough to induce a charge in the Earth. We can use this function to illustrate the impact subsurface geology and hence resistivity has on induced electric fields. Firstly, I assume the Earth is entirely homogeneous and hence has uniform resistivity. Using the conductivities of rock mentioned in Section 2.3.1, and evaluating the skin depth across the geoeffective periods ($\approx$ 10 – 10,000 s), the depth to which geomagnetic signals propagate can be estimated.

In Figure 2.21, a dramatic difference between the most and least resistive rocks is present. For the conductive rock (10 Ω m), the skin depth barely reaches below 10 km and cannot even propagate below 1 km for weak signals. In the case of a resistive rock

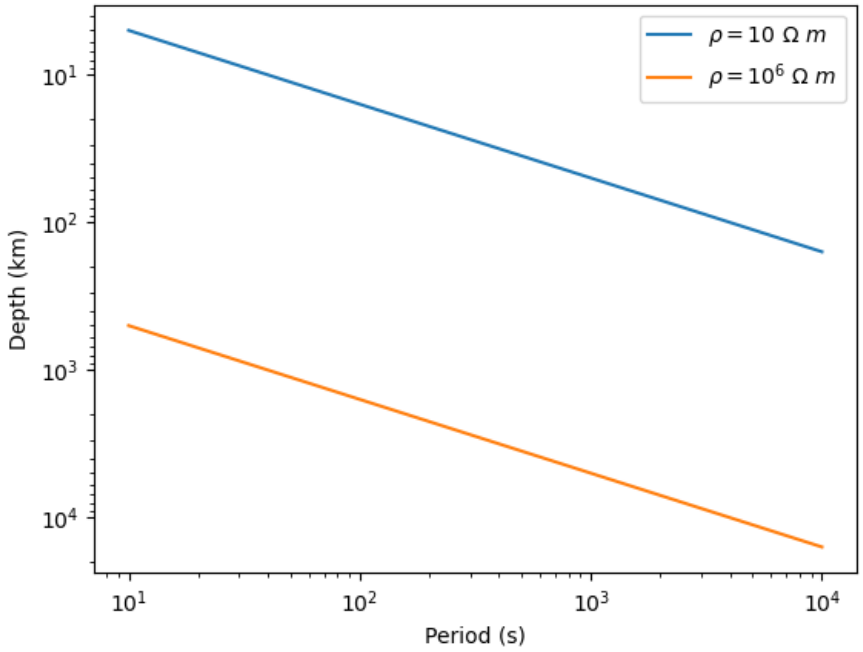

Figure 2.21: Equation 2.35 plotted across the main period range affected by geomagnetism (10 – 10,000 s), for two different resistivity settings between which most rock are present, $\rho = 10 - 10^6\ \Omega$ m.

($10^6\ \Omega$m), the signal can easily propagate down 100 km for most periods and 1,000 km for longer periods. When the rock is more resistive it can much more easily become charged. In reality, the surface of the Earth is not at all homogeneous and some of the patterns seen here are not observed in nature. Notably, the resistivity of rock falls off dramatically below the lithosphere, with the asthenosphere and below are composed of relatively conductive rock and hence induction below a few hundred kilometres usually falls off significantly (hence higher periods then 10,000 s are usually not required for this reason, but should be considered if the lithosphere extends deeper).

2.3.5 Galvanic Distortion

Galvanic distortions are frequency-independent distortions in the regional electric field measurements caused by local, near-surface inhomogeneities , commonly observed in MT surveys (Ledo et al., 1998; Rao et al., 2014; Delhaye et al., 2017, Figure 2.22). The main issue with galvanic distortions is that they alter the appearance of deeper regional structures driving the geoelectric field. Galvanic distortions can both alter the amplitude of the electric field at a site, sometimes by orders of magnitude, as well as change the dominant orientation as a result of the geoelectrical structures (Chave and Jones, 2012). In terms of mapping subsurface resistivity, galvanic distortion is noise (see Figure 2.23), with much research into these distortions by the MT community in order to remove or mitigate their effects. Near-surface inhomogeneities that can accumulate

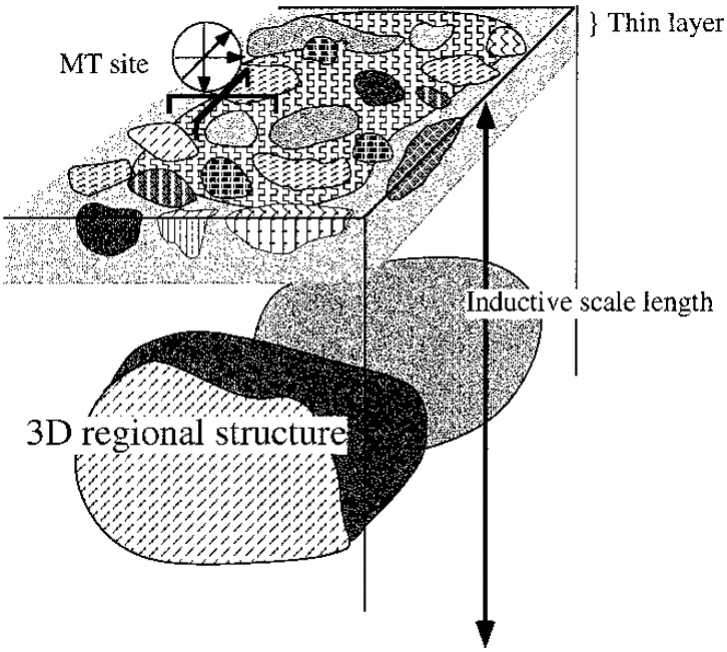

Figure 2.22: A representation of the localised near-surface inhomogeneities, that cause galvanic distortions in measured geoelectric fields, from Utada and Munekane (2000).

significant charge are generally responsible for this distortion, though topography can also generate these distortions (Käufl et al., 2018).

While for resistivity maps galvanic distortion can be considered noise, in terms of modelling GICs these galvanic distortions should be considered. These local effects alter the geoelectric fields that drive GICs, so hence individually they can also generate a current, albeit at a smaller scale. Most space weather studies include distortions for this reason. There is an issue with this, however, in that galvanic distortions are highly localised. When interpolating between sites a local effect is extrapolated across a larger region, causing a similar issue to the subsurface mapping. Whether or not including galvanic distortion in models or removing it would produce a better model has not been well researched, hence in chapters 5, 6, 7 we analyse this topic in more detail, using separate models with and without a distortion correction.

2.4 Geomagnetically Induced Currents in Power Grids

During large geomagnetic storms large $d\mathbf{B}/dt$ can drive significant electric fields, which pose a hazard to power-lines, pipelines, among other infrastructure. Here, we mainly focus on its effect on power grids. GICs are a collection of alternating currents (AC) of slow time-varying frequencies directly dependent on the frequency of geoelectric fields, whose sum acts like a direct current (DC). GICS in Ireland could reach over 100 A which is more than sufficient enough to cause damage to transformers in power grids (Blake et al., 2018). In the case of power-lines, GICs can cause damage to transformers

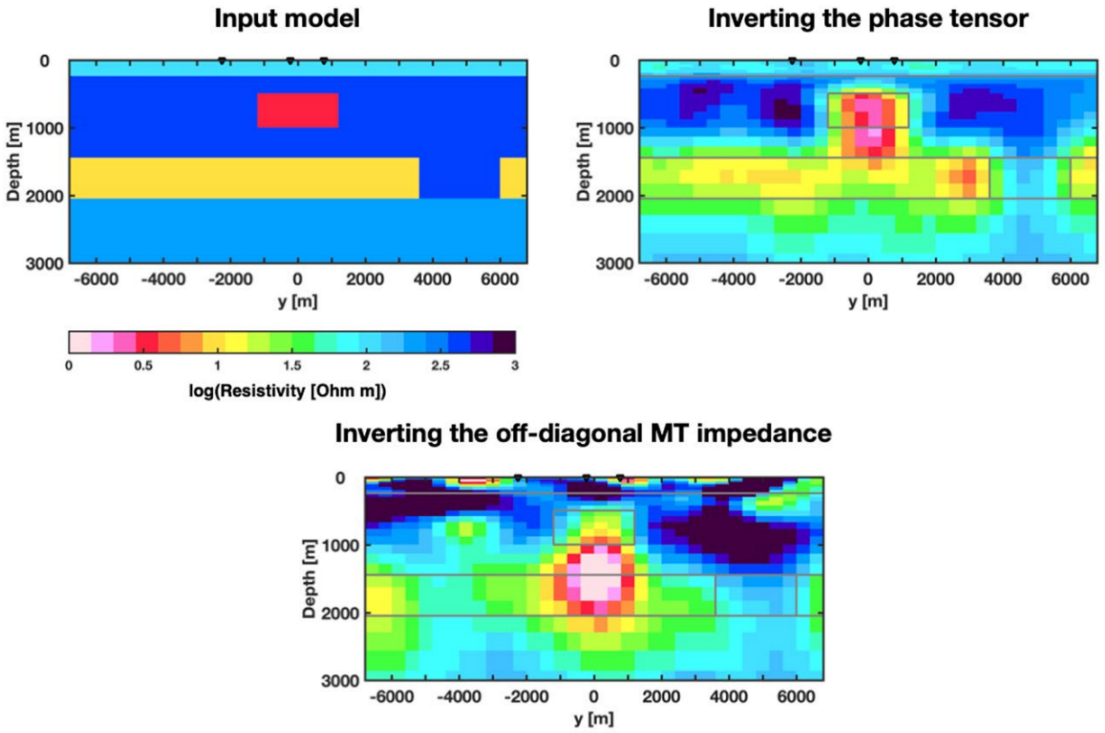

Figure 2.23: The effect of galvanic distortion demonstrated for an artificial resistivity profile from Rung-Arunwan et al. (2022). Three imaginary measurement sites at the surface are denoted by the small black triangles. The true profile is on the top left, the estimated profile using these measurement sites is on the top right. At the bottom, galvanic distortion is introduced near the surface, which changes the apparent resistivity profile at depth and creates artefacts in the profile.

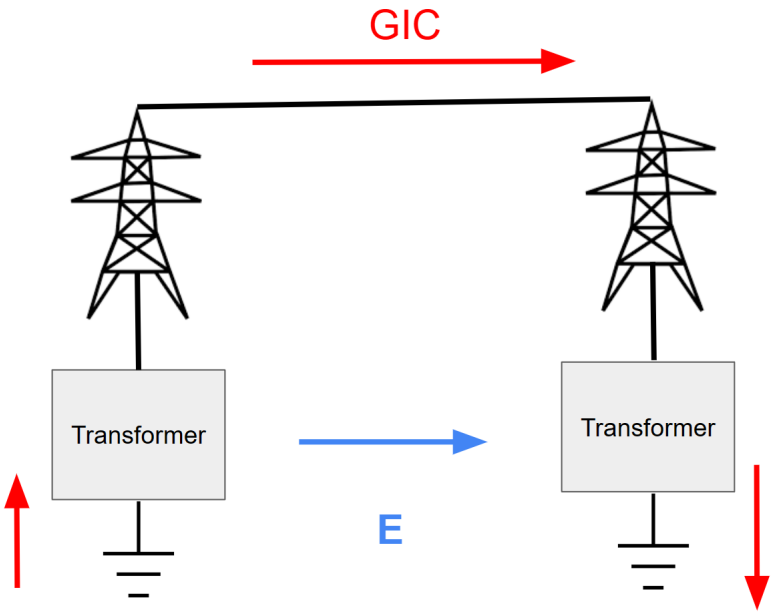

Figure 2.24: A visual representation of the GIC induction (red) in a power grid through grounded transformers, driven by the inducing geoelectric field, **E** (blue).

by causing overheating, due to the saturation of the power-grid's AC currents, caused by the addition of the DC-like GIC. In the case of pipelines, GICs act like a catalyst, accelerating corrosion in the pipeline via electrolysis. These electric fields can induce GICs, according to the formula:

$$V_{ab} = \int_a^b \mathbf{E} \cdot d\mathbf{S} \tag{2.36}$$

where a and b are the two grounding points, V is voltage and **S** is the displacement between points a and b (Figure 2.24).

While Equation 2.36 works for a simplified single line of a power grid, other factors need to be accounted for. This includes the resistances of components of the power grid, line resistance and grounding resistance at transformers, how different power lines are connected to one another and interact and types of transformer winding configurations. Estimating GIC requires looking at the summed effects of all these factors together.

2.4.1 Transformers and the Effect of GIC

Transformers are devices in power grids used to convert electrical energy from one alternating circuit to another voltage either higher or lower, or to a different form (i.e., AC to DC). When electricity is produced at a power plant, it is immediately stepped up to a higher voltage (V) by reducing the current (I), thus conserving power (P) according to Ohm's law.

$$P = VI \tag{2.37}$$

The purpose of stepping up the voltage is in order to allow for long distance transport of electrical power as reducing voltage reduces the voltage drop, or essentially lost power along the line according to:

$$\Delta V = 2ISR \tag{2.38}$$

where R is the resistance along the line, S is the displacement. After transmission along the line, the voltages are then reduced again by a transformer, for use in commercial and domestic applications. Standard high voltage power networks use three-phase AC with transformers to readily convert between different voltage levels (Boteler and Pirjola, 2014). These consist of three power lines with the voltage of each wire 120^o phase shifted relative to the other wires but at the same amplitude and frequency (hence why high voltage transmission lines have three lines instead of one). These three phase transmission lines are connected at transformers to a neutral point connected to ground at each end as a safety feature. During normal conditions, the sum of the power between the three lines is zero and thus no power is transferred to ground. If there is an imbalance in one, the excess power flows into the ground.

The connection to ground is where the issues related to GIC begin, however. The connection allows for current to flow from ground into the grid and from the grid to ground. As mentioned before (Section 2.3.1), the geoelectric field can drive GIC between transformer sites along transmission lines. The transmission lines form an effective short circuit, which electric fields can use to dissipate built up electrical energy. When the GIC enters the network, its path is subject to Kirchoff and Ohm's laws, which depend on the topology and resistance of the network. While the power lines are relatively unaffected by this current, the transformers are not.

The mentioned transformers are designed for AC of a specific frequency, 50Hz in the case of the Irish power grid. GIC are not induced at this frequency and are instead similar to inducing a DC current (see Figure 2.25). GIC are in fact AC currents also, but very slow varying and induced at multiple frequencies between the geomagnetic inducing frequency range (Oyedukun et al., 2020, $\approx$ 0.1 – 0.0001Hz) and act DC-like compared to the fast varying 50Hz signal. Introducing DC to AC offsets the AC sinusoid and leads to half-cycle saturation. Transformers are designed to be very efficient, so the addition of even a small GIC can cause significant saturation every half-cycle (Gaunt and Coetzee, 2007). This produces three main issues: transformer overheating, harmonic generation and reactive power losses.

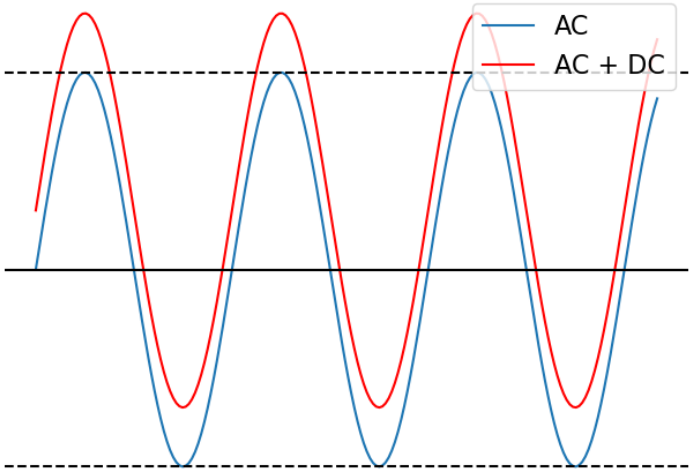

Figure 2.25: An example of the half-saturation cycle generated by introducing an additional DC signal onto an AC current. The saturation point, denoted by dashed lines, can become exceeded which leads to the loss of magnetic flux, which can in turn lead to overheating.

Overheating

With an added DC component, the non-magnetic shields used to control magnetic flux in the transformer will begin to hold more and more flux. This can generate eddy currents which encounter internal resistance in the transformer, with the energy dissipated in the form of heat. Large and sustained GICs have the potential to completely destroy the transformer in this manner, and repeated heating of the transformer can damage its thermal insulation, leading to reduced performance and lifespan (Koen and Gaunt, 2003; Gaunt and Coetzee, 2007). For instance, the example shown in Figure 1.6 was first damaged by a geomagnetic storm in Halloween 2003 before a geomagnetic storm in November 2003 further damaged it beyond repair. In extreme cases however, a transformer can be damaged beyond use in a single geomagnetic event.

Harmonic Distortions

Transformers are normally designed to only generate signals with only odd harmonics (i.e. 50, 150, 250 Hz, see Section 3.5.2 later for an example of this) and thus generally built to only cope with odd harmonics. Half-cycle saturated transformers are a source of even and odd harmonics however (Dong et al., 2001; Clilverd et al., 2020). Harmonic distortions can result in a series of malfunctions in a transformer, such as tripping of circuit breakers and to the reduced performance of control systems, which can ultimately lead to failures. Harmonics generated by GICs were the main cause for the Quebec blackout in 1989 (Bolduc, 2002).

Reactive Power Losses

Reactive power losses are not only an issue related to GIC, but an issue generally for power grids as saturated transformers have a higher reactive power consumption (Qin et al., 2011). Large changes in the reactive and real power balance can cause voltage fluctuations in the system (Pulkkinen et al., 2017), as well as reducing the long-term efficiency of the transformer. This lack of synchronisation can end up leading to faults within a system. Coupled with overheating problems and harmonic distortion in individual transformers, this can lead to a failure across the grid.

2.4.2 Potential Mitigation of GIC

A few different techniques and/or upgrades can be employed to mitigate GIC damage. However, due to the complex nature of power grids, there is no simple fix or solution. The most common way is by installing large capacitor banks at individual transformers. These capacitors are installed at the neutral point of these transformers and effectively block any GIC from entering the power grid. There are two main downsides to these however. Capacitor banks are quite expensive and difficult to install, meaning they can't feasibly be installed across an entire grid of hundreds of transformers. Often these banks simply offload the GIC to other transformers instead, so if they are installed, they should be installed with caution to ensure they don't worsen the issue across a power grid (Marti, 2014; Mac Manus et al., 2023).

An alternative approach is to use neutral earth resistors (Divett et al., 2018). Neutral earth resistors (NER) increase the effective resistance between the neutral grounding point and the higher voltage levels within the transformer, without completely cutting off GIC from entering. Their effectiveness was tested in the New Zealand south island power grid by artificially introducing large DC currents into the network, with the NER not used experiencing saturation before using NER to reduce the effects (Lapthorn et al., 2023; Clilverd, 2023).

The use of transformers of differing ages and types can also be considered. Newly installed transformers are more robust than older transformers and can withstand GIC for longer. Old transformers can slowly accumulate damage which makes them more susceptible to saturation and overheating (Koen and Gaunt, 2003). The ferromagnetic core material of the transformer can be changed to increase the saturation point caused by GIC (Fritsch and Wolter, 2023; Zeraati et al., 2021). Simple two-winding transformers are usually less prone due to added shielding compared to the more complex and efficient auto-transformers. How well a transformer is performing can also be monitored. Transformers that are struggling especially due to overheating begin to out-gas compounds in oils used in their operation. Out-gassing measurements can be

taken intermittently to monitor the performance of the transformers and help determine whether a transformer is struggling after a space weather event and needs to be replaced (Gaunt and Coetzee, 2007).

2.4.3 Modelling GIC: The Lehtinen-Pirjola Model

The most widely used model to estimate GIC in power grids is the Lehtinen-Pirjola (LP) model (Lehtinen and Pirjola, 1985; Boteler and Pirjola, 2014). This is the method of modelling GIC in power grids implemented later in this work (Chapter 7). Power grids consist of many grounded transformers, with power transmission lines connecting each node that these ground points lie on, forming a complex circuit system. The LP model is based of Kirchoff's current law, a net current flowing into a node, k, branches of into the other nodes within the circuit, n:

$$i_k = \sum_{n=1}^{N} i_{nk} = -\sum_{n=1}^{N} i_{kn} \tag{2.39}$$

where i denotes current in a specific branch, N is the number of branches. The current branch i_{kn} is driven by an electromotive force (emf, e_{kn}), the potential difference between the two nodes ($v_k - v_n$) and the admittance(i.e. how easily a current can flow in a circuit, measured in Siemens, S) of the branch y_{kn}.

$$i_k = y_{kn}[e_{kn} + (v_k - v_n)] \tag{2.40}$$

Equating Equations 2.39 and 2.40 yields:

$$i_k = -\sum_{n=1}^{N} y_{kn}[e_{kn} + (v_k - v_n)] \tag{2.41}$$

The emf across an individual transmission line can be represented by a current source:

$$j_{kn} = e_{kn} y_{kn} \tag{2.42}$$

The summed currents provide the current directed toward each node in the network:

$$J_k^e = -\sum_{n=1}^{N} j_{kn} \tag{2.43}$$

where $n = k$. Substituting Equations 2.42 and 2.43 gives:

$$i_k = J_k^e = J_k^e - v_k \sum_{n=1}^{N} y_{kn} + \sum_{n=1}^{N} v_n y_{kn} \tag{2.44}$$

The first sum in Equation 2.44 represents the dependence of current i_k on voltage v_k while the second sum gives the dependence of the current relative the voltage on the other nodes v_n. The first summation gives diagonal elements of a network admittance matrix, Y,

$$Y_{kk}^n = \sum_{n=1}^{N} y_{nk} \tag{2.45}$$

as opposed to the second summation whose elements are off-diagonal:

$$Y_{kn}^n = -y_{kn} \tag{2.46}$$

Combining Equations 2.44, 2.45 and 2.46, and re-writing each term in matrix form gives:

$$\mathbf{I^e} = \mathbf{J^e} - \mathbf{Y^N V^n} \tag{2.47}$$

where $\mathbf{I}$ is the column matrix of currents, $\mathbf{V}$ is the column matrix of voltages. The voltage matrix can be related by Ohm's law provided the impedance is known:

$$\mathbf{V^n} = \mathbf{Z^e I^e} \tag{2.48}$$

Equating Equations 2.47 and 2.48 and solving for $\mathbf{I^e}$, leads us to an equation we can estimate the current out to be:

$$\mathbf{I^e} = (\mathbf{1} - \mathbf{Y^n Z^e})^{-1} \mathbf{J^e} \tag{2.49}$$

where $\mathbf{1}$ is the identity matrix.

2.4.4 Calculating GIC from Geoelectric Fields

A method to theoretically calculate the current across a power grid has now been provided. Now for the purpose of this work, a method to relate the electric field at each node of the power network to the current is desired.

The admittance matrix is defined by the resistances between the nodes of the network

$$Y_{ij} = -\frac{1}{R_{ij}} = \sum_{n=1}^{N} \frac{1}{R_{ki}} \tag{2.50}$$

where i and j are nodes of the network, assuming $i \neq j$ and k is the end point along the line. If the nodes i and j aren't connected then R_{ij} is assumed to be infinite.

The column vector $\mathbf{J^e}$ has components:

$$J_i = \sum_{k \neq i} \frac{V_{ki}}{R_{ki}} \tag{2.51}$$

The voltage across the network can be calculated use an electric field values, provided the path of the network is known:

$$V_{ki} = \int_k^i E dS \tag{2.52}$$

where dS is the differential path. Hence, the electric field can be used to estimate the current at each node. The current between nodes is sent over 3 sets of power transmission lines as opposed to a single, parallel to one another. The resistance along each of these lines (R_p) is assumed to be equal and thus, the equivalent resistance (R_e) across each conductor is given by:

$$\frac{1}{R_e} = \frac{1}{R_p} + \frac{1}{R_p} + \frac{1}{R_p}, \qquad R_e = \frac{R_p}{3} = R_{ij} \tag{2.53}$$

Provided enough information about the power grid is known, electric fields can be used to make practical estimates of the GIC. This information includes transformer winding resistances, coordinates of the transformers and details on the connections between separate transformers, the grounding resistance at each node and resistance along transmission lines. Ireland has a small, effectively isolated power grid, only connected to external grids between high voltage DC interconnectors. This makes the island an ideal case to study the effects of GICs across an entire grid, as any GIC induced in the power grid should solely be due to GICs entering from grounded transformers in the Irish power grid, with no other external source.

2.4.5 Transformer Types and Windings

There are two main transformer types used throughout power grids, two-winding and auto-transformers (Figure 2.26), which each have to be accounted for separately in a GIC model. The auto-transformer consists of a single coil, used for both the primary and secondary winding in the circuit, between a high and low voltage node. Two-

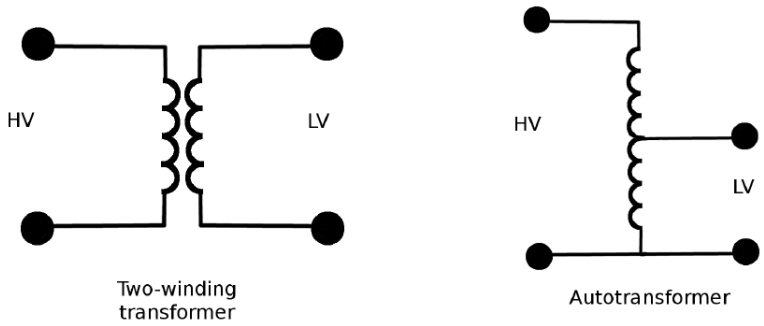

Figure 2.26: A schematic of a two-winding transformer (left) and an autotransformer (right) for a single phase. The two winding transformer consists of single coil between voltage busbars while the two-winding consists of two separate coils, from Blake (2017).

winding transformers (YY or YΔ) in contrast, are made up of a separate primary and secondary winding connecting to a higher and lower winding busbar (bus) within a substation. The benefit of auto-transformers is that they reduce the amount of copper used and are thus cheaper. Two winding transformers are beneficial in that they are generally safer to operate as the primary and secondary windings are separate. Both have different design features and thus this need to be considered differently in GIC models. The solution to this when modelling is to consider high and low voltage nodes of YY transformers to have infinite resistance (Boteler and Pirjola, 2014, 2017), as virtual nodes. Similarly, autotransformers are considered to have an infinite resistance at the high voltage node.

3 Monitoring Geomagnetic Storms

In this chapter, more of the physical and operational aspects of the project as a whole are discussed. This is focused mainly on the Magnetometer Network of Ireland (MagIE), which includes the maintenance of the DIAS/TCD operated geomagnetic observatories, upgrades to the network and the magnetometer website (www.MagIE.ie). The network monitors and archives magnetic variations during geomagnetic storms and is thus pivotal to the work regarding the modelling of ground-based effects of space weather in later Chapters. Prior to the outline of the network in this Chapter, a general overview on geomagnetic observatories is provided, describing how magnetometers work, the types used for ground-based monitoring and then how they can be used to classify geomagnetic activity.

3.1 Magnetometers

A magnetometer is a device which is used to measure magnetic induction, and estimates the magnetic field strength based on the induction. Magnetometers are used in many sectors, with common and simple everyday examples in sensors for cars, traffic lights and fridges. The most basic form of magnetometer is the Hall effect sensor, which is used to measure the voltage difference across a surface in response to a magnetic field. The magnetic field can then be estimated by:

$$V = R(\frac{I}{t} \times B) \tag{3.1}$$

where V is the voltage, I is the current, t is the thickness of the conductor and B is the magnetic field strength, R is the Hall effect coefficient, dependent on the material.

Most of these magnetometers are too simple for the purposes of space weather monitoring and need a higher level of sensitivity. A more complex version of a magnetometer with increased sensitivity is the inductive coil magnetometer. An inductive coil's core is made up of a material, which becomes magnetised due to the magnetic field strength, with a loop of wire or a solenoid, wound around the magnetised material. A voltage is induced by a change in the magnetic flux of this conductor according to Faraday's law:

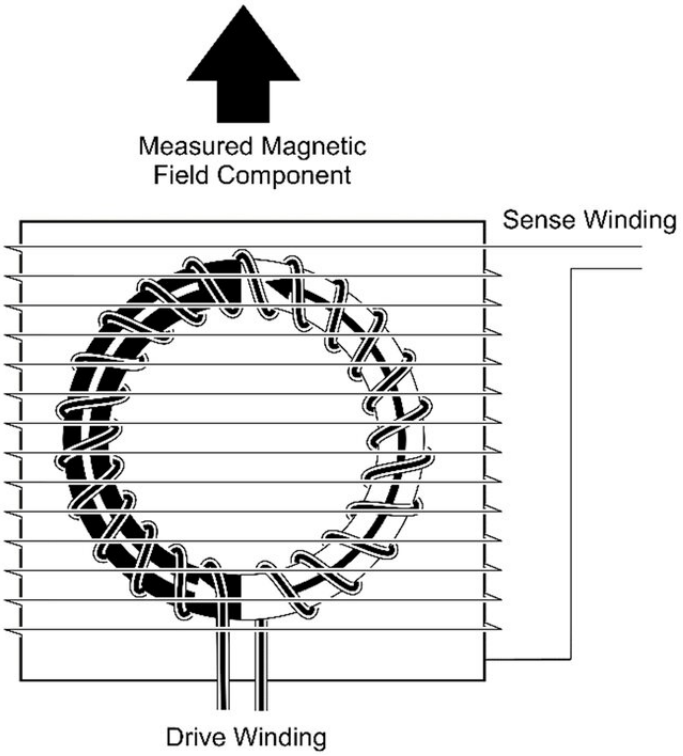

Figure 3.1: A schematic of a drive winding and sense winding surrounding a ferromagnetic core, in this case a loop (Miles et al., 2017). The drive winding magnetises and demagnetises the core, while the sense winding picks up external signals.

$$V = -N\frac{d\Phi}{dt} \tag{3.2}$$

where Φ is the magnetic flux, N is the number of windings. The magnetic field can be calculated provided the current is measured through the use of the relationship:

$$B = \mu_0 NI \tag{3.3}$$

Generally the magnetised materials used are ferromagnetics, as they are highly sensitive to magnetic field variations and hence even small changes in the magnetic field can be determined from the output voltage.

3.1.1 Fluxgate Magnetometers

The magnetometers used to monitor space weather are mostly fluxgate magnetometers, including the magnetometers used in this project (Section 3.4). Fluxgates are a more sensitive version of an inductive coil magnetometer, originally developed in 1936 to detect submarines via naval aircraft (Janosek, 2017), which counters some of the issues with simple inductive coil magnetometers, improving sensitivity. The core of fluxgate consists of a ferromagnetic core which has a high magnetic susceptibility, surrounded by two sets of coils: a drive winding and a sense winding (Figure 3.1). In contrast

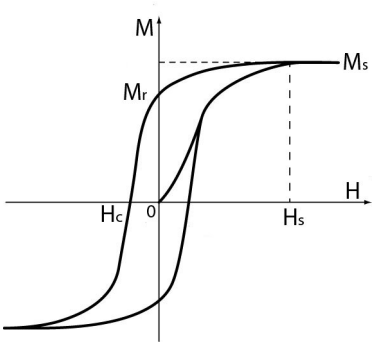

Figure 3.2: The schematic of magnetic hysteresis, comparing the magnetic field intensity (H) and magnetisation (M). The material's original state is at origin, non-magnetised with no external field. An external field is applied, and increased until the material reaches its magnetisation saturation point (M_s). The external magnetic field source is then removed. At point M_r, no magnetic field is applied however the material is still somewhat magnetised. By symmetry, the same is observed when a magnetic field is applied in the opposite direction.

to a simple inductive coil, an alternating current is passed through the drive winding, driving the core in an alternating cycle of magnetising the core till saturation in one direction, followed by the other direction and back again. The sense winding is designed to pick up any external magnetic field along with the internal magnetic field, while the drive winding is shaped so the sum of any external magnetic field is zero. If no external magnetic field is applied to the core, the sum of the internal induced field is zero due to the currents in the drive and sense winding being opposite and equal in direction. In the presence of an external field however, the magnetic field strength will be greater in one direction than it is in another, and thus a signal can be reproduced.

The main benefit of the fluxgate over a simple induction coil is that the ferromagnetic is cycled through each stage of its hysteresis loop (Figure 3.2) as the magnetic field is measured, from saturation of the material in one direction to the other (Figure 3.3). Hysteresis is the behaviour in ferromagnetic material whereby if a magnetic field is applied to a material and the magnetic field is then removed, the material's magnetic moment still aligns in the direction of the magnetic field (i.e. the material remains magnetised). By cycling through the loop the external magnetic field will not introduce an additional magnetised state and thus the current can be more accurately measured. Three separate sensors are used for the different orientations (B_x, B_y and B_z) to build a full image of the magnetic field. In this configuration, the voltage returned for a single axis due to magnetic field changes can be estimated using the equation:

$$V(t) = -NS\mu_0\left(\frac{dB_i}{dt} + K\mu_0\mu_r\frac{dH_e}{dt} + K\mu_0 H_m\frac{d\mu_r}{dt}\right) \tag{3.4}$$

where V is voltage, B_i is the internal magnetic field due to the internally induced

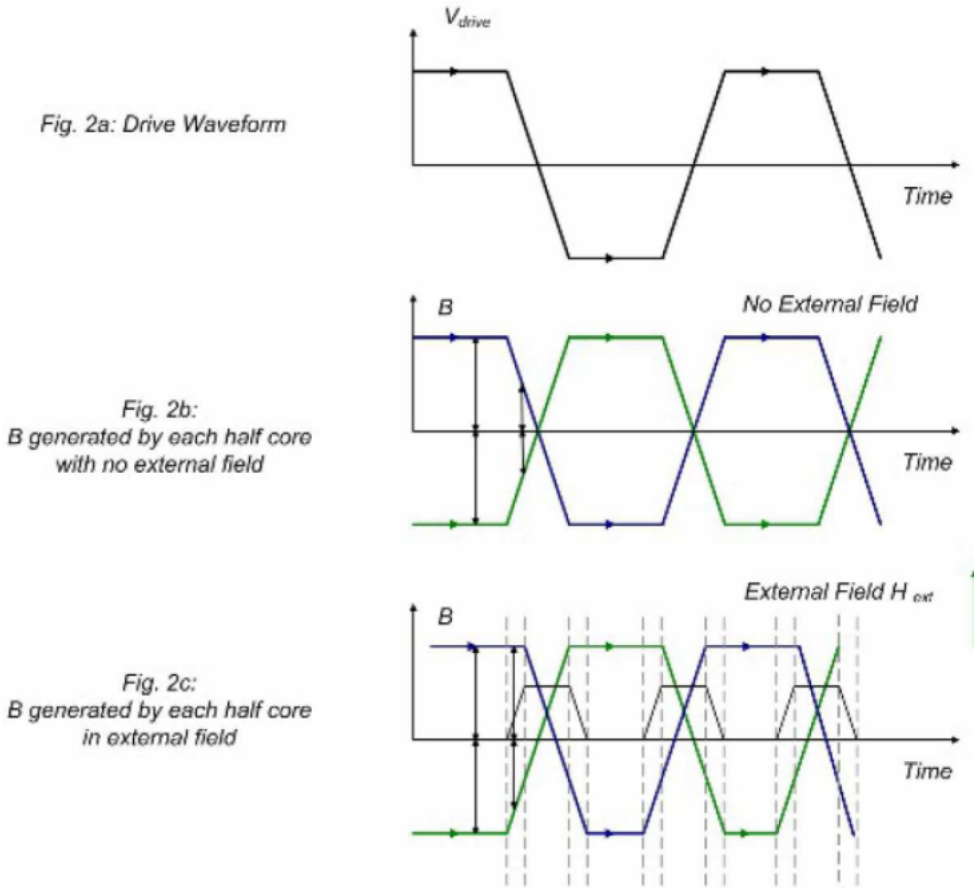

Figure 3.3: The excitation voltage of the drive winding, sense winding and the effect of an external field within a magnetometer (from the Imperial College, Space and Atmospheric Physics website `https://www.imperial.ac.uk/space-and-atmospheric-physics/`).

current, μ_r is the susceptibility of the core, $H_e = \Phi B_e$ is the magnetic field intensity, Φ is the magnetic flux, S is the cross-section and K is a constant scaling factor (Janosek, 2017). Thus, provided each parameter is known, B_e can be calculated from $V(t)$.

Two main internal sources of noise exist in fluxgates that are considered in design: Barkhausen noise (sudden jumps in magnetisation due to defects in the crystal lattice of the core) and thermal white noise. Modern methods to mitigate this noise generally alter physical parameters of the ferromagnetic core, to respond less to noise. These include changing shape, and using materials with a low demagnetisation and high permeability, such as cobalt-based amorphous materials and using stress annealing to reduce the abundance of defects in the core (Janosek, 2017).

3.2 Evaluating Magnetic Activity

3.2.1 Magnetic Coordinates Systems

The two typically used coordinate systems for ground-based magnetic field measurements are the XYZ and HDZ systems (Matzka et al., 2021). The X, Y and Z (or B_x, B_y, B_z) system is a simple geographic based coordinate system, where X is the magnetic field in direction of the geographic north pole, Y is the magnetic field in eastward direction and Z is the vertical component of the magnetic field. The HDZ system is a system of measuring the magnetic field with the geomagnetic pole as the focal point instead of the geographic pole (Figure 3.4). H or the horizontal component (not to be confused with the magnetic field intensity) is the magnetic field strength in the direction of the magnetic pole, D or the declination (not to be confused with the displacement field) is the angle between the magnetic and geographic pole, while the vertical component Z remains the same. The two coordinate systems can be related by coordinate geometry as follows:

$$H = \pm\sqrt{X^2 + Y^2} \tag{3.5}$$

$$\cos D = \frac{X}{H} \tag{3.6}$$

The standard unit used for magnetic fields is the nanoTesla (nT), with the Earth's magnetic field varying between approximately 30,000 - 80,000 nT, dependent on latitude (Thébault et al., 2015).

3.2.2 Magnetic Indices

Magnetic indices exist to compare and classify geomagnetic activity, both quiet times and storms. Indices give a simple quantification of the level of geomagnetic activity

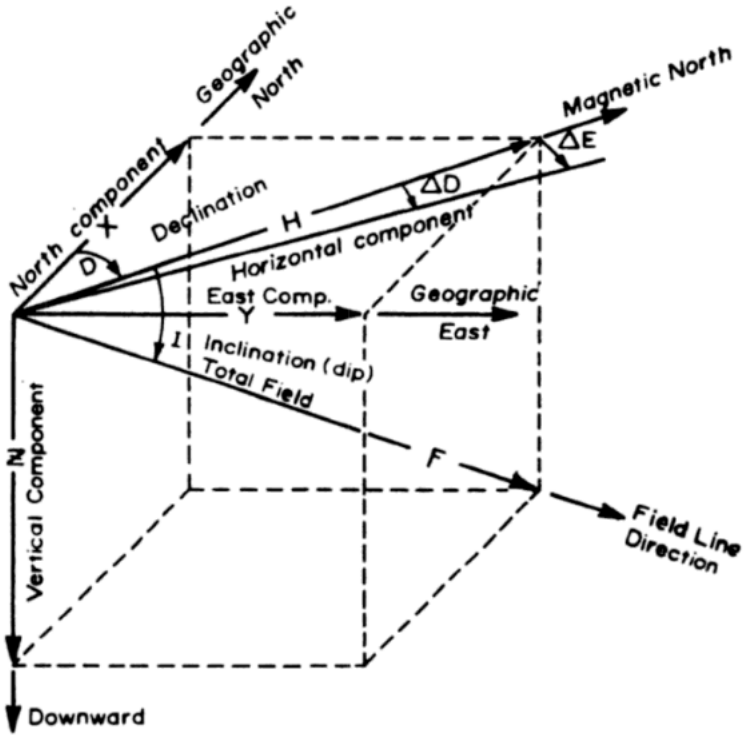

Figure 3.4: A comparison of the XYZ geographic coordinate system, to the HDZ geomagnetic coordinate system (Campbell, 2003).

which can be advantageous to space weather research in terms of looking back over historical storms and forecasting the effects of coming storms.

K-Index

The K-Index (Kennziffer indicator) and its variants (e.g., planetary K-Index or Kp) are the most commonly used indicators used to quantify geomagnetic activity, first introduced by Bartels et al. (1939). The K-Index provides three hour windows of the local horizontal variation in the geomagnetic field, obtained from magnetometer measurements. The scale for the K-Index is quasi-logarithmic and ranges from 0 – 9, where K = 0 indicates completely quiet conditions, K = 5 indicating a small storm and K = 9 indicates a severe storm, roughly a once in a solar cycle (11-year) event. The index factors diurnal variations into account, mitigating the magnetic variation due to the convection of ionospheric currents induced by the X-ray and UV emission during the quiet time Sun (no solar flaring), the Solar regular curve (S_r, see example in Figure **??**). After the S_r curve, a thresholding approach is used, whereby the K-Index is defined by maximum recorded horizontal component of the magnetic field within the 3-hour window. Originally the S_r curve was manually calculated by hand, with the K indices calculated after, however many digital techniques now exist to calculate the S_r curve, as well as adaptive smoothing methods like frequency filtering (Clark, 1992). The K-Index works best in mid-latitude countries ($40 - 65^o$), as these regions tend to be less affected by large low altitude ionospheric currents, which tend to be

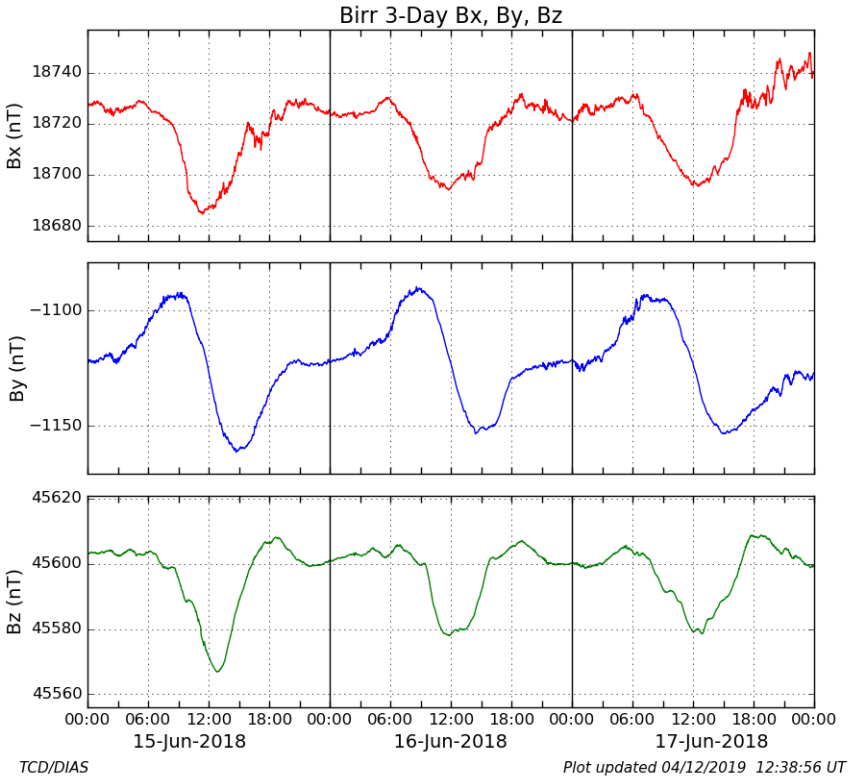

more localised such as the auroral and equatorial electrojets (Rostoker, 1972). At other latitudes, indices like the auroral electrojet index (60 – 75°) or ring current index (0 – 30°) are more appropriate. In this work, however, the K-Index can be used, due to Ireland falling entirely between its latitude range (52 – 55°).

FMI Method

The Finnish Meteorological Institute method, or FMI method is the method used here to calculate K-Indices at MagIE magnetometers. The FMI method is advantageous for the following reasons:

- The method is simple and can be applied to any observatory within an appropriate latitude range, provided a scaling factor is known.
- The method is fully automatic.
- It is the most accurate method compared to hand drawn K-Indices, among the four models endorsed by the International Association of Aeronomy and Geophysics (Menvielle et al., 1995; Matzka et al., 2021).

The FMI method is implemented as follows:

1. Raw geomagnetic time series are re-sampled to minute data. A one hour moving window cleans any values out which deviate by more than 3σ
2. The minimum and maximum variation of the horizontal component of the magnetic field (compared to the baseline) are subtracted from one another within a

Table 3.1: The range of quantified K-Indices between Niemegk and Armagh (one of our observatories in Ireland) are compared, after a scaling factor is applied to the K-Index of Armagh.

K-Index	**Max Threshold - Niemegk (nT)**	**Max Threshold - Armagh (nT)**
0	0 – 5	0 – 6.1
1	5 – 10	6.1 – 12.2
2	10 – 20	12.2 – 24.4
3	20 – 40	24.4 – 48.8
4	40 – 70	48.8 – 85.4
5	70 – 120	85.4 – 146.4
6	120 – 200	146.4 – 244
7	200 – 330	244 – 402.6
8	330 – 500	402.6 – 610
9	500+	610+

Table 3.2: The estimated values of the solar regular curve, m, for the FMI method.

Hour of day	**m (nT)**
21:00 – 03:00	120
03:00 – 06:00	60
18:00 – 21:00	60
06:00 – 18:00	0

three hour UTC time frame (i.e. 00:00 – 03:00 UTC, 03:00 – 06:00 UTC, etc.), separately for B_x and B_y.

3. The largest variation is multiplied by a scaling factor and compared to Table 3.1 to get a preliminary K-Index.

4. An estimated S_r curve is smoothed (Table 3.2) and subtracted from the horizontal value.

5. The final K-Index is then calculated.

The scaling factor mentioned is dependent on the latitude of a country, the closer a country is to auroral regions, the greater the magnetic activity and hence the greater the factor needs to be. The factor is scaled relative to the Niemegk observatory in Germany, upon which the K-Index was originally based, relative to the threshold for a K = 9 storm, 500 nT.

Blake (2017) originally scaled the observatories to be 540 nT for the observatories in Ireland (Armagh, Birr and Valentia, see Section 3.4) by comparing magnetic observations from Birr to the Eskdalemuir geomagnetic observatory in the UK. This worked well for Birr, however Armagh and Valentia are approximately 1° further North and South respectively, which is significant. Therefore the K-Indices were re-scaled for the old and new observatories via peak-to-peak analysis and estimated to be 610, 570, 540 and 480 nT for Armagh, Dunsink, Birr and Valentia respectively (see Table 3.1 for

an example). After rescaling, the K-Indices agreed more between the separate magnetometers (see Figure 3.5). However, small discrepancies in storm strength can exist between sites due to local effects in geomagnetic storms (e.g. due to ionospheric turbulence/local enhancements.)

Kp-Index

The Kp-Index, or planetary K-Index is a version of the K-Index that is applied to give a representation of geomagnetic activity across the globe, as opposed to locally, introduced by Bartels et al. (1939). The Kp-index is derived by calculating the weighted average of the K-Indices between 13 pre-selected magnetic observatories, located between 44 – 60^o geomagnetic latitude. Kp index is considered the global standard for magnetic activity index, however it is somewhat biased due to the latitude range, as well as the lack of an even distribution of sites (most observatories are located in North America and Europe, with only two representatives from the Southern hemisphere) and thus these limitations should be factored in when using the index. However in the case of Ireland, neither of these limitations apply and thus the Kp index is a good proxy for activity here. Some benefits of the Kp index include accounting for diurnal variations from the solar regular variation, as well as not being strongly affected by seasonality in geomagnetic activity (Rostoker, 1972). Throughout the manuscript, K- and Kp- indices are used more often than other indices, however caution is taken relative to their limitations.

DST

Due to the limitations of the Kp index, often other magnetic indices are used to quantify activity in different regions. One of these indices is the disturbed storm time index (DST). The disturbed time index is derived from four near-equally spaced equatorial geomagnetic observatories, taking the mean of each (Sugiura, 1964). The DST is traditionally calculated hourly, however can also be calculated per minute. The DST focuses on measuring the activity in the equatorial electrojet. While limited to the equator, the DST is a useful proxy for estimating the magnetic field at the initial and main phase of the storm worldwide, however it performs poorly on the nightside of the Earth, related to sub-storms caused by reconnections on this side of the Earth.

AE Index

The auroral electrojet (AE) index is generally used to quantify the activity of a geomagnetic storm in auroral region, using (roughly) evenly distributed geomagnetic observatories between 60 – 70^o geomagnetic latitude as inputs, with a 2.5 minute cadence (Rostoker, 1972). Thus AE index is usually more useful for higher latitudes, however it can be more useful for particularly large storms, when the auroral electrojet spreads to mid latitudes. Contrary to DST, the AE is much more useful in determining

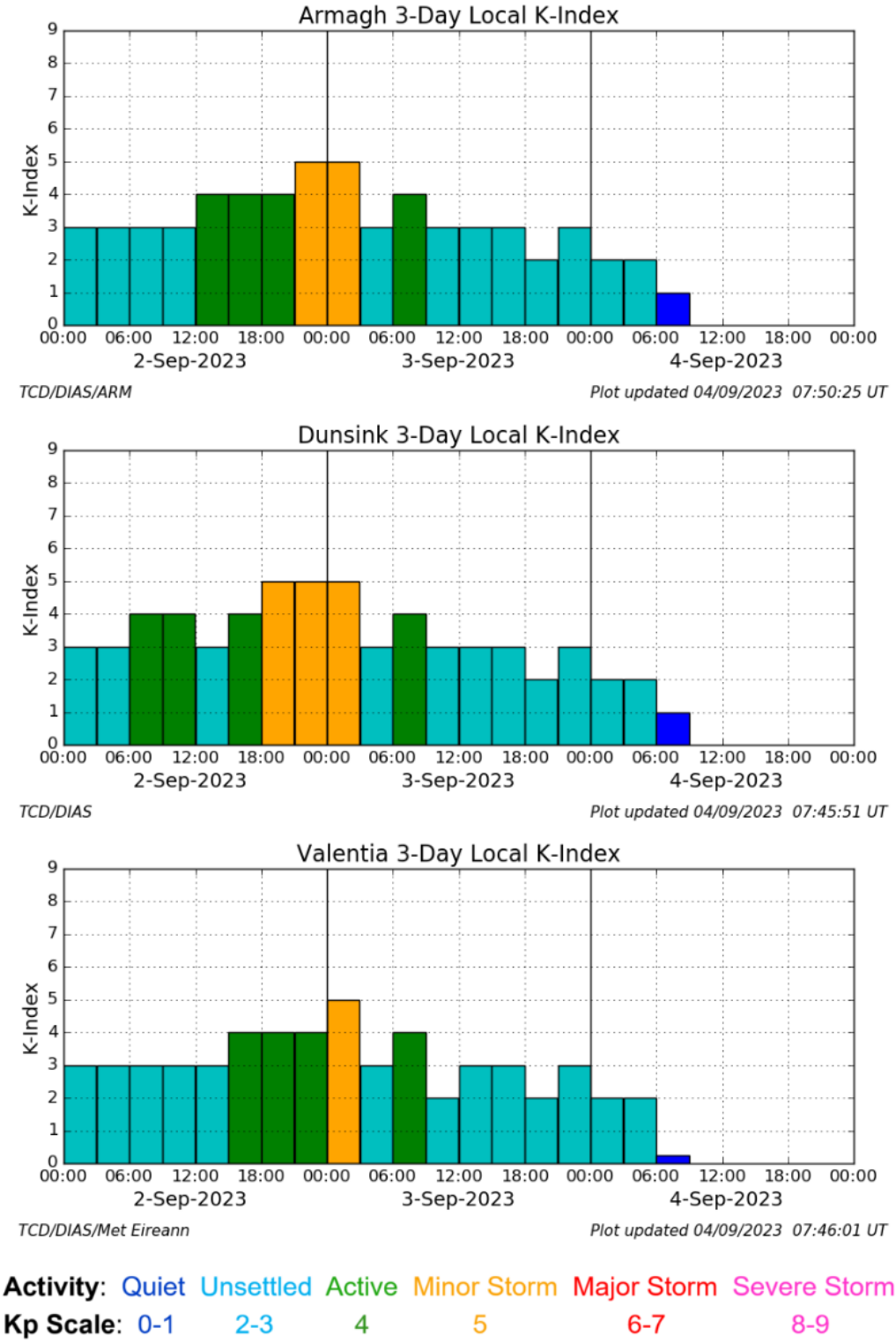

Figure 3.5: An example of the live K-Indices from three of the geomagnetic observatories (Armagh: top, Dunsink: middle, Valentia: bottom). The amplitude of the K-Indices are denoted by the colour scale at the bottom.

when a sub-storm occurs. The index calculates the maximum difference between the eastward electrojet (AU index) and westward electrojet (AL index) on the dusk ($\approx$ 15 – 21 Local time, LT) and dawn sides ($\approx$ 03 – 09 LT) of the Earth respectively, AE = AU - AL. A strongly negative AE indicates an enhancement in the westward electrojet, likely due to a substorm. For the purposes in this thesis I do not use AE index, as the focus here is more on the storm as a whole, however, it is useful to know of the existence of the separate index in terms of distinguishing substorms.

3.3 INTERMAGNET

INTERMAGNET (International Real-time Magnetic Observatory Network) is a global network of geomagnetic observatories, which was established in 1991 to collect data from magnetometers worldwide and provide it online, following the digitisation of magnetic field data. The network is made up of approximately 160 stations distributed worldwide (Figure 3.6) and provides daily magnetic field time series and plots from these sites (`https://intermagnet.org/`). Geomagnetic observatories in the network have to exceed a variety of categories to ensure only suitable and accurate data are utilised, including low magnetometer noise levels, and high resolution ($>$ 0.1 nT) and cadences (1-minute data, Table 3.3). The network is currently increasing cadences to one-second data, as while most geomagnetic effects related to space weather are captured by 1-minute cadence data, a significant amount of the signal is present between 10 – 60 s Oyedukun et al. (2020). Throughout this manuscript, data from INTERMAGNET observatories is used, particularly when using magnetic field data from countries outside Ireland, but also for analysis using older data.

In the Valentia meteorological observatory, County Kerry, Mét Éireann operates Ireland's single INTERMAGNET observatory. The Valentia geomagnetic observatory was originally established in 1886 alongside the transatlantic cable, with part of the reason to "study the relation between magnetic storms and earth currents" (Fitzgerald and Cullum, 1889). Valentia has digitised one-minute resolution data (useful for space weather) available from 1987 onwards, with lower cadence one hour data extending back to the 1950s. Data from the INTERMAGNET network is used for some analysis in later chapters.

3.4 MagIE - Magnetometer Network of Ireland

MagIE is a magnetometer network established in Ireland in 2012 jointly between DIAS, TCD and Met Éireann, made up of temporary and permanent magnetometers. At present, three permanent housed magnetometers belong to the network, the Armagh, Birr and Valentia magnetometers (which Mét Éireann operates), with a new temporary

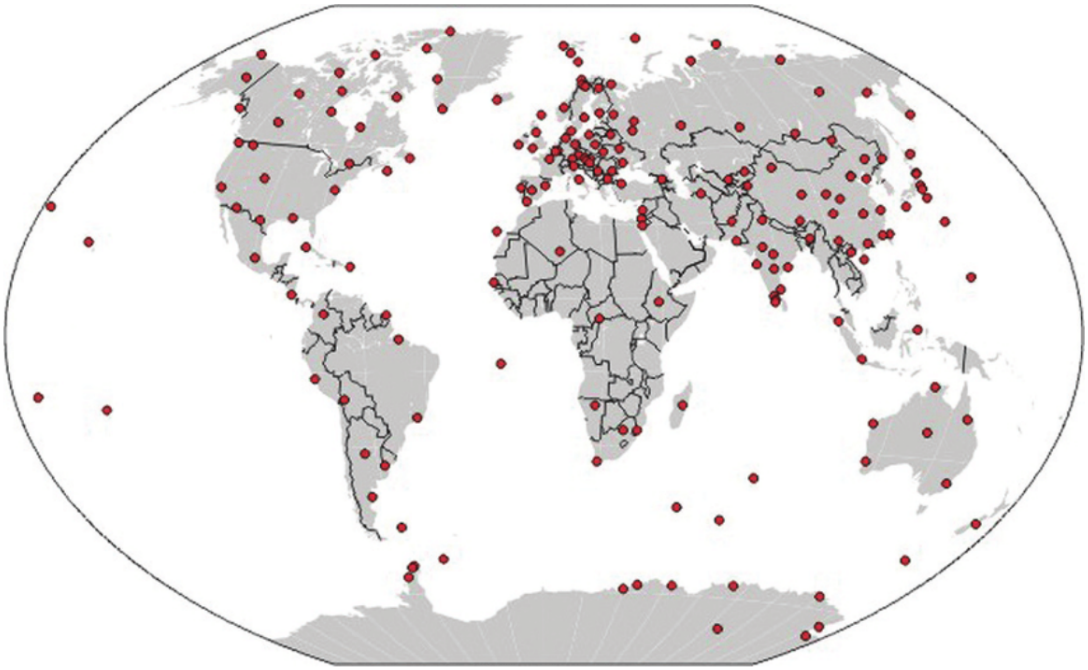

Figure 3.6: The geomagnetic observatories across the world part of the INTERMAGNET network marked by red dots (from the BGS website, `www.geomag.bgs.ac.uk/`).

site tested and added to Dunsink observatory (Figure 3.7). Data recorded by these magnetometers is later used as the main source to model magnetic field variations across the island. A website (www.magie.ie) and server were set up in 2019 to archive and store all the data from each observatory as well as provide real-time data and magnetic activity plots. One of the main goals of this work was to both maintain and expand this network. In this Section, an overview of the equipment used in the network and how said equipment is installed is explained.

3.4.1 Instrumentation

The magnetometers used for this project were all fluxgate magnetometers (Section 3.1.1). While the same type of magnetometer is used, brands of varying quality are used throughout this project. Three different brands of magnetometers are used, LEMI-417M, SENSYS FGM and raspberry pi (Rpi), each with varying performances. The quality of each is assessed in Table 3.3, with an image of each in Figure 3.8.

LEMI 417M

The LEMI 417M magnetometer is the best magnetometer type used in the network, both in terms of sensitivity and robustness. The LEMI 417M is specifically designed for field conditions and measures magnetic field time series, but can also measure geoelectric fields (See Section 5.1.2 for description of measured geoelectric fields). The LEMI 417M meets each of INTERMAGNET's standards (Section 3.3), so is used as the main observatory type magnetometer in the network. The magnetometer observatories

Figure 3.7: The location of each of the MagIE magnetometer observatories. The Armagh and Birr magnetometer are older magnetometers operated by DIAS and TCD. In this project, the new Dunsink magnetometer was installed. The Valentia magnetometer is operated by Mét Éireann and is also part of the INTERMAGNET network.

Table 3.3: The performance of the different magnetometers in the network is shown. On the right, the magnetometer criteria for INTERMAGNET (a standard for observatory grade magnetometers) are shown for comparison. Data for the LEMI and SENSYS magnetometers was given by manufacturers, while data for the raspberry pi magnetometer roughly constrained in the Rpi project from Beggan and Marple (2018). In terms of quality, the LEMI-417M is best, with the Rpi magnetometers being the worst.

Metrics	**LEMI 417M**	**SENSYS FGM**	**RPi**	**INTERMAG**
Sample Rate (Hz)	1	400 – 2400	0.5	1 min
Thermal Drift (nT/K)	0.2	0.3	> 3.85	0.2 max
Resolution (nT)	0.01	0.15	1.5	0.1 max
Approximate Cost (€)	18,000	3,500	300	N/A
Long term Drift (nT)	5	5	> 5	5

Figure 3.8: Each magnetometer brand is shown; the LEMI 417M magnetometer is on the left, the SENSYS FGM3D in the middle and raspberry pi on the right frame of the image. (left) The LEMI magnetometer is made up of the fluxgate on the left side, data logger in the middle, with the option to attach electrodes (the cylinders on the right side) for electric field measurements. (middle) The SENSYS logger is on the left and magnetometer on the right side. (right) The raspberry pi magnetometer is made up of the three FLC-100 magnetic sensors oriented inside a perspex block.

in Armagh and Valentia both use LEMIs.

SENSYS FGM3D

The SENSYS FGM3D is a slightly less precise magnetometer that is significantly cheaper. While the SENSYS magnetometer does not reach the INTERMAGNET standard for thermal drift (set more for long-term trends in the geomagnetic field), it is just below the standard and is capable of accurately characterising geomagnetic field variations caused by space weather events. This high quality in the INTERMAGNET network is required for recording precise long term changes in Earth's magnetic field strength and not for space weather. The SENSYS magnetometers also have a much higher sampling rate. This can be used to identify noise from high frequency signals, such as electricity at 50 Hz. This makes the FGM3D magnetometer ideal for testing sites for noise. Another benefit of this is that SENSYS magnetometers can be used to indirectly measure GIC in power lines, using the differential magnetometer method as magnetic fields due to power lines at 50 Hz and its harmonic frequencies can be separated (Matandirotya et al., 2016; Hübert et al., 2020, see Figure 3.9). A downside of FGM3D magnetometers are they are significantly less robust (they are not specifically designed for outdoor use) so more precautions need to be taken to ensure no damage. The temporary site in Dunsink currently uses the SENSYS FGM3D.

Raspberry Pi Magnetometer

The raspberry Pi magnetometers are less sensitive, very low cost magnetometers designed during a separate mini-project with the goal of installing them in schools. This makes them useful for collecting scientific data from a greater diversity of locations and improves outreach. A separate Section is dedicated to this mini project (Section 3.6)

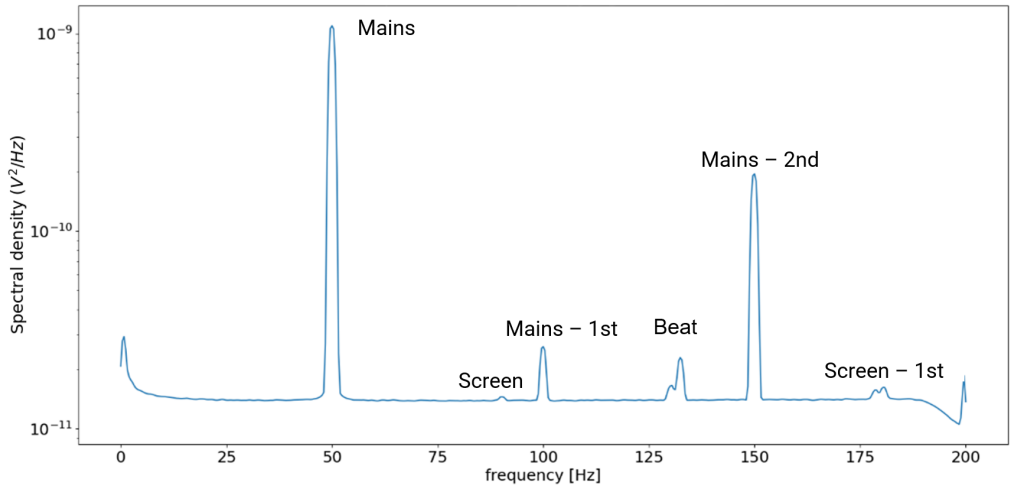

Figure 3.9: Examples of noise picked up on the SENSYS magnetometer when testing the magnetometer over the course of a day. An FFT is applied to a time series to extract frequency domain data. The peaks at 50 (fundamental oscillations), 100 and 150 Hz (harmonic oscillations, denoted by 1st, 2nd) are magnetic signatures of mains electricity. The small peak at 90, 180 Hz were the magnetic signatures of the frame rate of a PC screen. The beat frequency between the first harmonic of the screen and the fundamental of the mains is also observed at 130 Hz (180 – 50 Hz).

as their design and calibration must be explained.

3.4.2 Status of MagIE Observatories

Dunsink Magnetometer

A new temporary magnetometer location was set up in Dunsink observatory to test the potential to later install a permanent magnetometer here. A SENSYS magnetometer was installed firstly. There were two criteria which dictated where we could install the magnetometer:

1. The magnetometer needs to be at least 35 metres away from cars/power lines to keep noise below 5 nT (based on preliminary testing).

2. A USB device needs to connect the data logger to the PC.

The site chosen was in an area 45 m away from the main building, far from power lines and any ferrous objects, in the garden of Dunsink observatory. This distance presented a problem however. The SENSYS data logger requires a USB connection. Most USB devices have a maximum threshold of 20m. Our solution was to use ethernet to USB converters and provide power to the magnetometer using a power over ethernet (PoE) injector and splitter. Using a shielded cable ethernet allowed us to send signal and power across the same cable. Using this setup also meant that the computer and data logger could potentially be extended to 60m apart. Another problem also relates to sending 12 V 1 A power over longer distances. The voltage drop over this distance

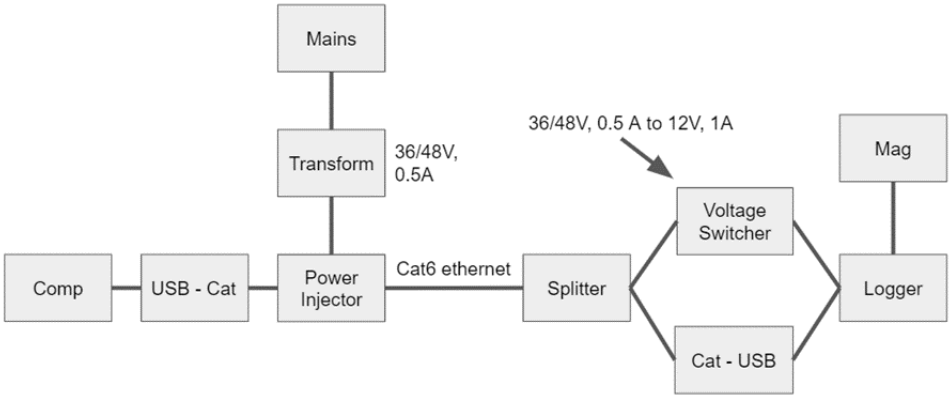

Figure 3.10: The wiring design for the installation of SENSYS magnetometer in Dunsink. From left to right the design is made up of: a recording computer with a USB connected to an ethernet adapter for communications. A power injector is used to add 48 V DC of power to the ethernet cable. At the end of the cable, a splitter splits the power and comms into two separate ethernet cables. The communications cable is reconverted to USB, while the voltage is stepped down from 48 V to 12 V.

is too significant using ethernet cables. This voltage drop can be estimated using the equation:

$$\Delta V = 2LrI = 2\ (45m)\ (0.106\Omega)\ (1A) = 9.54V \tag{3.7}$$

where r is resistance of the wire, L is its length. Instead 48 V 0.5 A voltage was sent out instead, with a voltage switcher was used to change the power from 48 V, 0.5 A to 12 V 1 A at the data logger to minimise any voltage losses to the logger (ΔV = 4.77 V). The switcher was designed to fully convert accounting for voltage drops down to 30 V 0.5 A, thus easily allowing for this voltage drop here.

During the installation the wiring design in Figure 3.10 was used. Two waterproof junction boxes were used to bury the magnetometer and all the components related to the data logger. The magnetometer was buried to improve shielding from noise and the thermal stability of the magnetometer. The junction box for the magnetometer was levelled. Ideally concrete should be poured to avoid later movement, but as this was designed as a temporary installation, was levelled on the ground. The magnetometer is fixed to a base plate, determining the X and Y values by comparing measurements of the magnetic field to the International Geomagnetic Reference Field (Alken et al., 2021, IGRF). The magnetometer was first oriented in the direction of magnetic north before slowly being rotated and then fixed in place when approximately correct (within 1^o). The magnetometer was then carefully buried to ensure the junction box did not move (Figure 3.11).

Figure 3.11: The magnetometer was buried about 50 cm down using waterproof junction boxes to house the magnetometer and data logger separately (right). The magnetometer was buried to reduce noise and help thermal stability.

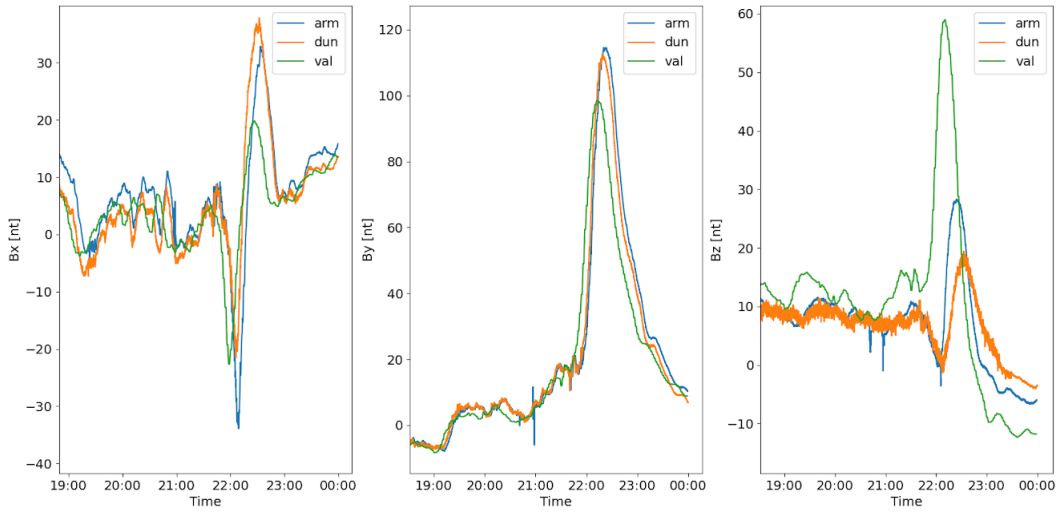

Figure 3.12: A later direct comparison of the magnetic field variation in XYZ coordinates, between the Armagh (arm), Dunsink (dun) and Valentia (val) magnetometers on the 8th December 2021.

Testing and Results of Installation

Testing and validating that the magnetometer was working correctly was essential to ensure the data received was of good quality. This first involved direct comparison between magnetic field data, followed by evaluating noise levels. An in-depth discussion of noise is later described in Section 3.5.2. To ensure the magnetometer was working accurately, the time series variations were compared between Armagh, Dunsink and Valentia. The time series should be different, but relatively similar in terms of shape of the signal and hence comparable.

The direct comparison in Figure 3.12 is an example of the installation relative to other magnetometers. The same shape can be seen between separate sites in each magnetic field component. Variance in amplitude relates to distance from the pole for

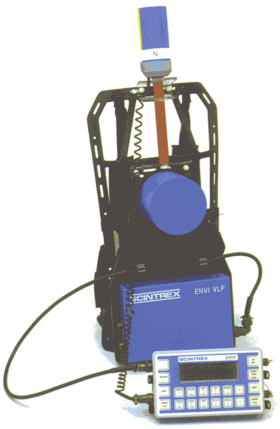

Figure 3.13: The ENVI geophysical system, made up of a magnetometer alongside a very-low-frequency (VLF) antenna (the magnetometer was only needed for our purpose). The device consists of the back-strap for carrying the magnetometer, the data logger (foreground) and the magnetic sensor (on top of the metal rod).

the X and Y components. The Z component often varies relative to local features as well as geomagnetic activity, so hence amplitude here is site specific. Noise in the Z component is seen at Dunsink, caused due to magnetic fields from electricity within the main building of the observatory. Hence a band-pass filter was applied to mitigate this (Section 3.5.2).

The magnetometer has since performed effectively, proving the test to be successful and hence a permanent installation is planned. The main issue we found was that we were slightly too close to the building and car park so there was some noise. Therefore for a future permanent installation a magnetometer (most likely a LEMI) is planned to be installed farther away (Figure 3.15) with a design shown in Figure 3.14, similar to the Birr design (Figure 3.17).

Survey Magnetometer

Before the installation of the permanent stationary magnetometers, a location for the magnetometer is required to be scouted and tested for sources of magnetic anomalies (generally related to buried iron and steel). A survey magnetometer can be used to test this. In our case, the ENVI geophysical survey magnetometer, borrowed from Geological Survey Northern Ireland (GSNI), was used to survey the area for sources of noise (Figure 3.13).

Ideally, the software for the magnetometer would have been used to plot a contour map of the area. Unfortunately however the equipment's memory recording system no longer works, so data was not downloadable. Instead, we manually recorded readings of the magnetic field strength from the data logger, and marked off areas were anomalies were recorded (Figure 3.15). From these measurements, we deduced a suitable site for

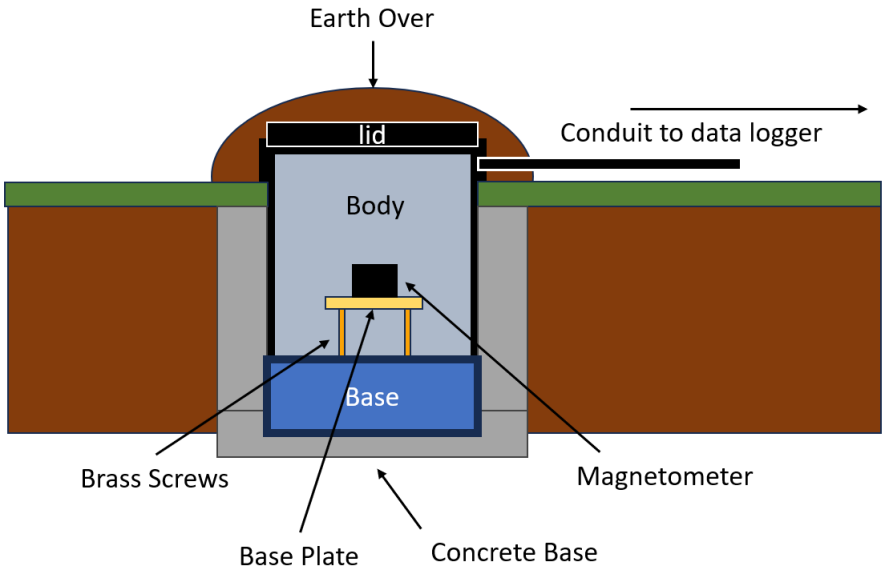

Figure 3.14: The design of the future permanent magnetometer chamber for Dunsink. The position of each component is displayed. The design is essentially the same as the Birr repair (Figure 3.17), but without the surrounding old chamber.

a permanent installation.

3.4.3 Birr Magnetometer

The Birr magnetometer was originally installed in 2012 and, in terms of quality of data, is the best magnetometer in the network (see Section 3.5.2 for example). Between 2013 – 2019 the magnetometer ran smoothly, with the exception of a few small water failures (e.g. a water breach/ingress in the chamber) and a lightning strike damaging the data logger (Blake, 2017). However, before the start of this PhD project in January 2020, a major water failure occurred in the Birr magnetometer chamber which required the chamber to be repaired. The water failure was not an easy fix (the biggest understatement of this manuscript), with the failure related to a fault in the original chamber design. There was a partial fault with the seams of the PVC walls of the chamber, likely due to abrasion with sounding soil. This was patched using sealant, however this did not solve the problem, and merely removed the exit of water from the chamber (hence it filled more). The real issue was with the concrete base. The concrete base is porous and overtime became saturated, which allowed water to seep up into the chamber during heavy rainfall.

The re-installation was delayed till 2023, firstly due to COVID and permission issues related to the lockdown, we could not easily install a new chamber. Ideally a complete new chamber would be installed, however permission to dig a new chamber was difficult to acquire. Luckily the old chamber was too big. Hence, with the help of Joe McCauley, I came up with a solution: build a new chamber inside the old one (Figure 3.16). The

Figure 3.15: A map of the area considered for installation of the permanent magnetometer in Dunsink, denoted by the blue box. Magnetic anomalies recorded are marked roughly using red circles, roughly marking the area affected by the magnetic anomaly (to approximately 5 nT). Letters were used to denote the sources: a) red brick wall, b) buried/visible iron related to the walls, c) unknown, d) manhole lid. The buried location of the currently installed temporary magnetometer and planned for permanent are also highlighted by orange and yellow crosses respectively.

Figure 3.16: The repaired Birr magnetometer chamber. The new chamber (in blue) is placed in the old chamber (in black) with a new magnetometer base plate at the centre for mounting. Brass screws are used to make slight adjustments to the alignment of the plate.

new design was installed with a new concrete base, as well as with a plastic base over it to stop water seeping through to the chamber (Figure 3.17). Non-magnetic material was used in the construction. The concrete mix was made up of regular Portland cement, a limestone sand and limestone aggregate. Brass screws were used to mount the plastic base-plate, to allow adjustment of the plate if necessary. Originally nylon screws were used in the old design, however the nylon expanded due to moisture which disabled the ability to adjust the plate, hence they were not used this time.

3.4.4 Armagh and Valentia Magnetometers

The Armagh observatory magnetometer was originally installed in 2016. The Armagh magnetometer remained relatively stable in terms of physical state and thus required little attention in terms of repair. The main issues with Armagh related to replacing the old PC, as well as replacing old rusted connectors. While physically the Armagh magnetometer is sound, its environment has become more noisy (See Section 3.5.2) with signals related to ongoing construction projects at the observatory and the opening of a car park near the magnetometer. While the data are still useful, for this reason in future the magnetometer should be moved to a new location, ideally after the construction projects. The Valentia magnetometer is operated exclusively by Mét Éireann and as

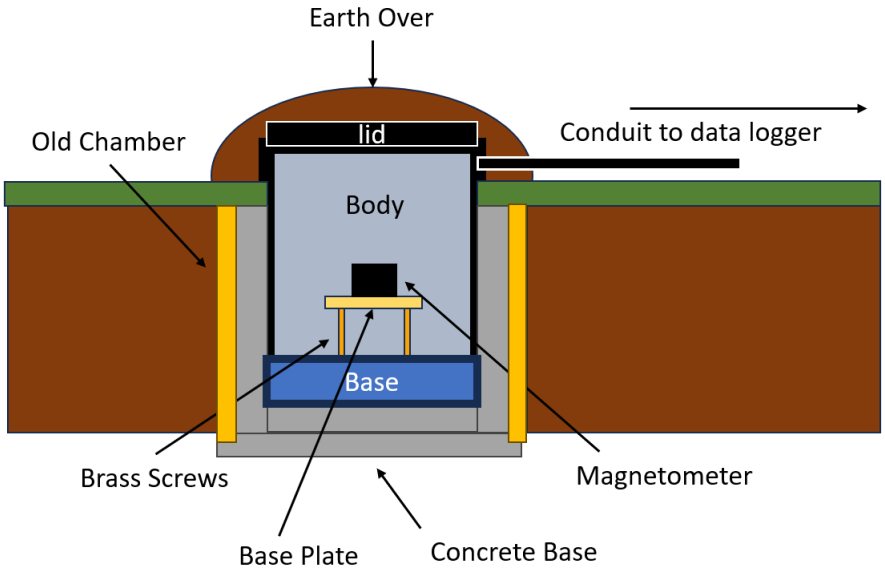

Figure 3.17: The design of the repaired Birr magnetometer chamber. The position of the old chamber is marked in orange. The position of each component is displayed. The main advantage of the previous designs are the inclusion of a plastic base layer, to stop water seeping up through the concrete, as well as surrounding the plastic with concrete, to ensure the plastic does not wear out.

a result no maintenance is required from the side of DIAS. The data from Valentia is highly reliable as it is a member of INTERMAGNET (International Real-time Magnetic Observatory Network but can suffer from temporary outages (see Section 3.3).

3.5 MagIE Website and Automation

In this Section, the website for the magnetometer network of Ireland (www.MagIE.ie) is explored. Namely how data are recorded, plots of activity generated and a general description provided of other products available on the website. The MagIE website was established in 2019 to automate plots of geomagnetic activity using live data from the magnetometer observatories. Prior to the MagIE website, the only source of live magnetometer data was the Birr magnetometer housed at www.rosseobservatory.ie. Blake (2017) developed python scripts to plot magnetic field time series and k-Indices (see Section 3.2). During this project, these scripts were adapted to work with each magnetometer in real time. An archive was also set up to store these data and plots (Figure 3.18).

3.5.1 Data Automation

The first main task for the website was to set up a PC server (henceforth referred to as Houdini) to store all the magnetic field time series collectively from a remote PC, before generating plots of the data. This is all done automatically using a mixture of python and bash/batch scripts with cronjobs/task scheduler running these scripts

Figure 3.18: An example of the homepage for the website from 24/11/2023. K-Indices are displayed, while the tabs in the top panel can be used to explore real-time activity and supplementary material in more detail.

every five minutes to update the website. The server is a Linux machine, however Windows machines are used for the local machines as they are required to run the appropriate software.The automation protocol of the MagIE magnetometer network works as follows:

1. Magnetic field time series are measured and recorded, using individual software on remote PCs related to the magnetometer type used.

2. A python script is run to format the time series correctly into a .txt file, and checks to ensure the measured timestamps are correct.

3. A batch script is run to send data from remote PCs to Houdini. This data are sent to a specific folder shared to the web, with formatted by time of year in the following structure: "data.magie.ie/year/month/day/txt/siteyearmonthday.txt".

4. A python script is run on Houdini to read in data from each of the magnetometers to plot data for the magnetometers, which:

   (a) Checks for noise in the time series. If noise is present, it is flagged and removed from the plotting procedure (a more in depth look at the filtering method is explained in Section 3.5.2).

   (b) Plots of magnetic field time series and K-Indices are generated using adapted python scripts to those first made by Blake (2017). A separate scaling factor is used for the k-Index at each of the magnetometers, due to differences in latitude.

   (c) Plots are recorded to the archive folder in the format "data.magie.ie/year/month/day/png/", as well as live files which are then pulled from the archive to the main website.

   (d) Fail-safes are employed in the event a magnetometer is down (due to a power outage for example), to ensure the script continues to work for each good magnetometer.

For more specific technical information on the automation of the network can be found on the github (https://github.com/TCDSolar/MagIE_Scripts) with permission from the DIAS/TCD Solar group.

3.5.2 Magnetometer Filtering and Noise Analysis

Each of the magnetometers were tested for noise from artificial sources with the goal of removing any significant noise from real-time data. Often FFT or wavelet transforms are used to identify or remove noise from time series. These methods do not work well at the edges of time series (including real-time) however, so a thresholding approach is used instead. To identify noise on the magnetometers, the rate of change of the

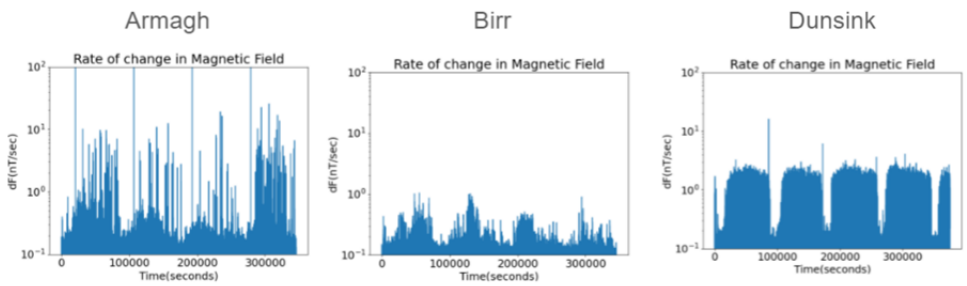

Figure 3.19: The rate of change of the total magnetic field (F) at an interval of one second over the course of four days. The sharp spikes are generally related to noise from cars, while the consistent bands during the day time are related to electrical noise (best seen for Dunsink on the right).

total magnetic field (dF/dt) was plotted at a one second interval. Variations in the geomagnetic field are usually gradual (10 – 10,000 s) (Oyedukun et al., 2020) as opposed to the short period artificial noise (0.1 – 10 s). To test for noise, all signals shorter than 1 s were removed, as the majority of the signal is unlikely to be geomagnetic or, if it is, its amplitude will be small.

In the Figure 3.19, two sources of noise can be seen:

1. Moving metal bodies (i.e. cars). The sharp peaks in the Armagh data are a good example of this; an old car park was reopened about 20 metres away from the Armagh magnetometer and we can now see large signals as cars pass by. An example of this is also seen at 80,000 seconds in Dunsink (related to a lawnmower!).

2. Electricity. The large continuous bands of signal at Dunsink are a good example of noise from electricity. Noise from electricity is constant throughout the day, but dies down during the middle of the night due to the decreased demand across power lines.

Ideally the Armagh magnetometer will need to be moved in future to lower this noise, while a permanent installation in Dunsink should be moved further away from the house to reduce noise from AC power-lines. The site in Birr needs no further action. We also examined the effects of thermal noise by looking at the long-term temperature stability in Armagh (2016 – 2021) and Birr (2013 – 2020). Daily stability is better than 1°C which was ideal, while yearly stability varied between 3 – 17 °C and 4 – 19 °C respectively. This will incur a drift of 3 nT maximum (see table, long term drift), which is below the INTERMAGNET standard of 5 nT (see Table 3.3), so thermal noise is insignificant. As a result, no change is needed for the magnetometer chamber design.

A general peak filter has been applied to flag any data where the one second field gradient exceeds 10 nT/s to ensure that the K-Index gives correct readings (Figure

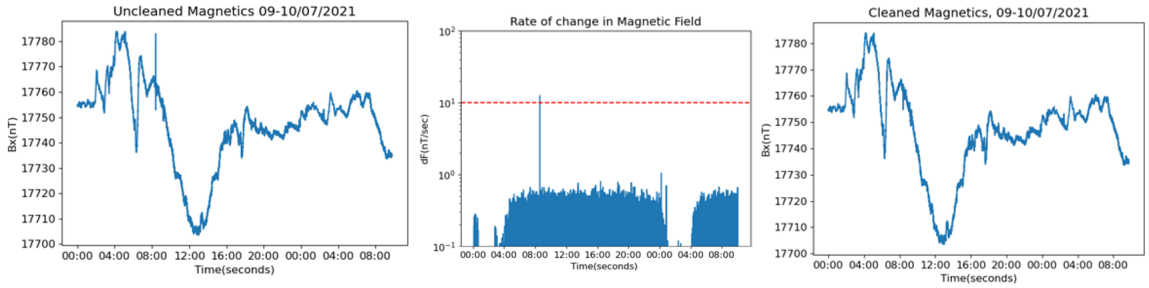

Figure 3.20: The peak filter in operation for a storm on 09 – 10/07/2021. The uncleaned Bx time series is shown on the left, the rate of change of Bx in the middle (with the cut-off point for the filter in red) and cleaned time series on the right for Dunsink. The noise at 08:00 UTC is removed by the filter.

3.20). This filter was tested for multiple K = 9 storms with clean data for the Valentia magnetometer, and we found that the filter flagged no data as the threshold is never exceeded. Therefore, this method of filtering is effective and hence applied. Due to the increased cadence of the SENSYS FGM3D magnetometer used in Dunsink (set to 400 Hz), he signals at higher frequencies related to electricity (fundamental 50 Hz and its harmonics 100 Hz, 150 Hz, 200 Hz, ...) can be identified and removed. The time series are converted to frequency space using an FFT. A simple Gaussian band filter is then applied to remove any data at these frequencies and hence mitigate the effects of noise. An inverse FFT is then used to retrieve the time series.

3.5.3 Network Outreach and Extra Services

Alongside the scientific data provided on the website, extra services are provided. The hope of this project was to create a website with scientific resources in a public friendly manner, alongside outreach material explaining space weather effects to a general audience.

Educational Material

Educational material is provided to any member of the general public on the website `www.magie.ie/education`. The material is generally simple and describes some of the basics of space weather, for example solar storms and how they lead to geomagnetic storms, how aurorae are formed and potential impact on technology (Figure 3.21). This was developed thanks to interns from the DCU STEM Teacher Internship Programme and UCD School of Education alongside, who focused on communicating the resources on the website in a public friendly manner, under the guidance of both myself and the DIAS technical officers (most notably Sophie Murray) for description of more complex concepts.

Aurora Forecast

An aurora forecast is available on the website for any users of the website who are interested in the topic. A version of the OVATION PRIME-2013 aurora forecast model, designed by Newell et al. (2014), was ported to python2 from MATLab by Diana Morosan, a former member of the Solar/Space weather group. Later, I ported this version to python3, and adapted it for use on the Houdini magnetometer server PC, to work on the MagIE website (`www.magie.ie/aurora`). This was automated in a similar manner to Section 3.5.1 to run in real time (Figure 3.22). OVATION PRIME is an empirical-based model which uses forecast Kp indices, solar wind conditions and times of day/year as inputs to estimate the probability of visible aurorae at three hour intervals for the following three days. A note on the model, the accuracy of predicting aurorae after more than three days is poor, as most CMEs/coronal holes driving the Solar wind reach the Earth within three days (Section 2.1.4).

Email Alert

An automated email messaging or alert system (`www.magie.ie/alerts`) was successfully set up to notify users when geomagnetic storms occur (Figure 3.23). This was originally designed by Blake (2017) for internal, which I adapted to be sent to a public audience. When a Kp = 5 storm or higher is recorded in the same three-hour window, at two or more magnetometer sites, an email is sent out to users. Currently over 250 users are subscribed to the email alert system, consisting of users from many branches of society including the general public, space weather and geological researchers in Ireland and abroad, photographers and power grid operators.

3.6 Raspberry Pi Magnetometers

In 2022, additional funding was received to develop a raspberry pi magnetometer network for schools, mainly for the purpose of space weather outreach. The idea is to use a set of three magnetic field sensors, which came from the project by the British Geological Survey (BGS), who originally developed this project for the UK (Beggan and Marple, 2018). FLC-100 magnetic field sensors were used to measure the magnetic field, developed by Stefan-Mayer instruments, `https://stefan-mayer.com/en/`. The sensors are relatively cheap (Table 3.3) and easy to use, making them suitable to set up in schools. The equipment setup (Figure 3.24) is made up of:

1. The raspberry pi computer to record (and potentially upload) data;
2. An analogue to digital converter (ADC) soldered to the raspberry pi;
3. Wiring to connect to the signal and power between the ADC and the sensors;
4. Three magnetic sensors;

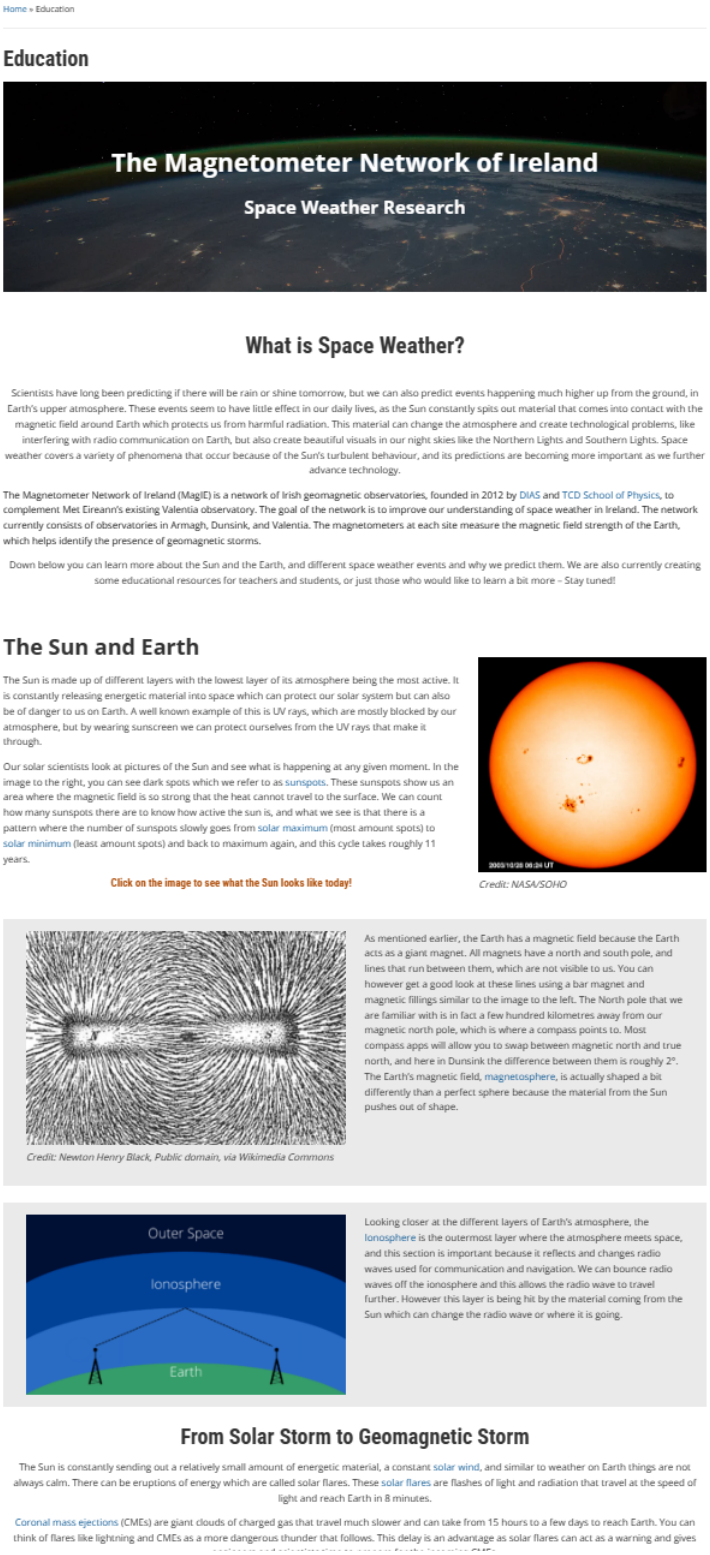

Figure 3.21: The educational page on the MagIE website zoomed out (`www.magie.ie/education`). The page is fully dedicated to explaining the fundamental concepts of space weather to members of the general public.

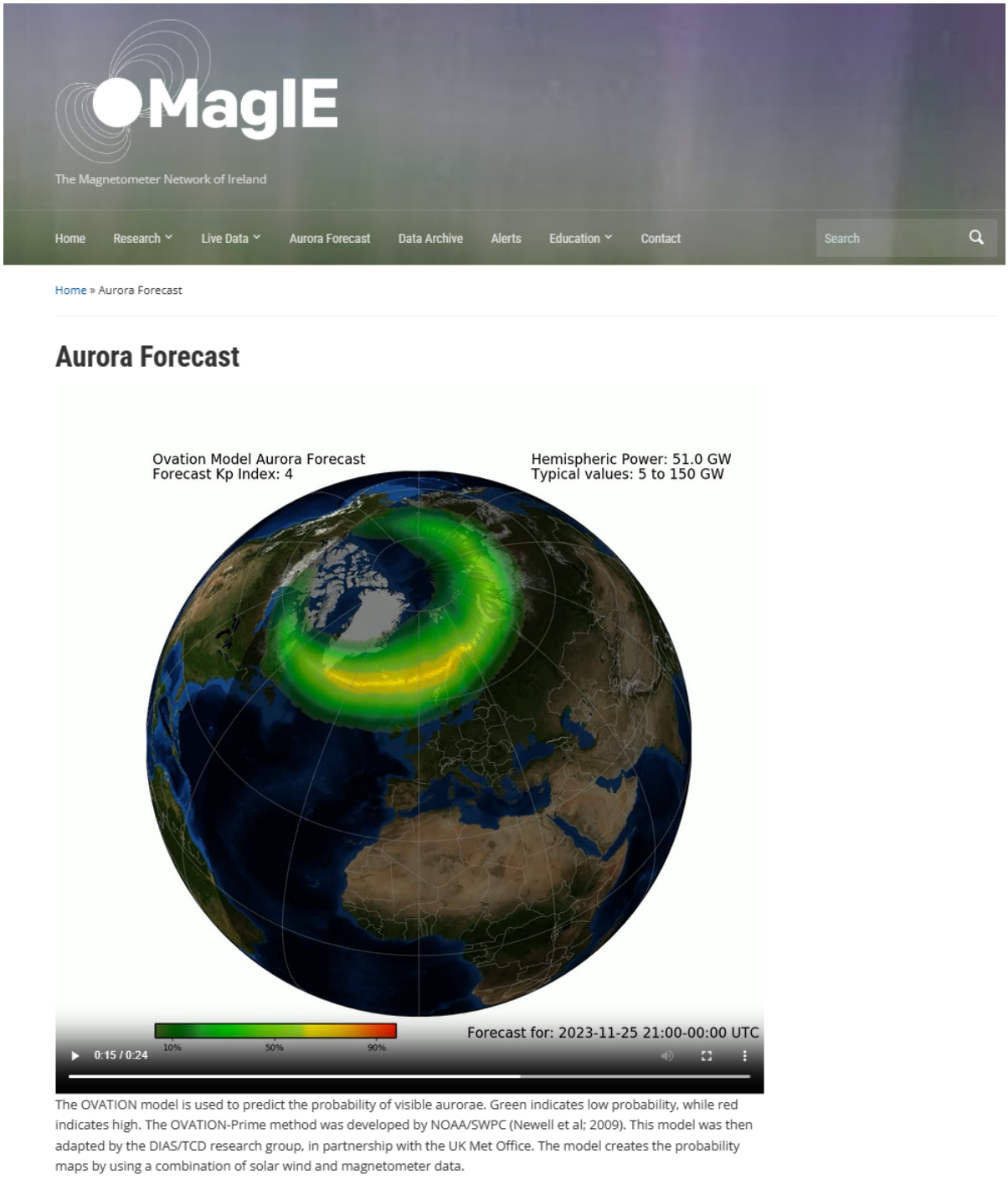

Figure 3.22: An example of the OVATION model aurora forecast operating on the MagIE website (`www.magie.ie/aurora`) on the 24/11/2023.

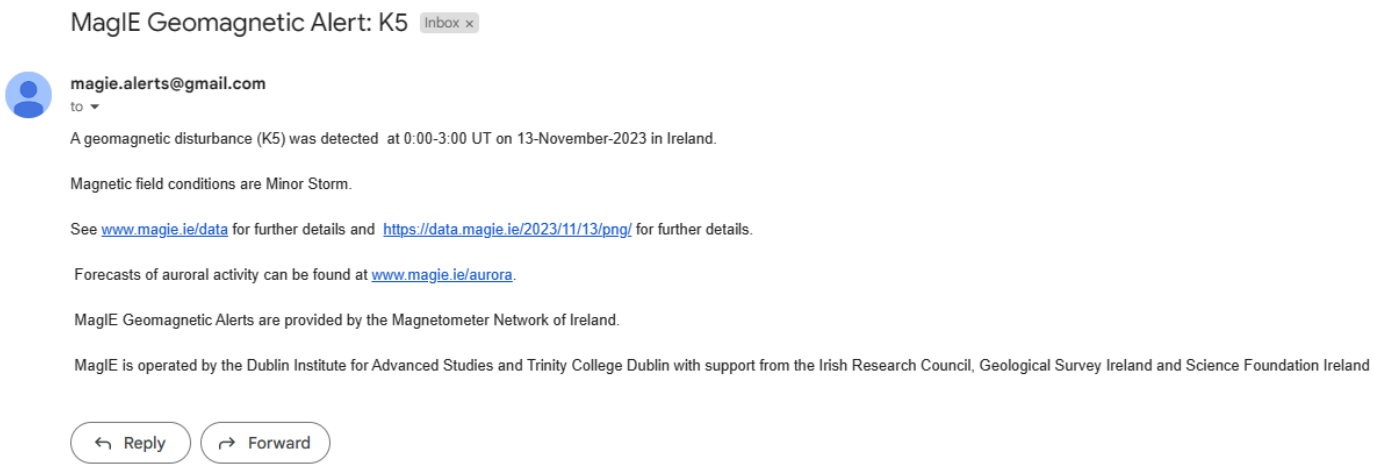

Figure 3.23: An example of the email alert from the MagIE website on 13/11/2023. The alert is automated to send magnetic conditions (Kp index), date of disturbance as well links to live and archived data.

5. A holder to correctly orient the magnetometers (in this case a perspex case was used).

To install the magnetometer, the following protocol was implemented:

1. The ADC ports were soldered to pins on a connection board, which can easily plug into the raspberry pi pins;
2. The ADC is connected and a python script is run to ensure the ADC is correctly soldered;
3. A single sensor is then connected to the ADC and another python script is run to ensure the magnetic sensor is working. The ADC connects a signal channel and a 5 V and ground to the ADC. A python script is run to ensure the sensor works correctly. This is repeated for all three sensors;
4. The circuit in Figure 3.25 is then connected using connectors and directly soldering;
5. The sensors are then put into the X, Y, and Z component drilled holes in a perspex block. They are fixed in point and then the magnetometer as a whole is ready for testing

The sensor's signal channel outputs analogue voltage. The ADC converts this signal to a digital format, which the raspberry pi can then read. The FLC-100 is calibrated to so the magnetic field can be estimated directly with voltage using the relation $B = 50{,}000(V - 2)$, where B is measured in nT, V in Volts. The "2" in this relation is the Voltage due to internal charging/discharging of the fluxgate (see Section 3.1.1).

A prototype of the magnetometer was tested in a deliberately noisy environment at Birr Observatory, near electronics and large radiators (which are ferrous) to see if useful measurements can be obtained in these noisy circumstances after applying a filter (as

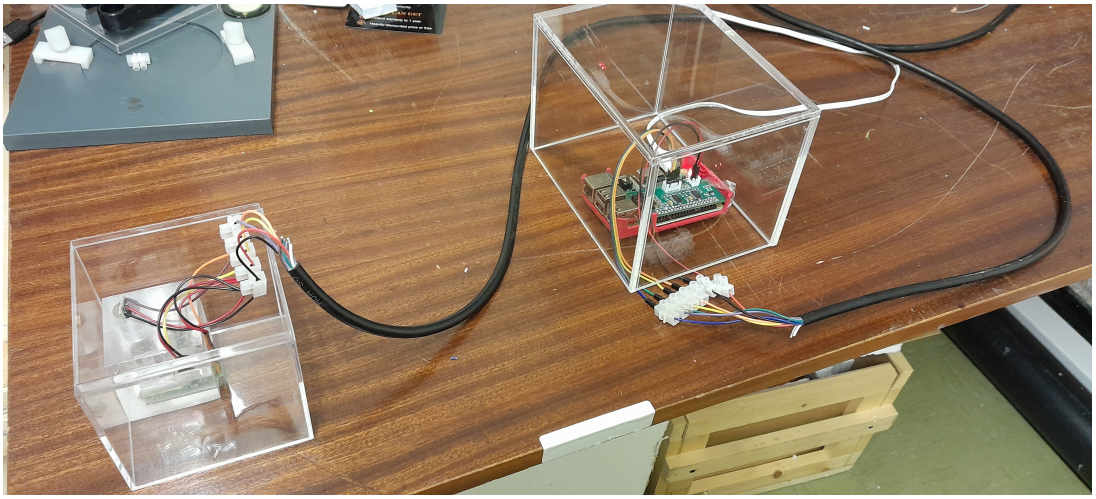

Figure 3.24: The raspberry pi magnetometer. (left) The three magnetic sensors are oriented X, Y, Z in a perspex block, inside a case. (right) The raspberry pi computer, inside a perspex case. Black and red cables feed power, with yellow, orange, green and blue (one spare) used as signal cables. The black wire connects the two, with connectors in between. Ideally for permanent installation, these connectors will be glued to the cases, with the magnetometer case fixed in place with non-magnetic screws such as brass.

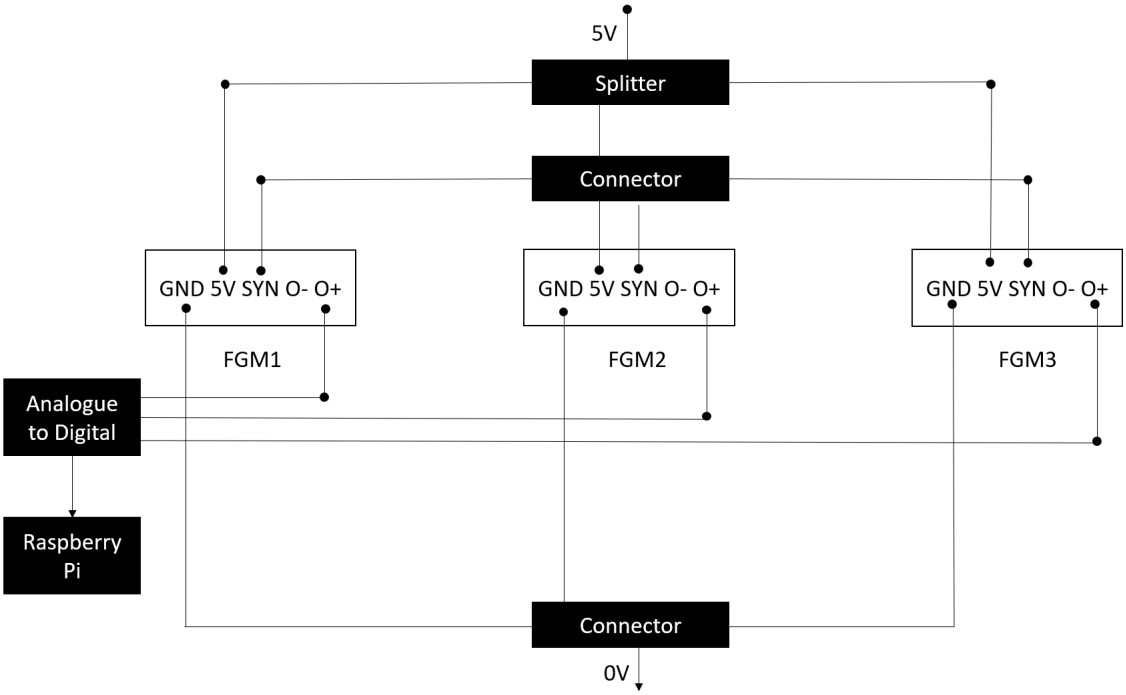

Figure 3.25: A circuit diagram of the raspberry pi magnetometer, modified from the original in Beggan and Marple (2018). The white blocks mark the magnetic sensors (FGM1, FGM2 and FGM3), with its corresponding inputs/outputs. A 5 V, ground (GND) and signal (O+) all connect back to the ADC pi which collects the signal and powers the sensors. A connector is attached between the sync channel (SYN) to ensure each signal runs in sync between separate measurement channels.

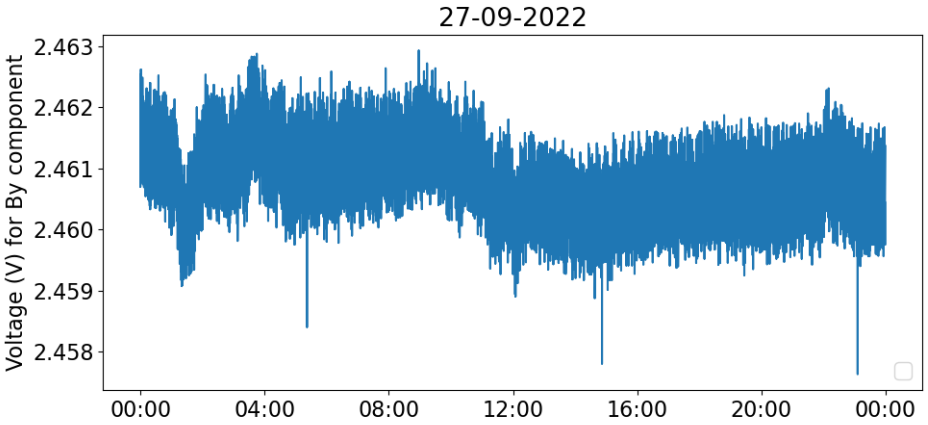

Figure 3.26: Raw raspberry pi magnetometer data for the By component of the magnetic field during the test in Birr measured in volts. Later the voltage can be converted to a magnetic field strength.

schools are likely to be noisy environments). Raw data obtained was very noisy below periods of 120 s, due to poorer sensitivity, but also more noise sources at these periods (Figure 3.26). However, digitally applying a band pass filter to the raw data between 120 s and 16,000 s (noise above 16,000 s is due to thermal variations) greatly increased the accuracy of the signal, to the point where data returned were of a similar quality to that of SENSYS and LEMI magnetometers, within this range (Figure 3.27). In Figure 3.27, the prototype worked well in the By and Bz components for a K = 5 storm on 27/09/2022, but did not work on the Bx component, with significant noise still present. The scientific utility of these data is limited by this noise. Ideally, the site of installation would be installed in a quieter area in schools to reduce any of these anomalies, perhaps in a cupboard away from electrical outlets and any ferrous objects. In the context of constraining ground-based effects, due to missing magnetic field data between 10 – 120s the geoelectric field (and hence GIC) will be estimated poorly. Some schools could potentially be used for scientific data provided they were installed in a quiet location (where this band-pass filtering is not required between 10 – 120s), although in terms of most schools this is not a realistic possibility. However, these data are still useful to constrain localised peaks in magnetic activity, local K-Indices and help with assessment of accuracy of the magnetic field interpolation method used in this manuscript (method discussed in Chapter 4).

Currently no raspberry pis are set up in schools, however three have been built, tested and are ready for future installation. The locations of seven schools were identified, with teachers contacted and happy to install. The idea for when the magnetometers are installed is to automate the data transfer, similar to the other magnetometers, to the server PC Houdini and hence have automated schools magnetometer data plotted and uploaded to the MagIE website.

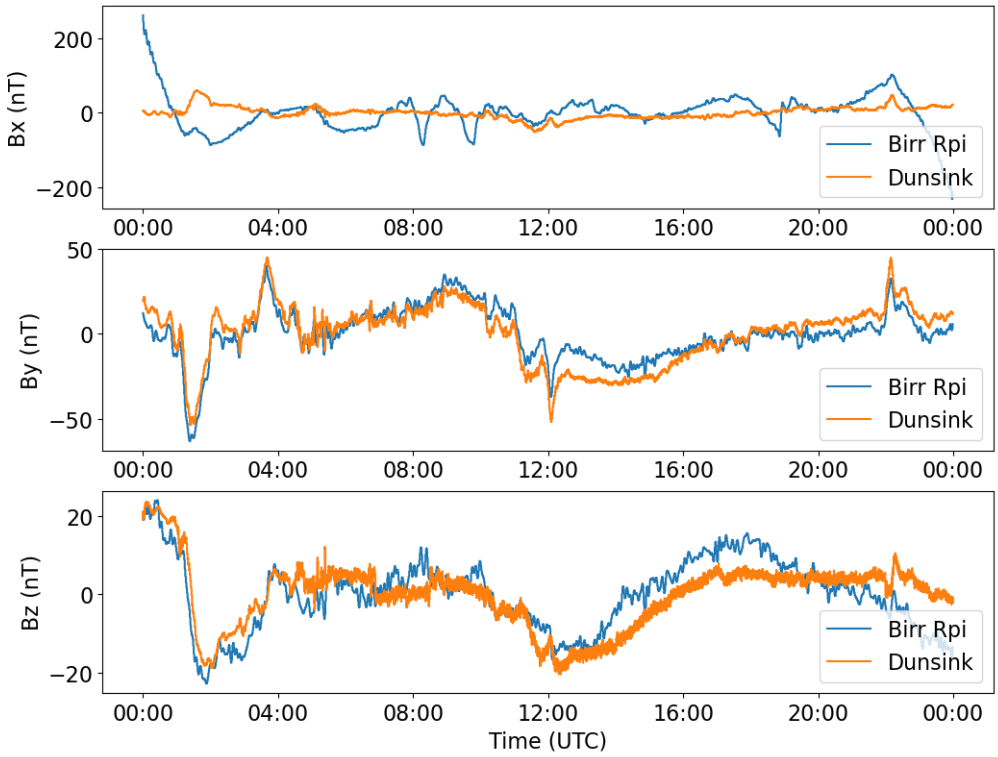

Figure 3.27: Band pass filtered raspberry pi magnetometer data is compared to SENSYS data from the Dunsink magnetometer on the 27/09/2022, during the test in Birr for the Bx (top) By (middle) and Bz (bottom) components. The By and Bz components capture the signal well, with external noise present in the Bx component.

3.7 Summary

Overall, the goal of maintaining the magnetometer network, as well as including new installations was a success. A new site in Dunsink was successfully tested, with the hopes of installing a permanent site here for future use. After a failure the Birr magnetometer was re-installed and is operational again. The levels of noise at each site was tested, to evaluate the performance of magnetometers. Real-time data for the magnetometer observatories is now available on the MagIE website, alongside plots of data such as XYZ time series and K-Indices with archived data also available online. In addition, outreach material was added to the website and a raspberry pi based magnetometer was successfully tested, with the plan to install these magnetometers in schools in future.

4 Modelling Geomagnetic Fields

In this chapter, detail regarding the method of modelling the geomagnetic field across Ireland is explored and outlined. The Spherical Elementary Current Systems (SECS) method was used to model the magnetic field between magnetic observatories. This technique was built upon the methods of the British Geological Survey (McLay and Beggan, 2010) and Blake (2017), who manipulated the aforementioned version of the model to work across Ireland. A description of the method is first discussed, followed by an explanation of the reasoning for using this method. Then the accuracy of the model is validated and quantified across Ireland. In later chapters, the modelled geomagnetic field variations are used as the input for both the geoelectric field and GIC models.

4.1 Spherical Elementary Current Systems

The SECS method is commonly used to estimate magnetic field variations at sites without magnetic field data and uses nearby magnetometers as inputs to construct a plane of equivalent sheet currents in the ionosphere, estimated at a single value for altitude which is manually set. The ground magnetic field can then be recalculated at any point as the sum of the magnetic fields generated by this plane of currents. The SECS method was first developed by Amm (1997); Amm and Viljanen (1998). A summary is given about the current system itself in Amm (1997), with a more comprehensive description and explanation offered in Amm and Viljanen (1998), including how to derive a magnetic variation using the current system. To begin with, an ionospheric current system current system, $\mathbf{J}$, can be decomposed (Figure 4.1) into a divergence-free ($\mathbf{J}_{df}$) and curl-free component ($\mathbf{J}_{dc}$):

$$\mathbf{J} = \mathbf{J_{df}} + \mathbf{J_{dc}} \tag{4.1}$$

$$\mathbf{J}_{df} = \frac{I_{0,df}}{4\pi R_I} cot(\frac{\theta'}{2}) e_{\phi'} \tag{4.2}$$

$$\mathbf{J}_{cf} = \frac{I_{0,cf}}{4\pi R_I} cot(\frac{\theta'}{2}) e_{\theta'} \tag{4.3}$$

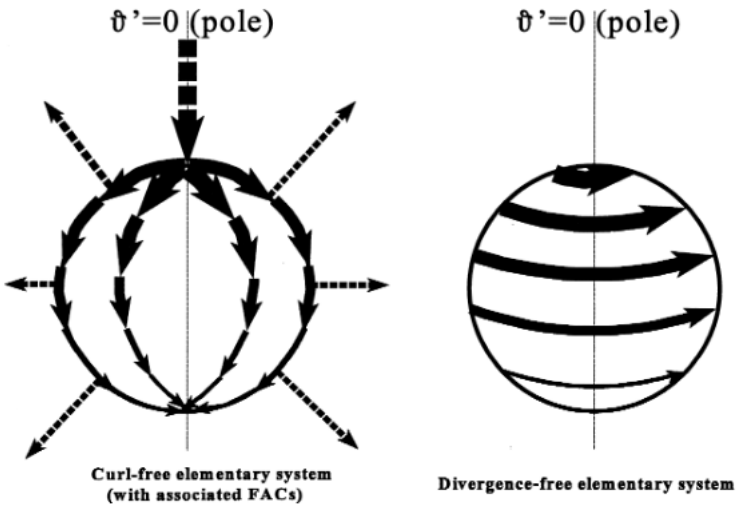

Figure 4.1: The two current system components of SECS are sketched: left) the curl-free component and right) the divergence-free component; from Amm and Viljanen (1998). From the perspective of a bystander on the Earth, the curl-free component is composed of vertical currents, with the divergence-free component composed of horizontal currents.

where $\mathbf{J}$ represents the current, I_0 is the scaling factor for the current, r', θ', ϕ are the spherical coordinates of the pole of the current system, R_I is the radius from the centre of the Earth to the estimated height of the ionosphere. Note that this "pole" is the position of the centre of the elementary current system (i.e. the point at which $\mathbf{J}$ is maximised, $\theta' = 0$). The divergence-free system physically describes Hall currents. The curl-free system describes the field aligned currents (FAC) which feed into ionosphere from the magnetosphere and vice-versa (see Section 2.2). Prior work by Fukushima (1976) demonstrated that this curl-free part of the current system does not produce any considerable magnetic effect at the surface of the Earth and can hence be neglected. By omitting this term, the true current system, $\mathbf{J}$, cannot be determined, but the equivalent current system $\mathbf{J}_{eq}$ due to horizontal currents in the ionosphere can be obtained. Thus,

$$\mathbf{J}_{eq} = \mathbf{J}_{df} \tag{4.4}$$

By manipulating Stokes' law and Gauss' law, the scaling factor can be obtained.

$$I_{0,df}(\mathbf{r}) = \int\int_{K_r,\ r\to 0} \nabla \times \mathbf{J}(\mathbf{r}\,')d^2r\,' \tag{4.5}$$

where K_r is the circular ionospheric area around radius $\mathbf{r}$.

Now, the current system is defined. However, the magnetic field variation due to the current system needs to be calculated, which is derived in Amm and Viljanen (1998). The current system's potential vector, $\mathbf{A}$ in spherical harmonics. The magnetic field $\mathbf{B}$ can then be obtained from of A by applying a rotation matrix, $R(\theta)$:

$$\mathbf{B} = R(\theta)\ \mathbf{A} \tag{4.6}$$

By assuming that the point $r < R_I$ and θ' to be the pole angle of the coordinate system, they derive the radial, $B_{r'}$, and axial $B_{\theta'}$ components of $\mathbf{B}$:

$$B_{r'}(r,\ \theta') = \frac{\mu_0 I_0}{4\pi r}\left(\frac{1}{\sqrt{1 - \frac{2rcos\theta'}{R_I} + (\frac{r}{R_I})^2}} - 1\right) \tag{4.7}$$

$$B_{\theta'}(r,\ \theta') = \frac{-\mu_0 I_0}{4\pi r\ Sin(\theta')}\left(\frac{\frac{r}{R_I} - cos(\theta')}{\sqrt{1 - \frac{2rcos\theta'}{R_I} + (\frac{r}{R_I})^2}} + cos(\theta')\right) \tag{4.8}$$

Through a careful analysis they note that the peak $B_{r'}$ is expected at the pole, with the $B_{\theta'}$ peak slightly away from the pole.

At this point, the current system is defined, and the magnetic effect of the current system has been explored. Now, a series of magnetic field time series from magnetometers need to be used, $\mathbf{Z}$, in order to form said current sheet, to extract the magnetic field at any point. The geomagnetic field at each observatory can be related to the scaling factor, $\mathbf{I}$, with the following matrix to relate the SECS to ground-based measurements, $\mathbf{T}$.

$$\mathbf{Z} = \mathbf{TI} \tag{4.9}$$

$\mathbf{Z}$, $\mathbf{I}$ and $\mathbf{T}$ are given by the following expressions :

$$\mathbf{Z} = \begin{pmatrix} Z_{1,\theta} \\ Z_{1,\phi} \\ Z_{2,\theta} \\ Z_{2,\phi} \\ \vdots \\ Z_{n,\theta} \\ Z_{n,\phi} \end{pmatrix} \tag{4.10}$$

where the subscript "1, 2, ..., n" refers to the location of the nodes.

$$\mathbf{I} = \begin{pmatrix} I_{0,df,1} \\ I_{0,df,2} \\ \vdots \\ I_{0,df,n} \end{pmatrix} \tag{4.11}$$

$$\mathbf{T} = \begin{pmatrix} T_{11,\theta} & T_{12,\theta} & \dots & T_{1n_{el},\theta} \\ T_{11,\phi} & T_{12,\phi} & \dots & T_{1n_{el},\phi} \\ T_{21,\theta} & T_{22,\theta} & \dots & T_{2n_{el},\theta} \\ T_{21,\phi} & T_{22,\phi} & \dots & T_{2n_{el},\phi} \\ \vdots & \vdots & \vdots & \vdots \\ T_{n_{obs}1,\phi} & T_{n_{obs}2,\phi} & \dots & T_{n_{obs}n_{el},\phi} \end{pmatrix} \tag{4.12}$$

Each element of $\mathbf{T}$ in the form $T_{k,l,\theta/\phi}$ relates the radial or axial component of the ground magnetic field of an elementary current system with a scaling factor I and its pole at l, to an observation point k while θ and ϕ are the spherical coordinates of the point.

The number of ground magnetic measurements is almost always less than the number of nodes of SECS required to give a reasonable approximation of currents in the ionosphere, with usually less than twenty magnetometers at most, compared to hundreds or thousands of nodes. Thus, Equation 4.12 is poorly conditioned for this circumstance. Singular value decomposition (SVD) is employed to separate out the poorly conditioned elements of $\mathbf{T}$. SVD decomposes a matrix $\mathbf{T}$ into:

$$\mathbf{T} = \mathbf{U}\omega\mathbf{V}^{\mathbf{T}} \tag{4.13}$$

where $\mathbf{U}$ and $\mathbf{V}^{\mathbf{T}}$ are orthogonal matrices and ω is a 2D diagonal matrix. By manually setting any of the diagonal components of ω, which are less than 1% the maximum value of ω, to zero, the poorly conditioned parts of $\mathbf{T}$ are separated out. $\mathbf{I}$ can then be solved using:

$$\mathbf{I} = \mathbf{V}\mathbf{U}^{\mathbf{T}}\mathbf{Z} \tag{4.14}$$

Thus, using the measured magnetic field variations, $\mathbf{Z}$, $\mathbf{I}$ can be estimated. When $\mathbf{I}$ is solved, the magnetic effect of the ionospheric currents can be computed at any ground point, solving Equation 4.14 in terms of $\mathbf{Z}$. It is important to reiterate that the elementary current systems constrained using the above method are only representative of the actual currents flowing in the ionosphere. Actual magnetic measurements at a site may include magnetic contributions from local magnetic disturbances, for example, due to plasma turbulence in the Hall and FAC current systems (Guio and Pécseli, 2021),

or separate driving current systems higher in the magnetosphere. If used as an input for SECS, these purely local effects will be assumed to be caused by ionospheric currents, which can lead to inaccuracies in the SECS calculation. In addition, the steps taken to solve for $\mathbf{I}$ also mean that the equivalent currents give slightly over-smoothed magnetic fields at the surface.

Before continuing, it must be noted that SECS do not produce accurate results in every region. Other models exist for lower latitudes, as SECS can no longer accurately reproduce the effects of geomagnetic storms accurately (Torta et al., 2015), likely due to the decreased occurrence of the auroral electrojet and FAC at these latitudes. For geomagnetic latitudes above 75°, the dominant current systems can also change (Northward Bz current system for example). Thus a different interpolation method should also be used for these latitudes.

4.2 Implementation of SECS in Ireland

4.2.1 State-of-the-Art

The SECS method was designed to replicate the effects of strong ionospheric Hall currents in particular, such as the auroral electrojet, as well as FAC currents. These current systems are strongest in the auroral region (60 – 75°) provided enough magnetometers are present to capture local variations. However, this method can also be used at mid-latitudes, particularly for larger geomagnetic storms, as the auroral oval can expand further south, and hence the auroral electrojet and FAC migrate South. McLay and Beggan (2010) tested the degree of accuracy of these current systems in the UK and found that SECS can also accurately replicate magnetic fields at this middle latitude. They also observed that the model can also produce accurate results using only a limited number of magnetometers (5 – 6). A minor modification to the standard model is made, the altitude setting of the model. For auroral regions, the height is generally set to approximately 85 – 90 km (Marshalko et al., 2021; Bosse et al., 2022), however, McLay and Beggan (2010) found 110km to be optimal in their case.

Due to the success of the McLay and Beggan (2010) version of the SECS model, Blake (2017) adopted this model for Ireland. The model was tested and validating for two or three isolated sites with the (ARM, BIR, VAL) MagIE magnetometers (Figure 3.7) and found that SECS could work in Ireland, even limited to three magnetometers with the altitude set to 110 km. This is a comparable density of magnetometers to McLay and Beggan (2010). Campanyà et al. (2019), then elaborated on the analysis of Blake (2017). They quantified the degree of accuracy of the measured magnetic fields, vs. modelled magnetic fields, relative to the displacement from the nearest magnetometer.

The three aforementioned MagIE magnetometers were used alongside six other European magnetometers from the INTERMAGNET network (Figure 4.6). The further a magnetometer is from the site of estimation, the less accurate the geomagnetic field estimation becomes. To quantify this accuracy they, performance metrics were used, specifically coherence and signal-to-noise ratio (SNR):

$$SNR = 10log_{10}\frac{\sum_{i=1}^{N} B_{data}^2}{\sum_{i=1}^{N}(B_{data} - B_{mod})^2} \tag{4.15}$$

$$Coh = \frac{\sum_{i=1}^{N}(B_{data} - \bar{B}_{data})(B_{mod} - \bar{B}_{mod})}{\sqrt{\sum_{i=1}^{N}(B_{data} - \bar{B}_{data})^2(B_{mod} - \bar{B}_{mod})^2}} \tag{4.16}$$

where B_{data} is measured magnetic field data, B_{mod} is modelled magnetic field data, the barred over-script, $\bar{B}$, is used to denote mean, while N is the length of the time series.

A coherence analysis was used to determine the degree of accuracy between shape of the time series, i.e., how well the sinusoidal waves of both signals match, with a SNR analysis focused on analysing the amplitude difference of the signal. Campanyà et al. (2019) demonstrated that SECS produce highly accurate results within 100 km of any observatory locations (coherence > 0.95, signal-to-noise > 8). Within 200 km of these locations, decent results (coherence > 0.9, signal-to-noise > 5) are achieved, but outside this range (> 200 km), the accuracy falls off rapidly. Almost the entire island of Ireland lies within 200 km of each of the geomagnetic observatories (with the exception of some very remote areas on the west of Ireland, the coastline of Mayo), and thus one would expect the magnetic field to be accurately reproduced.

Now, we get to the research and analysis performed during this project based off of the aforementioned work. The relative position of the site relative to the magnetometers has an important bearing on the accuracy of the interpolation, i.e., an output site between input sites will work, but a site not between will not work quite as effectively. If a site lies between two magnetometer sites the method works more accurately, though if not, the method works more like an extrapolation rather than an interpolation. Hence, I focus on expanding this analysis here to include position, using maps to compare the level of accuracy. The methodology in later sections of this manuscript is focused on using measurements from the three magnetometers from Ireland (the three sites in Figure 4.3) for real-time automation (Section 5.5), thus the performance of SECS interpolation was assessed for cases two cases: when other INTERMAGNET magnetometers are available and when they are not available.

Site	Coherence	SNR
SW02	0.94	8.9
SW07	0.92	8.2
SW13	0.92	7.5

Table 4.1: The coherence and SNR metrics between measured and modelled magnetic field variations in Figure 4.2

4.2.2 Validation Using Measured Data

To validate the SECS interpolation, a comparison of modelled magnetic fields to measured magnetic fields from surveyed sites from the Space weather Electromagnetic Database in Ireland, or SWEMDI (see Section 5.1.2 for a more detailed explanation) was analysed.

The assessment of the potential for SECS was validated using both measured time series at the MT sites (Figure 4.3) and modelled time series with differing numbers of magnetometers (nine, three, two). This comparison visually examines the measured magnetic field compared to modelled magnetic field, calculates the performance metrics for all 14 available measurement sites from the SWEMDI network with comparison to geomagnetic activity, maps the performance relative to the position of magnetometer observatories. To compare the accuracy of SECS in Ireland relative to the position of the geomagnetic observatories, the coherence and SNR metrics are used in a similar manner to Campanyà et al. (2019) to determine the accuracy of SECS relative to measurements.

Direct Comparison

The three sites chosen here to visually demonstrate the predicted magnetic field are sites that are not directly between magnetometer sites, so hence a lower accuracy was anticipated for these sites. Snapshots of the magnetic field are presented during enhanced geomagnetic conditions for each (Figure 4.2). In general between the three, the shape of the signal is retained, with a small error relative to the amplitude of the observed signal. Interestingly, the accuracy of the SECS interpolation appears to scale with increased geomagnetic activity. This likely relates to the increase in SNR as signal increases but background noise sources remain relatively stable, but also due to the Hall and FAC currents which begin to dominate during storm time. The largest disagreement in peak-to-peak strength is present for SW13. This site is both furthest from the magnetometers and positioned outside the range of any pair, so larger errors occur as a result (Table 4.1).

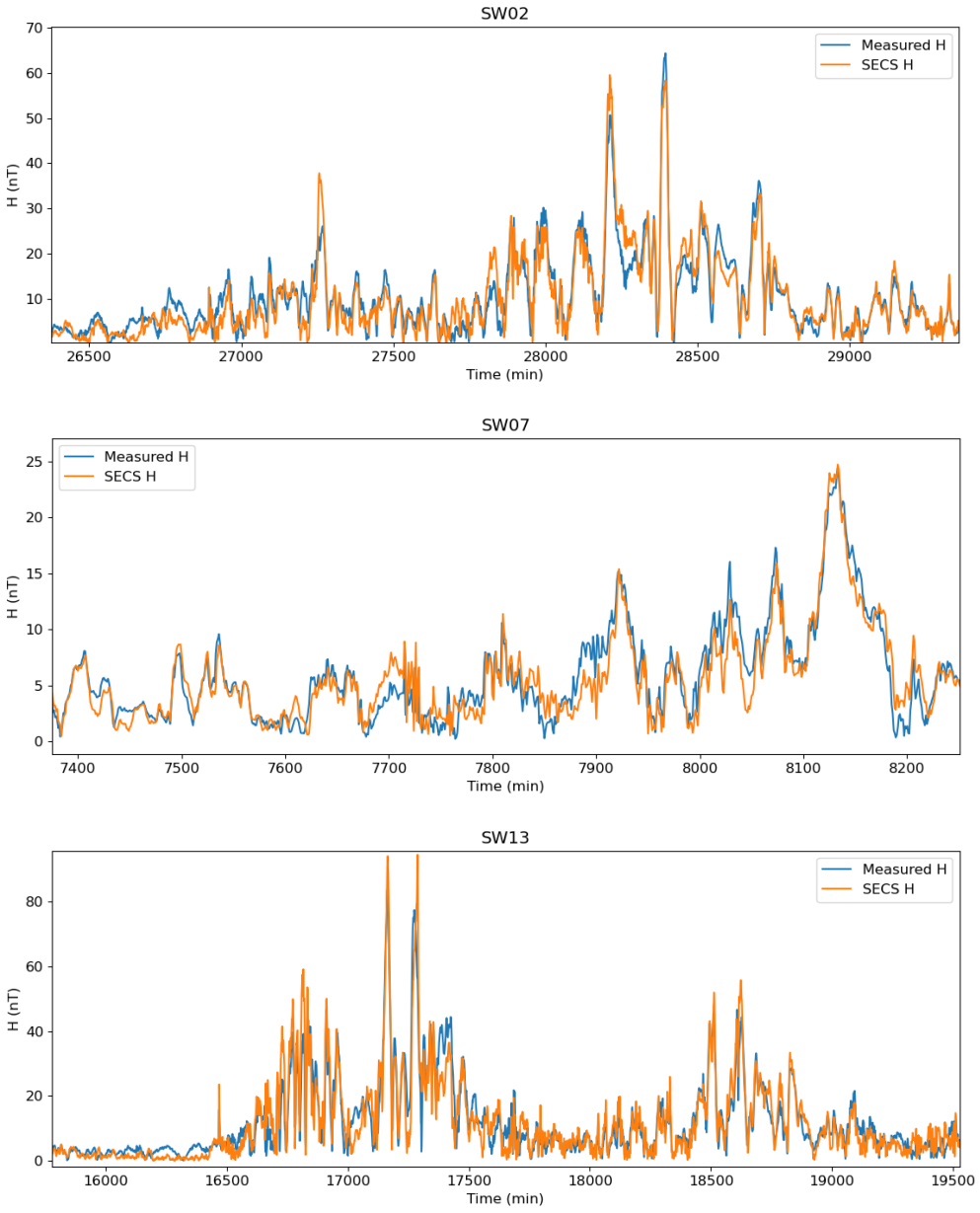

Figure 4.2: A snapshot of the magnetic field is presented for three sites, with similar accuracy between measured (blue) and SECS modelled (orange) time series.

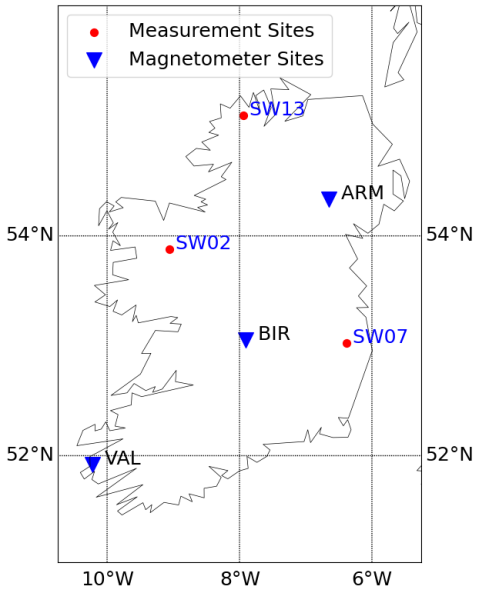

Figure 4.3: The location of example measurement sites. Magnetometer sites are denoted by blue triangles with MT sites, from the SWEMDI network, denoted by red dots.

Comparison to Geomagnetic Activity

Due to the relationship between geomagnetic activity and accuracy of the SECS interpolation, the validation of the SECS method was quantified with comparison to the observed Kp indices. In total, 14 sites out of the total 43 sites from the SWEMDI network had measured magnetic fields, when the Armagh, Birr and Valentia magnetometers were operational. Only these 14 sites were used to validate the model. For each three hour window, the individual coherence and SNR were calculated and binned with the Kp value for that window. The mean of the SNR and coherence in each bin was then estimated.

A clear trend is present in Figures 4.4 and 4.5: both metrics improve with increasing Kp value and therefore magnetic activity. Even during weak periods of geomagnetic activity (i.e., Kp = 0) the coherence is generally still reproduced well (≈ 0.7). The SNR is very poor at this stage however ($\approx 2-3$), thus the amplitude of the signal may not be as accurately reproduced during quiet periods. However, ultimately the magnetic field at storm time is the crucial variable here, as this is when Hall and FAC currents are most prominent and when damage related to a geomagnetic storm can occur. Hence, the SECS interpolation method is proven to be effective in Ireland provided active geomagnetic conditions are present.

Mapping the Accuracy

The degree of accuracy with regards to position of the geomagnetic observatory (i.e. far away or close, between magnetometers or isolated) was investigated, using the

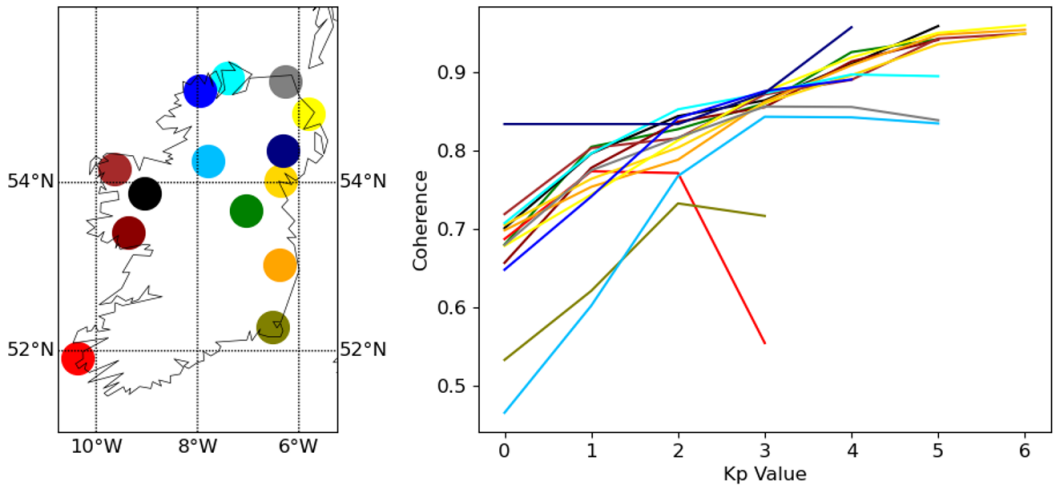

Figure 4.4: The total coherence of the time series between measured and modelled SECS time series is compared to an ascending Kp value, for all fourteen MT sites with measured data at the same time the ARM, BIR and VAL magnetometers were operational. The location of these sites is denoted using the same colour as the line plots in the map on the right. In general, coherence correlates well with larger kp indices but also distance from the observatories.

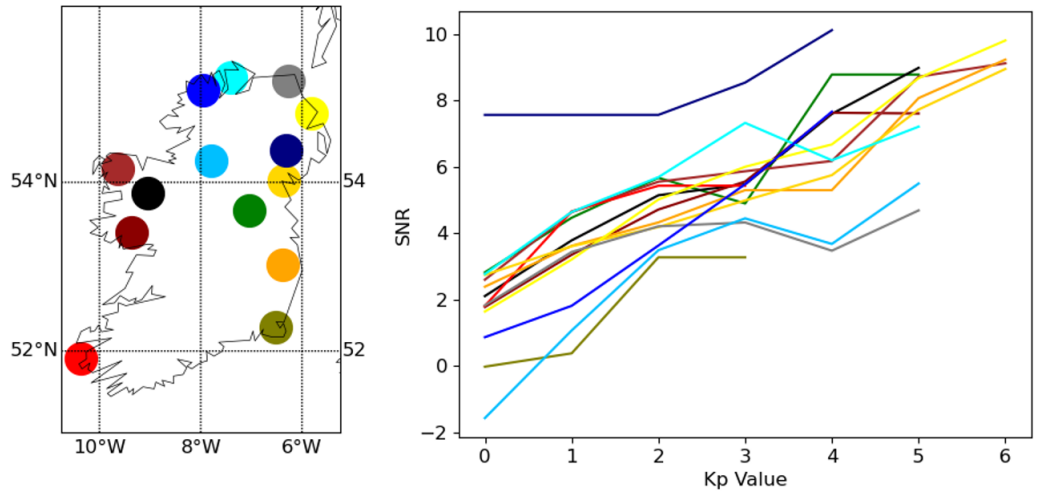

Figure 4.5: The total SNR of the time series between measured and modelled SECS time series is compared to an ascending Kp value, for all fourteen MT sites with measured data. The location of these sites is denoted using the same colour as the line plots in the map on the right. In general, the SNR correlates well with larger kp indices but also distance from the observatories.

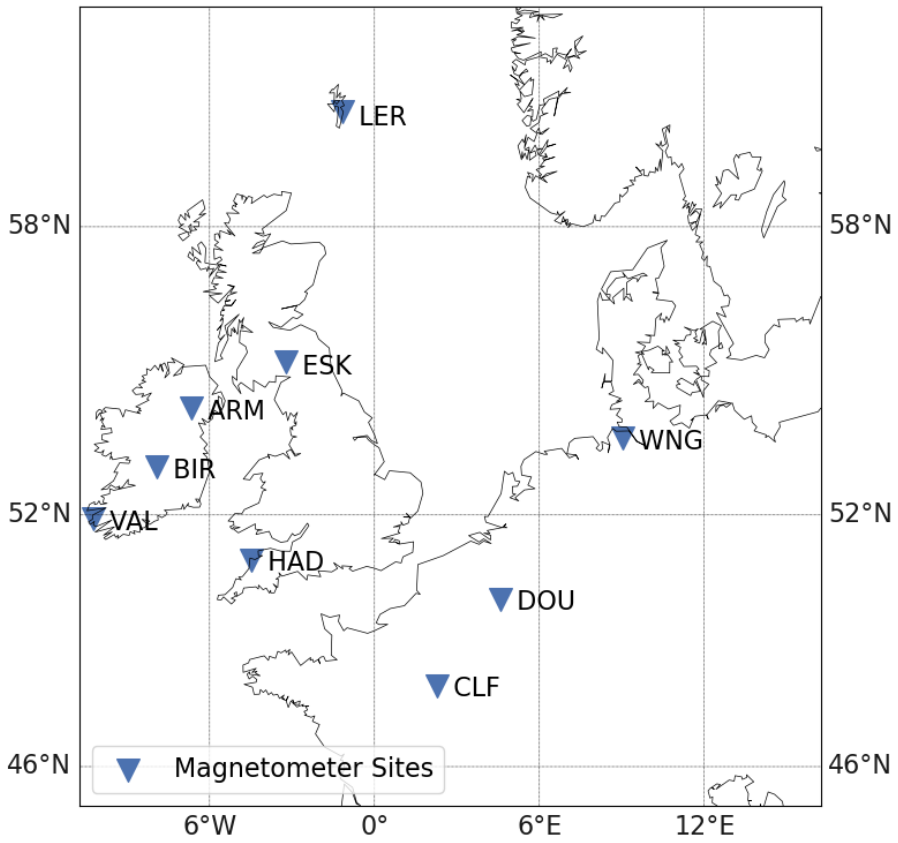

Figure 4.6: The magnetometer observatories used for the SECS interpolation. They include the Armagh, Birr and Valentia MagIE magnetometers (ARM, BIR, VAL), alongside the Chambon-la-Foret, Dourbes, Eskdalemuir, Hartland, Lerwick and Wingst INTERMAGNET magnetometers (CLF, DOU, ESK, HAD, LER, WNG).

performance metrics. The analysis was performed assuming that the three geomagnetic observatories are operational, but also with the hypothetical case where the Armagh magnetometer is not present. SECS interpolations are more accurate during greater levels of magnetic activity, which is when we are more interested in the geoelectric field time series. However, not all MT sites have data acquired at storm times due to the installation dates, therefore we chose a magnetic activity of Kp = 4 as the minimum threshold for the site to be evaluated.

Figure 4.7 compares measured MT sites data with SECS-derived magnetic time series using magnetic time series from: (left) nine magnetic observatories (the three from MagIE (ARM, BIR, VAL) with the nearest six INTERMAGNET observatories (HAD, ESK, LER, CLF, DOU, WNG), (middle) three magnetic observatories (VAL, BIR, ARM), and (right) two observatories (VAL, BIR). Performance decreases with a lower number of magnetometers, in particular when going from three to two (without the

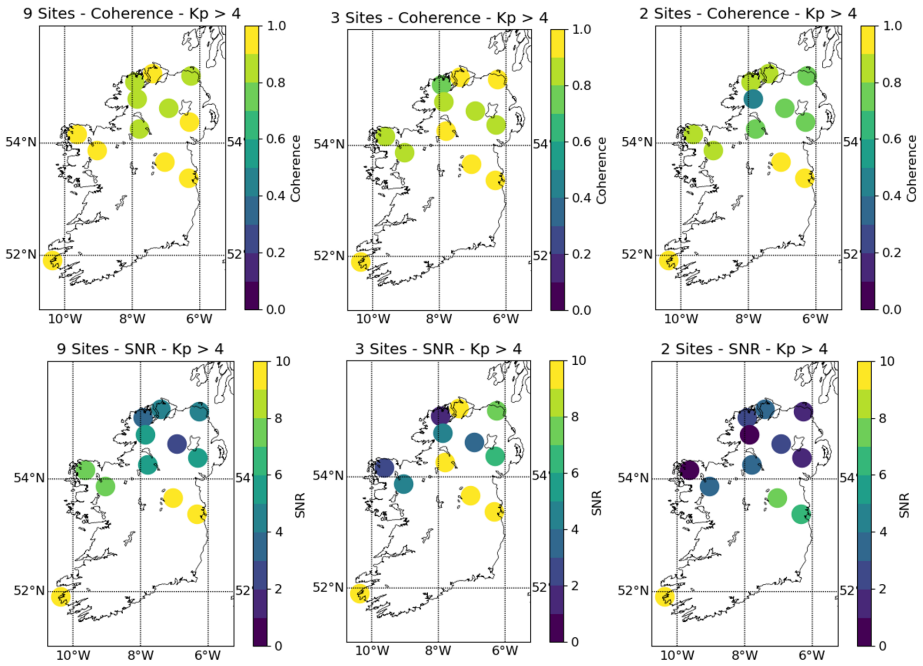

Figure 4.7: The coherence (top) and SNR (bottom) between the measured magnetic field at MT sites and modelled magnetic fields (SECS interpolation with nine, three and two magnetometer sites) for all MT sites with available data.

ARM magnetometer in the north), but no significant difference was observed between using nine or three magnetometers, which suggests that the current configuration is reasonable. However, it would improve the modelling of geomagnetic storms if all nine magnetometers were available in real time. The strongest decrease in performance is for the two sites further west, likely due to these sites being the furthest away magnetometers as well as their relative position on the edge of the island meaning the interpolation is more like an extrapolation.

4.2.3 Validation Using Modelled Data

Unfortunately, valid measured magnetic field data across the entire island were not available for analysis. Instead, modelled sites with more inputs were compared to modelled sites using less magnetometer observatories to assess the accuracy of the interpolation across the entire island.

The impact of using two or three magnetometers was also evaluated through a comparison with a nine magnetometer interpolation (Figure 4.8). When three magnetometers are used, the performance of the SECS method decreases for the northernmost sites, it retains a high coherence (> 0.85) but low SNR (> 4). When two magnetometers are used the performance of the SECS method decreases significantly for northernmost sites, with high coherence (> 0.8) but low SNR ($0 - 4$). The importance of using the ARM magnetometer for accurate magnetic fields time series at northern sites are emphasised by this. Despite the lack of a magnetometer in the south-east, these sites still

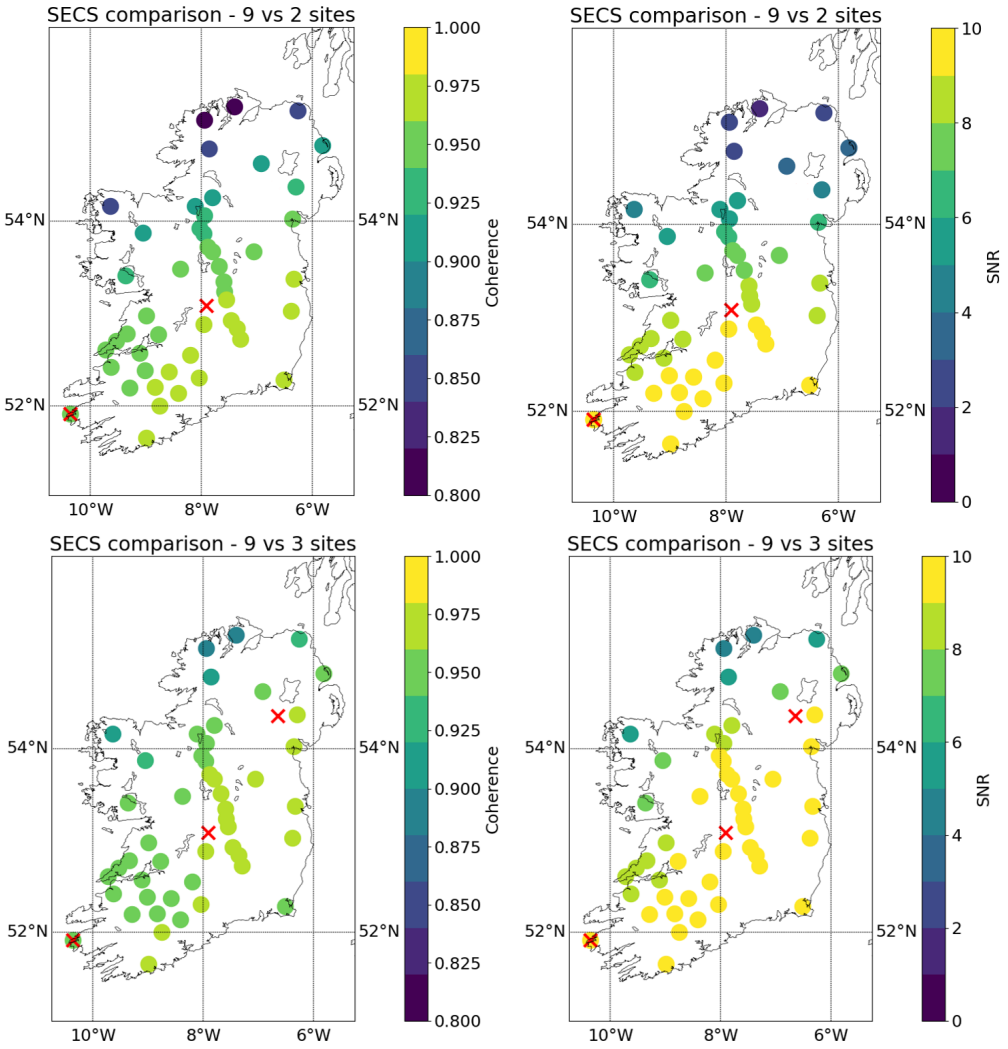

Figure 4.8: The coherence (left) and SNR (right) between a modelled magnetic field using SECS with nine sites, compared to modelled magnetic field using SECS with three magnetometers (top) and two magnetometers (bottom) for the 7 – 8 September 2017 storm (Kp = 8). Positions of the MagIE geomagnetic observatories are denoted by red x's

perform well (coherence > 0.95, SNR > 10). This is likely due to the magnetometers (particularly between Birr and Valentia) retaining the regional effects (which can be replicated by extrapolation), with weak local effects in the southeast, due to the lack of strong influence from the auroral electrojet, as opposed to the northwest, which is more strongly influenced.

4.3 Summary

This SECS geomagnetic field technique was evaluated, using both INTERMAGNET (nine total) and MagIE magnetometers (three total), for storm time conditions in Ireland. The method adopting SECS was demonstrated to be effective for most of the island, with accuracy of measurements quantified. The North-West/West region is replicated most poorly. As a result, I recommend the installation of a new magnetometer here. In the next Chapter, this geomagnetic field model will be used as an input to evaluate geoelectric field variations across the island

5 Surveying, Modelling and Nowcasting Geoelectric Fields

One of the main goals of this research was to monitor the effects of geoelectric fields during geomagnetic storms. Unlike geomagnetic fields, which can be easily monitored using long-term geomagnetic observatories, this cannot be done so easily for geoelectric fields. Modelling geoelectric fields across a region to monitor geoelectric fields is preferable to directly measuring geoelectric fields for two main reasons: a) geoelectric fields are highly variable between locations and thus a much denser network is required (tens for Ireland), this density of sites can be surveyed, but would be impractical to constantly maintain; b) measured geoelectric fields are highly susceptible to noise, both from natural and artificial sources. In this chapter, geoelectric field data acquisition from field surveys is described first, preprocessing is required to create magnetotelluric transfer functions (MT-TF). Then details about geoelectric field models of Ireland are explained, including the model used here. Finally, an explanation of how this model was manipulated, optimised and validated to work in near real time is then provided.

5.1 Measuring Geoelectric Fields

5.1.1 Magnetotelluric Data

The LEMI 417M system consists not only of a magnetometer, but can also record electric field measurements using a set of electrodes (Figure 3.8). The LEMI system electrodes use small plastic cylinders with a porous ceramic filled with a conductive copper sulphide solution. In total, the system is made up of four electrodes oriented in North, South, East and West directions. The top of each cylinder has a cable which is connected to the wires leading back to a data logger. The data logger measures the electrical potential difference ($\mathbf{V}$) between the two pairs of dipoles (North-South and East-West). Provided the length (l) of the wiring is known, the electric field ($\mathbf{E}$) can be calculated using Equation 5.1. The standard units used for geoelectric fields are generally millivolts per kilometre (mV/km) or volts per kilometre (V/km).

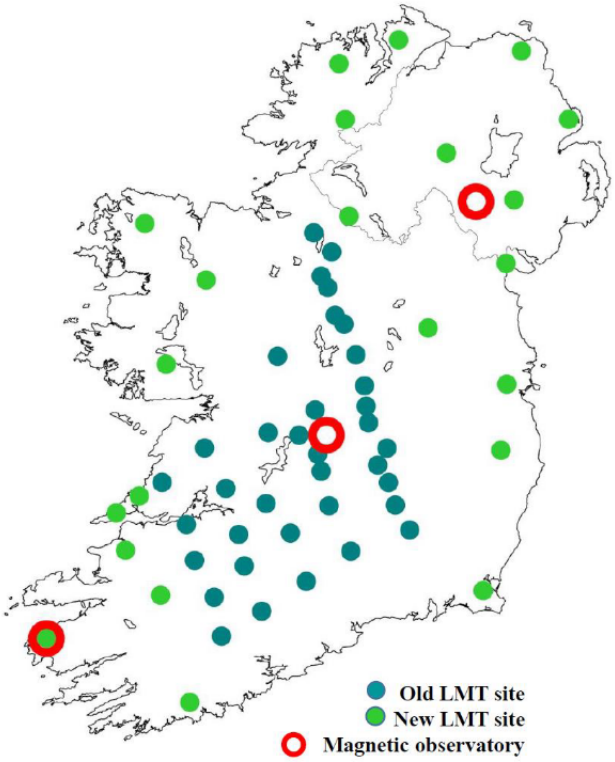

Figure 5.1: The 58 MT locations in the SWEMDI survey, distinguishing between older data and the newly acquired data (Campanyà et al., 2018).

$$\mathbf{E} = \mathbf{V}/I \tag{5.1}$$

5.1.2 Magnetotelluric Surveys

The electric field data used in this study, involved both MT data from older geophysics survey campaigns between 2004 – 2014, along with SWEMDI (Space Weather Electromagnetic Database in Ireland). The older projects consist of ISLE-MT, IRETHERM and IRECCSEM. ISLE-MT (Irish magnetotelluric lithosphere experiment) consisting of 39 MT site installations across the island, primarily investigating the structure of the Iapetus suture, a major geological fault across the centre of Ireland related to the early formation of the island (Rao et al., 2014). IRETHERM (Irish geothermal energy project) was a project that used MT measurements alongside other equipment to investigate if Ireland has the potential for geothermal energy sources (Jones et al., 2014). Data was measured in areas with sedimentary basins, granites and warm springs (Rathlin basin , Dublin basin; Galway and Leinster granite). These were, however, less useful for space weather as the only probed using shorter periods, meaning only shallower features can easily be resolved. The IRECCSEM (Irish Clare Carboniferous Seismic and Electromagnetic Survey) project was established to investigate the possibility of carbon sequestration in the Clare basin and Fermanagh basin (Campanyà et al., 2019). Five additional long period sites had data recorded during this survey.

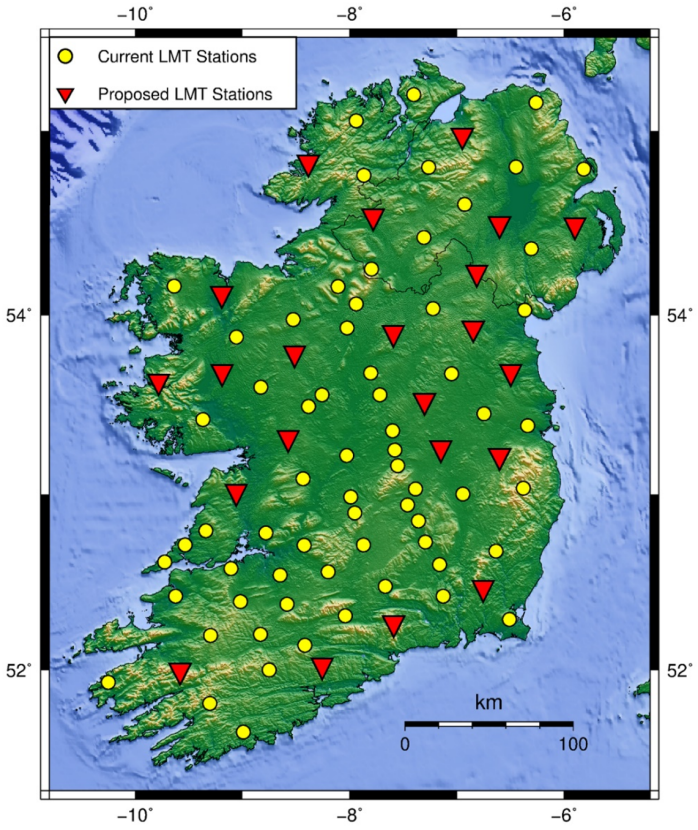

Figure 5.2: The approximate location of MT sites from the HI-RES survey, alongside the SWEMDI sites and earlier MT surveys (Kiyan et al., 2023). The site locations were chosen to improve the overall spatial coverage across the island.

The primary aim of the SWEMDI survey (Figure 5.1) was to study space weather across Ireland, by covering spatial data gaps of MT sites from the previous surveys to characterise the geoelectric field across the island as a whole. SWEMDI includes 22 new sites in these regions with a sparser collection of data. Magnetotelluric data from the aforementioned older surveys was recycled for 31 sites with data at sufficient period ranges and reanalysed to derive new transfer functions to relate to the resistivity structure (this was mostly performed by Joan Campanyà and Dugyu Kiyan). These are the primary sites used for a geoelectric field modelling throughout this work. Out of these 58 sites, 47 had an appropriate period range for modelling geoelectric fields for space weather. Of these 47, four pairs of sites were located effectively beside each other ($<$ 1 km) with a very similar transfer function,. Thus, later in this Chapter, I use 43 sites from the survey were used in total for ease of plotting.

An additional survey, the HIbernian Regional Electrical Structure survey (HIRES) was carried out between 2022 – 2023. These sites were installed with the primary aim of generating a 3D resistivity map of the entire island of Ireland, both for geophysical and space weather research (Kiyan et al., 2023). This survey added additional sites between the previous SWEMDI sites, with a significantly greater density of sites in the East, than MT sites from the SWEMDI survey. Work is still ongoing to process

the data and results from this survey. Data from this survey will be useful in terms of space weather and could be incorporated into future models to improve accuracy.

Installation

The installation of MT sites first involves scouting out the area to install the device in. However, a certain set of conditions should be met before installation. Site locations for electrometers have to be chosen carefully, as geoelectric fields are extremely sensitive to noise (Schmidt et al., 2020). Ideally, sites should be installed: a) $>$ 10 km from any major roads, power lines and towns due to the ferrous/electrical noise sources (electric fences also have an effect, but significantly smaller than power lines) b) $>$ 10 km from the coast , the movement of the tides can generate significant electric fields, c) $>$ 100 m from any rivers/streams/springs (changes in flow due to extra rainfall can generate significant electric fields), d) $>$ 20 m from any trees (strong winds cause tree roots to "sway" in surrounding soil, which can create noise by literally moving the earth around the electrometers). Sites are generally installed in farmers fields, after getting their permission. Each of the four electrodes must first be oriented to geomagnetic north using a tripod mounted compass. Approximately 40 m of cable is laid out away from the centre (depending on dimensions of the field this can change) and then the electrode is buried. In the case of short-term surveys, the electrode is buried roughly 30 cm below ground to reduce noise due to thermal variations (Chave and Jones, 2012). A conducting fluid is poured into the hole, usually salt water to improve the electrical contact resistance between the electrode and the ground. The wiring can be buried to eliminate the risk of animals chewing through the cables, but are often left above ground for surveys to reduce workload. A large battery ($\approx$ 800 W hr, 12V) is used to power the sites. A 50 cm hole is dug for the magnetometer, with a level balance used to ensure the magnetometer is flat, before being covered in plastic sheets to avoid waterlogging and carefully buried to ensure its orientation is maintained. A GPS is also used to accurately measure coordinates and to give a correct timestamp for recordings. Sites are left recording in the ground for $\approx 2-6$ weeks, with a checkup on the equipment halfway through to a) ensure no damage has been done and the device is still recording and b) swap the battery out with a fully charged one. An example of a site is in Figure 5.3. A big thanks has to be said to Colin Hogg from DIAS geophysics, who carried out the majority of this field work.

5.1.3 Electric Field Data Processing

Following the precautions described in the last section, electric field time series may still possess a significant amount of noise and need to be preprocessed. Generally the following protocol is employed; a band pass filter is used to remove for periods outside the sensitivity range of the electrometer, manual inspection for noise via comparison to magnetometer data which is normally less noisy and algorithms designed to detect

Figure 5.3: An MT site from the HI-RES survey. The data logger and battery are contained in the aluminium box (centre). The yellow wires extend out 40 m to the electrodes. The wire covered in foam insulation leads to the hole where the magnetometer is installed. The small pale-coloured orb on the other side of the aluminium box is the gps unit. The yellow wires were later buried at this specific site.

noise are used. Specific details of this analysis for the MT sites in Ireland are described in Rao et al. (2014) and Campanyà et al. (2018). After the removal of noisy data, data gaps are patched, and then the time series are detrended. The geoelectric field is then calculated using Equation 5.1.

5.2 Modelling Geoelectric Fields

5.2.1 MT Transfer Functions and Impedance relations

In this section, a method of practically deriving a transfer function to relate the magnetic field and electric fields is explained. The ability to derive geoelectric fields is essential as ultimately these electric fields induce potentially harmful GIC. As mentioned earlier in the chapter, the geoelectric field is highly susceptible to noise, so instead of constantly measuring the geoelectric field it is better to survey the geoelectric field. A transfer function can be derived by relating the geoelectric field and geomagnetic field. As discussed in the magnetotellurics Section (Section 2.3), the amount of induction caused by the magnetic variation depends on the frequency of the magnetic field, and how it interacts with the subsurface lithospheric resistive features. MT transfer functions can be used to represent this relationship:

$$\mathbf{E}(\omega) = \mathbf{Z}(\omega) \cdot \mathbf{B}(\omega) \tag{5.2}$$

where, $\mathbf{B}$ is the variation in the magnetic field, $\mathbf{E}$ is the electric field and $\mathbf{Z}$ is the complex impedance tensor relation, which relates to subsurface resistivity properties, and ω denotes the frequency dependence. Provided the impedance tensor and the geomagnetic field are known, the geoelectric field can be derived (or estimated). However this impedance tensor must first be derived. Firstly, noisy data is selectively removed for the sites as described in Section 5.1.3. After this, a fast Fourier transform (FFT) is then applied to convert the transfer functions from time to frequency domain. The transfer function can then be derived by Equations 5.3 and 5.4

$$\mathbf{Z}(\omega) = \frac{FFT[\mathbf{E}(t)]}{FFT[\mathbf{B}(t)]} \tag{5.3}$$

$$\mathbf{E}(\omega) = FFT[\mathbf{E}(t)], \mathbf{B}(\omega) = FFT[\mathbf{B}(t)] \tag{5.4}$$

The aforementioned surveys have calculated $\mathbf{Z}$ already. Hence, in this chapter we use $\mathbf{B}$ and $\mathbf{Z}$ to estimate the $\mathbf{E}(t)$ .When $\mathbf{Z}$ is known, the geoelectric field can hence be re-estimated when geomagnetic field data is present using Equation 5.5:

$$\mathbf{E}(t) = FFT^{-1}[\mathbf{Z}(\omega) \cdot FFT[\mathbf{B}(t)]] \tag{5.5}$$

5.2.2 The Impedance Tensor

$\mathbf{Z}$ relates the horizontal components of electric field ($\mathbf{E_x}$, $\mathbf{E_y}$) to the horizontal components of the magnetic field ($\mathbf{B_x}$, $\mathbf{B_y}$), by describing the resistive Earth below. The resistive Earth can be represented by $\mathbf{Z}$ using simple 1D tensors, or more complex 2D or 3D tensors which describe the full induction and direction of induction in the Earth below. Previous GIC studies in Ireland used 1D impedance tensors to model the geoelectric field time series (Blake et al., 2016, 2018). In this study, 3D impedance tensors are used, better constraining the influence of the subsurface geology when modelling the geoelectric fields. In future sections, the separate models will be compared. To start, a 1D Earth tensor is described by the relationship:

$$\mathbf{Z} = \begin{bmatrix} \mathbf{0} & \mathbf{Z_{xy}} \\ -\mathbf{Z_{xy}} & \mathbf{0} \end{bmatrix} \tag{5.6}$$

A full 3D Earth tensor can be expanded can be expanded to include the directional components of the geomagnetic and geoelectric field:

$$\mathbf{Z} = \begin{bmatrix} \mathbf{Z_{xx}} & \mathbf{Z_{xy}} \\ \mathbf{Z_{yx}} & \mathbf{Z_{yy}} \end{bmatrix} \tag{5.7}$$

where the components of $\mathbf{Z}$ are complex numbers used to relate the components of the magnetic ($\mathbf{B_x}, \mathbf{B_y}$) and geoelectric field ($\mathbf{E_x}, \mathbf{E_y}$). For example $\mathbf{Z_{xx}}$ relates to the electric field induced in the $\mathbf{E_x}$ component by the $\mathbf{B_x}$ component of the magnetic field variations (the left "x" denotes the orientation of the geoelectric field, the right "x" denotes the orientation of the magnetic field). The main difference between the 1D and 3D tensor (Equations 5.6 and 5.7) is that the 1D considers the amplitude of the resistive structures, while a 3D function considers both the amplitude and direction.

Figure 5.4 provides an example of one of these tensor relations. The individual components of Z are further subdivided into individual binned periods for convenience. A separate amplitude is present for each period range. The errors are largest outside the range of sensitivity of the instrumentation (20 – 32,000 s). When applying the FFT to derive the electric field (Equation 5.5), the magnetic field is subdivided into these same corresponding bins to get an equivalent output. For example, the first bin of $\mathbf{Z_{xx}}$ contained periods of between 10 – 15 s, so the input magnetic field is binned into this 10 – 15 s window and is applied to this corresponding period of the tensor component, with a second bin between 15 – 22 s and so on. $\mathbf{Z}$ can be decomposed into an apparent resistivity (amplitude) and phase at individual periods (Figure 5.5). In the resistivity

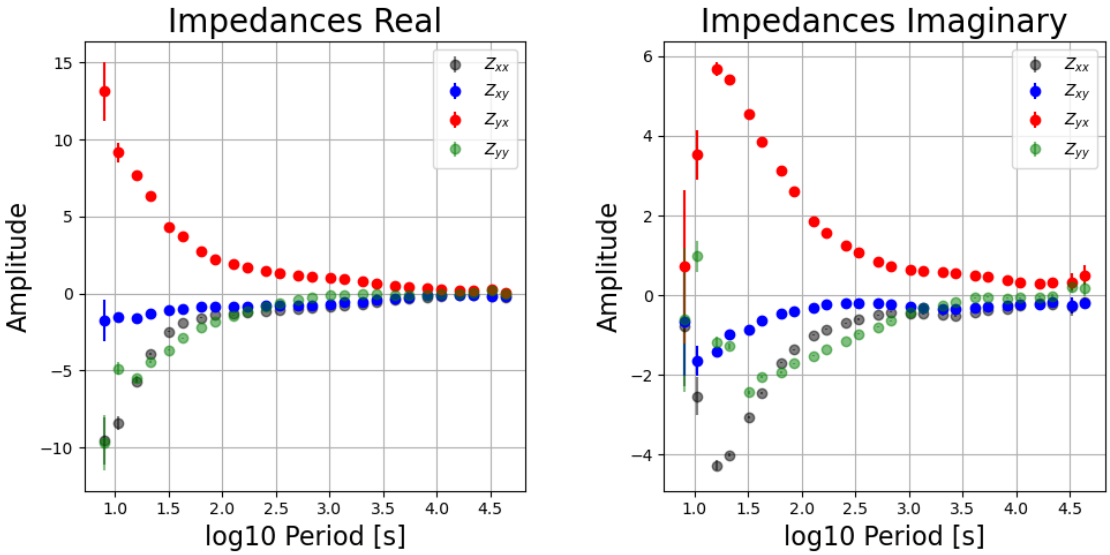

Figure 5.4: An example of the transfer function from the SWEMDI project, for each component of the transfer function (xx, xy, yx ,yy). The apparent resistivity and period are both logged (base10). The tensor is split between its real component (left) and its complex component (right). The bars indicate the uncertainty at particular periods.

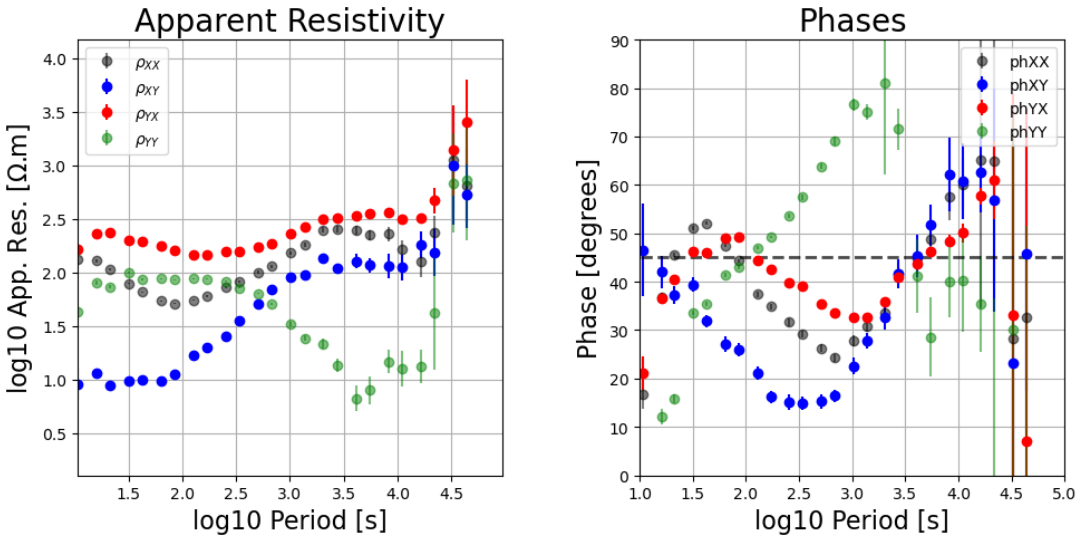

Figure 5.5: An example of the corresponding resistivity profile derived with a transfer function from the SWEMDI project to Figure 5.4, for each component of the transfer function (xx, xy, yx , yy) in terms of amplitude (left) and phase (right).The apparent resistivity and period are both logged (base10). The bars indicate the uncertainty at particular periods.

profile, there is a sharp contrast between the ρ_{XX} and ρ_{YY} components at all periods, with stronger resistivity expected for ρ_{XX}. Similarly, ρ_{YX} is usually stronger than ρ_{XY}. This indicates that most geoelectric field induction is generated by the X component of the magnetic field. This is not proportional on the induced geoelectric field, with more induction on the Y component than the X. This site is clearly not 1D, as the geoelectric field is more polarised in specific directions. This is something to note for later, as the GIC induced in a power line is ultimately induced by the geoelectric field in the same direction as the orientation of the power line.

Galvanic Distortion and MT-TF Correction

Galvanic distortion is a distortion of the geoelectric field caused primarily by real localised resistivity anomalies close to the surface, which distorts the perception of the underlying resistivity profile, changing amplitude and direction of the geoelectric field (see the more detailed description in Section 2.3.5). Galvanic distortion can affect the impedance tensor $\mathbf{Z}$, and has a relevant impact on MT geophysical studies as it can make accurate geophysical modelling difficult to impossible and, if ignored, can lead to erroneous conclusions, by extrapolating very local affects over a larger region (Chave and Jones, 2012). In terms of GIC studies, galvanic distortions may locally modify the geoelectric fields at a particular site, producing results not representative of the surrounding area between the site and the surrounding sites. Electric distortion is described by a real-valued, frequency independent tensor $\mathbf{C}$ which relates the observed MT impedance tensor $\mathbf{Z_d}$ to the regional MT impedance tensor $\mathbf{Z}$ in the absence of distortion:

$$\mathbf{Z_d}(\omega) = \mathbf{C} \cdot \mathbf{Z}(\omega), \tag{5.8}$$

where ω denotes frequency dependence (Bahr, 1987; Groom and Bailey, 1989). Theoretically if the distortion tensor $\mathbf{C}$ can be predicted then it can be removed from the tensor. However the effect of $\mathbf{C}$ is difficult to discern from measured data and instead complex methods must be employed to estimate it. The method of Neukirch et al. (2020) is employed here to reduce the influence of galvanic distortion within the MT tensors. Firstly, the distortion tensor $\mathbf{C}$ can be decomposed into a 2 x 2 matrix using the method of Groom and Bailey (1989)

$$\mathbf{C} = \begin{pmatrix} C_1 & C_2 \\ C_3 & C_4 \end{pmatrix} \tag{5.9}$$

Four parameters are used to describe $\mathbf{C}$; a gain parameter g, a twist ($\mathbf{T}$) angle $\phi_t \in (-90°, 90°)$, a shear ($\mathbf{S}$) angle $\phi_s \in (-45°, 45°)$ and an anisotropy ($\mathbf{A}$) parameter, a. Note angles are with respect to the geomagnetic reference frame. These parameters are all related

in Equation 5.10:

$$\mathbf{C} = \frac{g\mathbf{TSA}}{\sqrt{det(\mathbf{T})det(\mathbf{S})det(\mathbf{A}))}} = g'\mathbf{TSA} = \begin{pmatrix} C_1 & C_2 \\ C_3 & C_4 \end{pmatrix} \tag{5.10}$$

The effect of each can be physically explained. g is a scaling factor for the amplitude of the electric fields. The twist $\mathbf{T}$ performs a rotation of the tensor through the angle ϕ_t given in Equation 5.11:

$$\mathbf{T} = \begin{pmatrix} 1 & \tan\phi_t \\ -\tan\phi_t & 1 \end{pmatrix} \tag{5.11}$$

The shear tensor $\mathbf{S}$ develops directional dependence on axes which bisect the regional inductive principal axis, described by Equation 5.12:

$$\mathbf{S} = \begin{pmatrix} 1 & \tan\phi_s \\ \tan\phi_s & 1 \end{pmatrix} \tag{5.12}$$

The anisotropy tensor $\mathbf{A}$ adds anisotropy to the already existing anisotropy in the regional tensor in the direction of the inductive principal axis, Z_d, effectively stretching the tensor, described by Equation 5.13:

$$\mathbf{A} = \begin{pmatrix} 1+a & 0 \\ 0 & 1-a \end{pmatrix} \tag{5.13}$$

The terms of the distortion tensor $\mathbf{C}$ can be expressed in angular form using these angular descriptions. The method assumes the gain $g = 1$, as this component of the distortion is difficult to correct with a single site. The anisotropy parameter can be expressed as $a = \tan(\phi_a), \phi_a \in (-45^o, 45^o)$, with no loss of generality, i.e., the assumption doesn't affect the outcome). Hence,

$$\mathbf{C} = g' \begin{pmatrix} 1 & \tan\phi_t \\ -\tan\phi_t & 1 \end{pmatrix} \begin{pmatrix} 1 & \tan\phi_s \\ \tan\phi_s & 1 \end{pmatrix} \begin{pmatrix} 1+\tan\phi_a & 0 \\ 0 & 1-\tan\phi_a \end{pmatrix} \tag{5.14}$$

Algebraically, the distortion matrix mixes the complex-valued impedance components and therefore affects the amplitude and phase information of individual impedance components, which can lead to the aforementioned difficulties. Following the approach of Neukirch et al. (2019), the impedance tensor can be broken up into a seperate amplitude ($\mathbf{P}$, 5.15) and phase tensor (Φ, Eq. 5.16).

$$\mathbf{Z} = \mathbf{P}e(\phi) \tag{5.15}$$

The impedance phase tensor, the inverse imaginary part multiplied with the real part of the impedance, is shown to be unaffected by distortion (Caldwell et al., 2004):

$$\Phi = Re(\mathbf{Z_d})^{-1}\ Im(\mathbf{Z_d}) = \mathbf{C}^{-1}\ Re(\mathbf{Z})^{-1}\ \mathbf{C}\ Im(\mathbf{Z}) = Re(\mathbf{Z})^{-1}\ Im(\mathbf{Z}). \tag{5.16}$$

By comparing the phase and amplitude tensors, the effect on the galvanic tensor $\mathbf{C}$ can be identified and removed from the original impedance tensor $\mathbf{Z}$. A phase tensor has been used extensively to interpret MT data without most of the challenges pertained to galvanic distortion by disregarding the distorted amplitude tensor (Patro et al., 2012; Tietze et al., 2015; Bakker et al., 2015; Samrock et al., 2018). The phase tensor only holds information about subsurface induction processes, but the amplitude tensor describes galvanic and inductive effects that complement the phase tensor information (Neukirch et al., 2019).

Here, the model of Neukirch et al. (2020) is used to correct the transfer functions. Both the amplitude and phase tensors describe the same physical induction processes in the subsurface and it has been hypothesised that they should reflect similarly the present subsurface geometry, i.e. the electric strike (off-diagonal components of $\mathbf{Z}$, Z_{xy} and Z_{yx}), dimensionality and anisotropy, allowing computation of an optimal distortion matrix (i.e. the value for $\mathbf{C}$ for which $\mathbf{Z}$ and $\mathbf{Z_d}$ are most similar) that maximises this geometric similarity (Neukirch et al., 2020). To validate their results a synthetic example (Dublin secret model 2) was used to illustrate that the undistorted amplitude tensor parameters are more similar to the phase tensor than increasingly distorted ones (Miensopust et al., 2013). They provide empirical evidence for the predictability of their proposed hypothesis. By empirically selecting values for the angular components of the $\mathbf{T}, \mathbf{S}$ and $\mathbf{A}$ tensors for both the phase and amplitude tensors at separate frequencies, differences between the two can be predicted and hence removed.

This method of estimating galvanic distortion has been shown to be successful. It is important to note however that while the $\mathbf{T}$, $\mathbf{S}$ and $\mathbf{A}$ components are corrected by this method, the g parameter is not. The g parameter needs comparison to nearby sites, within kilometres to remove it (Delhaye et al., 2017). Hence not all distortion is removed. An example of this correction method in action is provided in Figure 5.6.

5.2.3 Geoelectric Field Modelling in Ireland

One-dimensional Models

Two standard approaches are used to map geoelectric fields across a region, with one estimating the geoelectric field assuming a homogeneous underlying conductivity profile, with the second assuming a variable conductivity (Beggan et al., 2013; Guo et al.,

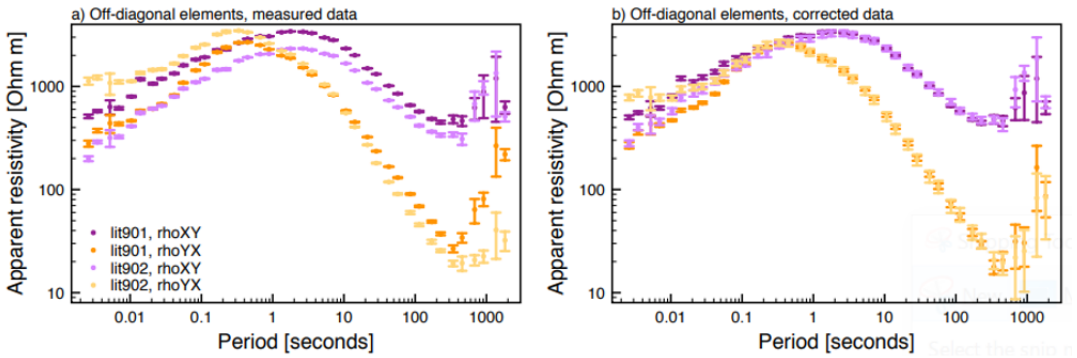

Figure 5.6: An example of the removal of galvanic distortion removal from Neukirch et al. (2020). Two nearby sites within 3 km tensor relationships are compared at different periods, one with and one without a large galvanic distortion (left). A correction is applied to both, such that after correction the two tensors have nearly identical profiles (right).

2015; Bailey et al., 2017; Kelly et al., 2017, among others). The first mapped models and maps of the geoelectric field in Ireland come from both Blake et al. (2016) and Blake (2017), who modelled and mapped geoelectric fields using both these approaches.

Blake et al. (2016) and Blake (2017) use 1D transfer functions (Equation 5.6) to estimate the geoelectric field across the island. MT sites used included sites mentioned before from the IRETHERM, IRECCSEM, so some less accurate regions in the models exist due to the low density of MT sites. The geoelectric field could then be estimated at each site using Equation 5.5. Each of the MT sites used in the model gave an average resistivity for different depths of the lithosphere down to 200 km. The values from these sites were interpolated using a linear radial basis function onto a 10 km $\times$ 10 km grid. These values were then used to make a layered Earth conductivity model at separate depths: $0 - 0.3$ km, $0.3 - 1$ km, $1 - 3$ km, $3 - 10$ km, $10 - 30$ km, $30 - 60$ km, $60 - 100$ km, and $100 - 200$ km. Skin depth (Equation 2.35) is used to approximate these depths with frequency of the signal. A resistivity value of 100 Ω m was set for depths greater than 200 km (including periods from 20 – 10,000 s).

The thin sheet approximation is a simplified model which only uses magnetic field inputs and neglects variability in the geoelectric field (Price, 1949). This method is most often used in regions with little or no geoelectric field measurements, and works best in regions where the geoelectric field is near-homogeneous. Blake (2017) incorporated a thin sheet model for the sea surrounding the island with the MT model to predict the geoelectric field across Ireland.

Three-dimensional Model

While one-dimensional models were more commonly used due to the lack of three-dimensional data in the past, the growing availability in data means 3D models of

geoelectric fields are becoming more common (Gannon et al., 2017; Alves Ribeiro et al., 2021; Torta et al., 2023). Using 3D-TF includes the directionality of the geoelectric field and not only the amplitude, which is ultimately useful when modelling GIC later, as GIC are induced by the geoelectric field in the direction of the power lines' path.

In Ireland, an updated 3D MT-TF geoelectric field model was created by Campanyà et al. (2019), using MT-TF from SWEMDI and previous MT surveys. This method modelled geoelectric fields at sites uses 3D-TF (Equation 5.7) to estimate the geoelectric field, including not only the amplitude of the geoelectric field but also for differing orientations. They design a method which estimates magnetic field variations using SECS, but also incorporates the standard deviation (STD) error in SECS into the model, and then use MT-TF to estimate the geoelectric field (SECS-MT). Campanyà et al. (2019) then validated and quantified the accuracy of the model compared to measured data, generally achieving coherences of > 0.8 and SNR of > 6 in the geoelectric field across the island. Here in this work, this SECS-MT method is used throughout to estimate the geoelectric field, expanding on it in order to map the variation.

5.3 Mapping Modelled Geoelectric Fields

The geoelectric field was modelled (described in Section 5.2.3) using the method of Campanyà et al. (2019) as a base, with an interpolation between sites to estimate the geoelectric field, an intermediate approach instead of using a full 3D conductivity profile. In this way a full 3D model can be constructed for the island easily, that is more accurate than a 1D method such as the thin-sheet method. This approach was chosen over a 3D conductivity model as it is:

a) it is computationally efficient;

b) it is an approach that is easily adaptable, i.e. new magnetometer and MT sites can be individually be added to the models;

c) it is an approach that can be used to estimate the error in the SECS magnetic field interpolation.

First, the geoelectric field was estimated at each site with the SECS-MT method. A cell size of 10 km x 10 km ($\approx 0.1^{o}$ x 0.1^{o}) was used. Then, to map the geoelectric field, a cubic-spline interpolation between sites is then used. This leads to artifacts in the modelled geoelectric field (i.e. something observed in a model that is not naturally present in the data). To mitigate this issue, a Gaussian filter was used on the interpolation to smooth out these artifacts in the image, an approach commonly used in mapping weather and climatological conditions (Chen et al., 2014; Morzfeld and Hodyss, 2019). The same interpolation method was used on the STD error for the SECS, to estimate error in the geoelectric field across the island. The Gaussian function is given by:

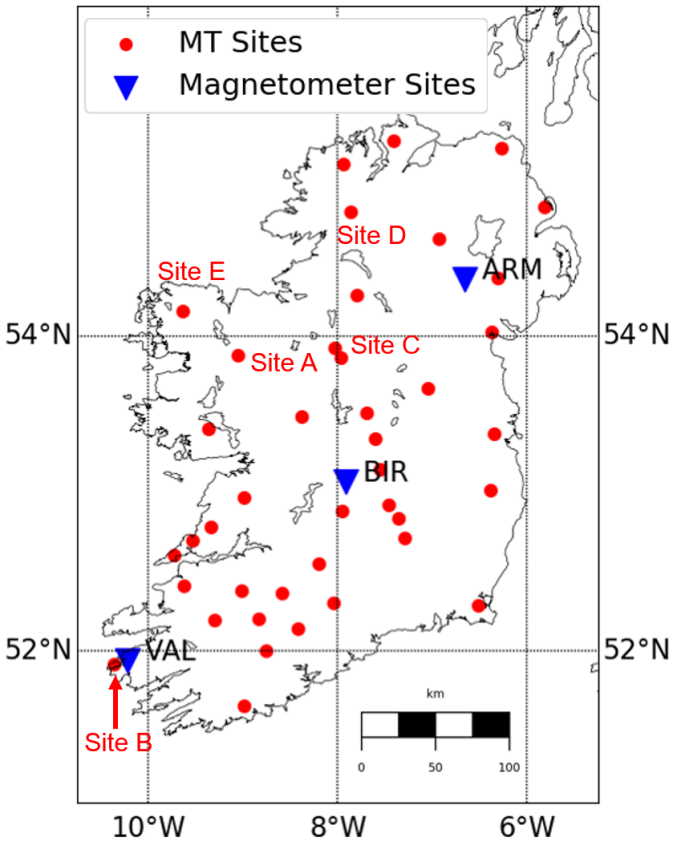

Figure 5.7: MagIE (ARM, BIR, VAL) magnetometer observatories (blue) and the 43 MT site locations (red) used in this study from the SWEMDI network. Select MT sites (A, B, C, D, E) analysed later in this chapter (Section 5.5), are marked with red text. Site A was an example site used when optimising a correction for the nowcast geoelectric field. Sites B – E were all used to validate the nowcast model.

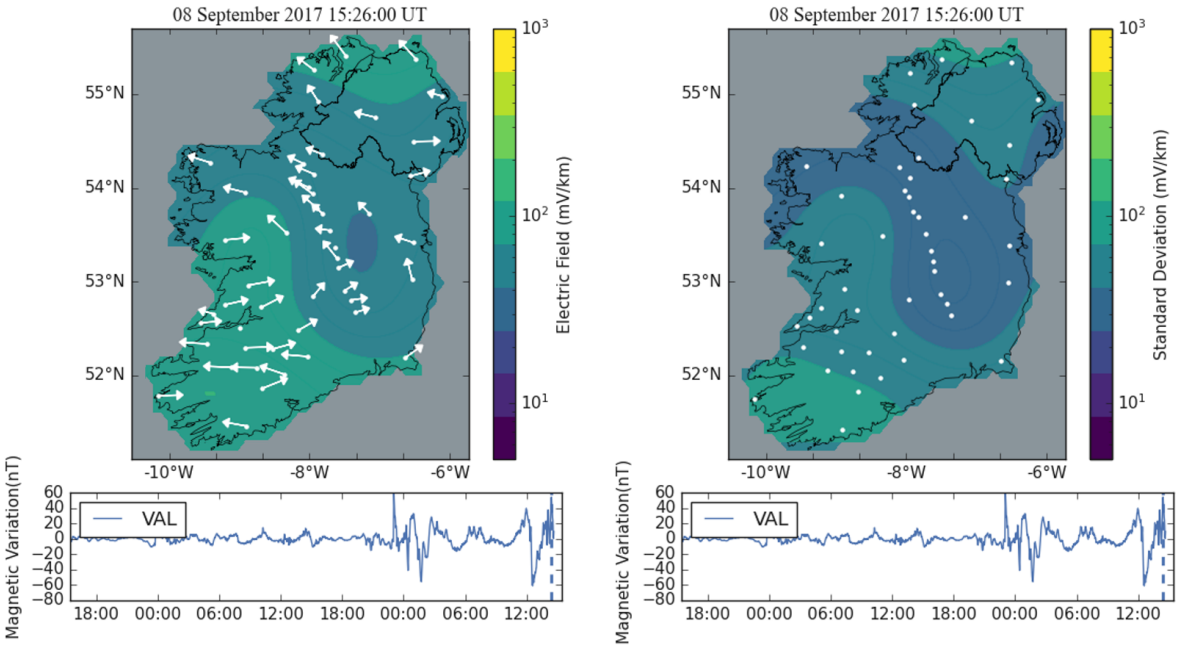

Figure 5.8: An example of the geoelectric field model operating for the 08 – 09 September 2017 storm. The modelled geoelectric fields were plotted across Ireland at the top, with colour indicating magnitude and the arrows indicating direction on the left and the standard deviation error of the model on the right. A cubic spline interpolation used to estimate the electric fields between impedance tensor sites. The horizontal (H) component of the Valentia geomagnetic observatory is on the bottom to illustrate the changing magnetic field. Peak regions are generally present in the south-west and along the northern coast.

$$G(x, y) = \frac{1}{2\pi\sigma^2} e^{-\frac{x^2+y^2}{2\sigma^2}} \tag{5.17}$$

where x and y are the longitude and latitude coordinates, σ is the spread of the distribution about the mean of the function. The σ value must be carefully set; it should be set not too low that artifacts remain in the data, but not too high that the real signal is removed (Figure 5.9). To establish the best value, comparison was evaluated at points of measurement to see if real signals were lost for values of σ. In this case, a $\sigma = 4$ cells (i.e. 40 km) was found to be optimal, when assessing the model and its performance relative to measurements (Section 5.5.2). Vectors (i.e. directional arrows) were included at each MT site to denote the direction of the geoelectric field. A binary mask applied to areas of the sea is used to remove any visually error-some regions here (see the grey regions in Figure 5.8).

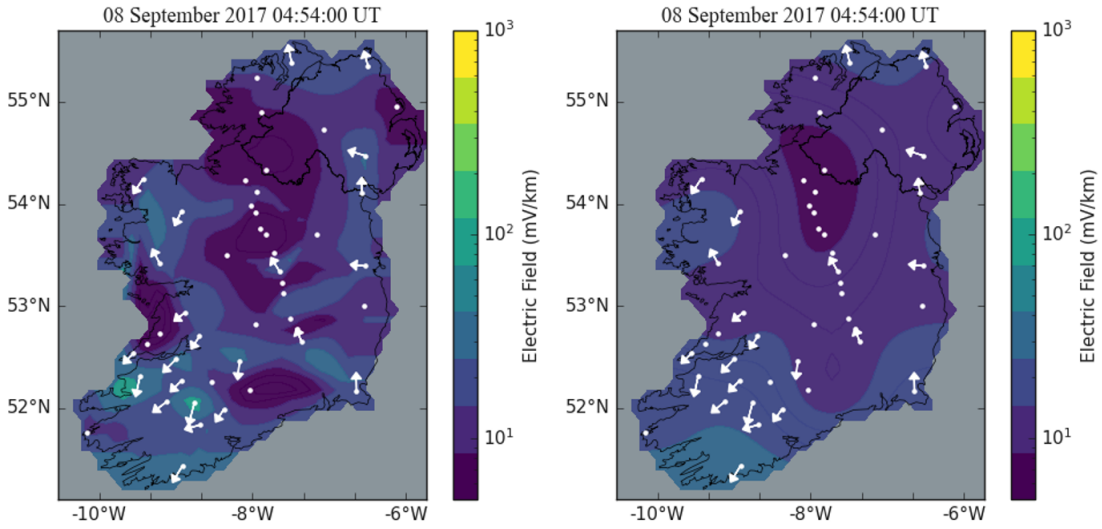

Figure 5.9: The geoelectric field model for an instant during the 08 – 09 September 2017 storm comparing the model both without use of a Gaussian filter (left) and with the use of a Gaussian filter, with a sigma value of 4 cells or 40 km (right).

5.4 Comparison With and Without Galvanic Distortion

Transfer functions with and without a galvanic distortion correction were both used when generating the maps. Galvanic distortions are near-surface homogeneities that can affect the geoelectric field (explanation in Sections 2.3.5 and Section 5.2.2). As it is not known whether a correction could improve or worsen the model, here a model that considers both approaches are used, to determine whether or not a large difference exists between models with and without these distortions. The regional effects of the model with and without galvanic distortion were examined:

The two main differences between the models are: 1) the local direction of the geoelectric field between sites is less homogeneous with galvanic distortion (Figure 5.10); 2) larger electric fields are generally observed when no correction is applied for galvanic distortion (Figure 5.11). One would also expect there to be more variable peaks in the model with galvanic distortion in Figure 5.10, however the cubic spline interpolation cleanses this effect. In Figure 5.10, some local patterns are also apparent, mainly sites in the centre of Ireland have comparably weak electric fields compared to the sites closer to the coasts and the Southwest, which could be explained by underlying lithospheric features in their respective regions. For example, the midlands is known to be rich in limestone, near to the surface, which are a relatively conductive rock type and hence generate weak electric fields. In the Southwest, a relatively resistive rock type is common, old red sandstone, and could be a source of the large geoelectric field here. It must be noted that this is merely an example. We don't know if these rock types

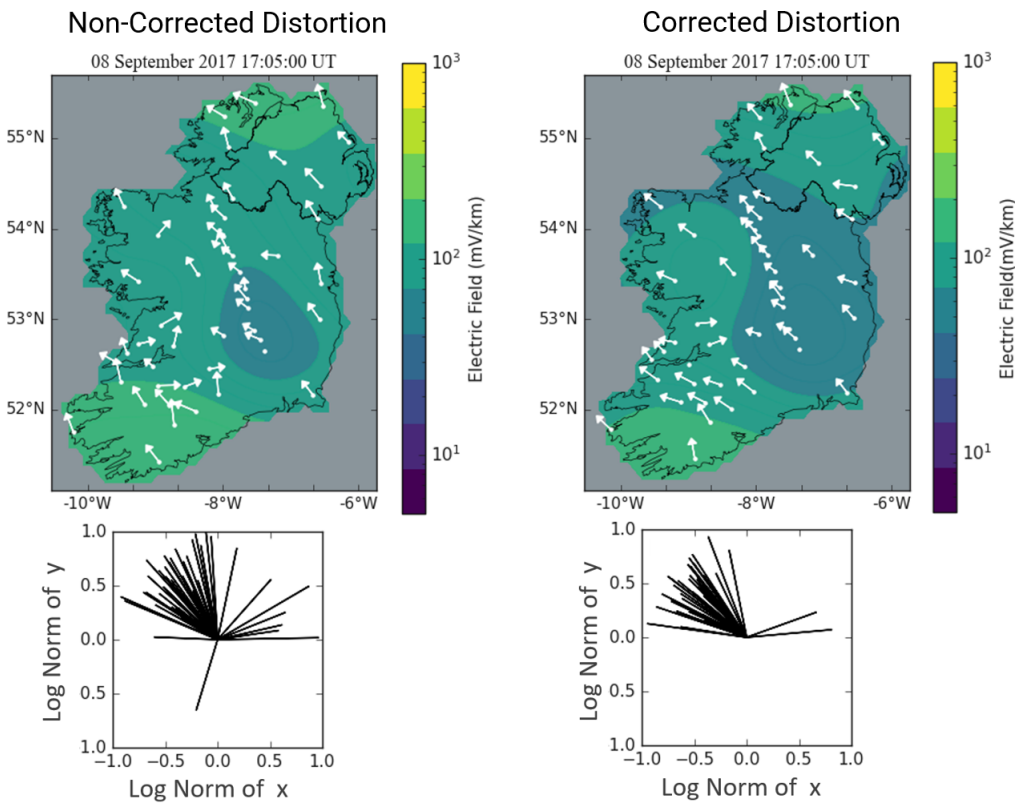

Figure 5.10: (Top) The non-corrected for galvanic distortion geoelectric field model (left) is compared to the model with corrected geoelectric field (right). (Bottom) The normalised direction of the vectors in the top panels are compared for significantly strong (> 5 mV/km) electric fields at the same point of origin.

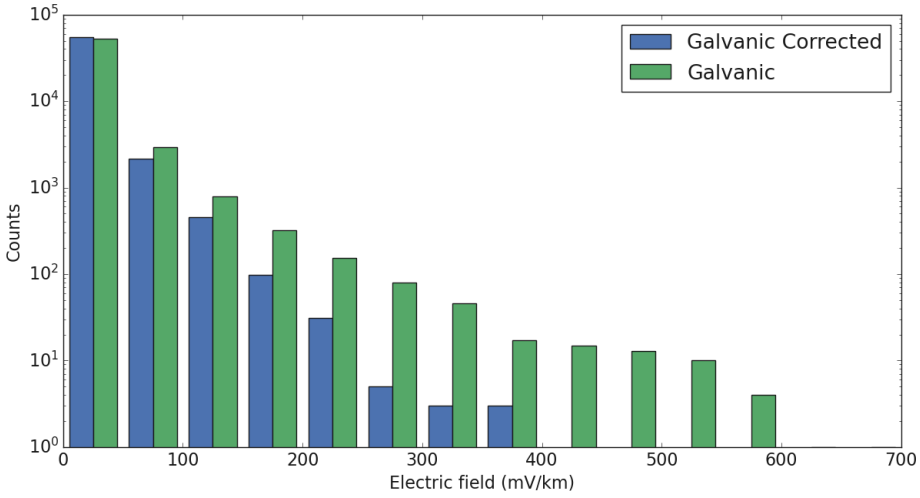

Figure 5.11: The frequency of amplitudes (50 mV/km bins) at each site, for the entire storm in Figure 5.10 are compared to models with non distorted geoelectric fields (blue) and distorted electric fields (green).

extend to deeper depths. But it may partially explain these findings.

5.5 Nowcasting Geoelectric Fields

Accurate real-time assessment of geoelectric fields (also referred to as nowcasting here) could significantly aid in reducing the hazard posed in real-time to ground-based infrastructure such as power grids and pipelines. Such a tool could be used to identify areas experiencing large geoelectric fields variations, which operators could identify and setup longer-term stations to monitor the geoelectric field . Hence, the standard geoelectric field model was altered to operate in real time for this purpose. This involved manipulating the magnetic field inputs, applying empirical corrections to the geoelectric field output and validating the new model with updates with comparison to performance metrics (relative error, RMS, SNR and coherence).

5.5.1 The Issue of Real-Time Modelling

Before computing the geoelectric fields, the measured input magnetic fields at MT sites were manipulated for nowcasting. FFT derived time-series commonly suffer from issues at the edge of the time series due to the lack of frequency information past the edge of the time series. Hence, a decrease in the electric field is observed. The time scale and intensity of the edge issues are dependent on the frequency/period range analysed. Analysis of geoelectric fields requires relatively long periods (here, between 20 – 32,000 s is used) and thus frequency information is missing on the scale of hours, so an accurate geoelectric field cannot be replicated anywhere near real time. Hence, the inputs and outputs of the geoelectric field model are adapted to mitigate this issue.

5.5.2 Manipulation and Optimisation

Two steps were implemented to optimise the geoelectric field model. Firstly, due to the edge issues, padding was added to the input magnetic field time series. Zero-padding is the standard tool for improving the performance of the FFT close to the edge of a time series which involves adding an array of zeros to the end of the input signal, which reduces errors in the output when the FFT is applied. Kelbert et al. (2017) successfully implemented a padding approach to estimate geoelectric fields using an adapted form of zero-padding, where the last recorded values were used instead of zeroes (end-padding Figure 5.12). Both padding approaches, and the combination of both (end-zero padding), were analysed. A "mirroring" approach, whereby the last values of the time series are copied and reflected, was initially considered also, but after poor performance after early testing was discarded. The performance of the FFT in real-time was evaluated by comparing padded near real-time (or nowcast) modelling of geoelectric fields with standard non-real-time modelling of geoelectric fields (where

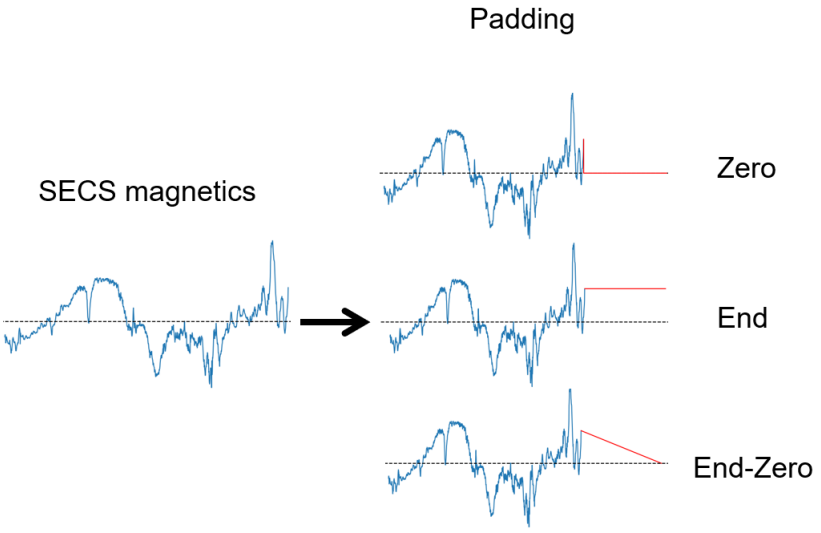

Figure 5.12: An example of the different padding types applied to the magnetic field time series, zero-padding, end-padding and end-zero padding.

Table 5.1: Storms used to optimise the model together with their corresponding Kp, local K-index maxima in Ireland during each storm. Storms of varying strength were studied to see whether storm strength influenced the padding or correction curve. The geomagnetic observatory sites (see Figure 5.7) used for the SECS interpolation are given in the right column.

Storm	**Local K Max**[a]	**Kp Max**[b]	**Local stations**
17-18 March 2015	7	8-	BIR, VAL
22-23 June 2015	8	8+	BIR, VAL
08-09 May 2016	6	6+	BIR, VAL
07-08 September 2017	7	8+	ARM, BIR, VAL
27-28 September 2017	5	6+	ARM, BIR, VAL
26-27 August 2018	7	7+	ARM, BIR, VAL

[a] Derived from local geomagnetic observatories.
[b] From German Research Centre for Geosciences (GFZ, `https://www.gfz-potsdam.de/en/kp-index/`).

electric field time series do not suffer from edge issues). Several storms (Table 5.1) were considered during the assessment. A single rectangular window function was found to be the optimal windowing function to use with the FFT, compared to Hanning and tapered cosine windows (with cosine fractions between 0 - 1 in increments of 0.05), indicating frequency resolution is more important than spectral leakage.

Length and type/shape of the padding were evaluated to select the parameters that provide more accurate geoelectric fields. Potential parameters were analysed over several spatio-temporal scenarios, considering all 43 sites over Ireland (Figure 5.7). Storms of varying strength (Table 5.1) were chosen to see whether the model performed similarly for strong and weak storms. Real-time electric field modelling, nowcasting, was compared to the modelled electric field (non real-time), to evaluate the performance of padded FFT. This was implemented as follows:

1. The real-time/nowcast model is calculated between the timeframe [t - 48 hours : t], where t denotes real time (i.e. the last point in the magnetic field time series, the nowcast magnetic field). The non real-time synthetic model (standard model) is calculated between [t - 43 hours: t + 5 hours] (data past the defined real time for the non real-time model, as in this training case the future magnetic field time series are recorded).

2. The points between [t - 5 hours: t] (at the edge for nowcast, away from the edge for standard) are compared between each model.

3. The relative error (Equation 5.19), root-mean-squared error (RMS, Equation 5.20), signal-to-noise ratio (SNR, Equation 4.15) and coherence (Equation 4.16) were calculated to compare the performance at different delays from real time (between [t - 5 hours: t]) and are recorded. Here, the delay (Δt) is defined as the interval of time between real-time/now (t), and the time series at an earlier point (T), $\Delta t = t - T$. The purpose of calculating these metrics at each delay between [t - 5 hours: t] is to improve the accuracy not only at t, but previous times close to real time, to provide the most accurate results at each delay for the generation of a real-time movie.

4. Steps 1) to 3) were recalculated, as the time series was moved along a sliding window for the course of the storm.

5. The mean of metrics from step 3) (relative error, root-mean-squared error (RMS), signal-to-noise ratio (SNR) and coherence) are calculated at each individual delay (i.e., 1 minute, 2 minute, ..., etc.).

5.5.3 Performance Metrics

A performance score (Equation 5.18) or parameter, P, was used to optimise the best correction curve for a single time series, first used by Torta et al. (2014). A performance score worked best when optimising a real-time correction factor compared to RMS, SNR or coherence. To optimise padding, the performance metrics, relative error, RMS , SNR, and coherence (Equations 5.19, 5.20, 4.15, 4.16), were analysed comparing a padded electric field time series at real-time to an unpadded time series away from real-time. Electric fields below 2 mV/km were discarded for this analysis to help avoid division/multiplication by 0 for SNR and relative errors. Signals below 2 mV/km also pose a negligible risk in comparison to larger electric fields. The relevant equations are given by:

$$P = 1 - \frac{RMS}{\sigma_0} \tag{5.18}$$

$$Rel = \frac{1}{N}\sum_{i=1}^{N}\frac{E_{data} - E_{mod}}{E_{data}} \tag{5.19}$$

$$RMS = \sqrt{\frac{1}{N}\sum_{i=1}^{N}(E_{data} - E_{mod})^2} \tag{5.20}$$

where E_{data} is the measured geoelectric field time series, E_{mod} is modelled geoelectric field, N is the length of the time series and σ_0 is the standard deviation.

5.5.4 Performance Analysis

The best length of the padding was evaluated by using lengths between 0 and 180 min with 5 min intervals. The types of padding considered included zero padding, end padding and end-zero padding (Figure 5.12). The best overall performance was obtained with a length of 105 min using either end padding or end-zero padding. The ratio of pad to time series (48 hours, 2880 min) is 0.036.

Firstly, the padding type was analysed. Figure 5.13 compares the performance of the FFT with three different types of padding (using 120 min of padding, an estimate). Both the start and end of the time series were padded by 120 minutes. End and end-zero padding outperform zero padding in each metric. The difference between end and end-zero padding is more subtle. Both perform at a similar level in each metric. The most significant difference between the two is in coherence, where end-zero padding is marginally better across all delays. For this reason, end-zero padding was chosen as the padding method from this point forth. Figure 5.14 expands on the analysis in Figure 5.13 by comparing the performance of end-zero padding using three different padding lengths. If the padding length was set too small (i.e. $<$ 60 minutes), the coherence was not accurately reproduced by the model. If the padding was set too large (i.e. $>$ 120 minutes), the SNR and RMS worsened (although coherence improved marginally). Note, despite the latter three storms in Table 5.1 missing ARM data for the interpolation, this had little impact on the performance metrics. This is likely due to the same input MT-TF being compared, so while the magnetic field will be more erroneous, this has little effect on the comparison between different padding types.

5.5.5 Correction Curve

A correction curve was considered to correct the underestimation of the nowcast geoelectric fields. The correction curve applies a scalar correction factor to the amplitude of the nowcast geoelectric fields for each time delay. This correction factor has been optimised, by comparing the real-time and non real-time models for 5 storms (Table

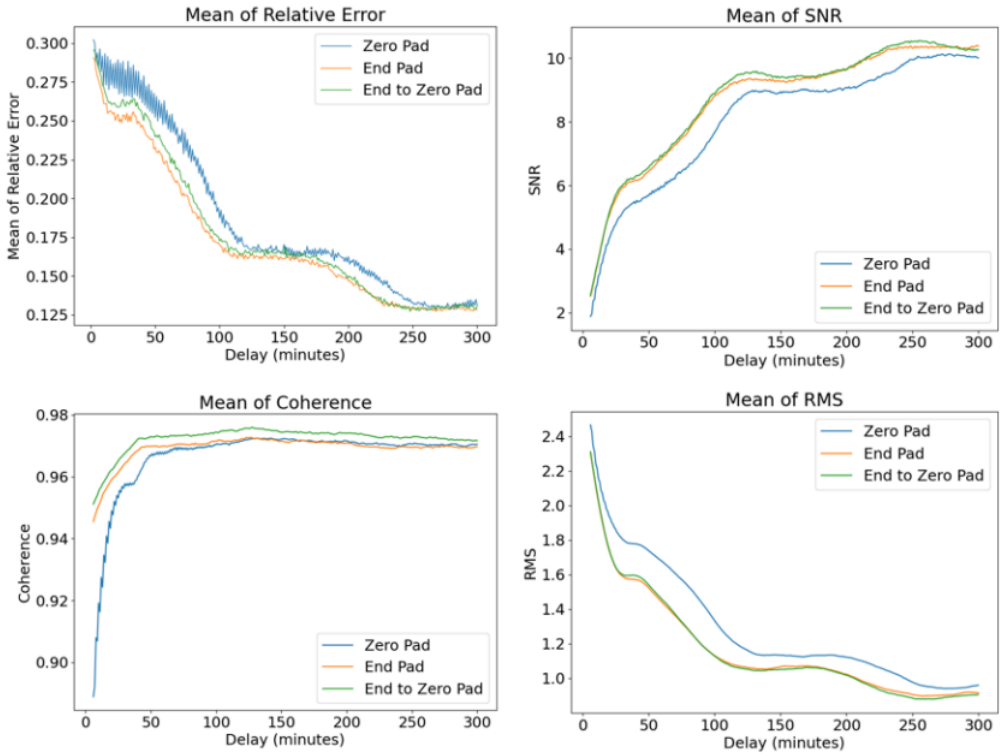

Figure 5.13: A comparison of the performance of "end-zero padding", "end padding" and "zero padding", with a mean average of the metrics taken across all sites and all storms.

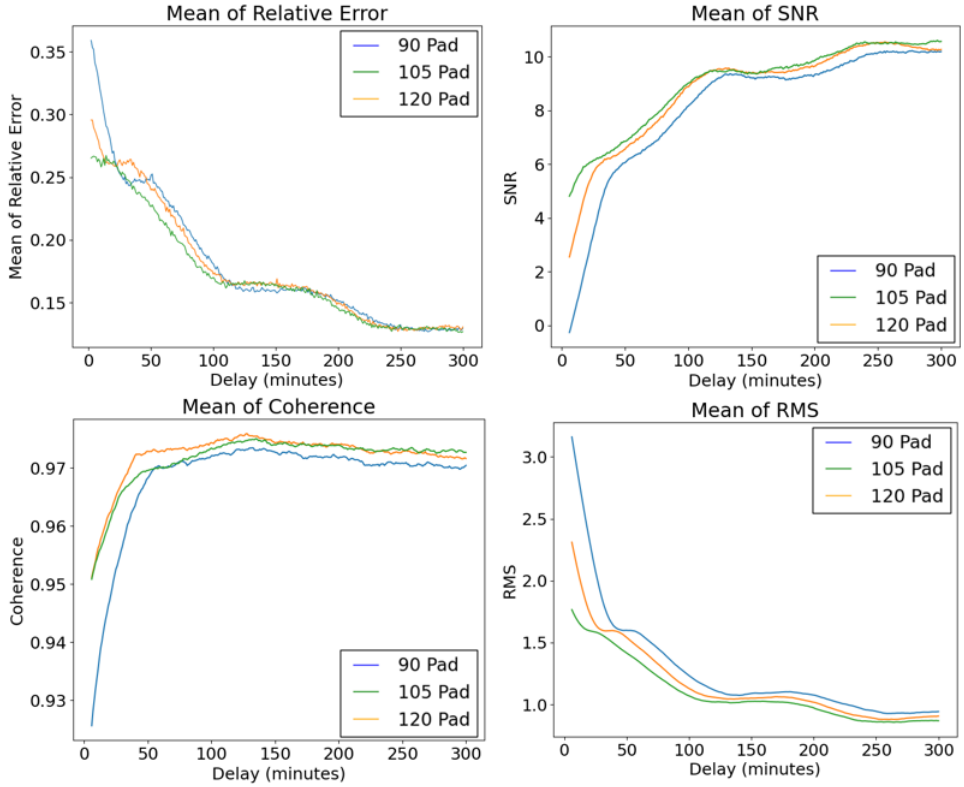

Figure 5.14: A comparison of the performance of end-zero padding with different lengths of padding (in minutes), with a mean of the metrics taken across all sites and all storms.

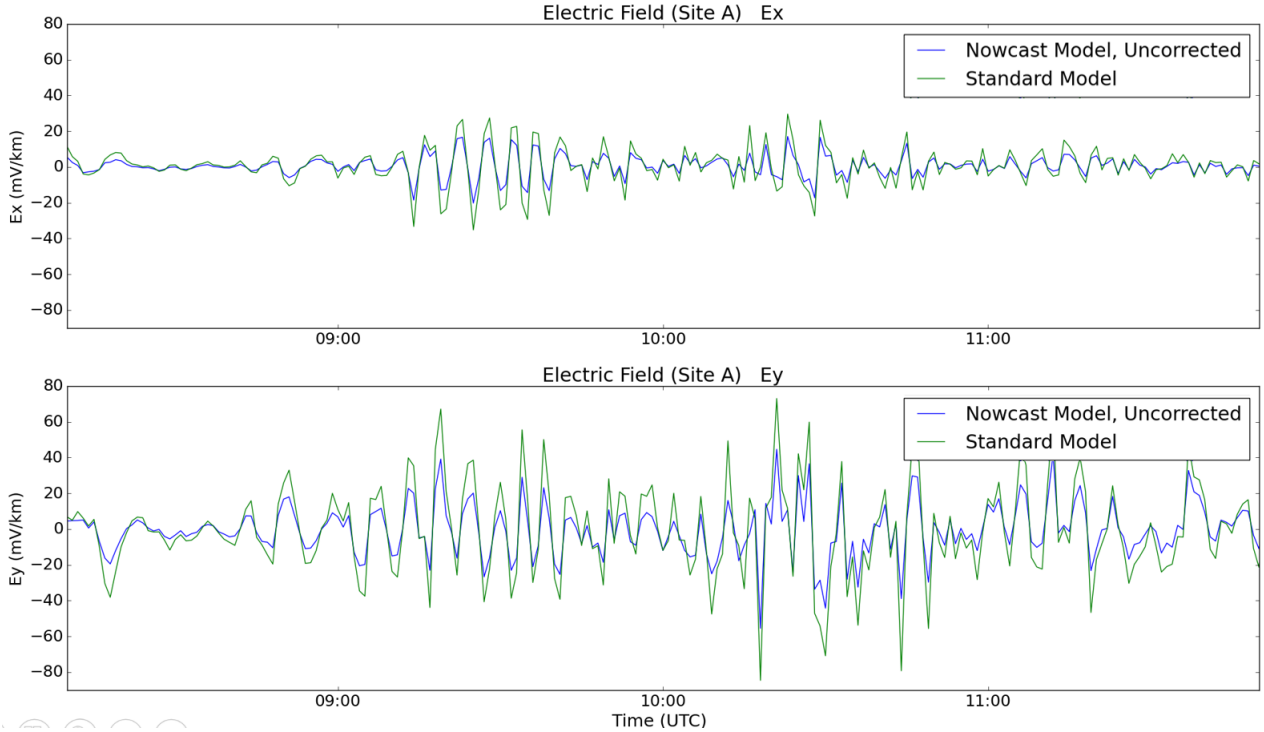

Figure 5.15: An example of the modelled time series of the electric field at a 1-minute delay (nowcast) plotted against a time series of the standard non real-time model for *Ex* (top) and *Ey* (bottom) for the 30 October 2003 for Site A (Figure 5.7).

5.1) and for all MT sites, by calculating the average ratio (example at 1-minute delay, Figures 5.15, 5.16, 5.17).

A performance score (Equation 5.18) was used to optimise the model's correction factor. The correction curve was defined by considering correction factors between 0.5 and 2 with 0.01 increments, constraining median, min and max correction factors for each time delay between 1 and 200 min. Figure 5.18 shows a graphical summary of the role of the correction curve. Figure 5.19 shows the median, minimum and maximum values of the correction curve for each time delay between each site and storm.

The correction curve is dependant on the length of time series used (48 hours in this case). The best fit of the equation in Figure 5.19 is given by Equation 5.21 and was optimised using the best relative error at each point:

$$f(t) \approx \begin{cases} -(3.01 \times 10^{-6} t^3) + (5.30 \times 10^{-4} t^2) - (3.08 \times 10^{-2} t) + 1.61 & \text{if } x/n \leq 0.024 \\ 1.00 & \text{if } x/n > 0.024 \end{cases} \tag{5.21}$$

where n is the length of the time series used, t is the time delay, 0.024 is derived from the length of the time series 2880, divided by delay 70, the edge of where a correction is needed (see Figure 5.19). The amplitude of the correction is greatest close to real-time

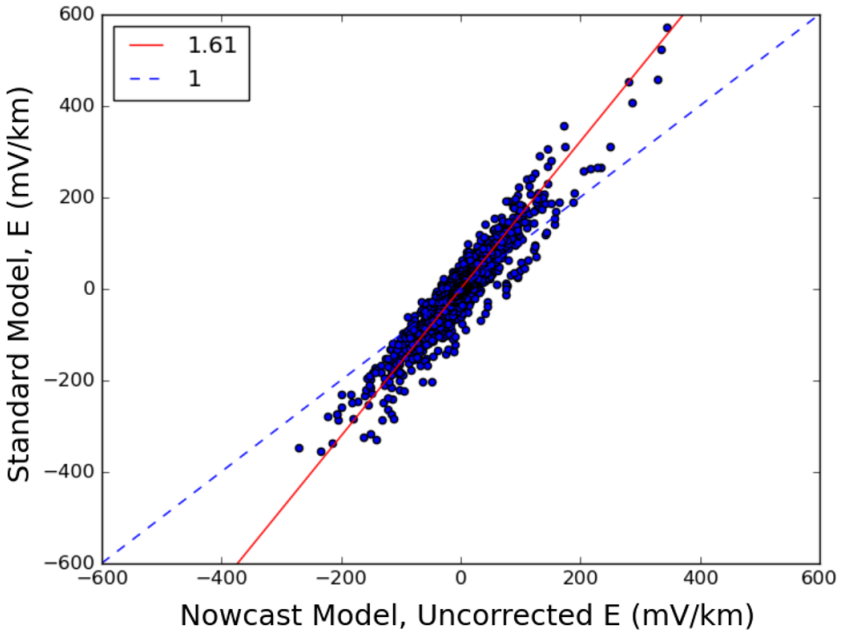

Figure 5.16: The amplitude of the standard electric field model (both *Ex* and *Ey*) are plotted against the corresponding 1-minute delayed from real time (nowcast) electric fields, for all sites in Figure 5.7 and storms in Table 5.1. The ideal correction factor (solid red line) is the best fit slope between the two models and is compared to a slope of unity (dashed blue line).

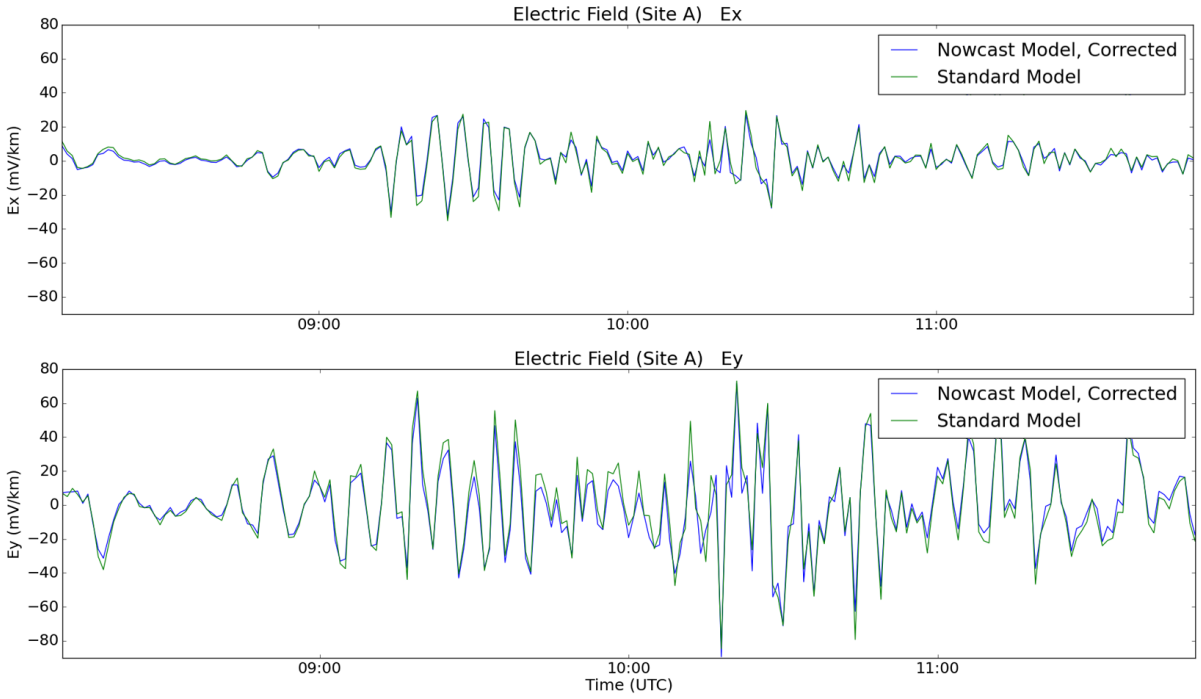

Figure 5.17: The corrected time series of the electric field at a 1-minute delay (nowcast) against the standard model for *Ex* (top) and *Ey* (bottom) from Figure 5.15, with a pre-optimised correction factor of 1.61 (Figure 5.16).

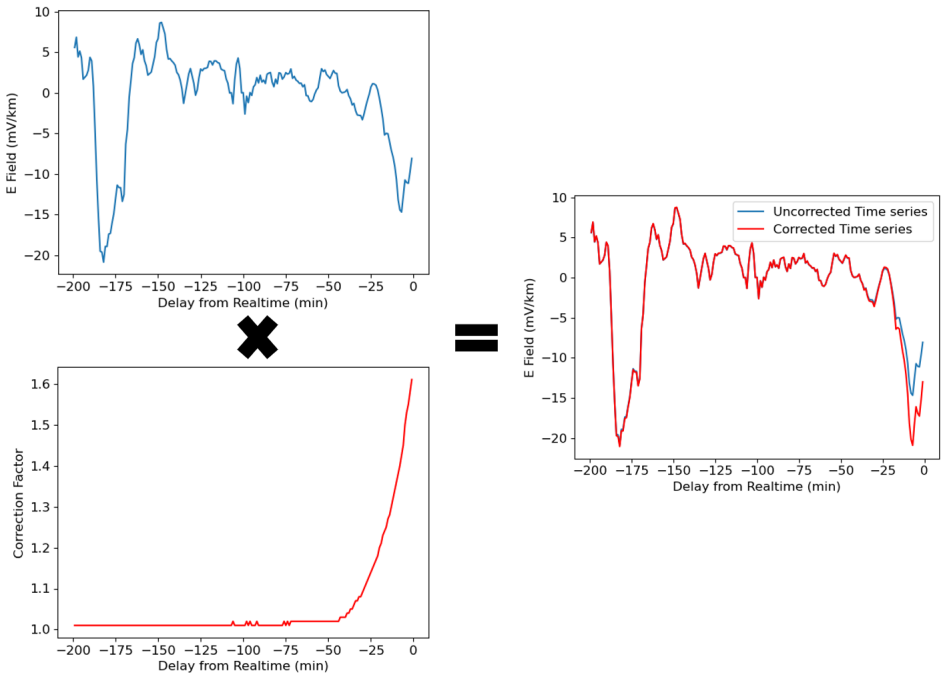

Figure 5.18: An example of the change in the time series near real time when the electric field time series is multiplied by the correction curve. The uncorrected time series (top left) are multiplied by a correction (bottom left), to give the corrected time series (right).

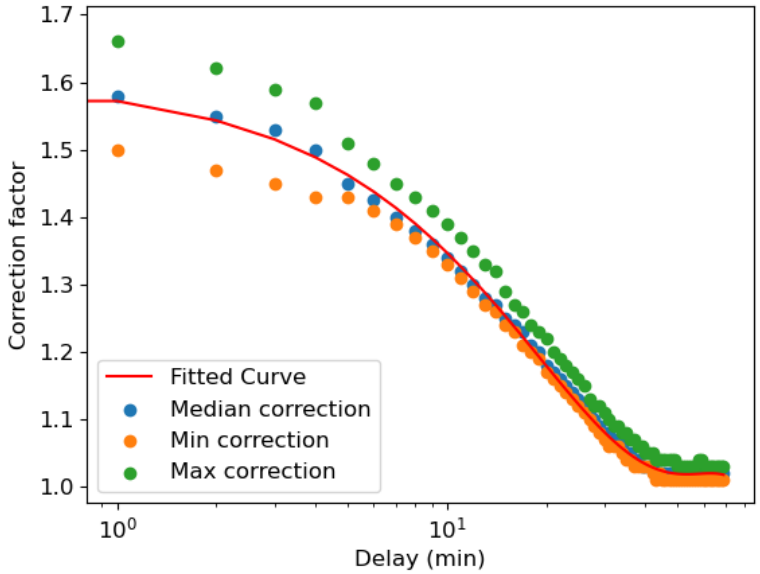

Figure 5.19: The median correction factor calculated at each time delay (the correction curve) combined for all sites and all storms. The maximum (green) and minimum (orange) extent of the curve at each delay are also marked, to give an idea of the range of errors in nowcasting.

Table 5.2: The storms used to validate the model with their corresponding Kp and local K-index maxima in Ireland during each storm. Storms of varying strength were studied to see whether storm strength influenced the padding or correction curve. The geomagnetic observatories (see Figure 5.7) used for the SEC interpolation are given in the right column.

Storm	Local K Max[a]	Kp max[b]	Local stations	MT Site
17-18 March 2015	7	8-	BIR, VAL	B
22 November 2021	6	8-	ARM, BIR, VAL	C
21 November 2017	5	5	ARM, BIR, VAL	D
07-08 September 2017	5	6-	ARM, BIR, VAL	E

[a] Derived from local geomagnetic observatories.
[b] From German Research Centre for Geosciences (GFZ, `https://www.gfz-potsdam.de/en/kp-index/`).

and falls for increasing delays (as more longer period variations are present closer to the centre of the time series) At approximately 70 minutes the correction factor approaches unity, indicating that any loss in long period information here and at larger delays is negligible.

The correction at each time delay is applied to construct a nowcast movie of geoelectric fields, to visualise how the electric fields develop up until real time. The correction curve multiplies the electric field time series by a correction factor at each time delay, close to real time, to account for lost longer period magnetic variations (i.e. the electric field time series is multiplied by 1.61 at 1 minute, 1.58 at 2 mins, etc.). Rather than re-calculate the correction at each delay individually, the curve can be used to account for the error at each delay. This significantly reduces computation time.

5.5.6 Validating the Nowcast Model

The presented approach for nowcasting geoelectric fields was validated with clean measured electric field data. During validation galvanic distortion was not corrected as it is present in the measured electric field data. Four measurement sites were used for validation (Table 5.2). Validation results are presented in Figure 5.20 and summarised in Table 5.3. Note that data measured at these sites during the selected storms were not used for implementing/optimising/calibrating the system for nowcasting geoelectric fields.

Each site in Figure 5.20 is ordered in terms of distance to geomagnetic observatories (Figure 5.7, B is the closest, E is the furthest). In terms of overall accuracy compared to measured data, site C and D perform best in terms of the performance metrics (Table 5.3). Site B is more erroneous as the MT site is located at the coast, with extra noise present in the electric field due to tidal effects. For site E, while the shape of the

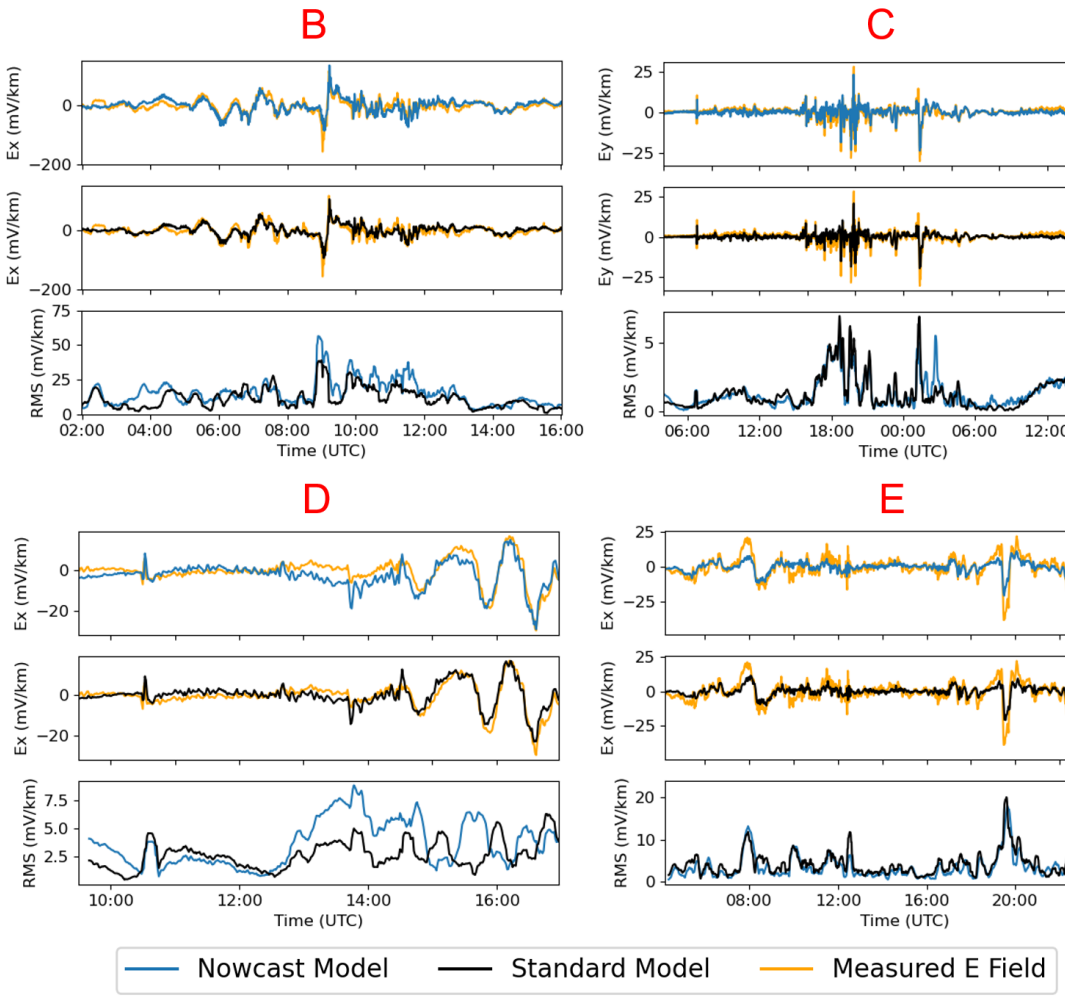

Figure 5.20: The measured and modelled E fields are compared for four example sites (Figure 5.7), (top left) 17 – 18/03/2015 (Kp = 8) for site B, (top right) 07 November 2021 (Kp = 7) for site C, (bottom left) 21 November 2017 (Kp = 5) for site D and (bottom right) 05 May 2018 (Kp = 5) for site E. The top subplot compares the measured electric field (gold) to the nowcast model at a 1-minute delay (blue), the middle subplot the measured electric field versus the standard model (black), with the bottom comparing the RMS (10-minute bins) between the models and the measured data.

.

Table 5.3: A table with performance metrics for each storm in Table 5.2, referenced by letters (B, C, D, E).

MT Site	Model	Coherence	SNR	RMS
B	Standard	0.80	4.3	1.3
B	Nowcast	0.75	3.2	1.7
C	Standard	0.89	5.4	17
C	Nowcast	0.81	6.5	15
D	Standard	0.90	7.0	3.9
D	Nowcast	0.84	4.0	3.8
E	Standard	0.83	3.8	4.0
E	Nowcast	0.89	4.5	3.3

signal is coherent, the electric field is underestimated, due to the underestimation in prediction of magnetic fields with SECS, related to distance and position relative to the observatories (Figures 5.15, 5.17). Comparing the standard model and nowcast model, a small decrease in accuracy (drop in coherence and SNR), is present in general, due to the loss of high frequency information near real time, when the FFT is performed. However, some discrepancy is observed. At some sites (C, E), SNR is higher for the nowcast, as the nowcast overestimates the standard model, which itself underestimates the measured data. And at site E, coherence of the nowcast is greater, indicating that there may have been noise present at longer periods, for measurements at this site.

5.6 Discussion

A framework has successfully been developed to model and nowcasting geoelectric fields across Ireland. The nowcast was calibrated using modelled geoelectric fields, and validated against measured geoelectric fields, producing reasonable, albeit slightly worse results, when compared to the standard non real-time model, which is to be expected given the loss in frequency information. The framework also considers correction for galvanic distortion of the MT-TF and evaluated its impact on modelled geoelectric fields across the region. The spatial resolution here is comparable to other national scale attempts to model geoelectric fields (i.e. NOAA for the US [1]), with no site in Ireland less than 200 km from magnetic observatories, and MT-TF at around 40 km distance between sites on average.

This framework was built in a way that it could be implemented outside Ireland, providing that real-time magnetic field variations and MT-TF for the area of study are available. However, it is important to highlight that the framework was calibrated using data from Ireland, that while no major changes are to be expected, I recommend that the calibration/optimisation process is repeated if implemented in a new region. The framework represents a key step for space weather and GIC studies in Ireland provides for the first time geoelectric field data in near real time for the whole island. Data will be stored at `www.magie.ie` where it can be used to assess the geoelectric field across Ireland for past events.

5.6.1 Nowcasting Geoelectric Fields

The nowcast geoelectric fields method used the FFT-based method of Kelbert et al. (2017) as its foundation and built upon it. This included a more detailed description of how to calibrate an ideal padding length. In addition, a correction curve was added to account for the underestimation at modelling geoelectric fields near real time. The

[1]NOAA Geoelectric Field 1-Minute, available at `https://www.swpc.noaa.gov/products/geoelectric-field-1-minute` as of 12/12/2023

considered correction curve approach is similar to the method used in Simpson and Bahr (2005), where they correct the individual MT-TF tensors, instead of correcting the electric field time series. However, the correction curve is more practical for this purpose (i.e., for a real-time movie), when correcting multiple delays from real time, as separate MT-TF would need to be made for each separate delay, which would increase computation time and would be tedious to perform for many MT sites. The correction curve improves the RMS of the modelled geoelectric field without affecting coherence. The simulation of the storms provides both intensity information as well as orientation at each individual site, adding approximately $10 - 20$ % additional relative error/RMS compared to a standard non real-time method, which is still sufficient to monitor geoelectric activity (Figure 5.20). The choice of ideal correction curve varies slightly from site to site and storm to storm, depending on what frequencies the site is most sensitive to. Figure 5.19 illustrates this difference in the correction curve obtained for each MT site, between the minimum and maximum extents. Due to this variability, the correction curve applied for the real-time model is not perfect, but does improve upon no correction (Figure 5.16). Moreover, almost no additional error is added, despite increasing the amplitude of the electric fields. Hence, the correction curve approach proved successful.

5.6.2 Galvanic Corrected Versus Non-Corrected

This study was the first attempt to apply a galvanic distortion correction, for space weather across an entire region. Previous work by Murphy et al. (2021) indicated that disregarding local information can misrepresent the regional effects and can lead to an over/underestimation of the electric field in a local area. Here, a similar conclusion is reached, observing that galvanic corrections lead to more homogeneity in the direction of the electric field, which is likely to be more representative of the regional lithospheric structure. The distorted MT-TF also contains local information about the smaller near-surface structures, which also generate electric fields and, for certain sites, can be up to an order of magnitude greater than the regional geoelectric field generated in the lithosphere. Individually, local near-surface effects are likely too weak to drive GIC on their own. As such, despite the relatively high density of MT sites used here (compared to other studies), one would still expect a model with a galvanic distortion correction to produce more temporally coherent results.

A combination of local inhomogeneities, related to a geological feature (e.g., a faultline), could have a relevant role on induced GIC for a particular powerline or pipeline, given that near-surface inhomogeneities can group together. In this case, inhomogeneities are more common along the coastline and in some mountainous regions like the Northwest, while the midlands remained very homogeneous. For sparse MT networks, using galvanic corrections would most likely improve GIC modelling, however this is less clear

if a high density of MT-TF were available and further study is needed to clarify this point. While galvanic corrections provide a better regional picture, and are likely to be more representative and provide more coherent results in the long term, uncorrected galvanic distortion also needs to be considered to highlight potentially larger geoelectric fields in certain areas, than what is implied by the corrected galvanic distortion. A galvanic distortion may or may not lead to better modelled GIC, which is analysed later in this work (Chapter 7)

5.6.3 Limitations

1. The plane wave approximation, assuming the surface of the Earth is relatively flat rather than curved, is likely to be more erroneous when local effects are present in geomagnetic storms. This could be solved by using a three-dimensional model of the lithosphere in Ireland and its interaction with the ionosphere and magnetospheric currents. However, this approach would be more computationally expensive and would require modification. Research by Kruglyakov et al. (2022) presents an alternative solution to this problem, by using a memory-based method to reduce computation time.

2. At present the geomagnetic observatory density is low. This leads to errors in the calculation of SECS at more isolated sites (such as site E, Figure 5.7). This, in turn, can lead to under/over estimations in the amplitude of the modelled geoelectric fields. The new magnetometer in Dunsink is present which should errors in the the East/Southeast, however another should be installed in the Northwest.

3. The correction for galvanic distortion considered in this study does not account for the scalar factor (see Section 5.2.2). This means that although the impact of galvanic distortion is largely reduced, some distortion may still be present, affecting the amplitude of the geoelectric field.

5.7 Summary

The MT-TF geoelectric field modelling approach from Campanyà et al. (2019), was expanded to map geoelectric fields across all of Ireland. An operational/automated geoelectric field monitoring approach was successfully implemented to accurately estimate amplitude, orientation and uncertainties of near real time (1-minute) geoelectric fields in Ireland. The nowcast model adds a greater uncertainty than standard modelling, with a coherence loss of approximately 5 % and an additional 5 – 10 % in the uncertainties of the total amplitude. Optimising the padded magnetic time series and applying a correction factor were crucial for real-time modelling with MT-TF, in particular the correction factor improved upon the previous state of the art for near

real-time modelling of geoelectric fields. The effect of galvanic corrections on electric fields across the entire network was investigated. The correction led to lower amplitudes in electric field strength and more homogeneity in electric field direction which may galvanic lead to improved temporal coherence in GIC modelling. The real-time model can be used as a proxy to highlight regions or power-lines that are more likely to be affected by GIC in near real time, which is more relevant than simply looking at magnetic variations as a proxy. The real-time model is available on the MagIE website at `www.magie.ie/geoelectrics`.

6 Geoelectric Field Hazard Mapping

In this chapter, the regions across Ireland most prone to large geoelectric fields during geomagnetic storms are investigated. To perform this investigation, geoelectric field time series are modelled over a 28-year time scale, using modelled geomagnetic field variations derived from magnetometer measurements. A SECS interpolation is applied to estimate the magnetic field at each site, before a MT-TF is used to convert to geoelectric fields, the same method used in the previous chapter. The main patterns in the modelled geoelectric field time series are established using hazard maps, including analysis into: a) peak variations; b) directional effects; c) the probability of exceeding a defined hazardous geoelectric field. The main aim of creating these hazard maps is to accurately identify regions at risk of large GIC, as a tool for power grid operators to help mitigate any damage related to GIC.

6.1 Hazard Mapping

Hazard mapping is a method to assess potential hazards or risks in a specific geographical area and represent them visually on maps. Hazard mapping is widely used in a variety of fields, but particularly in sectors related to natural disasters, to predict likelihood of occurrence of potentially damaging events. Common examples include mapping the prevalence of earthquakes (Frankel et al., 2000; Mualchin, 2011), groundwater flooding (Morrissey et al., 2020; McCormack et al., 2022) and the risk of landslides (Dahal and Dahal, 2017). The primary purpose of hazard mapping is to improve preparedness, response, and mitigation efforts for natural and human-made disasters. Geoelectric fields like many of these mentioned phenomena are both region specific and pose a potential hazard, in this case driving GIC which could affect and damage ground-based infrastructure. Hence, a hazard map approach to mapping geoelectric fields is applied in a similar manner here, to determine areas more susceptible to large geoelectric fields.

Hazard maps have previously been used to map geoelectric fields in the US. Love et al. (2018) and Love et al. (2022) pioneered a hazard mapping approach for geoelectric fields, evaluating the hazard posed by geoelectric fields across the US, using magne-

totelluric transfer functions (MT-TF), relations derived from measured magnetic and geoelectric fields, and simulated 100 year extreme values in geoelectric field amplitude. They successfully identify specific regions where induction is greater (e.g. the eastern coast) and hence more susceptible to large geoelectric fields. Here, this approach is used as our base to build our hazard map. Adaptations to this approach are made, however, mainly to analyse the effects of galvanic distortion and directionality on the maps.

6.2 Importance of Geoelectric Field Directionality

An important factor to consider when modelling the geoelectric field is the direction of induction, which was touched upon in the previous Chapter 5, hence, both the amplitude and direction should be considered. GIC are driven by the line integral of the geoelectric field along a single transmission line and can be represented by:

$$I = \frac{1}{R} \int \vec{E} \cdot d\vec{l} \tag{6.1}$$

where I is current, R is the resistance between two end nodes of the power grid, $\vec{E}$ is the geoelectric field along the power line and $d\vec{l}$ is the path along which the power grid lies.

The direction of the geoelectric field can have a significant influence on the output GIC along a power line. For example, if the geoelectric field is perpendicular to the power line, the induced current in the line will be zero, regardless of the amplitude of the geoelectric field (assuming this line is independent of other lines). While one might assume that the geoelectric field is near homogeneous in each direction, this is not true in most cases. The geoelectric field can be highly directionally polarised, due to the orientation of different resistivity structures present in the lithosphere, which is particularly true in more geologically complex regions. This effect was demonstrated by Murphy et al. (2021), where they consider the direction of the geoelectric field at magnetotelluric stations across multiple regions in the US, with some sites exhibiting near homogeneous geoelectric fields but many others have significant differences based on direction. Heyns et al. (2021), demonstrates the knock-on effect of directionality in geoelectric fields on measured GIC, where they note a strong north-south GIC, related to a strong north-south geoelectric field, with weak geoelectric fields and hence GIC in the east-west direction. In Ireland, a similar complex resistivity structure exists with significant differences in the orientation of the geoelectric field (Rao et al., 2014; Kiyan et al., 2018). For these reasons, directionality is considered alongside amplitude when creating the hazard maps.

6.3 Input Geomagnetic Field

To generate hazard maps of geoelectric fields across Ireland, 28-years of magnetic field were obtained from INTERMAGNET magnetometers. Joan Campanyà and Sean Blake collated this data and detrended the data to remove secular variations. They modelled this data across Ireland with the SECS interpolation technique (see Chapter 4). These time series were padded to avoid edge issues by myself (see Section 5.5.2), with 360 days of padding found optimal for the total 28-year time series. Geoelectric fields were then modelled, using magnetic field inputs with MT-TF, in the same manner to Section 5.2.1). Many of the methods used in this Chapter overlap with methods used in Chapter 5, with referrals to related previous Sections provided below.

6.3.1 Modelling Geomagnetic and Geoelectric Fields

The magnetic fields time series used in this chapter used 1-minute cadence (a lower cadence than the 1-second used previously as we need to analysis older datasets). Data prior to 1991 was recorded at too long a cadence (above minute-data) and thus not considered. The following INTERMAGNET magnetometer sites were used: Valentia, Eskdalemuir, Hartland, Lerwick and Chambon-la-Foret (Figure 6.1, i.e. the nearest sites to Ireland). The SECS method estimates the local ionospheric currents sheet above the surface using these magnetic fields as inputs and can then be used to estimate magnetic field variations between magnetometer sites. For our model, the grid spacing was set to $0.5^o \times 0.5^o$ while the current sheet height was set to 110 km, the same setting used in the previous Chapter 5. Compared to the earlier study in this manuscript (Chapter 4), the spatial density of magnetometers is more limited as only one Irish magnetometer (VAL) has a long enough time series to examine longer-term patterns. This is a factor that is considered when analysing results in more distant regions (i.e., more uncertainty due to extrapolation away from measurement sites). However, within 400km (approximately the limit in this study), acceptable results (coherence ≈ 0.8, signal-to-noise ≈ 4) are achieved but outside this range, accuracy falls off rapidly. The greatest error in the interpolation method is expected in the West and North-West (see Sections 4.2.3 and 5.5.4).

After modelling the geomagnetic field ($\mathbf{B}$) for the period 1991 – 2018, the same method as the previous chapter (Chapter 5) was used to model and map the geoelectric field. The Magnetotelluric (MT) method (Tikhonov, 1950; Cagniard, 1953) was used to model the geoelectric field time series, $\mathbf{E}(t)$ (Section 5.2.1) at each MT, in this case all 47 from the SWEMDI network were used (Section 5.1.2). A Gaussian filtered interpolation is then performed to estimate geoelectric fields between MT sites and then mapped (see Section 5.3). For similar reasons to Section 5.4, time series both with and without a galvanic distortion correction were produced.

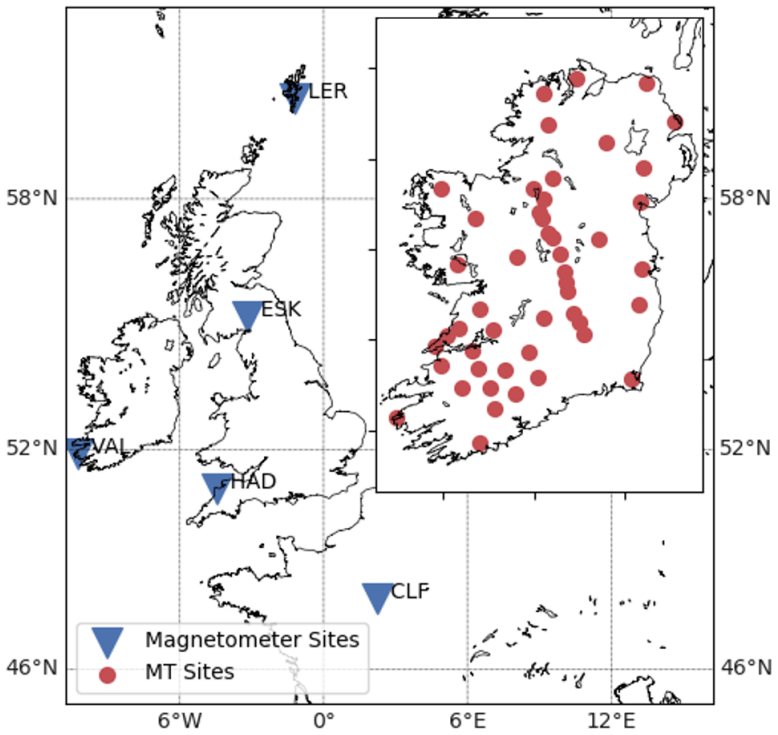

Figure 6.1: The five INTERMAGNET magnetometer sites (Valentia, Eskdalemuir, Hartland, Lerwick, Chambon-la-Foret) used for the SECS interpolations (blue) and the utilised forty-seven MT sites (red).

6.4 Geoelectrical Hazard Map Implementation

6.4.1 Workflow

Once the 28-year time series were calculated, patterns within the series could then be distinguished. The geoelectrical hazard map was developed using a similar binning/threshold approach to Smith et al. (2021), whereby data are binned into evenly-spaced individual windows, followed by calculating whether a specific threshold is exceeded within this time-frame. Geoelectric field time series were broken into three-hour bins and compared to a magnetic activity index, in this case Kp index. These three-hour bins were subdivided to include the maximum amplitude of the geoelectric field in each direction i.e. -15° to 15° (N – S), 15° – 45° (NNE – SSW), etc., where N – S refers to geoelectric fields in the geographic north and south direction, NNE – SSW refers to north-north-east and south-south-west, etc., denoted by directional vectors in the figures in the results section (Section 6.4.2). Note that declination for Ireland is between approximately -5° – 0° during this time period across the island (hence only a small difference between geomagnetic and geographical directions). The binning of the time series was performed as follows (a flow chart of the method is provided in Figure 6.2):

1. The 28-years of modelled geoelectric field time series were divided into 3-hour bins.

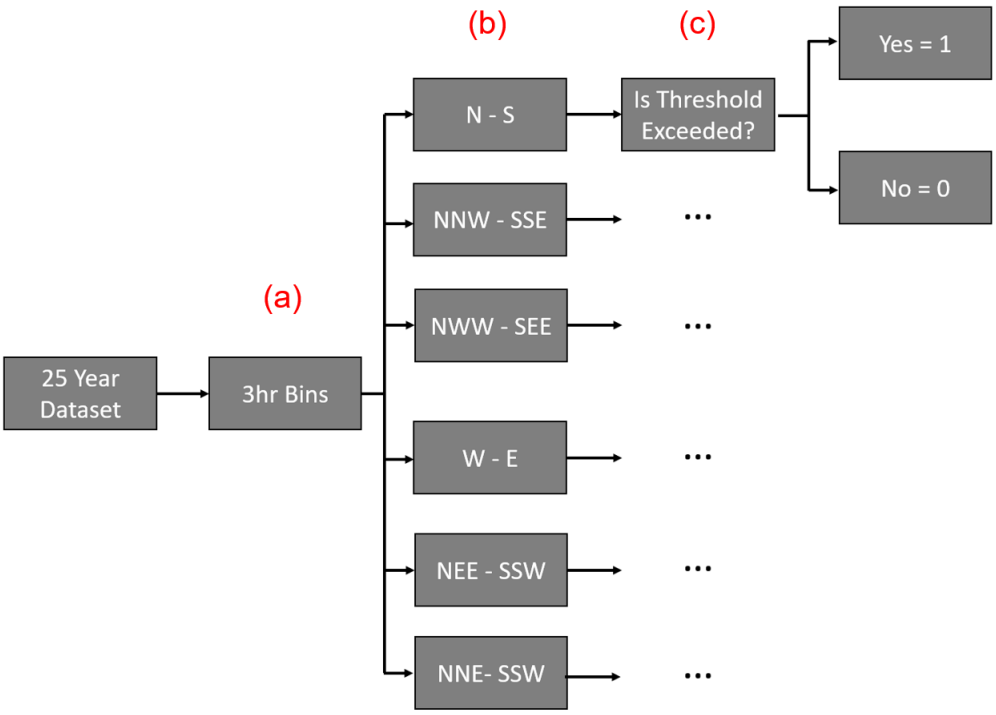

Figure 6.2: A flow chart of the binning process. Data are: a) divided into 3-hour bins; b) subdivided into separate directional bins, c) determine if these directional bins exceed a given threshold; d) assign a probability (yes, 100%; no, 0%) and calculate the mean average of these probabilities.

2. Each of these bins were then analysed as follows:

   (a) The direction of the geoelectric field vector at each minute within the 3-hour bin was calculated.

   (b) The bins were then sub-divided into directional bins. i.e. (all N – S geoelectric fields grouped together, same with NNE – SSW, ..., etc.).

   (c) Each directional bin was then tested to determine if a threshold is exceeded (i.e., $>$ 500 mV/km here). If the threshold is exceeded during the 3-hour window the directional bin returns an output of unity. If the threshold is not exceeded an output of 0 is returned.

3. The mean average of each directional output was then calculated across all three-hour bins, in each direction to determine probability of exceeding this threshold.

4. These steps were then repeated at each MT site.

The results of this binning process are then illustrated with maps, using a linear interpolation to interpolate values in the grid between MT sites. The 500 mV/km used here was chosen based upon results by: 1) Koen and Gaunt (2003); Clilverd et al. (2020), where they identify saturation in power transformers above GIC of $\approx \pm 5$ A and ± 7 A, respectively and Rosenqvist et al. (2022), who categorize the hazard of GIC based on amplitude at transformers, with issues due to GIC expected to begin to occur for

GIC in excess of ±10 A. We compared these analyses to 2) Blake et al. (2016), who simulated GIC in the Irish power grid using modelled geoelectric field time series. A geoelectric field of ≈ 500 mV/km was required to generate GIC in excess of ≈ ±10 A. One thing to note is that time duration of large GIC is also an important factor when assessing damage to transformers, which generally but not always scales with amplitude. For example a result by Clilverd et al. (2020) measured ≈ 35 A at a transformer very briefly, but no saturation is seen at the transformer. This geoelectric field threshold is meant only as a proxy.

This threshold works for this specific configuration of the power network, but should be re-evaluated if using the same hazard map approach in a different region, as the density of transformers and distances between transformer pairs can significantly influence whether a strong GIC is induced. Maps with varying Kp indices are generated, as forecast Kp indices are easily available and could be used with the hazard maps to forecast geoelectric field conditions. Analysis for other thresholds is included in the Appendix, as different thresholds may be more appropriate for different infrastructure, i.e. weaker thresholds for pipelines that wear-down due to continuous induction as opposed to large amplitudes. In contrast, larger amplitudes in the geoelectric field more often affect railways (Patterson et al., 2023).

6.4.2 Hazard Map Results

The hazard maps were subdivided based upon the percentage threshold exceeded at separate Kp indices, similar to the probabilistic hazard assessment method of Richardson and Thomson (2022). A linear interpolation between each MT site was then performed to estimate the probability of exceeding a threshold between sites. A Gaussian filter was then applied to the image (like the method used in Section 5.3). Both cubic and linear interpolation methods were tested here with negligible differences between each. The maps were generated with and without correcting galvanic distortion, with the aim of providing a regional understanding of the geoelectric fields and also to characterise the magnitude of potential local effects. The geoelectric hazard maps for Kp = 8 [8-, 8o, 8+] and Kp = 9 [9-, 9o], considering both with and without a galvanic distortion correction, are presented in Figure 6.3 and 6.4, with a summary including each direction in Figure 6.5. Smaller Kp indices are not presented as the probability of exceeding the 500 mV/km threshold was zero, or negligibly close to zero, for all sites. After this, general trends in the geoelectric field are briefly analysed, including estimated peak geoelectric field as well diurnal and seasonal effects.

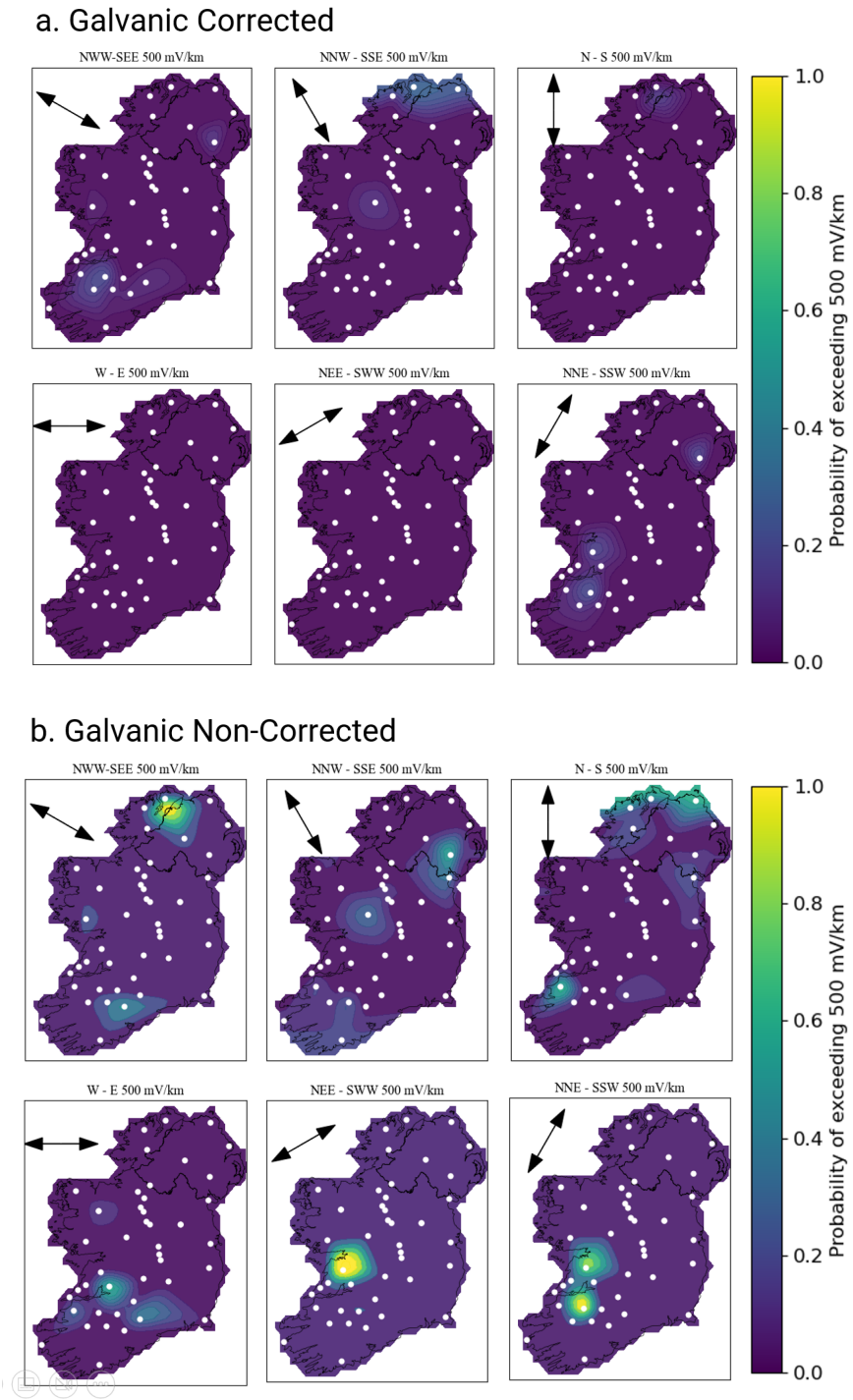

Figure 6.3: The probability of exceeding a geoelectric field threshold of 500 mV/km with galvanic corrected and galvanic non-corrected geoelectric fields is mapped for Kp = 8 storms. The direction the threshold is exceeded in, is denoted in each subtitle, as well as by vectors within each subplot (top left of each panel).

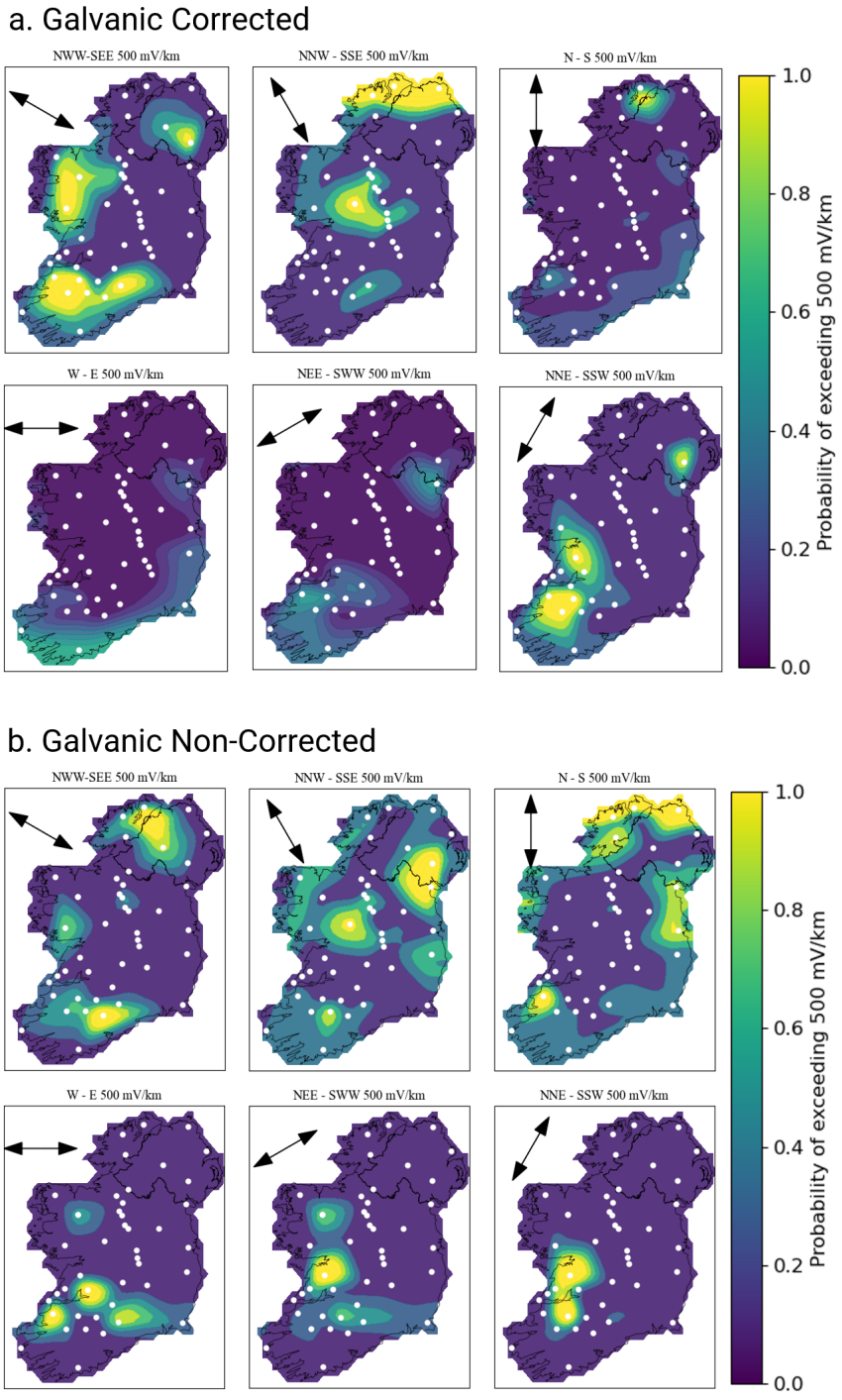

Figure 6.4: The probability of exceeding a geoelectric field threshold of 500 mV/km with galvanic corrected and galvanic non-corrected geoelectric fields is mapped for Kp = 9 storms. The direction the threshold is exceeded in, is denoted in each subtitle, as well as by vectors within each subplot (top left of each panel).

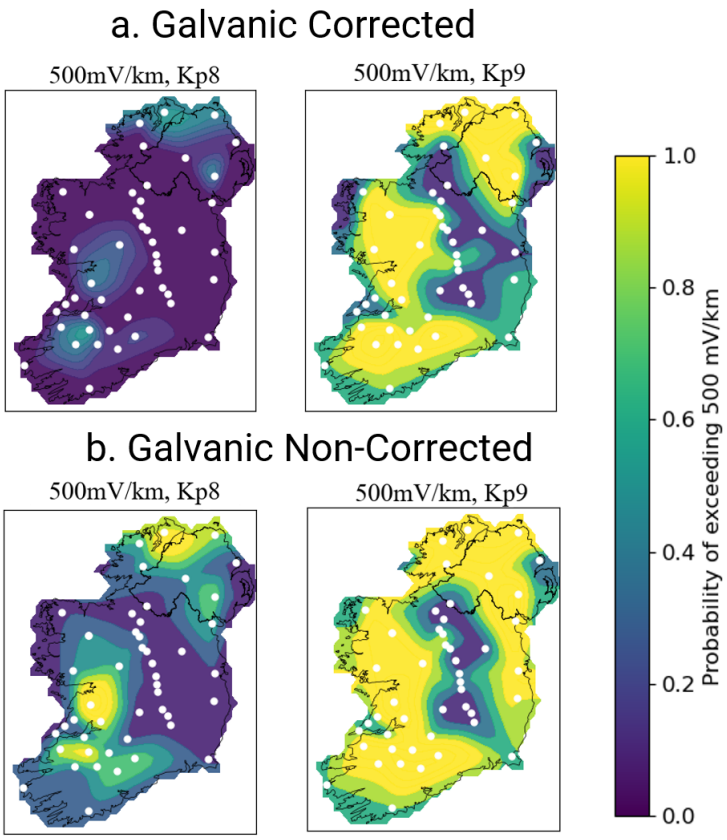

Figure 6.5: A summary plot of Figure 6.3, without subdividing between directional bins. The probability of exceeding a geoelectric field threshold of 500 mV/km for Kp = 8 (left) and Kp = 9 (right) bins is mapped.

6.4.3 The Effect of Directionality

The contrast between the directional plots (Figures 6.3 and 6.4) and the summary plot is significant (Figure 6.5). The summary plot highlights that for Kp = 9 storms, a large geoelectric field is expected across most of the island, but most regions affected in both the galvanic and non-galvanic models are the same. The directional plot however, illustrates that for most cases the geoelectric field is only exceeded in a single direction. For Kp = 8 events, there is a low probability of exceeding the threshold in small localised pockets. For Kp = 9, the area covered by these pockets expands significantly with a strong increase in probability. Generally, the geoelectric field is: a) very directionally polarised, with little overlap between different vectors; b) strongest in three regions, the northern coast, the west and south-west; c) weakest in the midlands of the island; d) is stronger in the NNW – SSE direction, NNW – SSE and NWW – SEE). The regions with strongest and weakest induction match particularly well with preliminary results of resistivity structure maps (Kiyan et al., 2018), with the highest probabilities located on highly resistive lithosphere and low probabilities located in regions dominated by lower electrical resistivity values.

The NNW – SSE induction bias is most likely present due to lithospheric resistivity features as opposed to ionospheric. With a uniform resistivity model, one would expect the induction of electric fields, and hence GIC, to be greatest in the west – east geomagnetic direction (Pulkkinen et al., 2012; Torta et al., 2023). This is due to a stronger impact from westward and eastward ionospheric currents, related to the auroral electrojet (the geoelectric field is anti-parallel to the inducing magnetic field, and parallel to the induction direction of GIC). A strong W –E component is not seen in the geoelectric field here however, with fewer hazardous regions present in both the W – E and NEE – SSW directions. The NNW – SSE (including N – S and NWW – SEE) induction bias seen in the geoelectric field is likely due to the complex geoelectrical resistivity features of the island's lithosphere (Rao et al., 2014).

6.4.4 Galvanic Corrected Vs. Non-Corrected

The main difference between the galvanic non-corrected maps with the corrected is a slight increase in amplitude and but significant change in the direction of the vector that is exceeded both for Kp = 8 or Kp = 9. The amplification of the geoelectric field at isolated sites with non-corrected distortion is a well-known effect, due to localised features of galvanic distortions (Bakker et al., 2015; Samrock et al., 2018). The change in direction likely relates to the local subsurface features distorting the perceived direction of the regional geoelectric field (Ledo et al., 1998; Rung-Arunwan et al., 2022). A good example of this is in the very north, where the peak direction of the geoelectric field changes from NNW – SSE to N – S (Figure 6.4) between corrected (top) and non-corrected (bottom). This change in orientation also leads to the breakup of larger

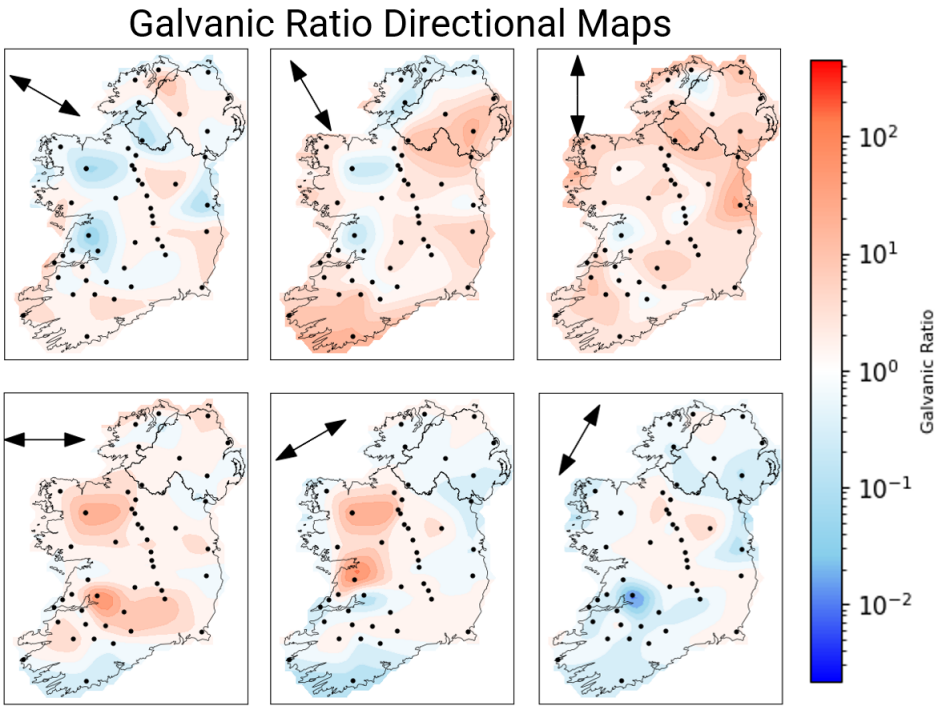

Figure 6.6: Ratio maps between galvanic corrected and non-corrected time series for the geoelectric field in six directions (3D), denoted by the arrows. Red implies galvanic non-corrected has a greater amplitude, blue implies a galvanic correction is greater. The locations of MT sites are marked in black.

pockets, such as the large region in the SW (Figure 6.4).

To further emphasise areas largely affected by galvanic distortion, a ratio between the two calculated geoelectric field models during storm time (Kp $>$ 4) was mapped at each individual site:

$$R = \frac{\sum_{i=1}^{N} |E_{dist}|}{\sum_{i=1}^{N} |E_{corr}|} \tag{6.2}$$

where R is the ratio, N is the length of the time series, E_{dist} is the galvanic-distorted time series and E_{corr} is the galvanic-corrected time series. Equation 6.2 was used to calculate a geoelectric field ratio independent of direction (Figure 6.6) and then separated into directional bins (Figure 6.7), in the same manner as Section 6.4.1. Overall, the ratio hazard maps demonstrate that a significant difference in total amplitude is present (Figure 6.7) but an even greater source of error is related to the rotation of the regional feature caused by the galvanic distortion (Figure 6.6), often leading to geoelectric field estimates orders of magnitude greater in specific directions (Jones and Groom, 1993).

A maximum geoelectric field over the 28-year time series was also calculated at each site to highlight the maximum expected strength of the geoelectric field locally and regionally. The peak values in the geoelectric field were analysed regardless of direction. The maximum estimated geoelectric field both with and without a correction at each

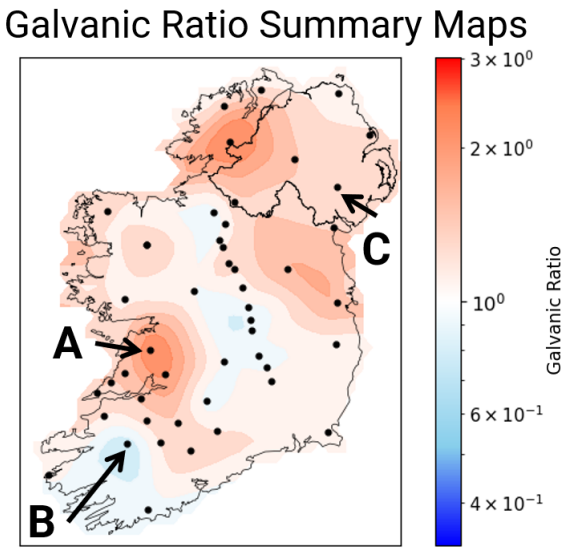

Figure 6.7: A summary map of the effect of galvanic distortion on the geoelectric field. Selected sites discussed later in the text, are denoted by the letters A, B, C.

individual site is shown in Figure 6.8. Overall, the peak maps match well with the summary hazard maps (Figure 6.7). The largest geoelectric field is expected along the northern coast and south-west, with the weakest geoelectric field expected in the midlands. The largest geoelectric field values estimated to occur were 3 V/km and 9 V/km for corrected and non-corrected models respectively. The homogeneity of the geoelectric field between the plots is also noteworthy. The geoelectric field is largely variable for the non-corrected model across the island, with the exception of the midlands, while the corrected model is smoother across the map.

6.4.5 Geoelectric Field Seasonality

Peaks in the measured geomagnetic field follow seasonal/diurnal patterns at the surface of the Earth. These may relate to a) the substorm phase of geomagnetic storms with peaks present in the pre-midnight sector at Ireland's latitude (Fogg et al., 2023), and b) increased coupling between the solar wind and magnetic field at equinox globally, often referred to as the Russell-McPherson effect (Russell and McPherson, 1973). An interesting observation in the 28-year time series, which is important to consider when using the hazard maps, is that seasonal and diurnal variations are also present in the geoelectric field. While the resistive structure is independent of seasonality, the driving magnetic field variations are not. To demonstrate these seasonal/diurnal trends here, the geoelectric field was subdivided into 3-hour bins relating to time of the year and time of day, considering only storm time (Kp $>$ 4). The sum of the geoelectric field time series at every site was then calculated (Figure 6.9). A negligible difference was observed between galvanic corrected and non-corrected models, as the resistive structure is independent of seasonality, hence only a plot of the corrected is included. The

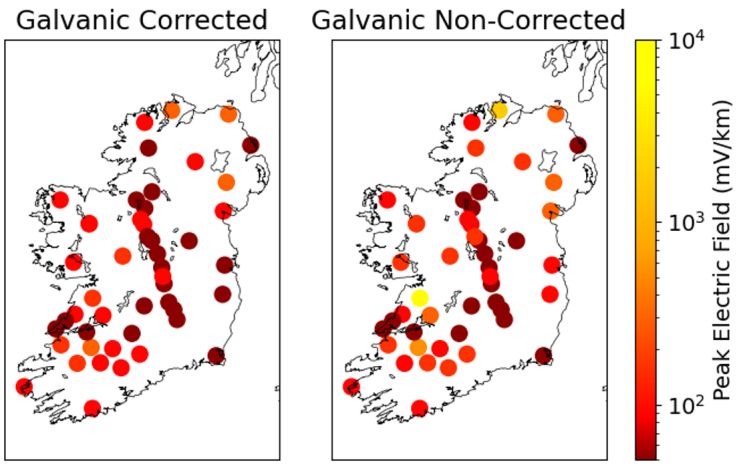

Figure 6.8: The peak geoelectric field modelled between 1991 – 2018 at each MT site, modelled with (left) and without (right) a galvanic correction. A maximum of 60 mV/km was never exceeded in regions of the midlands, while the largest geoelectric field expected are 3 V/km and 9 V/km for the corrected and non-corrected models respectively

peak geoelectric field is observed around equinox in the pre-midnight sector, matching the expected peak in the geomagnetic field.

6.5 Implications and Discussion

6.5.1 The Effect of a Galvanic Correction

A galvanic correction can have a significant influence on the modelled geoelectrical field. Here, the implementation of the correction led to significantly different results between both models (Figures 6.3 and 6.4). Applying no correction highlights more regions, likely related to local galvanic distortions distorting underlying regional features, with a general increase in the geoelectric field across the map as a whole. Considering a galvanic distortion is important, as large distortions could be present at individual MT sites and could be extrapolating to neighbouring regions where this distortion is not present. A correction will remove most of this effect, however a correction can introduce a new source of error, as GIC can be driven by the sum of these distortions, particularly if they align, such as along a geological feature. Therefore, both maps, with and without a galvanic correction, should be considered in terms of impacts on GIC modelling until further evaluation can prove one or the other to be better. The ratio maps, Figure 6.6, highlight that certain areas are more prone to galvanic distortions, like the south-west and north-west. The cumulative plot (Figure 6.10) demonstrates how peak geoelectric fields change, when a correction is applied across all thresholds, for three different cases (A, B, C). Site A (Figure 6.7), is the site where the large geoelectric field is predicted across the island, before a correction is applied. While a geoelectric field of approximately 9 V could have potentially been exceeded locally, we didn't

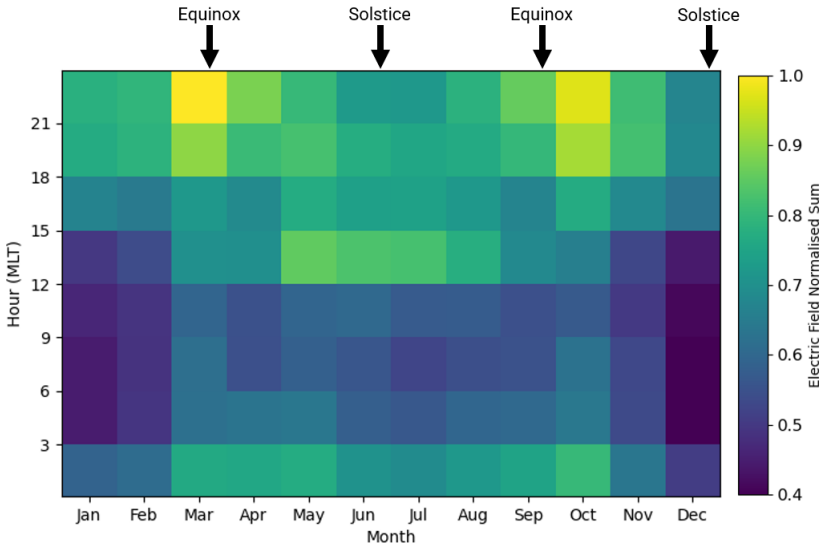

Figure 6.9: The normalised sum of the geoelectric field subdivided into bins related to time of year and time of day, for all MT sites in Figure 6.1 at magnetic local time (MLT) during storm time (Kp $>$ 4). A strong peak in electric fields exceeding this threshold is present at the equinoxes, pre-midnight.

expect regional values larger than the non-corrected value of approximately 3 V (Figure 6.8) for the time period 1991 – 2018. Site B is an example of a site where applying a galvanic correction increases the geoelectric field amplitude. When a correction is applied to the geoelectric field, site B overtakes site A in terms of amplitude, indicating site B is in an area where a greater regional geoelectric field is expected. Site C is a site more characteristic of the general trend in Ireland, where applying a correction slightly decreases the total amplitude of the geoelectric field. These less affected sites are generally found in the midland regions, while coastal regions, in particular the north-west and south-west, are most strongly affected by galvanic distortions. The higher variability in the galvanic-corrected model suggests that more measurements are required in these regions more susceptible to galvanic distortions, to accurately reproduce the geoelectric field. In summary, constraining the effect of near-surface inhomogeneities is essential to accurately assess the hazard caused by geoelectric fields regionally.

6.5.2 Implications for Power Grid Stability

The main subject of this Chapter is ultimately to highlight areas prone to large geoelectric fields and hence more likely to generate large GIC. Both regions and directions were identified in which the geoelectric field is more prone to be driven. We found a substantial directional component in the 3D modelled geoelectric fields on agreement with other studies such as Cordell et al. (2021); Murphy et al. (2021); Love et al. (2022), with the direction of the geoelectric field strongly inhomogeneous, often an order of magnitude greater in specific direction (Figure 6.6). With the growing availability of new 3D MT data, more research is now beginning to use 3D models (Torta et al.,

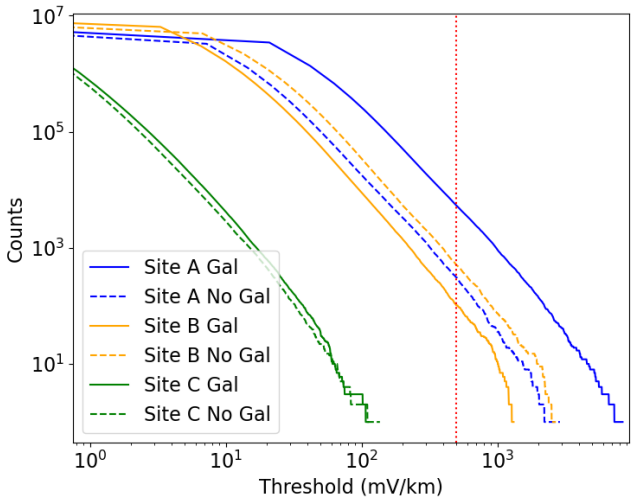

Figure 6.10: A 28-year cumulative plot of the geoelectric field for the three sites in Figure 6.7, for corrected galvanic (dashed line) and uncorrected galvanic (solid line) electric fields, demonstrating the effect of a galvanic distortion on amplitude. The red dotted line denotes the 500 mV/km threshold adopted here.

2021; Marshall et al., 2019; Alves Ribeiro et al., 2023) to simulate GIC, to include the effect of directionality. This should significantly improve the accuracy of modelling. The directionality can drastically change the output GIC, as explored by Heyns et al. (2021), where they measure the effect. A GIC will be only induced significantly in the direction of the geoelectric field (Equation 6.1). If for example, a power grid is in a region with large N – S geoelectric fields, but is oriented exactly perpendicular (i.e., W – E) an insignificant GIC will be induced.

The hazard maps, together with the galvanic distortion maps, can be used to identify regions where additional geoelectrical data should be measured to improve our models accuracy, as well as sites to potentially measure GIC for power grids, but also other conductors such as pipelines and railways. This localised measurement could be implemented, for example, with the differential magnetometer method (Campbell, 1980; Matandirotya et al., 2016; Hübert et al., 2020). Areas with large discrepancies between galvanic corrected and non-corrected (like site A in the South-West, Figure 6.7) should especially be prioritised, to determine whether or not a correction improves or worsens GIC modelling with this density of MT sites and to ascertain if an increased density of MT sites are required. Extra consideration should be taken into account in Ireland due to the coastal effect as Ireland is an island. The increase in charge carriers close to the coast will likely enhance GIC by decreasing the ground resistance in these regions (Liu et al., 2019, for China). We also demonstrate the seasonal aspect of geoelectric field variations, with the power grid in Ireland potentially more vulnerable at the equinox within the pre-midnight sector. Overall, using 3D geoelectric field models as inputs for GIC modelling will significantly increase the capability to accurately determine areas

at greatest risk to damage, due to the strong directionality of the geoelectric field.

6.5.3 Potential Uses

Aside from the primary goal of the model for use as a proxy for regions with large GIC, the maps provide other potential uses, such as a forecasting aspect alluded to earlier in the Chapter. Increasingly in the last decade, machine learning has been used alongside physical models, to forecast space weather events (Murray, 2018; Garton et al., 2018; Smith et al., 2020; Bailey et al., 2022). In their current form, the hazard maps could already be incorporated with forecast Kp indices and used for forecasting geoelectric field conditions in Ireland as a benchmark forecast model. The inclusion of Kp indices in this analysis was with this forecasting potential in mind, as forecast Kp indices are readily available. However, the seasonal and diurnal variations observed here (Figure 6.9) should be considered for a more accurate model. Kp indices should mostly account for seasonal variations, as the increased coupling between the solar wind and geomagnetic field related to the Russell-McPherson effect is a global phenomenon. However, diurnal variations do not correlate well with Kp index, as they are highly dependent on local geomagnetic conditions and thus diurnal variations should especially be considered (Cid et al., 2020).

Alternatively, the 28-year analysis could be expanded to model longer term extreme event analysis, such as a one-in-a-hundred year event analysis or worst case scenario event. This analysis can be done using power-law or log-normal distributions, which other studies have applied successfully, to extrapolate across cumulative distributions (Rodger et al., 2017; Love et al., 2018; Lucas et al., 2020). However for this analysis, due to the limited time period of data available, longer term considerations, such as changes in the intrinsic geomagnetic field should be taken into account. Across these longer time scales, the strength and orientation of the geomagnetic pole can change marginally, decreasing in strength by ≈ 94 %, moving by $4°$ in the last 120 years (Thébault et al., 2015). This is significant enough that it could drastically affect the strength of magnetic field variations during geomagnetic storms, which are strongly dependant on position from the geomagnetic pole. This factor is particularly important near the $50°$ latitude mark, the latitude at which Ireland lies, and thus should be considered (Pulkkinen et al., 2012; Rogers et al., 2020).

6.5.4 Limitations

Additional physical considerations could be accounted for to improve on the model. First and foremost, the density of magnetometer sites across Ireland is low, and hence the SECS interpolation magnetic field estimation is not as accurate in some regions. While one long-term magnetometer was used in this study from Ireland, two new

magnetometers now exist in the centre and north of the island, hence an increased accuracy in interpolation of the magnetic field (Malone-Leigh et al., 2023). Most regions are relatively close to magnetometers (i.e. < 200 km) which is sufficient to estimate magnetic fields using SECS (Section 4), but not in all regions. In the very north-west and west of the island errors in the interpolation are greatest (Section 4.2.2) with a coherence of ≈ 0.8 and signal-to-noise of $\approx 2-3$ in these regions. Methods of mitigating these issues are explored more in the future work Section (Chapter 9.)

6.6 Summary

The first geoelectric hazard map for Ireland is presented, mapping amplitude and direction of the geoelectric field under several conditions. The south-west, west and northern coast were observed to be most susceptible to large geoelectric fields. Peak geoelectric fields of 3 V/km and 9 V/km are expected for the corrected and non-corrected models over the course of the 1991 – 2018 respectively. Regions of enhanced galvanic distortion were identified, with coastal regions near the south-west and north-west most affected, with the midlands and south-east least affected. Both a galvanic corrected and non-corrected model should be considered to ensure the regional geoelectric field is accurately reproduced. Seasonal and diurnal variations are present in the geoelectric field and must also be accounted for, should the hazard maps be used for forecasted geoelectric field conditions. In Chapter 7, the effects of directionality and a galvanic correction on GIC modelled will be explored in more depth. While at regional scales differences exist, whether these differences affect the power grid needs to be investigated to truly validate whether a) the large directional discrepancies in the geoelectric field affects the power grid as a whole and b) whether a galvanic correction improves or worsens GIC modelling across Ireland.

7 Modelling GIC in the Irish Power Network

In this chapter, approaches to modelling GIC in the Irish power network are analysed. The previous state-of-the-art for network modelling in Ireland, the model of Blake et al. (2018) is explained, followed by changes implemented to this model during the course of this project. The new model was updated from a one-dimensional (1D) Earth model to a three-dimensional (3D) Earth model. The change in GIC between the 1D and 3D models is explored. The impact of corrected (3D) galvanic distortion and the grounding resistance on GIC estimates was then investigated.

7.1 Power Network Model

Two sets of information are required to model GICs: information about the physical installations in a power grid, and the geoelectric field driving the GIC. The prior includes transformer types, transmission line resistance, grounding resistance of the transformer, winding resistances, etc. The process of gathering these data can be tedious and time consuming. Fortunately, however, Blake (2017) gathered available information and wrote a python package to model the power network, called the power network model generator (PNMG, www.github.com/TCDSolar). Here, this model is used as a base to calculate the GICs in the Irish power grid. This program accounts for: a) different types of transformers, two-winding and autotransformers (Section 2.4.5); b) multiple connected transformers within substations; c) transformer grounding switches that can be turned on and off; d) dual-circuit connections between substations. These features are input into the LP model (see Section 2.4.3), along with the electric field model and the corresponding GICs are calculated across the network. For simplicity (as well as due to available data), this model assumes the path between substations to be the displacement between both. Blake (2017) validated this model compared to the artificial test case used in Horton et al. (2012). This involved modelled GIC across a simplified power grid, with the electric field assumed to be a homogeneous 1 V/km across the grid. The geoelectric field is input into the PNGM model and the GIC is then estimated at each transformer within substations of the artificial grid. This approach

proved successful, with negligible differences in estimates at each transformer. This approach was then tested after for the Irish power grid, but instead using estimated geoelectric fields from measurements rather than an homogeneous model.

7.2 The Irish Power Network

Details about the Irish power grid were collated from Blake (2017), Eirgrid and System Operator for Northern Ireland (SONI) annual reports (who operate the power grids in Republic of Ireland and Northern Ireland, available at https://www.eirgrid.ie/ , https://www.soni.ltd.uk/) as well as general infromation on their websites. The Irish Power Network consists of five 400 kV, ten 275 kV, twenty-six 220 kV and forty-five 110 kV stations.

Blake (2017) received coordinates of each transformer, along with transmission line connections from Eirgrid, which was used to construct the model of the Irish power grid (Figure 7.2). The model consists of 274 substations. Each of the 400 kV, 275 kV and 220 kV substations have multiple sets of transformers, while the 110 kV stations have only a single transformer. Connections between substations used calculated line resistances, accounting for the three-phase equivalent resistance value. In contrast to the deep subsurface driving the geoelectric field, GICs scale with increasing conductance as opposed to resistance at the surface. A greater grounding resistance will decrease the current that will flow along a power line. The current between the transmission lines and the earthed points flows better the more conductive the grounded connection is.

Winding resistances for the transformer types and configurations range from 0.043 Ω – 0.685 Ω (see Section 2.4.5 regarding more information on transformer types). Ground resistances were provided for most, but not all transformers. These resistances range from 0.246 Ω – 6.35 Ω with unknown resistances estimated as 1 Ω (the grounding resistance the ESB aims to acheive for their substations). This model was extensively tested using many different input geoelectric fields and partially validated against measured GIC from a Hall-Probe at the Woodgate power station. Later here, this 1 Ω estimate is re-evaluated.

7.2.1 1D Input Conductivity Model

The previous GIC model for the Irish power network developed by Blake et al. (2016) used a 1D conductivity model (outlined in Section 5.2.3) for the geoelectric field input. A performance score, Pearson correlation (similar to coherence) and RMS were used to validate the accuracy of their model, with mean average values respectively of approximately 0.2, 0.6 and 0.6. Overall correlation was good, but both the performance and RMS were poor. An interesting observation they found was that the model par-

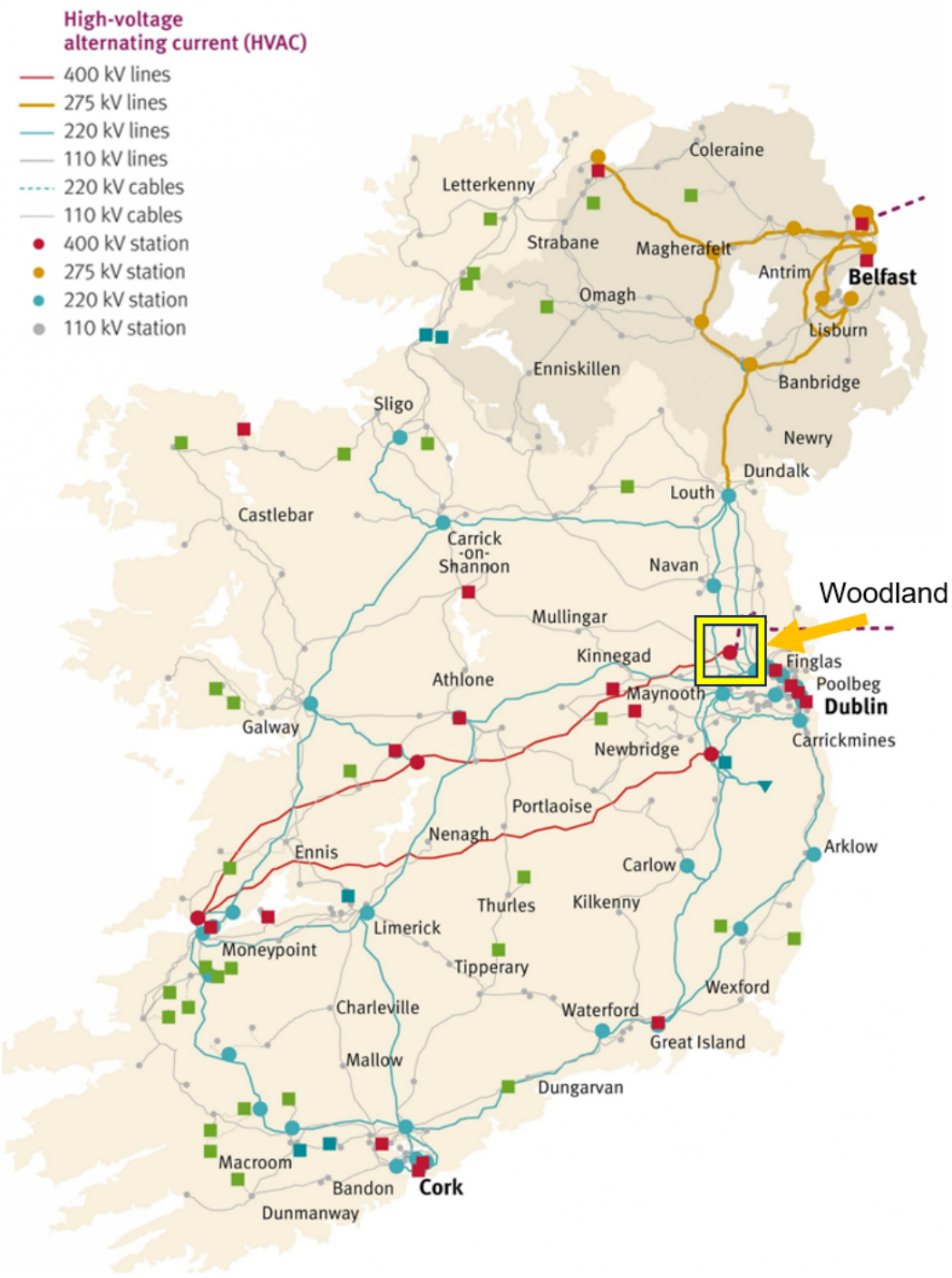

Figure 7.1: The Eirgrid Transmission system in 2021. The power lines are illustrated using red, gold, blue and grey lines to represent 400 kV, 275 kV, 220 kV and 110 kV lines respectively. The main stations are marked by circles. The green, red and blue squares and blue triangles denote areas of power generation. The Woodland measurement site is highlighted within a yellow box.

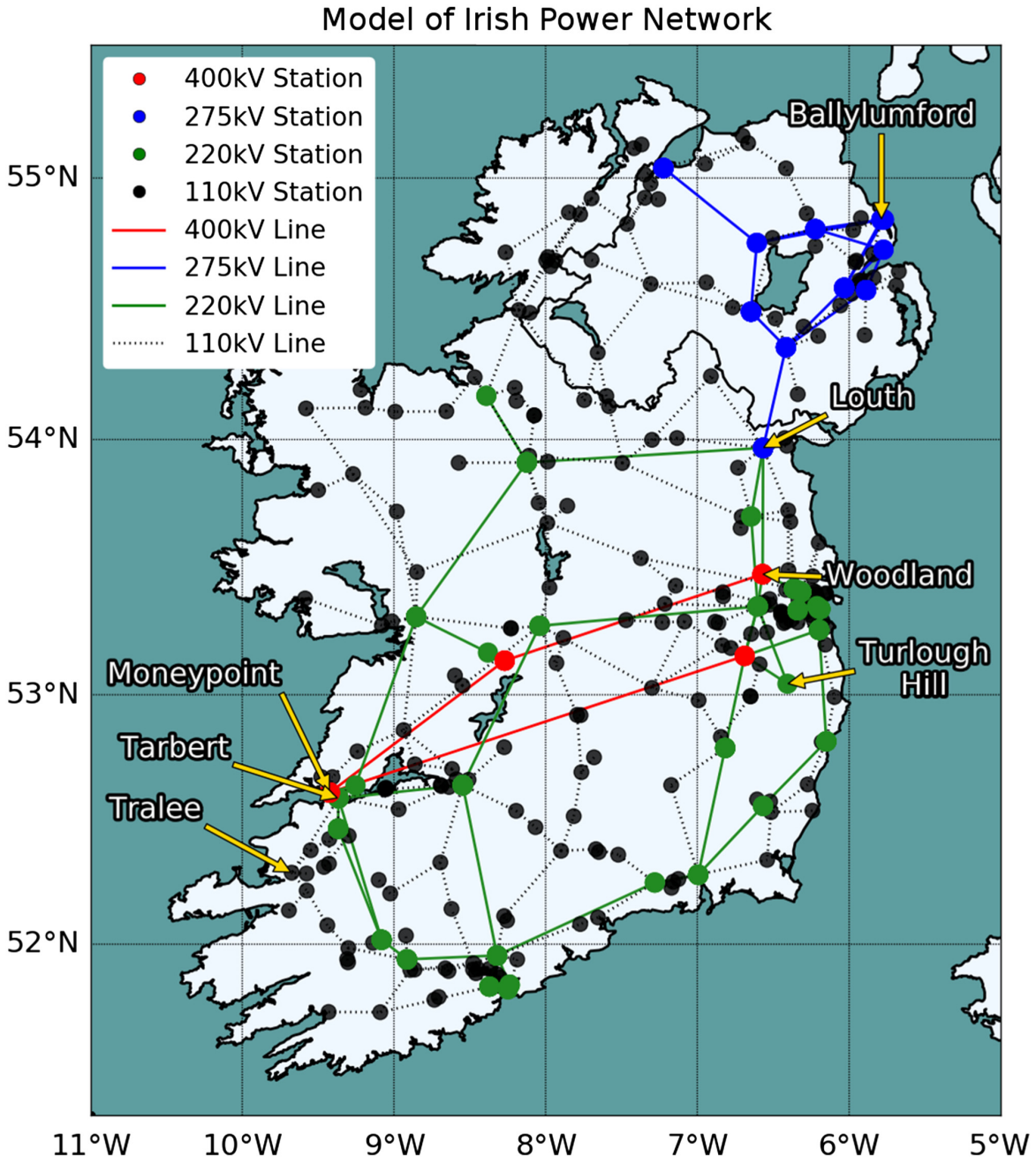

Figure 7.2: The model of the Irish power grid produced by Blake et al. (2018). Power grid transmission lines are denoted by the solid and dotted lines, while dots indicate substation locations. Note the Woodland measuring site on the East coast, later used to validate the models.

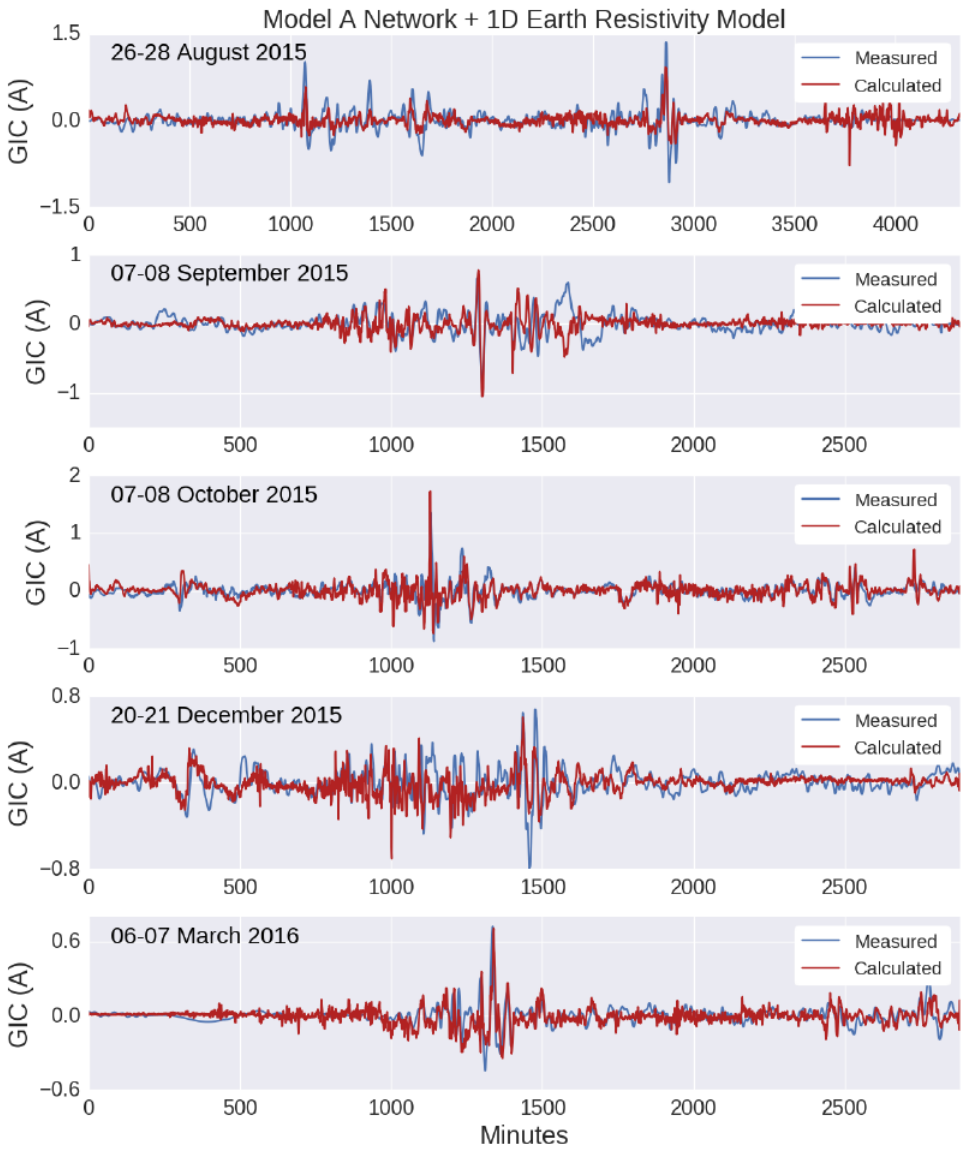

Figure 7.3: The modelled GIC from Blake (2017) compared to measurements at the Woodland transformer site (see Figure 7.2), for five different storms, using a 1D Earth conductivity model. Shape-wise, the signal matches well for all storms, but there is a notable difference in amplitude for some like the 26th – 28th August 2015.

ticularly underestimated the amplitude of 26 – 28 August 2015 (Kp = 6), which they suggest may relate to rainfall briefly increasing ground conductivity, but retained the coherence or shape of the signal (see Figure 7.3). Though this is only a hypothesis, similar increases have also been observed related to changes in the configuration of power networks, e.g., the removal of a substation from the network for maintenance for example (Bailey et al., 2017; Mac Manus et al., 2022).

7.3 3D Transfer Function Input Model

The main update to the Blake et al. (2016) model is the introduction of a 3D information about the subsurface. The aforementioned 3D transfer function interpolation

Date	Max K-Value	1D	3D	3Dgal
26 – 28/08/2015	5	0.54	0.74	0.74
07 – 08/09/2015	6	0.21	0.33	0.38
07 – 08/10/2015	6	0.62	0.64	0.64
20 – 21/12/2015	5	0.40	0.60	0.65
06 – 07/03/2016	6	0.71	0.82	0.84

Table 7.1: The coherence between measured GIC time series compared to the 3D models analysed here, the 1D, 3D and 3D galvanic. This validation is done for five test storms at the Woodland monitoring site between 2015 – 2016. 07 – 08/09/2015 appeared to be a noisier storm, with best coherence achieved for the 06 – 07/03/2016 storm.

approach (Section 5.2.3) was used here. The estimate for the ground resistance range was reevaluated (explained in Section 7.3.2) for each separate model (1D, 3D and 3Dgal, where 3D is a galvanic corrected model, 3Dgal is galvanic non-corrected).

7.3.1 Initial Validation

The five storms analysed by Blake et al. (2018) were re-used for the validation of the 3D model relative to the 1D at the Woodland GIC station (see Table 7.1, Figure 7.1), alongside the new 3D and 3Dgal models, as unfortunately no new GIC data has been recorded since. These were the largest storms between 2015 – 2016, with data relatively unaffected by noise. In general, the amplitude was underestimated, which I believe is partly due to the assumption of the ground resistance value. For this reason, when re-validating the 1D GIC model alongside the new 3D models, coherence was used as the main metric to compare between models, as it is independent of amplitude differences and focuses on the shape or sinusoids in the signal. Hence, amplitude biases due to the ground resistance estimate will be avoided. The coherence of the time series was estimated during only storm time (local $K > 4$) conditions, as the geomagnetic field is most accurately represented only during these storms times (demonstrated in Section 4.2.2), and hence a similar trend is observed in the geoelectric field and GIC.

The 3D and 3Dgal models, compared to the 1D model (Table 7.1), exhibit a large increase in coherence, demonstrating that the two models better replicate the variation in signal (example in Figure 7.4). There is some variance between separate storms, in terms of coherence which mostly relates to noise in the data, but also somewhat relates to strength and duration of the peak during the storm, i.e., impulsive moments not captured well.

7.3.2 Calibrating the Ground Resistance

The ground resistance of the 1D GIC model of (Blake, 2017) was estimated by comparing the amplitude of the 1D geoelectric field to the measured GIC, setting an ap-

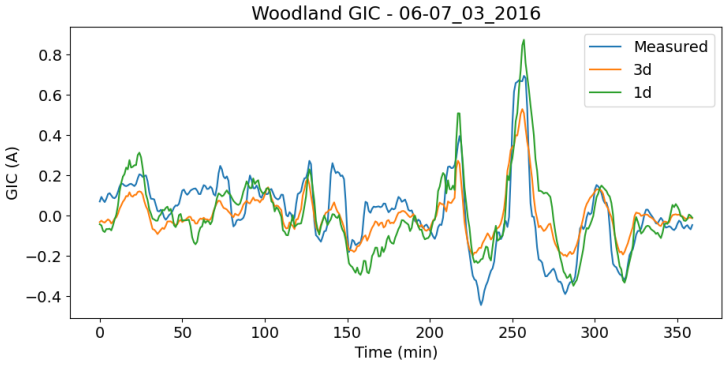

Figure 7.4: A comparison between the modelled geoelectric field for the 1D, 3D and measurements at the Woodland transformer station before calibration (ground resistance = 1 Ω). The 1D model matches the amplitude of the signal better than the 3D model, however the 3D model is more coherent.

propriate estimate for the ground resistance at transformer sites to be 1 Ω. Ground measurements only exist at a few separate transformer sites (Figure 7.5), which worked well with the previous model (Blake, 2017). For the 3D model however, setting a resistance of 1Ω consistently underestimates the GIC. Instead of estimating the ground resistance, I attempted to use a ground resistivity survey, with shallow electromagnetic geophysical data, as a proxy.

Testing Ground Resistance with Resistivity Maps

The possibility of using ground resistivities as proxies for ground resistances was investigated, using data from the Tellus electromagnetic survey (Figure 7.6). Tellus was a survey undertaken by Geological Survey Ireland to gather geophysical and geochemical data across the island (`https://www.gsi.ie/en-ie/programmes-and-projects/tellus/Pages/default.aspx`). High spatial resolution electromagnetic data (at 12 kHz and 3 kHz) was collected by Tellus using an airborne survey. As mentioned in the MT section when discussing complex skin depth (Section 2.3), EM waves will only propagate to a specific depth based on the frequency of the signal. The TELLUS survey used these very high frequency signals specifically to map the resistivity of the near-surface. If we input our higher frequency signal, 12 kHz, into the skin depth formula (Equation 2.35), we can derive the depth to which this signal should propagate (in metres):

$$\delta = 503\sqrt{1.4 \times 10^{-4}\rho} \tag{7.1}$$

The resistivity lies between the range (10 – 1,000 Ωm), an appropriate range for the near-surface (IEEE, 2015) Assuming the resistivity profile to be homogeneous, the range of depths derived is approximately 20 – 175 m (Equation 7.1). In reality, the resistivity profile is not homogeneous with depth, with it almost always less resistive

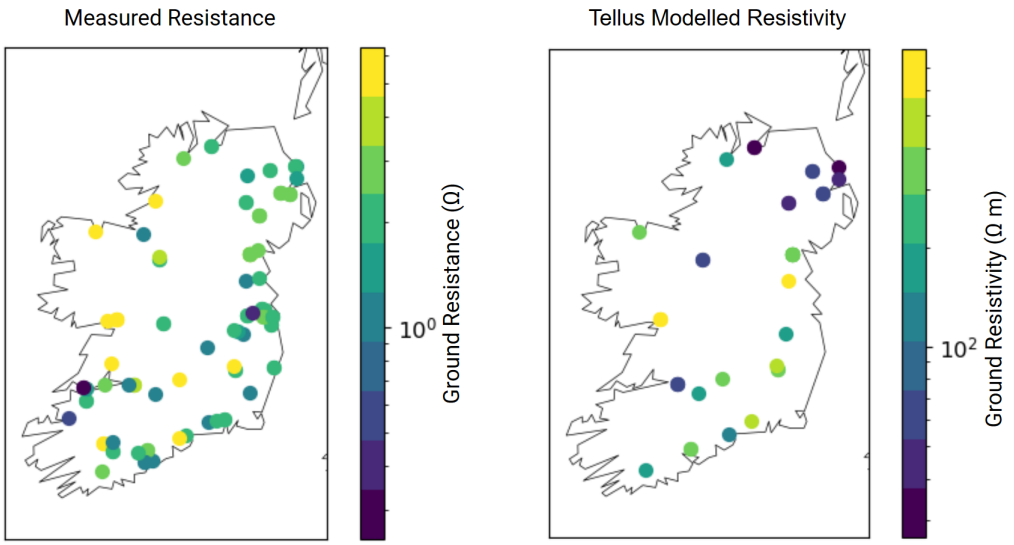

Figure 7.5: (left) The measured ground resistances at transformer sites. (right) The measured ground resistivity for the Tellus survey at the same transformer sites. Note that if there was no corresponding resistivity measurement available to the resistance measurement on the left, no value was included in the plot. This is due to these areas being transformer sites near towns, which were blind spots for the survey.

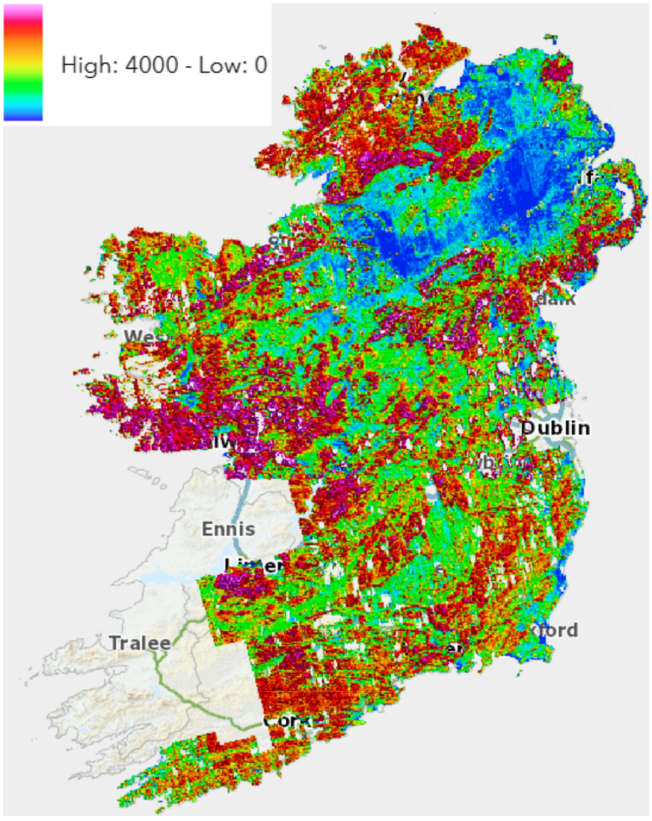

Figure 7.6: The Tellus electromagnetic survey map for 12 kHz. The colours represent the resistivity estimated at each location (in Ω m). Some areas in Ireland were not included in this survey, and no colour has been plotted for these regions. Some distinct regions of low resistivity exist, such as in the North-East, as well as high resistivity in Galway and Donegal in the West.

at the surface (due to less resistive soil near the surface, then more resistive rock at depth). Other factors such as flight altitude becomes a factor, so this maximum depth the signal propagates to is likely to be less, at maximum depth of approximately 50 m (Beamish, 2004). The capability of using this resistivity as a proxy for the resistance at each transformer station was tested, with the desire of obtaining a better proxy than the estimate of 1Ω, as while resistivity and ground resistance are not exactly the same, they can be correlated. Large scale resistivity mapping has been carried out in a variety of other countries monitoring GIC (Ley-Cooper et al., 2020; Steuer et al., 2020; Delsman et al., 2018, for Australia, Germany and the Netherlands respectively) and thus could be useful not only in the case of Ireland but also in these regions as well.

To test the potential usefulness of the Tellus data, we compared the resistance measured by Eirgid at transformer stations, to the resistivity predicted at the same locations by the Tellus model, to see if there was a correlation, at locations where a Tellus measurement was taken. Unfortunately, in most cases, the sites of transformers were generally in more built-up areas like towns. These were blind spots for the electromagnetic survey, as towns are "no-fly" zones for low altitudes (< 200m). As a result, most resistance measurements could not be compared to resistivity measurements. This led to a statistically insignificant amount of data left for comparison with a total of 15 data points (Figure 7.5). A brief baseline test was performed to see if the correlation was statistically significant. Fifteen random points were generated in a model with the correlation between each calculated. This model was iterated one-hundred times, with a maximum correlation of 0.67, compared to 0.45 here. Hence, while a slight correlation was observed (Figure 7.7), there was simply too little data from which to draw any conclusions. Therefore, another method was used to estimate the ground resistance.

Estimating the Ground Impedance

As the grounding impedance could not be accurately estimated using resistivity data, we instead estimate this using comparisons between measured and modelled geoelectric fields. The 1 Ω estimate by Blake (2017) is higher than the resistance setting used in GIC from other countries with 1 Ω usually being the upper limit used, with values most often estimated between 0.05 – 1Ω used (Torta et al., 2014; Myllys et al., 2014; Hübert et al., 2020; Divett et al., 2018; Alves Ribeiro et al., 2023). Hence this parameter was re-calibrated.

The performance score (Equation 5.18) was used to calibrate the resistance setting of the model, in a similar manner to calibrating the nowcast geoelectric field model in Section 5.5 and the Spanish GIC model by Torta et al. (2017). The performance score was calculated between bins and then averaged within the range approximately 0.01 – 10 Ω, with the maximum score recorded (Figure 7.8) . This was then repeated for each of the validation storms in Table 7.4.

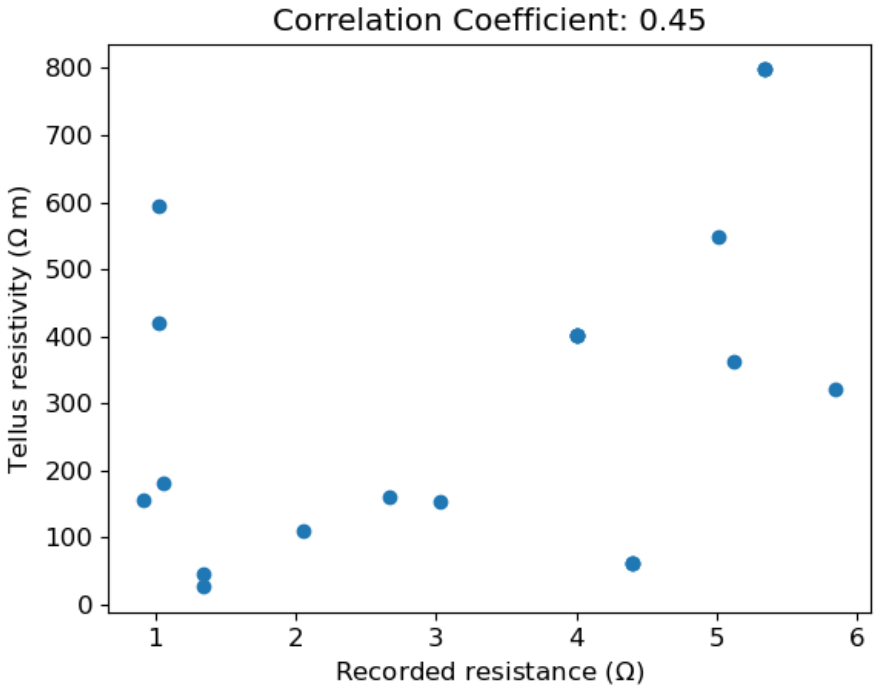

Figure 7.7: The measured ground resistances from Figure 7.5 are plotted against the corresponding ground resistances. The correlation coefficient between the data is 0.45.

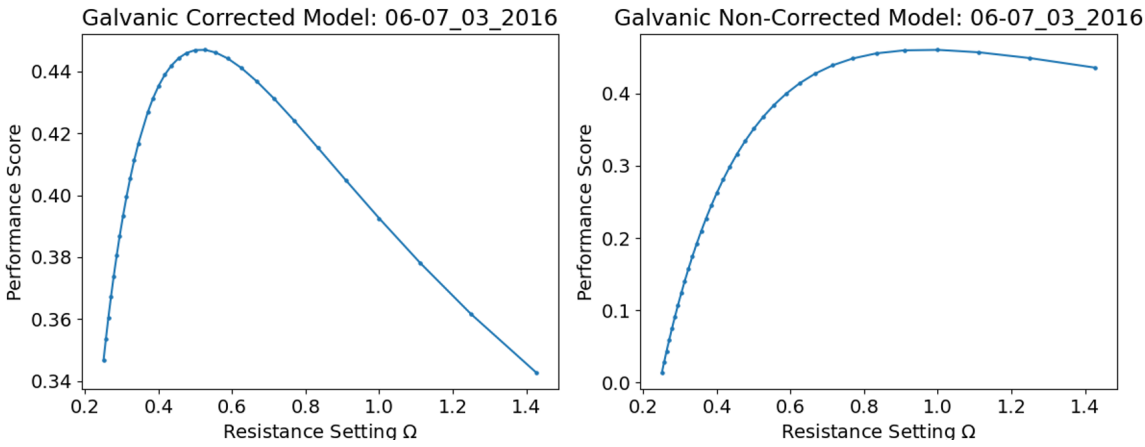

Figure 7.8: An example of the performance score using different settings for the estimated ground resistance at transformers for the 06 – 07/03/2016 geomagnetic storm for the corrected (left) and non-corrected models (right).

Storm	Max Performance	Resistance (Ω)
26 – 28/08/2015	0.30	0.05
07 – 08/09/2015	0.06	0.7
07 – 08/10/2015	0.26	0.5
20 – 21/12/2015	0.20	0.5
06 – 07/03/2015	0.44	0.5

Table 7.2: The maximum performance achieved for varying settings of the resistance, for the 3D model

Storm	Max Performance	Resistance (Ω)
26 – 28/08/2015	0.26	0.07
07 – 08/09/2015	0.07	1.1
07 – 08/10/2015	0.23	0.6
20 – 21/12/2015	0.23	0.7
06 – 07/03/2015	0.46	0.9

Table 7.3: The maximum performance achieved for varying settings of the resistance, for the 3Dgal model.

An example of the separate performance scores for different ground resistance settings is presented in Figure 7.8. The expected improvement when the resistance setting is decreased slightly is observed, for this storm peaking around 0.5 Ω for the galvanic corrected model and 0.9 Ω for the galvanic non-corrected model. The shape of the curve is also important with the decrease in performance below the peak settings (0.5 Ω, 0.9 Ω) is sharper than the decrease above these settings, demonstrating the quasi-logarithmic dependence. Hence, the logarithmic mean is used to estimate an average as opposed to the standard mean here for calculation of a standard value to accept for later modelling.

A few conclusions can be gathered from Tables 7.1, 7.2 and 7.3:

1. The 3D models perform on roughly the same level to each other, with no clear indicator to suggest that one model performs better than the other at this validation site.

2. The previously used ground resistance of 1 Ω works well for the old 1D model, but is demonstrated to be sub-optimal and should be lowered for the 3D models.

3. When considering some of the outliers the resistance seems variable. In particular for the storm of 26th – 28th August 2015, the ideal resistance is much lower for all models.

4. The resistance setting is generally lower for the 3D than the 3Dgal model.

The storm of the 26th – 28th August 2015 is the major outlier in terms of resistance. The coherence between measurements and modelled GIC matches very well but the

amplitude is quite different, which suggests that geomagnetic variations were driving the GIC and not unrelated noise, but something was amplifying the signal. Blake et al. (2018) hypothesised that it could have been due rainfall, as significant rainfall fell before the storm of 26th – 28th August 2015 ($>$ 50 mm for the three days before the storm). However, other studies also point to changes in power network configuration changing GIC amplitude significantly (as mentioned in Section 7.2.1). If it is assumed that this discrepancy is due to rainfall or a configuration change in the network or both, then the 0.05 Ω expected in Table 7.2 may be physical as opposed to a random outlier. Overall, based on the results we take 0.7 Ω for standard conditions, but also consider a potentially more severe case with lower resistance, if an increase due to large rainfall or network change occurs. The same resistance was chosen for both models (despite not being ideal for either), to directly compare estimates between each model across the grid. While a factor difference might exist at the validation site, this may not be true for the entire power grid. Hence more validation sites are required.

7.4 Expected 35 year GIC extremes

After calibrating the model, the GIC time series for all of the largest storms, between Kp = 8 and Kp = 9, were analysed to determine peak returns of GIC for each between 1991 – 2023. The famous March 1989 geomagnetic storm responsible for the Quebec power outage was also included for analysis as data for each of the geomagnetic observatories was present for this event. For most of these, events with weak GIC ($<$ 10 A) were predicted. Hence, this analysis focused only on larger storms, listed in Table 7.4. As most of these events were between Kp = 8, 9, the local dH/dt at Valentia observatory was used as a proxy to quantify magnetic field strength between each storm. Duration of time with currents above 10 A at transformers was also recorded for more context to examine not only the peak, but to give a proxy for the total time over which the transformers remained saturated. When transformers become saturated they become more prone to damage (see Section 6.4.1 which explains the use of $>$ 10 A as a proxy for saturation in transformers in more detail).

A few observations can be made from Table 7.4:

1. Generally the galvanic non-corrected model amplitude slightly exceeds the corrected model in terms of amplitude and duration of time $>$ 10 A;

2. The November, 1991 is only the fifth largest storm in terms of dH/dt amplitude, but the largest GIC is predicted for this event, demonstrating why additional context alongside magnetic field variations is required to estimate the GIC amplitude. In terms of duration, the Halloween storm, 2003 exceeded the 10 A GIC threshold for the longest time span, while the March, 1989 storm is a close second in terms of both total GIC amplitude and duration. The 20 – 22/11/2003 geo-

Date	dH/dt (nT/min)	3D Max	3Dgal Max	3D Time	3Dgal Time
09 – 11/03/1989	253	97 A	74 A	128 min	153 min
23 – 24/03/1991	95	18 A	17 A	21 min	24 min
29 – 31/10/1991	23	13 A	12 A	11 min	5 min
09 – 10/05/1992	51	10 A	11 A	1 min	7 min
08 – 10/11/1991	197	105 A	120 A	51 min	61 min
26 – 27/08/1998	19	11 A	11 A	1 min	4 min
06 – 07/04/2000	71	29 A	33 A	15 min	19 min
14 – 16/07/2000	91	31 A	36 A	53 min	61 min
17 – 18/09/2000	48	17 A	20 A	9 min	11 min
30 – 31/03/2001	61	15 A	18 A	10 min	16 min
11 – 12/04/2001	54	24 A	27 A	14 min	17 min
05 – 06/11/2001	48	25 A	28 A	18 min	20 min
23 – 25/11/2001	42	17 A	19 A	15 min	18 min
29 – 30/05/2003	31	19 A	21 A	12 min	15 min
29 – 31/10/2003	169	75 A	81 A	153 min	181 min
20 – 22/11/2003	265	31 A	35 A	53 min	64 min
25 – 28/07/2004	67	16 A	18 A	11 min	16 min
07 – 10/11/2004	85	16 A	22 A	37 min	50 min
14 – 15/05/2005	45	16 A	17 A	14 min	14 min
17 – 18/03/2015	42	14 A	15 A	6 min	7 min
22 – 23/06/2015	68	11 A	13 A	3 min	6 min
07 – 08/09/2017	57	14 A	16 A	4 min	6 min
23 – 24/04/2023	35	17 A	19 A	2 min	3 min
11 – 12/05/2024	109	73 A	82 A	79 min	94 min

Table 7.4: The storms for which maximum GIC at an individual transformer were estimated for the model between 01 January 1991 – 13 May 2024, where a GIC in excess of 10 A for the 3D models was predicted (including the March, 1989 geomagnetic storm for comparison). The dH/dt at Valentia observatory is shown in the second column. The maximum GIC was estimated at the same site for every storm, Moneypoint, in the South-West (Figure 7.2) in the middle columns while the length of time where 10 A is exceeded is recorded for both models in the two right columns (3D and 3Dgal). Note that results for the 11 – 12/05/2024 storm are provisional.

.

magnetic storm is another good example of this, the highest dH/dt is recorded for this event due to a strong impulsive SSC, but a lack of longer period magnetic field variations leads to a relatively weak GIC;

3. The largest density of storms exceeding 10 A occurred between 1996 – 2008, two solar cycles ago, with only three storms in the last solar cycle (2008 – 2019) exceeding this mark, demonstrating how weak the last solar cycle was in comparison. Currently, two storms from the current cycle have exceeded this threshold.: April, 2023 and May, 2024.

The maximum amplitudes and durations are only for the Moneypoint site, the largest power station on the South-West of the island (see Figure 7.2). This station always peaks compared to other substations across the grid, irrespective of the storms analysed here. Hence, a ratio map between the models is then created to evaluate how the models compare across the entire grid. This including comparison to the old 1D model including both maximum amplitude and coherence of the time series, in Figures 7.9, 7.10, 7.11. The main points from these figures are that across the grid, the 1D and 3D models are completely different. This differences are largest in the South of the island in terms of coherence. The 1D model predicts largew GIC across most of the island, while the 3D models predict them to be more localised, confined mostly to the Eastern coast and South-West of the island. The impact of correcting for galvanic distortion is noticeable but the differences are significantly smaller than observed between results based on 1D or 3D Earth. The largest differences are observed in the East coast.

7.5 Discussion

7.5.1 Comparison Between 1D and 3D Models

Overall, the difference between the 1D and 3D models is stark. A general reduction in the GIC is observed across most regions. In terms of coherence, with the exception of some sites in the Midlands and the East, the time series change dramatically also. As a whole the hazard maps in the previous chapter demonstrate how the geoelectric field is very directional and hence we see the effect on the modelled geoelectric field. While in some less geologically complex regions, a 1D model may suffice, this is not the case for Ireland. In these Eastern/Midland regions, the weakest geoelectric field was generally observed. The validation site in Woodland on the East happens to be one of these sites (see Figure 7.2 for location). Thus when validating the previous 1D model using only one site from Blake (2017) the model appeared to work well. For all we know this may be the case for the 3D models as well when compared to measurements. Hence, more measurements of GIC at other sites are essential to ensure the model actually replicates the GIC. However, the 3D model does significantly improve in terms of performance metrics compared to the 1D models (Tables 7.1, 7.2, 7.3). Now that the model has been

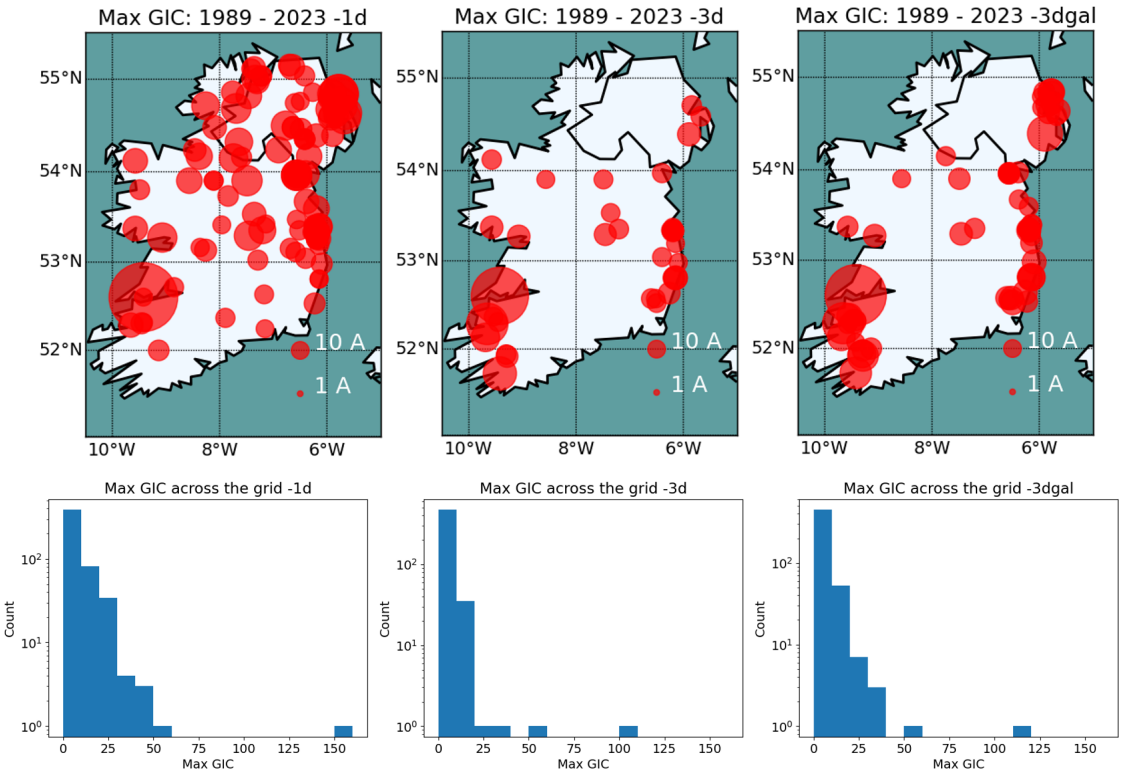

Figure 7.9: (top) The largest expected GIC using the 1D, 3D and 3D galvanic models between 1989 – 2023 for the transformer sites with the largest GIC. Only sites where 10 A is exceeded are included. The 1D model expects large GICs in most regions, while the 3D models expect the GIC to be more localised to the South-West and Eastern coast. (bottom) A histogram of the largest GIC for 1D, 3D and 3Dgal models from the map.

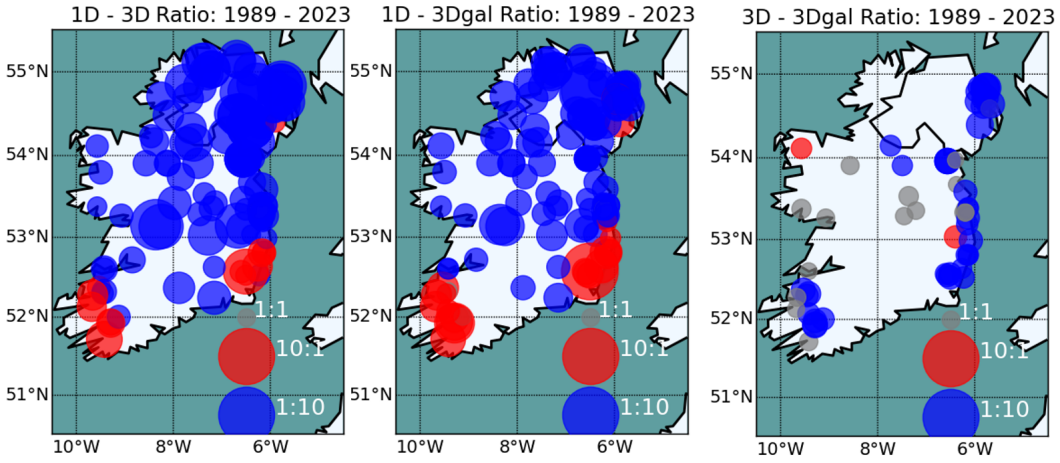

Figure 7.10: The ratio (R) between the largest expected GICs using the 1D, 3D and 3D galvanic models between 1989 – 2023 for the transformer sites with the largest GIC. Red signifies an increase, blue a decrease, with grey indicating a negligible change ($0.80 < R < 1.25$). Relatively little change is present between the galvanic and non-galvanic models, with the North-East most affected. A significant difference exists between the 1D and both 3D models.

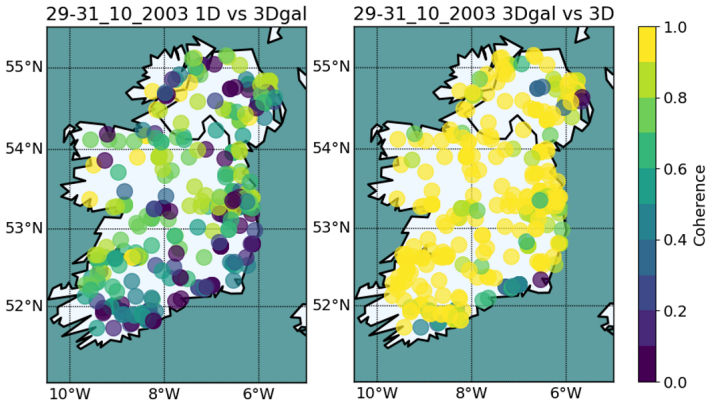

Figure 7.11: A comparison of the coherence between a model 1D and a 3D galvanic corrected and non-corrected time series for the Halloween storm, 2003 across all transformer sites. The 1D and 3D models disagreee significantly across the grid, while the 3D models mostly agree, with the exception of a few locations. The same pattern is observed for other storms in Table 7.4.

created, the areas where the largest GICs are likely are known and hence measurements should be taken. The 3D models predict the GICs to be localised mostly to the Eastern coast, North-East and South-West as opposed to the 1D prediction of the whole island. Installing validation sites in these areas, as well as a control site in an area predicted to have very weak GIC would be the ideal method of truly validating the model.

7.5.2 Galvanic Vs. Non-Galvanic Input

In contrast to the large variation between the 1D and 3D models, a minor difference is observed in the modelled GIC when correction for galvanic distortion is considered or not. In terms of the maximum amplitude, the ratio between the two models is mostly confined within a factor of 0.5 – 2 (Figure 7.10), with a strong coherence between the time series for most of the island (Figure 7.11). The main difference in the maximum GIC along the east coast can be explained using the geoelectric field hazard maps from Chapter 6. A large North – South geoelectric field is expected using the galvanic non-corrected geoelectric field model along the eastern coast, but not using the galvanic corrected model (Figure 7.12). The power lines along here are N – S aligned too, thus a larger effect can be expected. Given that the galvanic distortion appears to align along the coast, it may prove that using a galvanic non-corrected model is more accurate than a corrected model, but this fact would need to be validated. In terms of the performance metrics at the single validation site at Woodland (Tables 7.1 7.2, 7.3) the galvanic corrected and galvanic non-corrected model perform to the same level, hence no conclusions can be drawn as of yet. More measurement sites are required to evaluate which model performs better. In terms of coherence, the biggest difference is seen along coastlines. Most likely it is due to galvanic distortions occurring more commonly along coastlines (Chave and Jones, 2012). Measured GIC could be used to confirm this, with prime candidate sites being the poorest matched sites in the North-east near Belfast

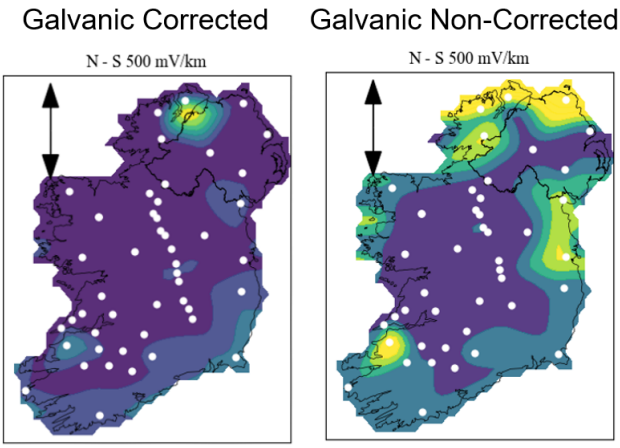

Figure 7.12: A comparison of the hazard maps N – S component for the galvanic corrected (left) and non-corrected (right) models. The exceeded region on the east coast in the non-corrected model explains the increase in modelled GICs in Figure 7.10.

and the South-East near Wexford (coherence $\approx 0.1 - 0.4$).

7.5.3 Possibility of Variable Ground Resistance

The low grounding resistance value for the storm of 26th – 28th August 2015 storm is unusual. Given that the time series are so coherent in Table 7.1, with a relatively high performance (Tables 7.2 and 7.3) for the storm, it is unlikely that the larger values were due to noise, but more likely that the signal was being amplified somehow. A change in grounding resistance, or a network configuration change could cause this. Resistance changes could be explained by some soil chemistry: the number of charge carriers increases in the soil with rainfall, as water soluble salts/minerals dissolve, increasing the number of ions in the soil (Wagner et al., 2006; Card et al., 2023). Factors such as temperature can significantly affect soil conductivity (Miller et al., 1988) and may also need to be considered. Blake et al. (2018) noted that the 26th – 28th August 2015 geomagnetic storm occurred during a period of heavy rainfall ($>$ 50 mm over three days) and soil saturation and hypothesised that this rainfall could be to blame. Given that the majority of the Irish power grid runs along the coastlines, where the quantity of salts in soil is enhanced, this hypothesis may hold and explain why such a large difference is observed. A worst resistance case map (Figure 7.13), with the ground resistance of each unknown transformer set to 0.05 Ω (in reality the "known" transformers would also change in this scenario, but these values are left the same for simplicity here). The maximum GIC at the Moneypoint station remains roughly the same, however across the island a large increase is observed, particularly in the peak regions of the South-West and Eastern coast. Evidence of this soil moisture affected GIC is observed by Kazerooni et al. (2017); Blake et al. (2018); Divett et al. (2018). Another possibility is it could be somehow related to changes in the configuration of the power network during this geomagnetic storm. Often, power grids change with

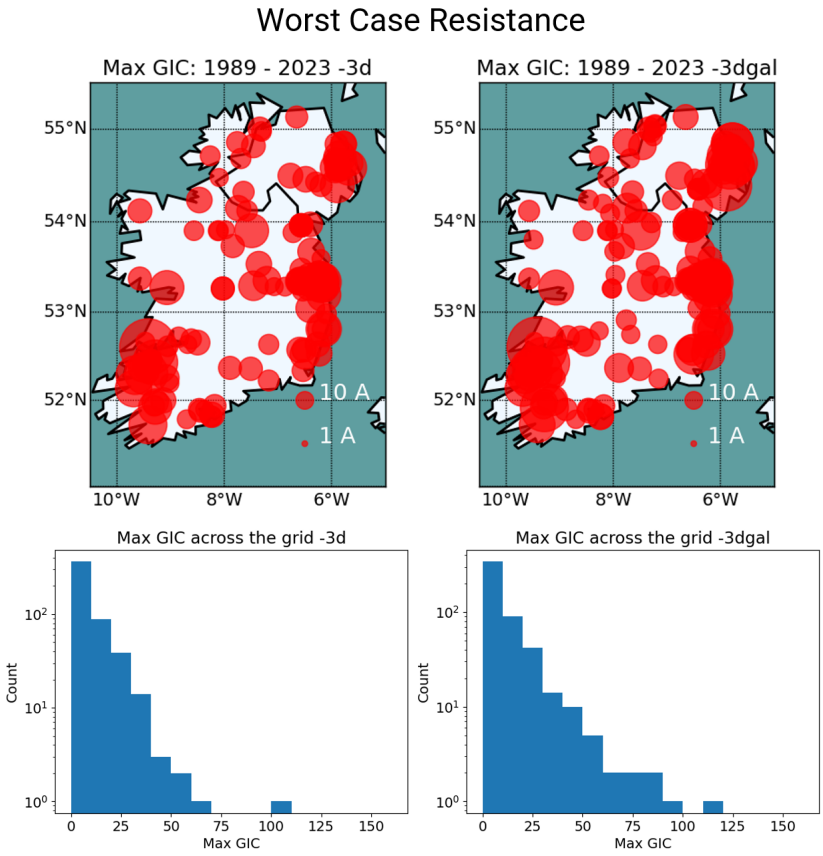

Figure 7.13: (top) The expected 35 year extreme mapped across all transformer locations assuming a worst case resistance value of 0.05 Ω for unknown sites. (bottom). A histogram of the maximum GIC at each transformer.

transformers grounded within a power grid. This can lead to offset GIC entering nearby transformers instead, enhancing GIC amplitude. Thus a study with measured ground resistances and information on grounded transformer during geomagnetic storms could be used to deduce whether this case is a simple change in network configuration, or if a change in the grounding resistance due to rainfall is to blame.

7.6 Summary

1. The 3D and 3Dgal models were validated and showed improvement to the previous 1D model. Comparisons between the 3D models and 1D models show that GIC in Ireland are strongly affected by the directionality of the geoelectrical structures of the subsurface

2. Galvanic distortion is shown to have an effect on modelled GIC. Whether it improves or worsens the model as a whole still must be investigated. For the one measurement site available, they perform at approximately the same level. New measurement sites would help demonstrate which model performs.

3. A maximum GIC of 105 A or 120 A was predicted by the 3D and 3Dgal models respectively (Table 7.9) for the November 1991 storm, with a maximum duration $>$ 10 A of 153 minutes or 181 minutes for the Halloween 2003 storm. This amplitude and duration of induction is significant enough that damage could have been caused to the transformer.

4. Measurements should be made at the Moneypoint site which experiences this largest GIC by far, using all three models. Other measurements should also be taken at sites more affected along the Eastern coast and in the South-West to truly validate the model.

5. Future measurements of GIC should be compared to rainfall and/or soil moisture levels alongside power network reconfigurations during geomagnetic storms to assess the impact of heavy rainfall on measured GIC.

8 Conclusions

This project furthered research into the ground-based effects of space weather across the island of Ireland, which has been published in two papers, Malone-Leigh et al. (2023, 2024) detailed here between Chapter 4, 5 and 6. A paper on the last work chapter is currently in preparation. The magnetometer network was maintained, with a new magnetometer installed in the East of the Country at Dunsink. A geoelectric field model was designed to monitor disturbances in real time using MT stations from the SWEMDI network with magnetometer measurements using TF to convert between the two. Two separate sets of geoelectric field models were used, one with a set of galvanic corrected MT-TF and one with a set of non-corrected MT-TF. Longer term patterns (1991 – 2023) in the geoelectric field were then modelled to identify areas more susceptible to possible hazards. Finally, these two geoelectric field models were used as an input for a GIC model in the Irish power grid and used to identify the potential impact to the grid between 1989 -– 2023, and used it to predict a worse case scenario over the last 35 years.

8.1 MagIE

Overall, the maintenance and upgrades for the magnetometer network were a success but certainly were not without its challenges. Four magnetometers are now operational across the island. The MagIE website is now operational as well, which provides real-time data for the magnetometers, which has proven a success, with extra material now added including outreach. This network appears sufficiently dense to model magnetic fields across the entire island except for some more remote areas in the West and North-West of the island. Of all the challenges faced during the project, the reinstallation of the Birr magnetometer was certainly the toughest. The timing, at the start of the project, made it difficult (the start of the pandemic) as well as the fact that the equipment had to return to Ukraine for repair. Thus the magnetometer was not installed until 2023. However, in terms of the future of the network, due to its ideal location in the centre of Ireland in a quiet site, this magnetometer should especially be maintained. During the course of the four years of this research, two severe geomagnetic storms were recorded in April 2023 (Kp = 8+) and in May 2024 (Kp = 9) at the end

of the project. The continued operation of the network is necessary to record large storms across the island which can be used to validate the geomagnetic, geoelectric and GIC models.

8.2 Geoelectric Field Modelling

A geoelectric field model was successfully developed across Ireland for multiple purposes. Firstly, the model generated by Campanyà et al. (2019) was expanded to map geoelectric field variations. This included both the amplitude of the signal, but importantly, also the direction. The geoelectric field in Ireland was demonstrated to be highly directionally polarised, which is important as GIC induction in power-lines is dependent on both this amplitude and direction on the geoelectric field. The impact of using a galvanic distortion correction was also investigated. This work was amongst the first research addressing the inclusion of a corrected galvanic distortion in terms of space weather research. For the standard/nowcast models using a galvanic correction, a small decrease in the geoelectric field amplitude is present, with more homogeneity in the direction of the geoelectric field. Most likely a galvanic distortion correction will improve the model, provided the density of magnetometers is lower than the spatial scale of galvanic distortions, i.e. approximately 0.5 – 10km (Neukirch et al., 2020), however this must still be proved. The hazard map expanded on the standard and nowcast models. The hazard map divided the probability of exceeding a 500 mV/km threshold in specific directions between 1991 – 2019. The hazard map was used to demonstrate the directional dependence more effectively. In particular, the contrast between a galvanic distorted and non-distorted model could be observed. A significant difference between the two in terms of the direction of induction exists, which suggests that this could ultimately affect GIC modelling. A maximum geoelectric field of 3V/9V was expected for the 28 years for the corrected/non-corrected models at separate sites in the South-West of the island.

8.3 GIC Modelling

The previous GIC modelling from Blake (2017) was expanded to use 3D geoelectric field inputs as opposed to 1D. Both 3D models analysed, a galvanic corrected and non-corrected, perform better than the 1D model at the validation site in Woodland, with the two 3D models performing at the same level at this site. In terms of the network, using the 3D model predicts the induced GIC to completely change across the grid, demonstrated by modelled maximum values over 35 years compared at each transformer site and coherence between time series. The 1D model previously predicted significant GIC ($>$ 10 A) across most of the island. The 3D model simplifies this, with significant GIC only observed in more localised pockets, in the South-West and along

the Eastern coast. A relatively small change (ratio usually between 1 – 1.5 times) is observed between the galvanic corrected and non-corrected GIC models across Ireland. The biggest difference is observed along the eastern coast, relating to a driving N — S geoelectric field in the non-corrected model that is not present in the corrected. The max GIC using both models between 1989 – 2023 was also estimated with 105A/120 A respectively, expected for the November 1991 storm. The longest duration above a hazardous threshold ($>$ 10 A) was 153/181 minutes for the Halloween storm, 2003. No storms between 2006 – 2022 exceed this threshold demonstrating how relatively weak the last solar cycle, 24 was, compared to the prior cycle, 23. The Moneypoint transformer in the South-West was always the location of the largest GIC. It likely has the highest GIC, as it is the grounding point of the longest 400 kV power line, with a large geoelectric field along the western part of this line. A hypothetical worst case ground resistance was briefly investigated also, with a substantial increase, approximately by a factor of 2 or 3, observed across most of the grid. This could be a problem for the power-grid and further research should be carried out on the topic.

9 Future Work

The work in this thesis expanded the scientific instrumentation for MagIE, and knowledge of the ground-based effects of space weather across Ireland. Like most projects, while a large stride forward was taken regarding previous research during the four years, there is always more to do. Both improvements to existing work and expansion to new projects could be performed. An outline of the possible future work is explained in this chapter, related to improvements on existing work followed by new avenues and analyses that could be explored.

9.1 Monitoring Geomagnetic Fields

The main improvements to the monitoring of geomagnetic storms relate to the density of magnetometers and the raspberry pi magnetometer network. In Chapter 4, the performance of magnetic field interpolation across the network was analysed. The main conclusion from this was that the magnetic field is replicated well across most of the island, but most poorly in the very North-West and West of the island. Ideally, a new magnetometer should be installed in those areas to mitigate this, ideally away from sources of noise like large roads and towns. The DIAS/TCD Solar and Space Weather group already have a site in mind at Malin Head, Donegal. This site was previously tested successfully by Blake (2017) and thus would be most suitable for this installation. The continuing operation of the magnetometer network is also essential. While many of the models used have been validated for relatively weak storms, more validation related to large storms (i.e. Kp = 8, 9) is needed to confirm that the models perform similarly (or perhaps to a higher degree based on results from Sections 4.2.2 and 5.5.6), as we care most about induced currents during the largest events which are most hazardous. Larger substorms occur during large geomagnetic storms, which usually requires a greater density magnetometer sites to correctly capture the magnetic effects, as substorm enhancements generally lead to more localised magnetic variations (Partamies et al., 2011). Thus, the impact of large geomagnetic storms needs to be evaluated with the currently installed magnetometers.

A prototype of the raspberry pi magnetometer has been designed (Section 3.6), and

in the next few years six of these can be installed in schools. This will help the spatial resolution of the network as a whole. Ideally these will be installed in noise-free environments

9.2 Modelling Geoelectric Fields

The method of modelling and measuring the geoelectric field was an intermediate approach that bypassed the need for an underlying resistivity model, with some upsides including faster computation, and an ease in manipulating the models inputs, but also downsides such as a slight decrease in accuracy due to using the plane-wave approximation. After the completion of the HI-RES survey, more MT data will be available. All of these data, alongside previous survey data should be used to construct a full 3D conductivity model of the lithosphere, which could then be used to estimate the geoelectric field. A comparison between these two methods could be performed, to examine the relative impact on accuracy. The effect of galvanic distortion should be investigated further. The areas most affected by galvanic distortion have been identified here, but could be enhanced with data from the HI-RES survey, particularly in the East, and by adding new validation sites in key areas.

9.3 GIC Measuring and Modelling

The most significant limitation of this study was the lack of measured GIC to validate the model. The model here only had validation measurements at one transformer with max storm conditions of Kp = 6. Ideally, more measurements are needed, both for larger geomagnetic storms and at more substation/transformer sites. Measurements could be taken using the traditional method of using a Hall effect sensor directly on transformers. The alternative approach is to use the more non-invasive differential magnetometer method (Matandirotya et al., 2016; Hübert et al., 2020), which could be set up by installing pairs of magnetometers along sections of the power lines. The hazard maps and GIC models highlight areas where larger geoelectric fields and GIC are expected (the East coast, North-East and South-West), which would be best suited to these installations. Along the large 220 kV line from Moneypoint to Dublin for example would be very beneficial. Either way, given that solar maximum is fast approaching in 2025, with a likely geomagnetic maximum following this in 2026 – 2027 (see Section 2.1.5), the sooner these installations are completed the better.

During this validation of GIC, a comparison between geoelectric field models with and without galvanic distortions should be considered, to truly demonstrate whether one geoelectric field input model (corrected or non-corrected) outperforms the other, which we could not prove here. In addition, the effect of rainfall on ground conductivity

should be researched in more depth alongside GIC measurements. Evidence of rainfall increasing charge carriers and hence ground conductivity and GIC was presented in Blake et al. (2018). However this needs to be confirmed, as well as the degree of the effect. It may prove that rainfall or ground saturation measurements from Mét Éireann may also be needed to more accurately model the GIC for Ireland.

Thermal and outgassing reading can be used at a transformer site to determine if it is more affected by GIC. Thermal readings can be used to determine if the transformer overheats during geomagnetic storms, while outgassing measurements of oil used in transformers, can be used to determine if any damage was sustained after a geomagnetic storm (Koen and Gaunt, 2003). As well as this, Very-Low-Frequency (VLF) antenna measurements near transformer sites would be useful to determine when saturation occurs and could be used to monitor transformers in real time (Clilverd et al., 2020). The DIAS/TCD solar group already use these types of antennae to monitor the SFe at Dunsink and Birr, hence the expertise required to set up these antennae is already present within the group. The Moneypoint site in the South-West, which is most susceptible to GIC, would be the best site for these measurements.

9.4 Historical Analysis

Some historical analysis into the geomagnetic field has been researched by Fogg et al. (2023), to determine patterns in the geomagnetic field peaks, for example timing of extreme peaks and the phase of the storm (i.e. sudden commencements, main phase or substorm phase) and relevant driving mechanism. A similar analysis could be applied to geoelectric fields and GIC. This type of analysis has been explored in other countries (Love et al., 2022) and could be applied to Ireland, with some preliminary analysis by Blake (2017) used as a basis for the study.

9.5 Forecasting

A geoelectric field and GIC system forecast system could be used to predict extreme geoelectric fields and GIC during geomagnetic storms. Many others have tried to predict time series, however the utility of these is physically limited by lack of spacecraft measuring solar wind, to approximately an hour before real time (Bailey et al., 2022; Madsen et al., 2022). Power grid operators need longer than this to effectively prepare for a geomagnetic event. Hence, prediction of likelihood or conditions over longer time scales is thus preferable at this moment in time.

A version of the geoelectric field hazard map could already be used as a benchmark model to predict geoelectric field conditions using predicted Kp values as its input. As

discussed in Chapter 6, the hazard mapping model is currently not ideal for forecasting however. Seasonal and diurnal variations need to be accounted for, and at latitudes around 50° like Ireland, even long-term changes (over decades) in the geomagnetic field itself may need to be considered. Forecasting could benefit from historical analysis in this sense, both for seasonal and long term trends. The inclusion of solar wind conditions as an input should be investigated as it drives magnetic field variations. The time within the solar cycle may be useful input to analyse as well. A machine learning model could be employed to generate this prediction. If successful, this could be automated to send alerts to power grid operators about potential impact to the grid, perhaps days in advance to give them time to prepare for the event, alongside information on substations/transformers at most risk.

Bibliography

Alken, P., Thébault, E., Beggan, C. D., Amit, H., Aubert, J., Baerenzung, J., Bondar, T., Brown, W., Califf, S., Chambodut, A., et al. (2021). International geomagnetic reference field: the thirteenth generation. *Earth, Planets and Space*, 73(1):1–25.

Alves Ribeiro, J., Pinheiro, F. J. G., and Pais, M. A. (2021). First estimations of geomagnetically induced currents in the south of portugal. *Space Weather*, 19(1):e2020SW002546.

Alves Ribeiro, J., Pinheiro, F. J. G., Pais, M. A., Santos, R., Cardoso, J., Baltazar-Soares, P., and Monteiro Santos, F. A. (2023). Toward more accurate gic estimations in the portuguese power network. *Space Weather*, 21(6):e2022SW003397.

Amm, O. (1997). Ionospheric Elementary Current Systems in Spherical Coordinates and Their Application. *Journal of geomagnetism and geoelectricity*, 49:947–955.

Amm, O. and Viljanen, A. (1998). Ionospheric disturbance magnetic field continuation from the ground to the ionosphere using spherical elementary current systems. *Earth, Planets and Space*, 51(6):431–440.

Anderson, D. L. (1995). Lithosphere, asthenosphere, and perisphere. *Reviews of Geophysics*, 33(1):125–149.

Axford, W. I. and Hines, C. O. (1961). A unifying theory of high-latitude geophysical phenomena and geomagnetic storms. *Canadian Journal of Physics*, 39(10):1433–1464.

Bahr, K. (1987). Interpretation of the magnetotelluric impedance tensor: Regional induction and local telluric distortion. *Journal of Geophysical Research*, 62:119–127.

Bailey, R. L., Halbedl, T. S., Schattauer, I., Römer, A., Achleitner, G., Beggan, C. D., Wesztergom, V., Egli, R., and Leonhardt, R. (2017). Modelling geomagnetically induced currents in midlatitude central europe using a thin-sheet approach. *Annales Geophysicae*, 35(3):751–761.

Bailey, R. L., Leonhardt, R., Möstl, C., Beggan, C., Reiss, M. A., Bhaskar, A., and Weiss, A. J. (2022). Forecasting GICs and geoelectric fields from solar wind data using LSTMs: Application in austria. *Space Weather*, 20(3).

Bakker, J., A. K., Samrock, F., Geraskin, A., and Pankratov, O. (2015). Introducing inter-site phase tensors to suppress galvanic distortion in the telluric method. *Earth, Planets and Space*, 67:160.

Barlow, W. (1849). On the spontaneous electrical currents observed in the wires of the electric telegraph. *Phil. Trans. R. Soc.*, page 13961–72.

Bartels, J., Heck, N. H., and Johnston, H. F. (1939). The three-hour-range index measuring geomagnetic activity. *Terrestrial Magnetism and Atmospheric Electricity*, 44(4):411–454.

Baumjohann, W. and Treumann, R. A. (1996). *Basic space plasma physics*. Imperial College Press.

Beamish, D. (2004). Airborne em skin depths. *Geophysical Prospecting*, 52(5):439–449.

Beggan, C., Richardson, G., Baillie, O., Hubert, J., and Thompson, A. (2021). Geoelectric field measurement, modelling and validation during geomagnetic storms in the UK. *Journal of Space Weather Space Climate*, 11(37).

Beggan, C. D., Beamish, D., Richards, A., Kelly, G. S., and P. Thomson, A. W. (2013). Prediction of extreme geomagnetically induced currents in the uk high-voltage network. *Space Weather*, 11(7):407–419.

Beggan, C. D. and Marple, S. R. (2018). Building a raspberry pi school magnetometer network in the uk. *Geoscience Communication*, 1(1):25–34.

Biermann, L. (1951). Kometenschweife und solare Korpuskularstrahlung. *Zeitschrift für Astrophysik*, 29:274.

Bilitza, D., McKinnell, L.-A., Reinisch, B., and Fuller-Rowell, T. (2011). The international reference ionosphere today and in the future. *Journal of Geodesy*, 85:909–920.

Birkeland, K. (1908). *On the cause of magnetic storms and the origin of terrestrial magnetism*. Number 1 in 1. H. Aschehoug & Company.

Blake, S. P. (2017). *Modelling and Monitoring Geomagnetically Induced Currents in Ireland*. PhD thesis, Trinity College Dublin.

Blake, S. P., Gallagher, P. T., Campanyà, J., Hogg, C., Beggan, C. D., Thomson, A. W. P., Richardson, G. S., and Bell, D. (2018). A detailed model of the irish high voltage power network for simulating gics. *Space Weather*, 16(11):1770–1783.

Blake, S. P., Gallagher, P. T., McCauley, J., Jones, A. G., Hogg, C., Campanyà, J., Beggan, C. D., Thomson, A. W. P., Kelly, G. S., and Bell, D. (2016). Geomagnetically induced currents in the irish power network during geomagnetic storms. *Space Weather*, 14(12):1136–1154.

Bolduc, L. (2002). GIC observations and studies in the Hydro-Québec power system. *Journal of Atmospheric and Solar-Terrestrial Physics*, 64:1793–1802.

Bosse, L., Lilensten, J., Johnsen, M. G., Gillet, N., Rochat, S., Delboulbé, A., Curaba, S., Ogawa, Y., Derverchère, P., and Vauclair, S. (2022). The polarisation of auroral emissions: A tracer of the e region ionospheric currents. *J. Space Weather Space Clim.*, 12:17.

Boteler, D. (2006). The super storms of august/september 1859 and their effects on the telegraph system. *Advances in Space Research*, 38(2):159–172. The Great Historical Geomagnetic Storm of 1859: A Modern Look.

Boteler, D. and Pirjola, R. (1998). The complex-image method for calculating the magnetic and electric fields produced at the surface of the earth by the auroral electrojet. *Geophysical Journal*, Volume 132:pp31–40.

Boteler, D. H. and Pirjola, R. J. (2014). Comparison of methods for modelling geomagnetically induced currents. *Annales Geophysicae*, 32(9):1177–1187.

Boteler, D. H. and Pirjola, R. J. (2017). Modeling geomagnetically induced currents. *Space Weather*, 15(1):258–276.

Butler, J. and Hoskin, M. (1987). The archives of armagh observatory. *Journal for the History of Astronomy*, 18(4):295–307.

Cagniard, L. (1953). Basic Theory of the magnetotelluric method of geophysical prospecting. *Geophysics*, 18:605–635.

Caldwell, T. G., Bibby, H. M., and Brown, C. (2004). The magnetotelluric phase tensor. *Geophysical Journal International*, 158(2):457–469.

Campanyà, J., Gallagher, P. T., Blake, S. P., Gibbs, M., Jackson, D., Beggan, C., Richardson, G., and Hogg, C. (2019). Modeling Geoelectric Fields in Ireland and the UK for Space Weather Applications. *Space Weather*, 17:216–237.

Campanyà, J., Gallagher, P. T., Kiyan, D., Blake, S. P., Hogg, C., Scanlon, R., Jackson, D., Gibbs, M., Reay, D., Fullea, J., and Rath, V. (2018). Swemdi: Space weather electromagnet database for ireland. Available at `https://www.gsi.ie/documents/2017-sc-037_FinalReport_CAMPANYA.pdf` as of 16/12/2023.

Campanyà, J., Ogaya, X., Jones, A. G., Rath, V., McConnell, B., Haughton, P. D., Ledo, J., Hogg, C., Blake, S., and Licciardi, A. (2019). Subsurface characterization of the pennsylvanian clare basin, western ireland, by means of joint interpretation of electromagnetic geophysical data and well-log data. *Journal of Geophysical Research: Solid Earth*, 124(7):6200–6222.

Campbell, W. (2003). *Introduction to Geomagnetic Fields: Second Edition*, volume Chapter 3, pages 152–165. Cambridge University Press.

Campbell, W. H. (1980). Observation of electric currents in the Alaska oil pipeline resulting from auroral electrojet current sources. *Geophysical Journal International*, 61(2):437–449.

Campbell, W. H. (1986). An interpretation of induced electric currents in long pipelines caused by natural geomagnetic sources of the upper atmosphere. *Surv Geophys*, 8:239–259.

Card, A., Finch, K., Kelly, D., Kemker, C., and Rose, K. (2023). Conductivity, salinity and total dissolved solids. Technical report, Fondriest Environmental Learning Center.

Carrington, R. C. (1859). Description of a Singular Appearance seen in the Sun on September 1, 1859. *Monthly Notices of the Royal Society*, 20:13–15.

Casanovas, J. (1997). Early observations of sunspots: Scheiner and galileo. In *1st Advances in Solar Physics Euroconference. Advances in Physics of Sunspots*, volume 118, page 3.

Centra-Technology-Inc. (2011). Geomagnetic Storms: Future Global Shocks. OECD International Futures Programme, available at https://web-archive.oecd.org/2022-10-18/99884-46891645.pdf as of 16/12/2023.

Chapman, S. and Bartels, J. (1940). *Geomagnetism, Vol. I: Geomagnetic and Related Phenomena*, chapter 5. Oxford University Press.

Chapman, S. C., McIntosh, S. W., Leamon, R. J., and Watkins, N. W. (2020). Quantifying the solar cycle modulation of extreme space weather. *Geophysical Research Letters*, 47(11):e2020GL087795.

Chave, A. D. and Jones, A. G. (2012). *The Magnetotelluric Method: Theory and Practice*, chapter Distortion of magnetotelluric data: its identification and removal, page 219–302. Cambridge University Press.

Chen, N., Qian, Z., Nabney, I. T., and Meng, X. (2014). Wind power forecasts using gaussian processes and numerical weather prediction. *IEEE Transactions on Power Systems*, 29(2):656–665.

Cid, C., Guerrero, A., Saiz, E., Halford, A. J., and Kellerman, A. C. (2020). Developing the ldi and lci geomagnetic indices, an example of application of the auls framework. *Space Weather*, 18(1):e2019SW002171.

Clark, T. (1992). Computer generated k indices adopted by the british geological survey. *Journal of Atmospheric and Terrestrial Physics*, 54(3):447–456.

Clement, K. (1860). Das grosse nordlicht in der nacht zum 29 august 1959 und die telegraphenverwirrung in nord-amerika und europe, (the great northern light on the

night before 29 august 1859 and the confusion of the telegraph in north america and europe). *Hamburg*, pages 1–21.

Clilverd, M. (2023). Very low frequency observations during an active dc injection campaign that simulated geomagnetic storm effects on high voltage transformers. presented at European Space Weather Week, 2023.

Clilverd, M. A., Rodger, C. J., Brundell, J. B., Dalzell, M., Martin, I., Mac Manus, D. H., and Thomson, N. R. (2020). Geomagnetically induced currents and harmonic distortion: High time resolution case studies. *Space Weather*, 18(10):e2020SW002594.

Cliver, E. W. and Dietrich, W. F. (2013). The 1859 space weather event revisited: limits of extreme activity. *J. Space Weather Space Clim.*, 3:A31.

Cordell, D., Unsworth, M. J., Lee, B., Hanneson, C., Milling, D. K., and Mann, I. R. (2021). Estimating the geoelectric field and electric power transmission line voltage during a geomagnetic storm in alberta, canada using measured magnetotelluric impedance data: The influence of three-dimensional electrical structures in the lithosphere. *Space Weather*, 19(10):e2021SW002803.

Dahal, B. K. and Dahal, R. K. (2017). Landslide hazard map: tool for optimization of low-cost mitigation. *Geoenvironmental Disasters*, 4.

de la Rive, M. A. (1859). *Aurore boréale du 29 aout 1859*, pages 424–128. Comptes rendus de l'Academie des Sciences.

Delhaye, R., Rath, V., Jones, A. G., Muller, M. R., and Reay, D. (2017). Correcting for static shift of magnetotelluric data with airborne electromagnetic measurements: a case study from rathlin basin, northern ireland. *Solid Earth*, 8(3):637–660.

Delsman, J. R., van Baaren, E. S., Siemon, B., Dabekaussen, W., Karaoulis, M. C., Pauw, P. S., Vermaas, T., Bootsma, H., de Louw, P. G. B., Gunnink, J. L., Dubelaar, C. W., Menkovic, A., Steuer, A., Meyer, U., Revil, A., and Essink, G. H. P. O. (2018). Large-scale, probabilistic salinity mapping using airborne electromagnetics for groundwater management in zeeland, the netherlands. *Environmental Research Letters*, 13(8):084011.

Divett, T., Richardson, G. S., Beggan, C. D., Rodger, C. J., Boteler, D. H., Ingham, M., Mac Manus, D. H., Thomson, A. W. P., and Dalzell, M. (2018). Transformer-level modeling of geomagnetically induced currents in new zealand's south island. *Space Weather*, 16(6):718–735.

Dong, X., Liu, Y., and Kappenman, J. G. (2001). Comparative analysis of exciting current harmonics and reactive power consumption from gic saturated transformers. *2001 IEEE Power Engineering Society Winter Meeting. Conference Proceedings (Cat. No.01CH37194)*, 1:318–322 vol.1.

Dungey, J. W. (1961). Interplanetary magnetic field and the auroral zones. *Phys. Rev. Lett.*, 6:47–48.

Earle, S., BCcampus, Panchuk, K., and Projectditor, B. O. T. (2019). *Physical Geology*, chapter Plate Techtonics, pages 341–342. BCcampus, BC Open Textbook Project.

Eastwood, J., Nakamura, R., Turc, L., Mejnertsen, L., and Hesse, M. (2017a). The scientific foundations of forecasting magnetospheric space weather. *Space Sci Rev*, 212:1221–1252.

Eastwood, J. P., Biffis, E., Hapgood, M. A., Green, L., Bisi, M. M., Bentley, R. D., Wicks, R., McKinnell, L.-A., Gibbs, M., and Burnett, C. (2017b). The economic impact of space weather: Where do we stand? *Risk Analysis*, 37(2):206–218.

Erickson, G. M., Spiro, R. W., and Wolf, R. A. (1991). The physics of the harang discontinuity. *Journal of Geophysical Research: Space Physics*, 96(A2):1633–1645.

Fabricius, J. (1611). Account of spots observed on the sun and of their apparent rotation with the sun. *Narratio de maculis in sole observatis et apparente earum cum sole conversione.*

Fitzgerald and Cullum (1889). Reports of the magnetic observations at valentia. *Proc. Roy. Irish Acad.*, 1:221–228.

Fitzgerald, G. F. (1892). Sunspots and magnetic storms. *The Electrician*, 30:48.

Fogg, A. R., Jackman, C. M., Malone-Leigh, J., Gallagher, P. T., Smith, A. W., Lester, M., Walach, M.-T., and Waters, J. E. (2023). Extreme value analysis of ground magnetometer observations at valentia observatory, ireland. *Space Weather*, 21(7):e2023SW003565.

Frankel, A. D., Mueller, C. S., Barnhard, T. P., Leyendecker, E. V., Wesson, R. L., Harmsen, S. C., Klein, F. W., Perkins, D. M., Dickman, N. C., Hanson, S. L., and Hopper, M. G. (2000). Usgs national seismic hazard maps. *Earthquake Spectra*, 16(1):1–19.

Fritsch, M. and Wolter, M. (2023). Saturation of high-frequency current transformers: Challenges and solutions. *IEEE Transactions on Instrumentation and Measurement*, 72:1–10.

Fukushima, N. (1976). Generalized theorem for no ground magnetic effect of vertical currents connected with Pedersen currents in the uniform-conductivity ionosphere. *Report of Ionosphere and Space Research in Japan*, 30(1-2):35–40.

Galilei, G. (1613). Istoria e dimostrazioni intorno alle macchie solari e loro accidenti: Comprese in tre lettere scritte all'illustrissimo signor marco velseri. *In Roma : Appresso Giacomo Mascardi.*

Gannon, J. L., Birchfield, A. B., Shetye, K. S., and Overbye, T. J. (2017). A comparison of peak electric fields and gics in the pacific northwest using 1-d and 3-d conductivity. *Space Weather*, 15(11):1535–1547.

Garton, T. M., Gallagher, P. T., and Murray, S. A. (2018). Automated coronal hole identification via multi-thermal intensity segmentation. *J. Space Weather Space Clim.*, 8:A02.

Gasdia, F. and Marshall, R. A. (2021). A new longwave mode propagator for the earth–ionosphere waveguide. *IEEE Transactions on Antennas and Propagation*, 69(12):8675–8688.

Gaunt, C. T. and Coetzee, G. (2007). Transformer failures in regions incorrectly considered to have low gic-risk. In *2007 IEEE Lausanne Power Tech*, pages 807–812.

Green, J. L., Boardsen, S., Odenwald, S., Humble, J., and Pazamickas, K. A. (2006). Eyewitness reports of the great auroral storm of 1859. *Advances in Space Research*, 38(2):145–154. The Great Historical Geomagnetic Storm of 1859: A Modern Look.

Griffiths, H. (2018). Oliver heaviside and the heaviside layer. *Philosophical Transactions of the Royal Society A: Mathematical, Physical and Engineering Sciences*, 376(2134):20170459.

Groom, R. and Bailey, R. (1989). Decomposition of the magnetotelluric impedance tensor in the presence of local three-dimensional galvanic distortion. *Journal of Geophysical Research*, 94, B2:1913–1925.

Guio, P. and Pécseli, H. L. (2021). The impact of turbulence on the ionosphere and magnetosphere. *Frontiers in Astronomy and Space Sciences*, 7.

Guo, S.-X., Liu, L.-G., Pirjola, R. J., Wang, K.-R., and Dong, B. (2015). Impact of the ehv power system on geomagnetically induced currents in the uhv power system. *IEEE Transactions on Power Delivery*, 30(5):2163–2170.

Hackmann, W. (1995). Instrument and reality: The case of terrestrial magnetism and the northern lights (aurora borealis). *Royal Institute of Philosophy Supplements*, 38:29–51.

Hapgood, M. (2019). The great storm of may 1921: An exemplar of a dangerous space weather event. *Space Weather*, 17(7):950–975.

Hathaway, D. (2010). The solar cycle. *Living Rev. Sol. Phys.*, 7.

Hathaway, D. (2015). *Living Rev. Sol. Phys.*, volume 12, chapter The Solar Cycle. Springer International Publishing.

Hayakawa, H., Ebihara, Y., Willis, D. M., Toriumi, S., Iju, T., Hattori, K., Wild, M. N., Oliveira, D. M., Ermolli, I., Ribeiro, J. R., Correia, A. P., Ribeiro, A. I., and Knipp,

D. J. (2019). Temporal and spatial evolutions of a large sunspot group and great auroral storms around the carrington event in 1859. *Space Weather*, 17(11):1553–1569.

Hayes, L. A., O'Hara, O. S. D., Murray, S. A., and Gallagher, P. T. (2021). Solar flare effects on the earth's lower ionosphere. *Solar Physics*, 296(11).

Heyns, M. J., Lotz, S. I., and Gaunt, C. T. (2021). Geomagnetic pulsations driving geomagnetically induced currents. *Space Weather*, 19(2):e2020SW002557.

Hodgson, R. (1859). On a curious Appearance seen in the Sun. *Monthly Notices of the Royal Society*, 20:15–16.

Horton, R., Boteler, D., Overbye, T. J., Pirjola, R., and Dugan, R. C. (2012). A test case for the calculation of geomagnetically induced currents. *IEEE Transactions on Power Delivery*, 27(4):2368–2373.

Hughes, W. J. (1995). The magnetopause, magnetotail, and magnetic reconnection. In *Introduction to space physics*, pages 227–287. Cambridge University Press.

Hübert, J., Beggan, C. D., Richardson, G. S., Martyn, T., and Thomson, A. W. P. (2020). Differential magnetometer measurements of geomagnetically induced currents in a complex high voltage network. *Space Weather*, 18(4):e2019SW002421.

IEEE (2015). Ieee guide for safety in ac substation grounding. *IEEE Std 80-2013 (Revision of IEEE Std 80-2000/ Incorporates IEEE Std 80-2013/Cor 1-2015)*, pages 1–226.

Infield, M. (2009). The Carrington Event: Flare or CME? A Report. Published on the Armagh Observatory Website, `http://www.climate.armagh.ac.uk/Carrington_Flare_Report.pdf`.

Janosek, M. (2017). *Parallel Fluxgate Magnetometers*, pages 41–61. Springer International Publishing, Cham.

Johnsen, M. G. (2013). Real-time determination and monitoring of the auroral electrojet boundaries. *Journal of Space Weather and Space Climate*, 3:A28.

Jones, A. G. and Groom, R. W. (1993). Strike-angle determination from the magnetotelluric impedance tensor in the presence of noise and local distortion: rotate at your peril! *Geophysical Journal International*, 113(2):524–534.

Jones, A. G., Ledo, J., Ferguson, I. J., Craven, James A. andUnsworth, M. J., Chouteau, M., and Spratt, J. E. (2014). The electrical resistivity of canada's lithosphere and correlation with other parameters: contributions from lithoprobe and other programmes. *Canadian Journal of Earth Sciences*, 51.

Jones, A. G., Muller, M. R., Hamilton, M. P., Miensopust, M., Spratt, J., Garcia, X.,

Evans, R., Fourie, S., Cole, P., Hutchins, D., Ngwisanyi, T., Evans, S., Mountford, A., Pettit, W., and SAMTEX team, t. (2007). Southern african magnetotelluric experiment (samtex): Project overview and regional results. In *10th SAGA Biennial Technical Meeting and Exhibition*. European Association of Geoscientists and Engineers.

Kamide, Y. and Baumjohann, W. (1993). *Current Issues of Magnetosphere-Ionosphere Coupling*, pages 123–157. Springer Berlin Heidelberg, Berlin, Heidelberg.

Katamzi, Z. T. and Habarulema, J. B. (2014). Traveling ionospheric disturbances observed at south african midlatitudes during the 29–31 october 2003 geomagnetically disturbed period. *Advances in Space Research*, 53(1):48–62.

Kauristie, K., Andries, J., Beck, P., Berdermann, J., Berghmans, D., Cesaroni, C., De Donder, E., de Patoul, J., Dierckxsens, M., Doornbos, E., Gibbs, M., Hammond, K., Haralambous, H., Harri, A.-M., Henley, E., Kriegel, M., Laitinen, T., Latocha, M., Maneva, Y., Perrone, L., Pica, E., Rodriguez, L., Romano, V., Sabbagh, D., Spogli, L., Stanislawska, I., Tomasik, L., Tshisaphungo, M., van Dam, K., van den Oord, B., Vanlommel, P., Verhulst, T., Wilken, V., Zalizovski, A., and Österberg, K. (2021). Space weather services for civil aviation—challenges and solutions. *Remote Sensing*, 13(18).

Kazerooni, M., Zhu, H., and Overbye, T. J. (2017). Improved modeling of geomagnetically induced currents utilizing derivation techniques for substation grounding resistance. *IEEE Transactions on Power Delivery*, 32(5):2320–2328.

Kelbert, A., Balch, C., Pulkkinen, A., Egbert, G., Love, J., Rigler, E., and Fujii, I. (2017). Methodology for time-domain estimation of storm time geoelectric fields using 3-D magnetotelluric response tensors. *Space Weather*, 15:874–894.

Kelly, G. S., Viljanen, A., Beggan, C. D., and Thomson, A. W. P. (2017). Understanding gic in the uk and french high-voltage transmission systems during severe magnetic storms. *Space Weather*, 15(1):99–114.

Kent, D. V. and Gradstein, F. M. (1985). A Cretaceous and Jurassic geochronology. *GSA Bulletin*, 96(11):1419–1427.

Kiyan, D., Campanya, J., Fullea, J., Hogg, C., Blake, S. P., Rath, V., Gallagher, P., and Scanlon, R. (2018). Electrical conductivity distribution of the lithosphere in Ireland revealed by magnetotelluric imaging. In *AGU Fall Meeting*, volume 2018.

Kiyan, D., Hogg, C., Campanya, J., Bean, C. J., Fullea, J., Blake, S. P., Malone-Leigh, J., Gallagher, P. T., Rath, V., Jones, A. G., and Scanlon, R. (2023). 3-d magnetotelluric assessment of the geo-resources potential of the irish crust. In *EGU General Assembly*.

Koen, J. and Gaunt, T. (2003). Geomagnetically induced currents in the southern african electricity transmission network. In *2003 IEEE Bologna Power Tech Conference Proceedings,*, volume 1, page 7.

Kruglyakov, M., Kuvshinov, A., and Marshalko, E. (2022). Real-time 3-d modeling of the ground electric field due to space weather events. a concept and its validation. *Space Weather*, 20(4).

Künzel, H. (1965). Zur Klassifikation von Sonnenfleckengruppen. *Astronomische Nachrichten*, 288:177.

Käufl, J. S., Grayver, A. V., and Kuvshinov, A. V. (2018). Topographic distortions of magnetotelluric transfer functions: a high-resolution 3-D modelling study using real elevation data. *Geophysical Journal International*, 215(3):1943–1961.

Lakhina, G. S. and Tsurutani, B. T. (2016). Geomagnetic storms: historical perspective to modern view. *Geoscience Letters*, 3:5.

Lanzerotti, L. (2017). Space weather: Historical and contemporary perspectives. *Space Sci Rev 212*, page 1253–1270.

Lapthorn, A., Beggan, C., Clilverd, M., Huebert, J., and Rodger, C. (2023). An overview of the unique dc injection campaign for replicating gics on high voltage transformers in new zealand. *Presented at Space Weather Week, 2023.*

Ledo, J., Queralt, P., and Pous, J. (1998). Effects of galvanic distortion on magnetotelluric data over a three dimensional structure. *Geophysical Journal International*, 132:295–301.

Lehtinen, M. and Pirjola, R. (1985). Currents produced in earthed conductor networks by geomagnetically-induced electric fields. *Ann. Geophys.*, 3:479–484.

Ley-Cooper, A. Y., Brodie, R. C., and Richardson, M. (2020). Ausaem: Australia's airborne electromagnetic continental-scale acquisition program. *Exploration Geophysics*, 51(1):193–202.

Liu, C., Wang, X., Zhang, S., and Xie, C. (2019). Effects of lateral conductivity variations on geomagnetically induced currents: H-polarization. *IEEE Access*, 7:6310–6318.

Lodge, O. (1900). Sunspots, magnetic storms, comet tails, atmospheric electricity, and aurorae. *The Electrician*, 46:249.

Loke, M. (2001). Tutorial: 2-d and 3-d electrical imaging surveys.

Love, J. J., Lucas, G. M., Kelbert, A., and Bedrosian, P. A. (2018). Geoelectric hazard maps for the mid-atlantic united states: 100 year extreme values and the 1989 magnetic storm. *Geophysical Research Letters*, 45(1):5–14.

Love, J. J., Lucas, G. M., Rigler, E. J., Murphy, B. S., Kelbert, A., and Bedrosian, P. A. (2022). Mapping a magnetic superstorm: March 1989 geoelectric hazards and impacts on united states power systems. *Space Weather*, 20(5):e2021SW003030.

Lucas, G. M., Love, J. J., Kelbert, A., Bedrosian, P. A., and Rigler, E. J. (2020). A 100-year geoelectric hazard analysis for the u.s. high-voltage power grid. *Space Weather*, 18(2):e2019SW002329.

Mac Manus, D. H., Rodger, C. J., Ingham, M., Clilverd, M. A., Dalzell, M., Divett, T., Richardson, G. S., and Petersen, T. (2022). Geomagnetically induced current model in new zealand across multiple disturbances: Validation and extension to non-monitored transformers. *Space Weather*, 20(2):e2021SW002955.

Mac Manus, D. H., Rodger, C. J., Renton, A., Ronald, J., Harper, D., Taylor, C., Dalzell, M., Divett, T., and Clilverd, M. A. (2023). Geomagnetically induced current mitigation in new zealand: Operational mitigation method development with industry input. *Space Weather*, 21(11):e2023SW003533.

MacAlester, M. H. and Murtagh, W. (2014). Extreme space weather impact: An emergency management perspective. *Space Weather*, 12(8):530–537.

Madden, T. and Nelson, P. (1964). A defense of cagniard's magnetotelluric method. *Magnetotelluric methods*, pages 89–102.

Madsen, F. D., Beggan, C. D., and Whaler, K. A. (2022). Forecasting changes of the magnetic field in the united kingdom from l1 lagrange solar wind measurements. *Frontiers in Physics*, 10:1017781.

Malone-Leigh, J., Campanyà, J., Gallagher, P. T., Neukirch, M., Hogg, C., and Hodgson, J. (2023). Nowcasting geoelectric fields in ireland using magnetotelluric transfer functions. *J. Space Weather Space Clim.*, 13:6.

Malone-Leigh, J., Campanyà, J., Gallagher, P. T., Hodgson, J., and Hogg, C. (2024). Mapping geoelectric field hazards in ireland. *Space Weather*, 22(2):e2023SW003638.

Marshalko, E., Kruglyakov, M., Kuvshinov, A., Juusola, L., Kwagala, N. K., Sokolova, E., and Pilipenko, V. (2021). Comparing three approaches to the inducing source setting for the ground electromagnetic field modeling due to space weather events. *Space Weather*, 19(2):e2020SW002657.

Marshall, R. A., Wang, L., Paskos, G. A., Olivares-Pulido, G., Van Der Walt, T., Ong, C., Mikkelsen, D., Hesse, G., McMahon, B., Van Wyk, E., Ivanovich, G., Spoor, D., Taylor, C., and Yoshikawa, A. (2019). Modeling geomagnetically induced currents in australian power networks using different conductivity models. *Space Weather*, 17(5):727–756.

Marti, L. (2014). Effects of series compensation capacitors on geomagnetically induced currents. *IEEE Transactions on Power Delivery*, 29(4):2032–2033.

Matandirotya, E., Cilliers, P. J., Van Zyl, R. R., Oyedokun, D. T., and de Villiers, J. (2016). Differential magnetometer method applied to measurement of geomagnetically induced currents in southern african power networks. *Space Weather*, 14(3):221–232.

Matzka, J., Stolle, C., Yamazaki, Y., Bronkalla, O., and Morschhauser, A. (2021). The geomagnetic kp index and derived indices of geomagnetic activity. *Space Weather*, 19(5):e2020SW002641.

McCarthy, A. J. P. (1957). The irish national electrification scheme. *Geographical Review*, 47(4):539–554.

McCormack, T., Campanyà, J., and Naughton, O. (2022). A methodology for mapping annual flood extent using multi-temporal sentinel-1 imagery. *Remote Sensing of Environment*, 282:113273.

McIntosh, S. W. and Leamon, R. J. (2014). On magnetic activity band overlap, interaction, and the formation of complex solar active regions. *The Astrophysical Journal Letters*, 796(1):L19.

McLay, S. A. and Beggan, C. D. (2010). Interpolation of externally-caused magnetic fields over large sparse arrays using spherical elementary current systems. *Annales Geophysicae*, 28(9):1795–1805.

Menvielle, M., Papitashvili, N., Häkkinen, L., and Sucksdorff, C. (1995). Computer production of K indices: review and comparison of methods. *Geophysical Journal International*, 123(3):866–886.

Miensopust, M. P., Queralt, P., Jones, A. G., and the 3D MT modellers (2013). Magnetotelluric 3-D inversion—a review of two successful workshops on forward and inversion code testing and comparison. *Geophysical Journal International*, 193(3):1216–1238.

Miles, D., Mann, I., Kale, A., Milling, D., Narod, B., Bennest, J., Barona, D., and Unsworth, M. (2017). The effect of construction material on the thermal gain dependence of a fluxgate magnetometer sensor. *Geoscientific Instrumentation, Methods and Data Systems Discussions*, pages 1–34.

Miller, R. L., Bradford, W. L., and Peters, N. E. (1988). Specific conductance: Theoretical considerations and application to analytical quality control. Technical report, U.S. Geological Survey Water-Supply.

Moorkamp, M., Özaydın, S., Selway, K., and Jones, A. G. (2022). Probing the southern african lithosphere with magnetotellurics—part i: Model construction. *Jour-*

nal of Geophysical Research: Solid Earth, 127(3):e2021JB023117. e2021JB023117 2021JB023117.

Morgan, H. and Taroyan, Y. (2017). Global conditions in the solar corona from 2010 to 2017. *Science advances*, 3(7):e1602056.

Morrissey, P. J., McCormack, T., Naughton, O., Johnston, P. M., and Gill, L. W. (2020). Modelling groundwater flooding in a lowland karst catchment. *Journal of Hydrology*, 580:124361.

Morton Briggs, J. (1967). Aurora and enlightenment eighteenth-century explanations of the aurora borealis. *Isis*, 54:491–503.

Morzfeld, M. and Hodyss, D. (2019). Gaussian approximations in filters and smoothers for data assimilation. *Tellus A: Dynamic Meteorology and Oceanography*, 71(1):1600344.

Mualchin, L. (2011). History of modern earthquake hazard mapping and assessment in california using a deterministic or scenario approach. *Pure and Applied Geophysics*, 168:383–407.

Murphy, B. S., Lucas, G. M., Love, J. J., Kelbert, A., Bedrosian, P. A., and Rigler, E. J. (2021). Magnetotelluric sampling and geoelectric hazard estimation: Are national-scale surveys sufficient? *Space Weather*, 19(7):e2020SW002693.

Murray, S. A. (2018). The importance of ensemble techniques for operational space weather forecasting. *Space Weather*, 16(7):777–783.

Myllys, M., Viljanen, A., Rui, O. A., and Ohnstad, T. M. (2014). Geomagnetically induced currents in norway: the northernmost high-voltage power grid in the world. *J. Space Weather Space Clim.*, 4:A10.

Nandy, D. (2021). Progress in solar cycle predictions: Sunspot cycles 24–25 in perspective: Invited review. *Solar Physics*, 296(3):54.

Neugebauer, M. (1997). Pioneers of space physics: A career in the solar wind. *Journal of Geophysical Research: Space Physics*, 102(A12):26887–26894.

Neukirch, M., Galiana, S., and García, X. (2020). Appraisal of magnetotelluric galvanic electric distortion by optimizing amplitude and phase tensor relations. *Geophysics*, 85:E79–E98.

Neukirch, M., Rudolf, D., Garcia, X., and Galiana, S. (2019). Amplitude-phase decomposition of the magnetotelluric impedance tensor. *Geophysics*, page E301–E310.

Newell, P. T., Liou, K., Zhang, Y., Sotirelis, T., Paxton, L. J., and Mitchell, E. J. (2014). Ovation prime-2013: Extension of auroral precipitation model to higher disturbance levels. *Space Weather*, 12(6):368–379.

Nilsson, A., Suttie, N., Stoner, J. S., and Muscheler, R. (2022). Recurrent ancient geomagnetic field anomalies shed light on future evolution of the south atlantic anomaly. *Proceedings of the National Academy of Sciences*, 119(24):e2200749119.

Ontiveros, V. and Gonzalez-Esparza, J. A. (2010). Geomagnetic storms caused by shocks and icmes. *Journal of Geophysical Research: Space Physics*, 115(A10).

Oughton, E. J., Skelton, A., Horne, R. B., Thomson, A. W. P., and Gaunt, C. T. (2017). Quantifying the daily economic impact of extreme space weather due to failure in electricity transmission infrastructure. *Space Weather*, 15(1):65–83.

Oyedukun, D., Heyns, M., Cilliers, P., and Gaunt, C. (2020). Frequency Components of Geomagnetically Induced Currents for Power System Modelling. *International Saupec Conference*, pages 1–6.

Parker, E. (1969). Theoretical studies of the solar wind phenomenon. *Space Science Reviews*, 9(3):325–360.

Parker, E. N. (1958). Dynamics of the interplanetary gas and magnetic fields. *Astrophyscical Journal*, 128:664.

Partamies, N., Juusola, L., Tanskanen, E., Kauristie, K., Weygand, J. M., and Ogawa, Y. (2011). Substorms during different storm phases. *Annales Geophysicae*, 29(11):2031–2043.

Patowary, R., Singh, S., and Bhuyan, K. (2013). A study of seasonal variation of geomagnetic activity. *Research Journal of Physical and Applied Sciences*, 2:1–11.

Patro, P. K., Uyeshima, M., and Siripunvaraporn, W. (2012). Three-dimensional inversion of magnetotelluric phase tensor data. *Geophysical Journal International*, 192:58–66.

Patterson, C. J., Wild, J. A., and Boteler, D. H. (2023). Modeling the impact of geomagnetically induced currents on electrified railway signaling systems in the united kingdom. *Space Weather*, 21(3):e2022SW003385.

Pirjola, R. (2000). Geomagnetically induced currents during magnetic storms. *IEEE Transactions on Plasma Science*, 28(6):1867–1873.

Prescott, G. (1875). *Theory and Practice of the Electrical Telegraph*. Osgood and Co.

Price, A. (1949). The induction of electric currents in non-uniform thin sheets and shells. *The Quarterly Journal of Mechanics and Applied Mathematics*, 2(3):283–310.

Pulkkinen, A., Bernabeu, E., Eichner, J., Beggan, C., and Thomson, A. W. P. (2012). Generation of 100-year geomagnetically induced current scenarios. *Space Weather*, 10(4):04003.

Pulkkinen, A., Bernabeu, E., Thomson, A., Viljanen, A., Pirjola, R., Boteler, D., Eichner, J., Cilliers, P. J., Welling, D., Savani, N. P., Weigel, R. S., Love, J. J., Balch, C., Ngwira, C. M., Crowley, G., Schultz, A., Kataoka, R., Anderson, B., Fugate, D., Simpson, J. J., and MacAlester, M. (2017). Geomagnetically induced currents: Science, engineering, and applications readiness. *Space Weather*, 15(7):828–856.

Pulkkinen, A., Viljanen, A., Pajunpää, K., and Pirjola, R. (2001). Recordings and occurrence of geomagnetically induced currents in the finnish natural gas pipeline network. *Journal of Applied Geophysics*, 48(4):219–231.

Qin, W., Wang, P., Han, X., and Du, X. (2011). Reactive power aspects in reliability assessment of power systems. *IEEE Transactions on Power Systems*, 26(1):85–92.

Rao, C. K., Jones, A. G., Moorkamp, M., and Weckmann, U. (2014). Implications for the lithospheric geometry of the iapetus suture beneath ireland based on electrical resistivity models from deep-probing magnetotellurics. *Geophysical Journal International*, 198(2):737–759.

Redmon, R. J., Seaton, D. B., Steenburgh, R., He, J., and Rodriguez, J. V. (2018). September 2017's geoeffective space weather and impacts to caribbean radio communications during hurricane response. *Space Weather*, 16(9):1190–1201.

Richardson, G. S. and Thomson, A. W. P. (2022). Probabilistic hazard assessment: Application to geomagnetic activity. *J. Space Weather Space Clim.*, 12:4.

Roberts, P. H. and Glatzmaier, G. A. (2000). Geodynamo theory and simulations. *Rev. Mod. Phys.*, 72:1081–1123.

Rodger, C. J., Mac Manus, D. H., Dalzell, M., Thomson, A. W. P., Clarke, E., Petersen, T., Clilverd, M. A., and Divett, T. (2017). Long-term geomagnetically induced current observations from new zealand: Peak current estimates for extreme geomagnetic storms. *Space Weather*, 15(11):1447–1460.

Rogers, N. C., Wild, J. A., Eastoe, E. F., Gjerloev, J. W., and Thomson, A. W. P. (2020). A global climatological model of extreme geomagnetic field fluctuations. *J. Space Weather Space Clim.*, 10:5.

Rosenqvist, L., Fristedt, T., Dimmock, A. P., Davidsson, P., Fridström, R., Hall, J. O., Hesslow, L., Kjäll, J., Smirnov, M. Y., Welling, D., and Wintoft, P. (2022). 3d modeling of geomagnetically induced currents in sweden—validation and extreme event analysis. *Space Weather*, 20(3):e2021SW002988.

Rostoker, G. (1972). Geomagnetic indices. *Reviews of Geophysics*, 10(4):935–950.

Rung-Arunwan, T., Siripunvaraporn, W., and Utada, H. (2022). The effect of initial

and prior models on phase tensor inversion of distorted magnetotelluric data. *Earth Planets Space*, 74.

Russell, C. T. and McPherson, R. L. (1973). Semiannual variation of geomagnetic activity. *Journal of Geophysical Research (1896-1977)*, 78(1):92–108.

Sabine, E. (1850). Ix. on the means adopted in the british colonial magnetic observatories for determining the absolute values, secular change, and annual variation of the magnetic force. *Philosophical Transactions of the Royal Society of London*, 140:201–219.

Samrock, F., Grayver, A. V., Eysteinsson, H., and Saar, M. O. (2018). Magnetotelluric image of transcrustal magmatic system beneath the tulu moye geothermal prospect in the ethiopian rift. *Geophysical Research Letters*, 45:847–855.

Schatten, K. H., Wilcox, J. M., and Ness, N. F. (1969). A model of interplanetary and coronal magnetic fields. *Solar Physics*, 6:442–455.

Schmidt, A., Dabas, M., and Sarris, A. (2020). Dreaming of Perfect Data:Characterizing Noise in Archaeo-Geophysical Measurements. *Geosciences*, 10:382–390.

Schrijver, C. J., Dobbins, R., Murtagh, W., and Petrinec, S. M. (2014). Assessing the impact of space weather on the electric power grid based on insurance claims for industrial electrical equipment. *Space Weather*, 12(7):487–498.

Schwabe, M. (1843). Die Sonne. Von Herrn Hofrath Schwabe. *Astronomische Nachrichten*, 20(17):283.

Simpson, F. and Bahr, K. (2005). *Practical magnetotellurics*. Cambridge University Press.

Smith, A. W., Forsyth, C., Rae, I. J., Garton, T. M., Bloch, T., Jackman, C. M., and Bakrania, M. (2021). Forecasting the probability of large rates of change of the geomagnetic field in the uk: Timescales, horizons, and thresholds. *Space Weather*, 19(9):e2021SW002788.

Smith, A. W., Rae, I. J., Forsyth, C., Oliveira, D. M., Freeman, M. P., and Jackson, D. R. (2020). Probabilistic forecasts of storm sudden commencements from interplanetary shocks using machine learning. *Space Weather*, 18(11):e2020SW002603.

Stempels, H. C. (2011). Anders Celsius' Contributions to Meridian Arc Measurements and the Establishment of an Astronomical Observatory in Uppsala. *Baltic Astronomy*, 20:179–185.

Steuer, A., Smirnova, M., Becken, M., Schiffler, M., Günther, T., Rochlitz, R., Yogeshwar, P., Mörbe, W., Siemon, B., Costabel, S., Preugschat, B., Ibs-von Seht, M.,

Zampa, L. S., and Müller, F. (2020). Comparison of novel semi-airborne electromagnetic data with multi-scale geophysical, petrophysical and geological data from schleiz, germany. *Journal of Applied Geophysics*, 182:104172.

Sugiura, M. (1964). Hourly values of equatorial dst for the igy. *Ann. Int. Geophys. Yr.*, Vol: 35.

Svalgaard, L. (2017). Reconstruction of solar extreme ultraviolet flux 1740-2015. *Solar Physics*, 292.

Thébault, E., Finlay, C. C., Beggan, C. D., Alken, P., Aubert, J., Barrois, O., Bertrand, F., Bondar, T., Boness, A., Brocco, L., Canet, E., Chambodut, A., Chulliat, A., Coïsson, P., Civet, F., Du, A., Fournier, A., Fratter, I., Gillet, N., Hamilton, B., Hamoudi, M., Hulot, G., Jager, T., Korte, M., Kuang, W., Lalanne, X., Langlais, B., Léger, J.-M., Lesur, V., Lowes, F. J., Macmillan, S., Mandea, M., Manoj, C., Maus, S., Olsen, N., Petrov, V., Ridley, V., Rother, M., Sabaka, T. J., Saturnino, D., Schachtschneider, R., Sirol, O., Tangborn, A., Thomson, A., Tøffner-Clausen, L., Vigneron, P., Wardinski, I., and Zvereva, T. (2015). International Geomagnetic Reference Field: the 12th generation. *Earth, Planets and Space*, 67:79.

Thomson, A., Gaunt, C., Cilliers, P., Wild, J., Opperman, B., Mckinnell, L.-A., Kotze, P., Ngwira, C., and Lotz, S. (2010). Present day challenges in understanding the geomagnetic hazard to national power grids. *Advances in Space Research*, 45:1182–1190.

Thomson, W. (1893). President's address. *Proceedings of the Royal Society of London*, 52:300–315.

Tietze, K., Ritter, O., and Egbert, G. D. (2015). 3-d joint inversion of the magnetotelluric phase tensor and vertical magnetic transfer functions. *Geophysical Journal International*, 203:1128–1148.

Tikhonov, A. (1950). On determining electrical characteristics of the deep layers of the Earth's crust. *Doklady*, 73:295–297.

Torta, J., Pavon-Carrasco, F., Marshal, S., and Finlay, C. (2015). Evidence for a new geomagnetic jerk in 2014. *Geophysical Research Letters*, 42:7933–7940.

Torta, J. M., Marcuello, A., Campanyà, J., Marsal, S., Queralt, P., and Ledo, J. (2017). Improving the modeling of geomagnetically induced currents in spain. *Space Weather*, 15(5):691–703.

Torta, J. M., Marsal, S., Ledo, J., Queralt, P., Canillas-Pérez, V., Piña-Varas, P., Curto, J. J., Marcuello, A., and Martí, A. (2021). New detailed modeling of gics in the spanish power transmission grid. *Space Weather*, 19(9):e2021SW002805.

Torta, J. M., Marsal, S., Piña-Varas, P., Hafizi, R., Martí, A., Campanyà, J., Canillas-

Pérez, V., Curto, J. J., Ledo, J., Queralt, P., and Marcuello, A. (2023). Expected geomagnetically induced currents in the spanish islands power transmission grids. *Space Weather*, 21(7):e2023SW003426.

Torta, J. M., Marsal, S., and Quintana, M. (2014). Assessing the hazard from geomagnetically induced currents to the entire high-voltage power network in Spain. *Earth, Planets and Space*, 66:87.

Tousey, R. (1973). Space research xiii. *Adakemie-Verlag, Berlin*, page 713.

Upton, L. A. and Hathaway, D. H. (2023). Solar cycle precursors and the outlook for cycle 25. *Journal of Geophysical Research: Space Physics*, 128(10):e2023JA031681.

Utada, H. and Munekane, H. (2000). On galvanic distortion of regional 3-D MT impedances On galvanic distortion of regional three-dimensional magnetotelluric impedances. *Geophysical Journal International*, 140(2):385–398.

van Driel-Gesztelyi, L. and Green, L. M. (2015). Evolution of Active Regions. *Living Reviews in Solar Physics*, 12(1):1.

Von Humboldt, A. (1808). Die vollftandigfte aller bisherigen beobachtungen über den einflufs des nords lichts auf die magnetnadel. *Annales der Physik*, 29.

Wagner, R. J., Boulger, R. W., Oblinger, C. J., and Smith, B. A. (2006). Guidelines and standard procedures for continuous water-quality monitors: Station operation, record computation, and data reporting. *USGS Techniques and Methods*, 1-D3.

Whitten, R., Poppoff, I., Edmonds, R., and Berning, W. (1965). Effective Recombination Coefficients in the Lower Ionosphere. *Journal of Geophysical Research*, Volume 70:1737–1742.

Wilkinson, P. J., Nielsen, E., and Luhr, H. (1986). Ionospheric conductances: Associations between ionospheric e region electric fields and ground magnetometer variations. *Journal of Geophysical Research: Space Physics*, 91(A5):5839–5849.

Xu, Z., Pankenier, D. W., and Jiang, Y. (2000). *Physics Today*, chapter East Asian Archaeoastronomy: Historical Records of Astronomical Observations of China, Japan, and Korea, page 56. London: Gordon and Breach.

Zeraati, M., Arshadizadeh, R., Chauhan, N. P. S., and Sargazi, G. (2021). Genetic algorithm optimization of magnetic properties of fe-co-ni nanostructure alloys prepared by the mechanical alloying by using multi-objective artificial neural networks for the core of transformer. *Materials Today Communications*, 28:102653.

Zhang, J., Temmer, M., Gopalswamy, N., Malandraki, O., Nitta, N. V., Patsourakos, S., Shen, F., Vršnak, B., Wang, Y., Webb, D., Desai, M. I., Dissauer, K., Dresing, N., Dumbović, M., Feng, X., Heinemann, S. G., Laurenza, M., Lugaz, N., and Zhuang,

B. (2021). Earth-affecting solar transients: a review of progresses in solar cycle 24. *Prog Earth Planet Sci 8*, 56.

A1 Additional Hazard Maps

Below, the hazard maps analysed for different thresholds are presented, both with and without a galvanic correction (Figures A1.1 and A1.2). The hazard maps are repeated for 100 mV/km, a weaker threshold that is more commonly exceeded, that may be more appropriate for pipelines than 500 mV/km, as pipeline degradation is affected more by induction duration rather than by extreme amplitudes. A hazard map of 2 V/km is also included, a map that may be better suited for railways, as more extreme amplitudes in the geoelectric field are usually required to generate a strong enough GIC to lead to false signaling (Figures A1.3 and A1.4). Note that 2 V/km is never exceeded during Kp = 8 events.

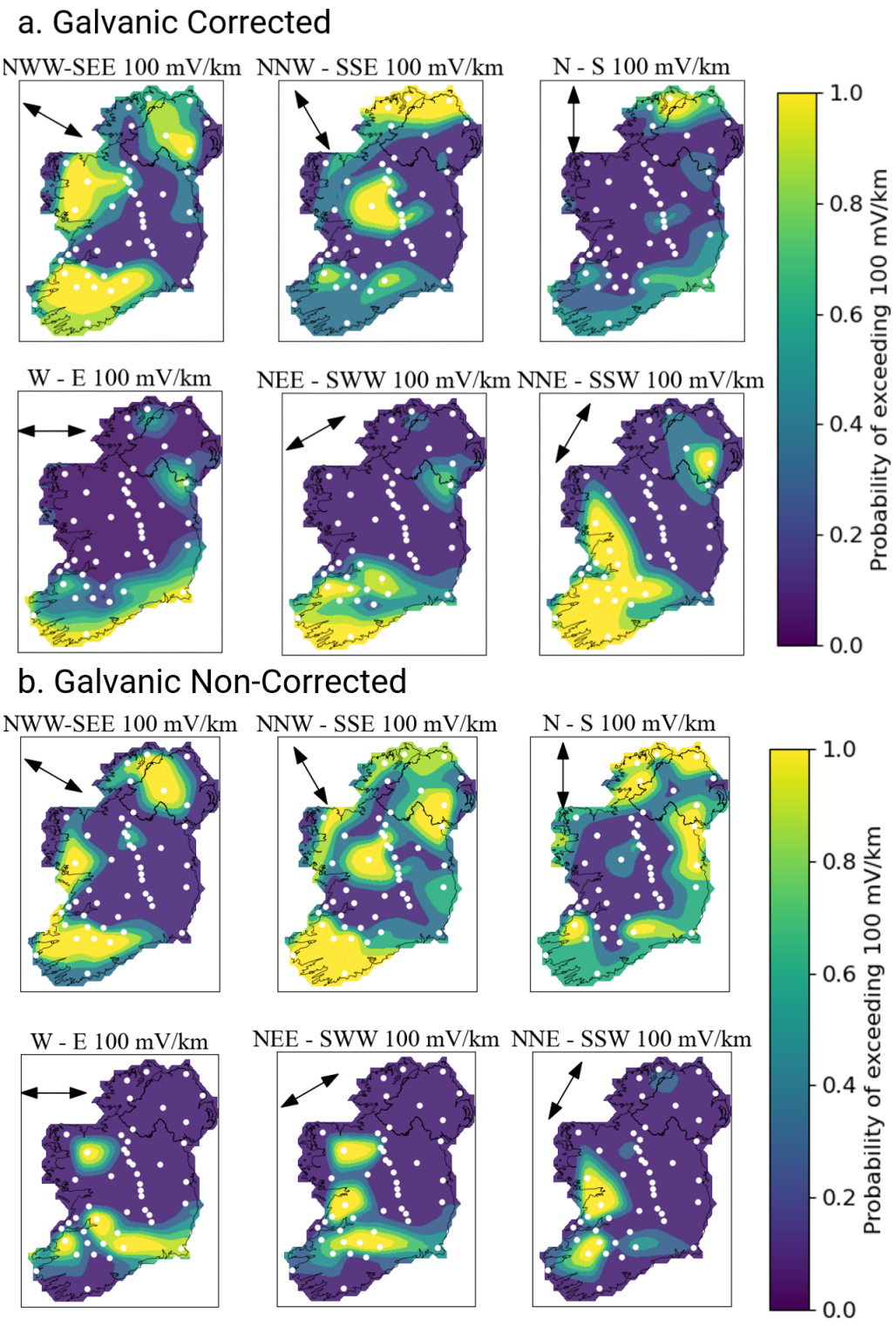

Figure A1.1: The probability of exceeding a geoelectric field threshold of 500 mV/km with galvanic corrected (top six panels) and galvanic non-corrected (bottom six panels) geoelectric fields are mapped for Kp = 8 storms. The direction the threshold is exceeded in, is denoted in each subtitle, as well as by vectors within each subplot (top left of each panel).

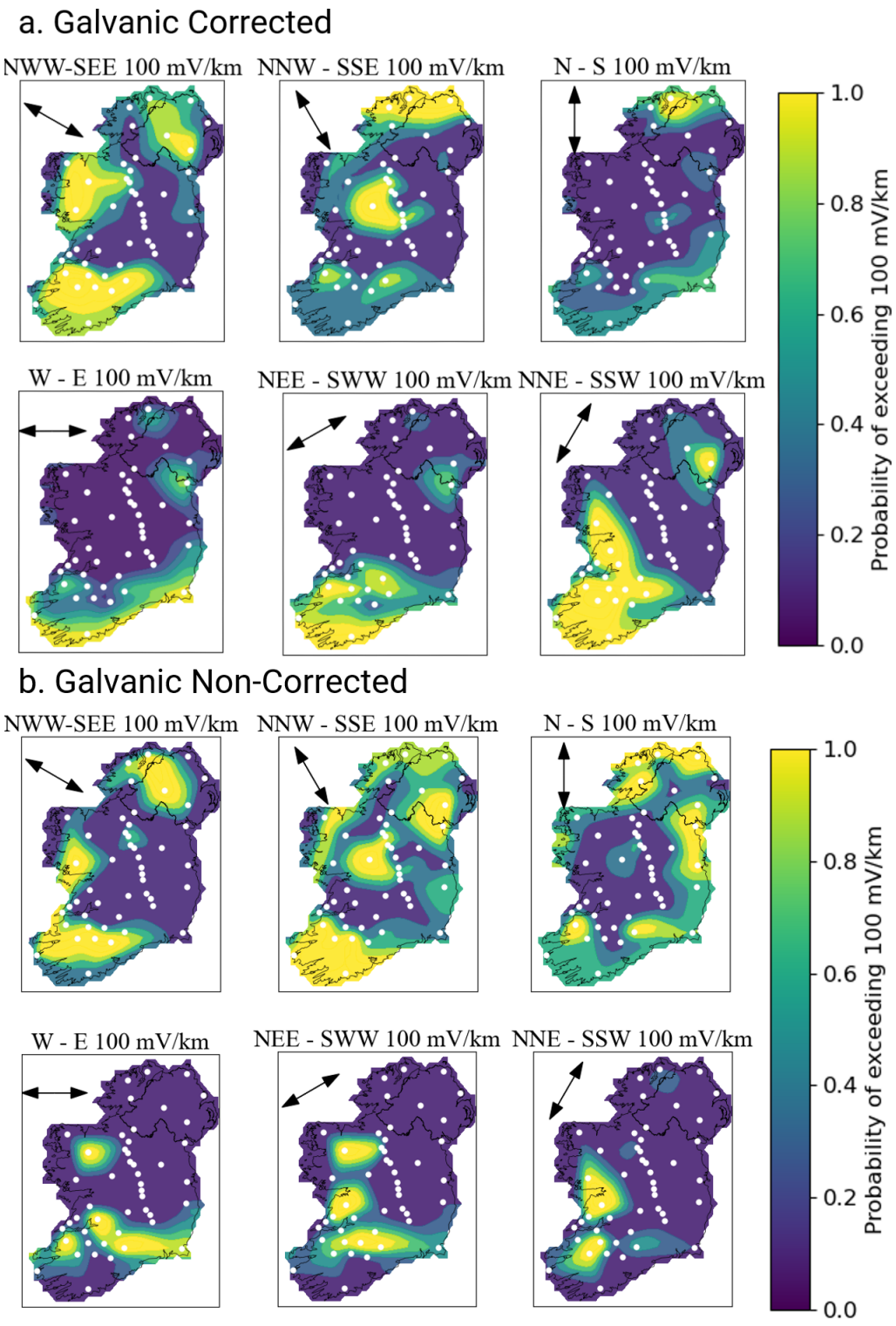

Figure A1.2: The probability of exceeding a geoelectric field threshold of 500 mV/km with galvanic corrected (top six panels) and galvanic non-corrected (bottom six panels) geoelectric fields are mapped for Kp = 9 storms. The direction the threshold is exceeded in, is denoted in each subtitle, as well as by vectors within each subplot (top left of each panel).

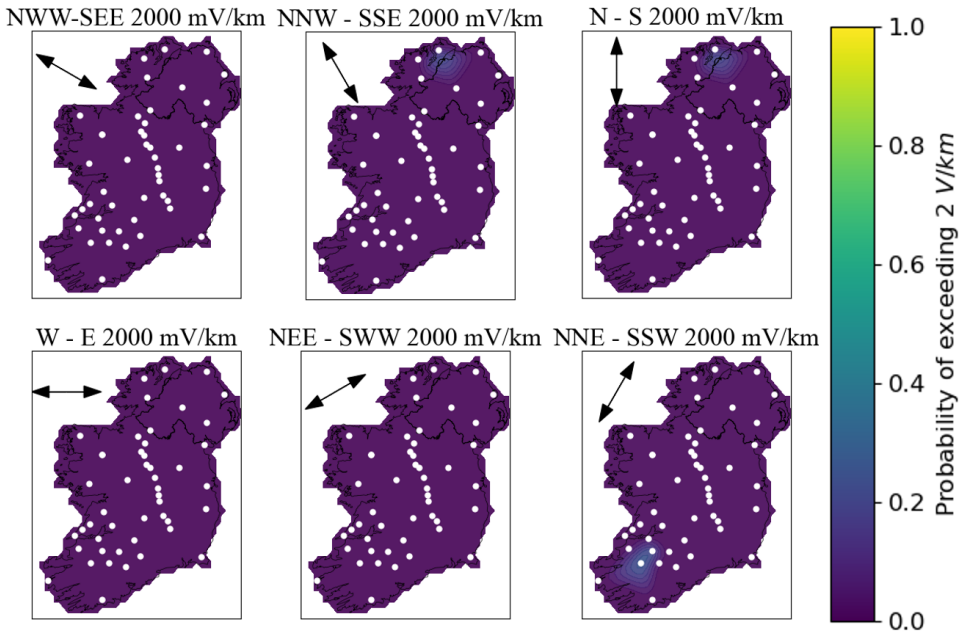

Figure A1.3: The probability of exceeding a geoelectric field threshold of 2000 mV/km for Kp = 9 mapped, corrected for galvanic distortion correction. The direction the threshold is exceeded in, is denoted in each subtitle, as well as by vectors within each subplot (top left).

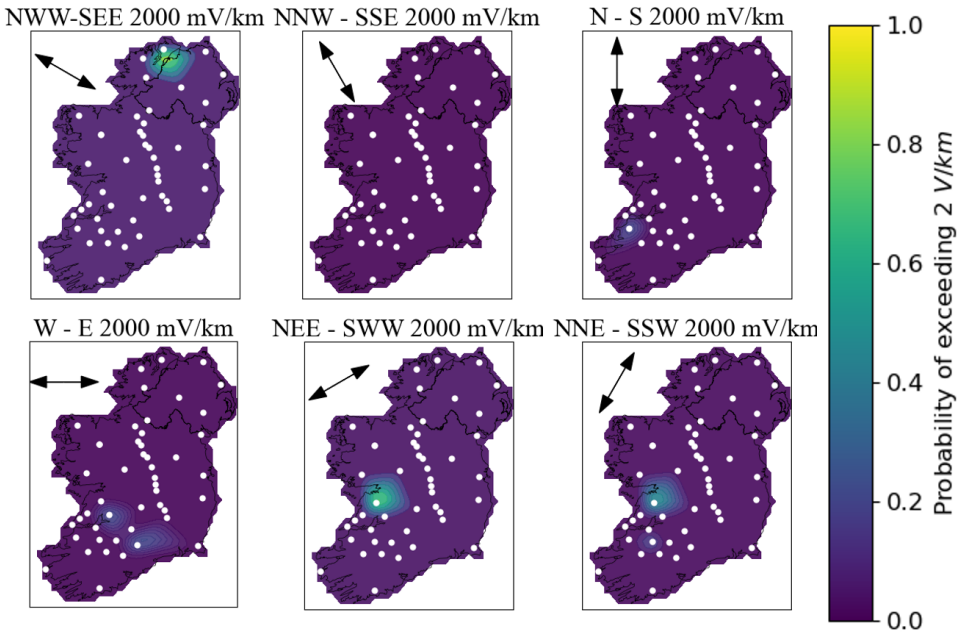

Figure A1.4: The probability of exceeding a geoelectric field threshold of 2000 mV/km for Kp = 9 mapped, without a galvanic distortion correction. The direction the threshold is exceeded in, is denoted in each subtitle, as well as by vectors within each subplot (top left).